



**HAL**  
open science

# Epitaxial growth, atomic structure and exchange coupling of ultrathin bilayers of oxides on metals

Anne Lamirand

► **To cite this version:**

Anne Lamirand. Epitaxial growth, atomic structure and exchange coupling of ultrathin bilayers of oxides on metals. Materials Science [cond-mat.mtrl-sci]. Université de Grenoble, Grenoble, France, 2014. English. NNT: . tel-01112939v1

**HAL Id: tel-01112939**

**<https://theses.hal.science/tel-01112939v1>**

Submitted on 3 Feb 2015 (v1), last revised 20 Sep 2016 (v2)

**HAL** is a multi-disciplinary open access archive for the deposit and dissemination of scientific research documents, whether they are published or not. The documents may come from teaching and research institutions in France or abroad, or from public or private research centers.

L'archive ouverte pluridisciplinaire **HAL**, est destinée au dépôt et à la diffusion de documents scientifiques de niveau recherche, publiés ou non, émanant des établissements d'enseignement et de recherche français ou étrangers, des laboratoires publics ou privés.

## THÈSE

Pour obtenir le grade de

### DOCTEUR DE L'UNIVERSITÉ DE GRENOBLE

Spécialité : **Physique de la matière condensée et du rayonnement**

Arrêté ministériel : 7 août 2006

Présentée par

**Anne LAMIRAND**

Thèse dirigée par **Maurizio DE SANTIS**  
et codirigée par **Hélio TOLENTINO**

préparée au sein de l'Institut Néel, CNRS/UJF  
et de l'Ecole Doctorale de Physique de Grenoble

# Croissance épitaxiale, structure atomique et couplage d'échange de bicouches ultra-minces d'oxydes sur métaux

Thèse soutenue publiquement le **16 octobre 2014**,  
devant le jury composé de :

**Mme Christine BOEGLIN**

Directrice de recherche CNRS à l'Institut de Physique et Chimie des Matériaux  
de Strasbourg, Rapporteur

**M. Roberto FELICI**

Primo Ricercatore CNR à l'Istituto superconduttori, materiali innovativi e disposi-  
tivi à Rome, en détachement à l'ESRF à Grenoble, Rapporteur

**M. Vincent REPAIN**

Professeur à l'Université Paris Diderot, Examineur

**M. Marc DE BOISSIEU**

Directeur de recherche CNRS au laboratoire de Science et Ingénierie des Matéri-  
aux et Procédés à St Martin d'Hères, Examineur

**M. Maurizio DE SANTIS**

Chargé de recherche à l'Institut Néel à Grenoble, Directeur de thèse











---

# Remerciements

*Merci.*

Ce mot, je le dis une dizaine de fois par jour. Et depuis ma soutenance, encore plus. C'est avantageux, en français, *merci* permet de cesser d'être redevable. Juste l'inverse des brésiliens, qui, les pauvres, ne comprennent pas notre amour de ce mot. Cette marque de politesse, bien utile au quotidien, me casse bien les pieds pour une fois. Comment rendre les mercis attendus dans cette page différents ? Après réflexion (prise de tête), je me suis dit que je n'y arriverais pas (manque de confiance en soi). J'ai opté donc pour la tentative de n'importe quoi. Beaucoup plus sympa et libératrice. Voilà. Tant pis pour vous.

Commençons comme le veut la tradition. Car la tradition, ça a du bon (disent les cons(ervateurs)). Un Grand Merci au Jury. Je suis contre tout attente, vivante, et même diplômée. Comme quoi, n'importe qui peut y arriver. L'émotion de la soutenance est toute fraîche. Le stress des derniers jours de doctorante est tout juste mis à terre. Grâce à Eux. Merci donc à Marc, qui a réussi à rendre cet instant solennel (mes proches étaient tout émus) sans que j'eusse l'impression de suivre mon exécution. Merci à Christine pour sa douceur et gentillesse. Merci à Roberto pour son entrain, ses remarques judicieuses et son millier de corrections. Merci à Vincent pour ses questions pertinentes, qui, me montrant les limites de ma science, ont propulsé ma curiosité vers le post-doc qui me tend les bras à Orsay. Merci à Maurizio.

Maurizio. Le directeur de thèse, depuis peu et depuis le début. Maurizio qui a tenu parole en renonçant pendant quelques mois aux manips et autres programmes nettement plus intéressants pour obtenir l'habilitation juste avant que je ne démarre l'écriture de mon manuscrit. Non pas que ce soit dur pour lui, ou compliqué. Simplement, en bon grenoblois, Maurizio préfère les randos. Oui, mais lui, il affectionne aussi les randos dans l'espace réciproque. C'est sûr, tout le monde n'a pas son espace de lumière. Maurizio, lui, navigue avec aisance dans celui des rayons X. Durant ces trois années, il m'y a peu à peu initié. Chapeau bas pour ta patience. Surtout, lorsqu'au bout d'un an, tu t'es rendu compte que je ratais, systématiquement (avec amour et patience), la première étape du traitement de données. La Normalisation (la blague). Surtout, lorsqu'au bout de deux ans, je te demandais encore pourquoi un rocking scan avait une variation en  $l$  (et que je trouvais la réponse dans mon cahier de stage). Avec son oeil de lynx et son main d'orfèvre, Maurizio m'a aussi initié à l'art de la croissance par MBE et réparations en tout genre. Mais là, il n'était pas seul.

D'abord, il y avait Hélios. Hélios et ses conseils avisés. Hélios, âme brésilienne mue par la curiosité et l'intuition. Toujours le sourire en coin, synchrotroniste jusqu'au bout des ongles (on ne sait plus bien si le premier synchrotron brésilien est né des mains d'Hélios ou l'inverse), Hélios nous a conduit dans une plongée au coeur du magnétisme de la matière (que c'est bien dit, on dirait une pub de Jean Louis). Hélios, c'est l'Interaction. L'interaction des rayons X

avec les électrons, l'interaction entre les spins, mais surtout, avant tout, l'interaction entre les gens. Hélio lie et fait du sens.

Et puis, il y avait Marcio. Marcio, la bonne humeur incarnée. Je me souviendrai longtemps de tes rires face à ma tête énervée, dépitée, désespérée et surtout affamée. Marcio, le grand frère aussi. Celui qu'on ne voit pas tous les jours, qui a ses soucis de grand (de coeur et de science) mais chaque fois qu'on le voit, on en ressort grandi. En quelques heures, un Marcio, ça vous refile tous ses programmes, vous explique en 10 minutes ce que vous essayez de comprendre tout seul depuis un mois et vous ouvre l'horizon. Ce fut un plaisir de marcher dans tes traces !

Mais rien serait possible sans Aline. Aline est celle qui vous ramasse sur le bord de la route, lorsque rien ne va, sort un chocolat chaud de sous son manteau, une couverture et trouve les mots qu'il faut. Aline est celle qui ne s'impose pas, mais s'oppose s'il faut. Avec finesse, elle rassemble, apaise les tensions, organise. Petite souris, elle se montre discrète et pourtant rappelle les impératifs de l'équipe, ce qui aide bien ces zozos-là. Les pieds sur terre, la persévérance et l'exigence du travail bien fait, elle équilibre.

Elle est depuis peu bien aidée par Stéphane. Discret, toujours calme, Stéphane n'a cessé de me surprendre. Avec un sourire amusé, il essaye de suivre Maurizio dans ses tribulations dans l'espace réciproque, il écoute patiemment... et sort une remarque hyper pertinente.

Parce que si nos séances synchrotron resteront si mémorables, c'est parce qu'on a quand même bien rigolé entre deux scans et théories plus ou moins sérieuses.

Bon, je vais aller un peu plus vite, parce que là, on n'est pas sorti. Et faut que je rende ce foutu manuscrit au plus vite pour démarrer à Paris.

Un Grand Merci à tous les permanents MCMF qui rendent l'atmosphère du labo si agréable, et surtout à l'équipe SIN et tous ses pains au chocolat. Jamais vu une aussi bonne idée pour commencer la semaine. Aude, Marie-Claire, Farid, Jean-Marc, Yves, merci de votre accueil !! Un merci spécial pour Yves, qui a fait bureau des plaintes pour tous les thésards qui me semblait en détresse. Un autre merci spécial pour Marie-Claire qui se bat pour rappeler nos droits. Et pour tout ceux qui résistent. C'est le cas de cette équipe. Chapeau bas !

Je remercie également tout ceux que j'ai pu rencontrer en manipant au synchrotron: Tao, Fabien, Nils, les Oliviers, Roberto, Erika, Katharina, Nathalie, Valentina, Gilles et ceux que j'oublie... qui m'ont chacun éclairé sur tout ce qu'on pouvait faire avec ce rayon et m'ont montré, que ce lieu de travail fermé, en lumière artificielle, était en fait une fenêtre ouverte sur le monde et sur une physique empreinte de poésie !

Durant ces trois années, j'ai eu la chance de faire un monitorat (dernière génération à en profiter !) au CPP, la prépa des INP (trop bien). J'ai pu ainsi commencer à enseigner dans des conditions optimales : avec formations de la part du DFI, soutien et conseils de la part de mon tuteur, discussions et réflexions avec d'autres moniteurs. Bravo à toute l'équipe du DFI-CIES qui fait un boulot formidable pour ouvrir nos oeillères. Une phrase restera gravée dans ma mémoire qui montre la complexité de la tâche d'enseignant : *Enseigner, c'est répondre à une*

*question que l'élève ne se pose pas.* (Voilà quoi. Moi, je dis ça, je dis rien). Merci beaucoup à Ilir Trimcev qui m'a conseillée, encouragée. Il m'a apporté sur un plateau des cours très bien constitués, les corrections bien expliquées et a été très présent tout au long des années. Merci aussi à Cilly Briot, Guillaume Parry, Carina Cataldi et toute l'équipe pédagogique pour m'avoir intégré avec tant de chaleur.

Les copains thésards, stagiaires, post-docs : C'était trop COOOOOL ! Je viens de retrouver mes pantoufles, offertes par vos soins pendant la 1ère année, la photo du canoë où je tire une tronche pas possible (qui a pris cette photo ???). Merci aux anciens, qui m'ont introduit avec indulgence dans ce monde subtil (ou pas): Audrey, Issam, Houmed, Vinicius, Sophie, Patricia, Vincent, Marta, Manue, Denis (sacré Denis)... Merci aux nouveaux qui prennent le relais avec courage (ou pas): Pauline, Elodie, Justin, Khalil, Sydney, William et le petit dernier Antoine. Nous avons refait le monde, autour d'une bière ou autour des plats qui coûtent de plus en plus de points (Scandale !)... Vous avez subi tous mes accès de colère et de joie. Vous avez coloré mes journées de vos soucis, joies et interrogations. Vous avez fait le quotidien. Merci surtout à ceux qui ont vécu la thèse en même temps que moi. Joséphine, un peu décalée par rapport à nous parce qu'avec quelques mois d'écart et surtout dans un autre bureau (il en faut peu !). Adrien et Mehdi, je ne dirai pas ici tout le bien que je pense de vous (cf quelques lignes plus tôt, pas le temps). Ces trois années n'auraient pas eu la même saveur sans vous. Des amis comme ça, on s'en fait peu dans la vie.

Faire de la recherche,  
 c'est tenter, tester, approfondir, creuser,  
 oser, et puis parfois laisser tomber,  
 ou saisir la perche que quelqu'un avait négligé  
 mais avant tout c'est avoir de la curiosité.  
 Voir un chercheur comme un conteur  
 ne jamais mentir pour ne pas rougir  
 accepter que le quotidien se conjugue avec le lointain.  
 laisser les précipices de doute au bord de la route,  
 avancer petit à petit l'écriture des publis  
 et déchiffrer, euh.. comprendre, ce que les autres ont dit.  
 Etre chercheur,  
 c'est avant tout partager  
 ses connaissances, ses envies,  
 ses intérêts, ses soucis,  
 et souvent un petit bout de sa vie.  
 Voilà ce que j'ai appris  
 ces 3 années, à vos côtés,  
 et si j'ai rien compris,  
 et ben, j'ai bien kiffé !

Rapidos, parce qu'il faudrait 5 pages de plus pour parler d'eux et que, j'ai pas le temps. J'ai quand même essayé de cacher des rimes. Elles sont pas toujours bien fines, mais vous allez me faire le plaisir de (faire semblant de) les apprécier.

Nina, prends soin de toi. Ivan, te casse pas les dents. Jérémie, langouille à la montagne, ça te dit ? A ta mine, Perrine, on dirait que c'est le bain. Jonas & Annette, Nico & Chloé, même à quelques milliers de kilomètes, nos routes ne cesseront de s'entrelacer. Pauline, nous te suivrons toujours, auprès de ton Yak ou juste dans un hamac. Hana, Emilie, Sylvain et Cie, Anne aime les si bons copains amis (si si ça marche. Faut le prononcer très vite. Et glisser une licence poétique pour que ça veuille dire qqc). Les autres copains, je vous aime bien. Surtout Salomé, Jérôme qui se sont déplacés pour ce diplôme. Les autres je vous ai pas mis, parce que j'ai la flemme. Celui qui veut un poème, commence par lire le manuscrit.

Quelques mots quand même pour ma famille qui m'a refilée cette énergie et ce sale caractère : on s'entrechoque, on s'étincelle, on s'éloigne et on se rappelle. Comme les branches d'un même arbre, nous nous tournons toujours vers la même lumière, nous subissons ensemble pluie et tonnerre, de près ou de loin, nous ne serions être plus frères. Lorsque je me pose et regarde au creux de ma vie ce qui compte avant tout, jamais je ne vous oublie, ma force vient de vous. Zut ! J'ai oublié Françoise, Sylvia et Annick ! Et Théo aussi ! Flûte.

Et puis, il y a Claire. Moi, j'ai soutenu ma thèse. Elle, ça fait un quart de siècle qu'elle me soutient. Ma plus grande fan, ma plus grande héroïne aussi. Ensemble, nos vies cheminent.

Et enfin, il y a Antoine. Beau, fort, intelligent, costaud. Le complice de mes jours et de mes nuits. Le plus beau et précieux cadeau que m'ait offert la Vie. Ke ya ho rata.

Quelques citations qui ont égaillé ces années (celles que je n'ai pas perdu):

Ah ! Il est midi et demi ! C'est pour ça qu'Anne n'est pas contente. (Maurizio)

- Tu pourras me donner une tête, Vincent ? - Non, j'en ai qu'une. (Patricia & Vincent, 01/07/12)

Et si on allait regarder les photos avant d'aller manger ? (Marcio, qui me fait tourner en bourrique)

UMP = Union pour la Majorité Présidentielle. Non ? (Adrien)

- J'ai besoin que mon gland soit autocollimaté. (Vincent, 02/07/12)

On est parti manger. (12h30) (Les copains, tous les lundis)

L'avantage, c'est que la prochaine fois, ce sera forcément mieux. (Adrien, 23/09/13)

Souvent les gens vont bien avec leur chien. (...) Les gens qui sont chien, sont pas chat. (...) Il a pris un pré dans un âne. (Manue, 23/09/13, en fin de thèse)

Nan, c'est moi Miranda. (Anne, 20/12/14)

F..y, old man. It's gif. You sold your invention to the internet. No, it's ours ! (internaute, contre l'inventeur du gif qui dit "guif" et non "jif", on devient geek avec le temps)

- Oh ! La balle était sur mon bureau ! - Dis donc, l'autre jour, tu prétendais pas savoir où est chaque chose sur ton bureau, même si c'est le bordel ? - Sauf les trucs qu'on me cache !! (Adrien, mauvaise foi & Mehdi, railleur)

Oui, on s'est engueulé. Mais s'il y a des moments où on se déteste, c'est qu'il y a des moments où on s'aime, non ? (Un thésard à propos de son directeur de thèse)

- Ca va, ta couche ? (Matthieu (nouveau permanent) à Mehdi (thésard), 5/12/13)

La thèse, c'est une succession de chocs émotionnels. (Vincent, 8/11/12, très fier)

- Mais ce sera dans ma thèse ! - Ah.... Ah. Ca change tout. Je vais le lire dans ce cas. (Maurizio, 18/09/14, à propos de mon résumé)

Je vais m'en sortir. Et après, je la verrai plus jamais. Et ça, ça me fera du bien (Un thésard, 20/06/14, fin de thèse)

Oh non, il vont encore me faire mal aux lèvres ! (Adrien, 24/02/14, parlant de répète de trompette bien sûr)

Si jamais, mais alors, si jamais, il touche à un enfant. (...) je lui démonte la gueule. C'est des gens, il faut les décapiter vivants, les lapider à coups de hache, et moi, j'en fais du pâté. (Yolande Moreau, barbare)

Pour finir, une petite image d'un jeu qui nous a bien fait marrer pendant les périodes d'écriture. On a 12 minutes pour citer les 196 pays du monde. Mehdi y est arrivé le premier, mais je détiens le record avec 10'38". Ca permet de bien décharger le stress. Recommandé pour tout thésard en 3ème année. En plus, après, on peut se la raconter sévère.

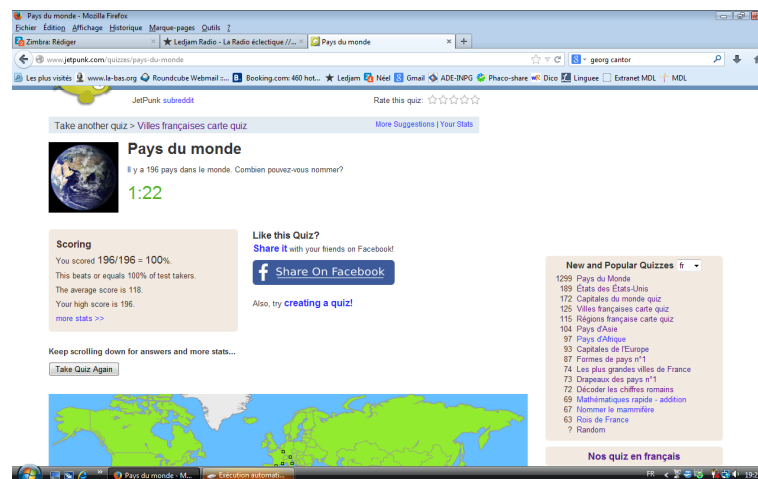


Figure 1: Jetpunk, ou la survie du thésard en 3ème année

Bon, c'est pas tout ça. Mais moi, je me casse.









---

# Acronyms

AES	Auger electron spectroscopy
AFM	antiferromagnetic
BL	bilayer
<i>bcc</i>	body-centered cubic
CRG	collaborative research group
CTR	crystal truncation rod
DFT	density functional theory
DW	Debye-Waller parameter
EB	exchange bias
eV	electron volt
ESRF	European Synchrotron Radiation Facility
EXAFS	extended X-ray absorption fine structure
FC	field-cooling
<i>fcc</i>	face-centered cubic
<i>fcc</i>	face-centered tetragonal
FM	ferromagnetic
GIXRD	grazing incidence x-ray diffraction
GMR	giant magneto-resistance
$H_C$	coercive field
$H_{EB}$ or $H_B$	exchange bias field
IP	in-plane
LEED	low-energy electron diffraction
MCA	magnetocrystalline energy
MBE	molecular beam epitaxy
ML	monoatomic layer
MOKE	magneto-optic Kerr effect
MRAM	magnetic random access memories
MTJ	magnetic tunnel junction
OP	out-of-plane

PMA	perpendicular magnetic anisotropy
PhD	Philosophiæ doctor
RHEED	reflection high energy electron diffraction
RT	room temperature
S	order parameter
SRT	spin reorientation transition
STM	scanning tunneling microscopy
SXRD	surface x-ray diffraction
TEY	total electron yield
$T_B$	blocking temperature
$T_C$	Curie temperature
TMR	tunnel magneto-resistance
$T_N$	Néel temperature
UHV	ultra-high vacuum
XANES	x-ray absorption near edge structure
XAS	x-ray absorption spectroscopy
XMCD	x-ray magnetic circular dichroism
XMLD	x-ray magnetic linear dichroism
XRD	x-ray diffraction
XRMS	x-ray resonant magnetic scattering
XRR	x-ray specular reflectivity

# Contents

<b>1</b>	<b>Introduction</b>	<b>1</b>
1.1	Basic concepts . . . . .	5
1.1.1	Magnetism in solids . . . . .	5
1.1.2	Exchange bias . . . . .	7
1.1.3	Surface physics approach . . . . .	10
1.2	Systems of interest . . . . .	12
1.2.1	Ag substrate . . . . .	13
1.2.2	A ferrimagnetic oxide: $Fe_3O_4$ . . . . .	14
1.2.3	Pt substrate . . . . .	16
1.2.4	A ferromagnetic alloy: FePt . . . . .	18
1.2.5	A unique antiferromagnetic oxide: CoO . . . . .	19
<b>2</b>	<b>Experimental techniques</b>	<b>23</b>
2.1	X-rays . . . . .	24
2.1.1	Electromagnetic waves and photons . . . . .	24
2.1.2	Synchrotron radiation . . . . .	26
2.2	X-ray scattering and diffraction . . . . .	26
2.2.1	X-ray diffraction . . . . .	28
2.3	Surface X-ray diffraction . . . . .	30
2.3.1	Pattern of x-rays diffracted by a surface . . . . .	31
2.3.2	Real surfaces and adlayers . . . . .	32
2.3.3	Experimental set-up . . . . .	35
2.4	X-ray specular reflectivity XRR . . . . .	36
2.5	X-ray Absorption Spectroscopy . . . . .	38
2.6	X-ray Dichroism . . . . .	41
2.6.1	X-Ray Magnetic Circular Dichroism (XMCD) . . . . .	41
2.6.2	X-Ray Magnetic Linear Dichroism (XMLD) . . . . .	43
2.6.3	Experimental aspects of XMCD / XMLD . . . . .	45
2.7	Magneto-optic Kerr effect (MOKE) . . . . .	45
2.7.1	Experimental aspects of MOKE . . . . .	47
2.8	Preparation and complementary analysis of the surface . . . . .	47

<b>3</b>	<b>Growth and structure of CoO(111)/FePt/Pt(001)</b>	<b>51</b>
3.1	FePt/Pt(001) . . . . .	52
3.1.1	FePt growth . . . . .	52
3.1.2	Modeling the FePt/Pt(001) structure . . . . .	54
3.2	CoO(111) on Pt(001) . . . . .	57
3.3	CoO(111) on FePt/Pt(001) . . . . .	60
3.3.1	Analyzing the CoO diffraction pattern . . . . .	60
3.3.2	Modeling the CoO structure . . . . .	65
3.3.3	Comparison with bulk CoO structure . . . . .	67
3.3.4	Impact on FePt layer . . . . .	69
<b>4</b>	<b>Magnetism of exchange coupled CoO(111)/FePt</b>	<b>75</b>
4.1	FePt magnetic properties . . . . .	76
4.2	CoO magnetic properties . . . . .	80
4.2.1	Considerations from structural anisotropy . . . . .	80
4.2.2	XLD angular dependance . . . . .	82
4.2.3	XLD features . . . . .	84
4.2.4	XLD temperature dependance . . . . .	86
4.3	Exchange coupling . . . . .	87
4.4	CoO magnetic anisotropy . . . . .	90
4.4.1	Strength . . . . .	90
4.4.2	Structural anisotropy . . . . .	93
<b>5</b>	<b>Growth, structure and exchange coupling of CoO(001)/FePt/Pt(001)</b>	<b>97</b>
5.1	(001) oriented CoO on Pt(001) . . . . .	98
5.1.1	Growth . . . . .	98
5.1.2	Structure . . . . .	100
5.2	CoO(001)/FePt grown on Pt(001) (Sample S19) . . . . .	104
5.2.1	Growth . . . . .	104
5.2.1.1	FePt . . . . .	104
5.2.1.2	Co . . . . .	105
5.2.1.3	Oxidization . . . . .	105
5.2.2	CoO structure . . . . .	106
5.3	Magnetic studies of CoO(100)/FePt(100)/Pt(100) . . . . .	108
5.3.1	Magnetic studies by MOKE . . . . .	108
5.3.2	Magnetic study by XMCD and XMLD . . . . .	111
<b>6</b>	<b>Fe/CoO - <math>Fe_3O_4</math>/CoO systems on Ag(001)</b>	<b>115</b>
6.1	CoO/Fe/Ag(100) system . . . . .	116
6.1.1	Fe/Ag(001) . . . . .	118
6.1.2	CoO/Fe/Ag(001) . . . . .	120
6.2	$Fe_3O_4$ /Ag(100) . . . . .	123

---

6.2.1	Growth . . . . .	123
6.2.2	Structure . . . . .	127
6.2.3	Distinction between magnetite and maghemite . . . . .	129
6.2.4	Mosaicity . . . . .	133
6.3	CoO/ $Fe_3O_4$ /Ag(001) . . . . .	133
6.3.1	Growth and structure of CoO on $Fe_3O_4$ /Ag(001) . . . . .	134
6.3.2	X-ray absorption (preliminary) study . . . . .	135
6.4	CoO/Ag(100) . . . . .	138
<b>Conclusion and Outlooks</b>		<b>143</b>
<b>A The spinel pattern in Ag(001) lattice</b>		<b>147</b>



# Chapter 1

## Introduction

Who could deny the amazing development of information technologies these last decades and their impact (whose benefits could be discussed) in our life ? In few years, computers have invested our house, then our pockets. Cellphones are now in all hands, even the smallest. This technological boom is the result of the collaboration between an active research and a prolific development where innovation and fundamental understanding have been treated with consideration and enthusiasm. Moreover, the constant seek for the reduction of dimensions in devices keeping or even improving their performance scales with the progressive availability of experimental possibility permitting the controlled fabrication and the study of low-dimensionality objects. The field of nanosciences, the sciences of small objects ( $1$  to  $100 \times 10^{-9}\text{m}$ ), is now widespread, extended today through a vast range of knowledge and technology branches, from fundamental physics to bio-materials or applications on energy production. And the dream of Richard Feynman[1] to arrange the atoms the way we want becomes slowly true.[2]

Because electronic, crystalline and magnetic properties are crucial in these applications, solid states physics research was particularly boosted during this evolution. In this context, promising topics such as quantum information technology or spintronics are emerging. In this latter, information is carried and stored by the spin of the electron and not only by its charge. The discovery of the giant magnetoresistive effect (GMR)[3, 4] is considered as the beginning of spintronics. The GMR effect appears in a layered system composed of ferromagnetic (FM) layers typically separated by a non-magnetic one. The electrical resistance of the system depends strongly on whether the ferromagnetic layers have parallel or antiparallel magnetizations. Electron diffusion could then be controlled by an external field. This concept gave rise to the spin valve and derivative devices.[5, 6]

In a spin valve, the differential switching of the two FM layers is often achieved thanks to an antiferromagnetic (AFM) layer which pins one of them, while the second one rotates under the influence of small fields as, for instance, the stray field above the stored bits in current high-density magnetic storage disks. The spin valve is indeed the main element of a high-sensitivity read-head. As a sensitive magnetic field sensor, it has a wide range of application.[7, 8, 9, 10]



Tunnel magneto-resistance (TMR) is a similar effect as the GMR one. The ferromagnetic layers are in this case separated by an ultrathin insulating barrier. The magnetoresistance facing the resulting tunneling current changes even more largely than in spin valves. This phenomenon is exploited in magnetic tunnel junction (MTJ) whose magnetic random access memories (MRAM) are based on.

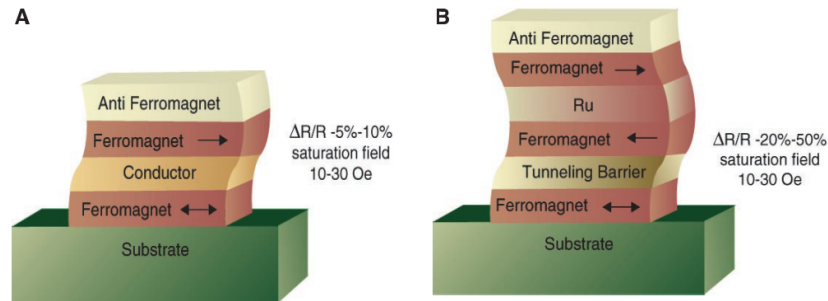


Figure 1.1: Spin-dependent transport structures (taken from ref. [11]). (a) Spin valve using GMR effect (b) Magnetic tunnel junction using TMR effect

In spintronics, a fundamental characteristic length is the spin diffusion length, corresponding to the distance that an electron travels in a material without changing its spin moment. Impurities, point defects and structural disorder reduce this distance. They also impact the magnetocrystalline anisotropy of the magnetic layers, key parameter for the high density magnetic recording. High anisotropy, expressed by the magnitude of  $K_u$  parameter, allows indeed to reduce the size of the storage grains without losing thermal stability.[12, 13] A stability metric for media is indeed the ratio  $(K_u.V)/(k_B.T) > 1$  where  $V$  is the unit volume of grain size,  $k_B$  is the Boltzmann constant and  $T$  the temperature in Kelvin. This stabilization, mandatory for the data storage, is problematic for the writing step involving high writing field. A way to bypass this issue is to heat the grain during this step. This strategy is in development for the next generation of MRAM, the heat-assisted magnetic recording (HAMR).[14]

Another relevant point in these systems is the features of the interfaces. First, an electron spin flip may take place at an interface leading to a problem of inefficient spin injection. Secondly, the magnetic coupling at the interface of nanoscale structures gives rise to unusual properties when compared to the bulk. The size reduction enhances the importance of surface and interfaces properties in regards to bulk ones. For instance the magnetization of a ferromagnetic layer could be pinned by contact with an AFM one. Such interaction leads to a unidirectional anisotropy called exchange bias effect. Ultrathin films could also relax partially or even not at all the epitaxial deposition constraints. Crystallographic structure modifications could change electronic and magnetic properties of the film. Even basic systems present a rich variety of phenomena.[15] Amongst other examples, one can cite the spin re-orientation transition for Fe layers grown on Ag(001)[16] or the ordering temperature of CoO layer on  $Fe_3O_4$  film enhanced compared to the bulk one.[17] More rarely, confinement gives rise to quantum effects and surprising properties as oscillatory magnetic anisotropy in iron thin films on Ag(1,1,10).[18, 19] All these effects conjugate in the systems and so are difficult

to disentangle. This explains why no clear quantitative picture of for instance exchange bias mechanism has been drawn despite its scientific relevance and its widespread use in magnetoelectronic applications since its discovery more than 60 years ago. Studying few samples in detail combining complementary techniques allows an overview of each sample and to hope to separate the different contributions.

In this context, we have investigated from a fundamental point of view the atomic and magnetic structures of ultrathin FM/AFM double-layers which could present exchange coupling. Experimental techniques using synchrotron radiation are well-adapted to the study of such buried interfaces, in particular surface X-ray diffraction (SXR) and absorption spectroscopy (XAS). Manipulating the polarization of the incident beam, XAS becomes x-ray circular and linear magnetic dichroism (XMCD and XMLD) and probes the magnetism of each element in the sample. The ability to grow ultrathin epitaxial films by molecular beam epitaxy has been used to synthesize samples as close as possible to ideal models. The growth, performed in ultra-high vacuum, has been followed *in situ* by SXR supported by Auger electron spectroscopy (AES) or controlled by low-electron energy diffraction (LEED) and scanning tunnel microscopy (STM). Magnetic properties have been mostly investigated *ex situ* using synchrotron techniques and magneto-optic Kerr effect (MOKE) experiments. The combination of all these experiments allows to have a nice picture of the structural, electronic and magnetic structures of several samples.

During this thesis, we tackled two different systems. The first one was CoO/Fe double-layer deposited on Ag(001). The Fe layer thickness was chosen close to the thickness of the spin reorientation transition. Indeed the out-of-plane spins reorient to in-plane at room temperature above 4-6 monolayers. However, the structural study revealed in this system a non negligible oxidation of the Fe layer, which has a tendency to increase with time. In spite of finding interesting properties related to such an oxidation, which is really playing a major role in the coupling at the interface, such an unstable and uncontrolled oxidation oriented our research toward a system with a  $Fe_3O_4$  layer, where the stoichiometry is more stable.

The second system we were interested in was CoO/FePt deposited on Pt(001). One of the advantages of this double layer system is naturally that the FePt layer is more resistant to corrosion and Fe oxidation is limited. In addition, FePt on Pt(001) possesses a huge perpendicular magnetic anisotropy in its chemically ordered  $L1_0$  phase. Each of these double-layer system are relevant from the technological point of view and present many exciting behaviors relevant to basic science.

This manuscript is organized as follows. In the first chapter the general background of this thesis is addressed. The fundamental concepts of magnetism in thin films and surface physics are introduced. It contains also a short review of each system studied. In Chapter 2 the main experimental techniques are described. The objective is to provide the reader with some essential concepts needed to follow the arguments made in this thesis. Chapter 3 and Chapter 4 are dedicated to the CoO(111)/FePt(001) deposited on Pt(001). The growth and

structure of each layer are presented in Chapter 3, while the magnetic properties of the system are detailed in Chapter 4. The orientation of CoO layer on Pt(001) can be tuned from (111) to (001) by interface chemistry. The growth method, the structure of this layer and its coupling with FePt layer are developed in Chapter 5. Chapter 6 concerns the study of CoO/Fe and CoO/ $Fe_3O_4$  bilayers on Ag(001). Finally a summary of the most relevant results and some outlooks on these systems concludes the manuscript.

## Contents

---

<b>1.1 Basic concepts</b>	<b>5</b>
1.1.1 Magnetism in solids	5
1.1.2 Exchange bias	7
1.1.3 Surface physics approach	10
<b>1.2 Systems of interest</b>	<b>12</b>
1.2.1 Ag substrate	13
1.2.2 A ferrimagnetic oxide: $Fe_3O_4$	14
1.2.3 Pt substrate	16
1.2.4 A ferromagnetic alloy: FePt	18
1.2.5 A unique antiferromagnetic oxide: CoO	19

---

## 1.1 Basic concepts

### 1.1.1 Magnetism in solids

The magnetic moment of an atom ( $\vec{\mu}$ ) is composed of two contributions which do not necessarily have the same direction. The first one, the spin  $\vec{S}$ , comes directly from the model of the atom in quantum mechanics. This intrinsic momentum is described by two values when projected on the quantization axis, spin up and spin down corresponding to  $\pm\hbar/2$  for the fermions (as electrons). Nucleus, due to its mass, contributes to the magnetic moment of the solid, some  $10^6$  to  $10^8$  smaller than electron and so is usually neglected. The second one, the orbital momentum  $\vec{L}$ , arises from the development of the total electronic kinetic energy in the presence of a field (created here by the rotation of the charge in the orbital).[20] In a classical view, spin momentum is interpreted as arising from the rotation of the electron around itself, while the orbital momentum comes from the rotation of the electron around the nucleus. Their discrete values remind that these pictures are only useful analogies. Neglecting the anomalous correction to the Landé factor  $g$ , the total magnetic moment is given by[21]

$$\vec{\mu} = -\frac{\mu_B}{\hbar}(2 * \vec{S} + \vec{L}) \quad (1.1)$$

where  $\mu_B$  is the Bohr magneton defined as  $\mu_B = \frac{e * \mu_0 * \hbar}{2 * m_e} = 1.17 \times 10^{-29}$  V.m.s,  $\mu_0$  the magnetic permeability of the vacuum,  $e$  and  $m_e$  the charge and mass of electron and  $\hbar$  the reduced Planck constant. In the literature, magnetic moments and spins are commonly confused neglecting the orbital momentum. Most of experiments only access the magnetic moments, or even only to the magnetization of the sample (which is the integral of all the moments). It is difficult to separate the spin contribution from the total moment. Both do not have even necessarily the same direction. Moreover, it is noteworthy that the total angular momentum  $\vec{J} = \vec{S} + \vec{L}$  is in general not collinear to  $\vec{\mu}$ .

The Hamiltonian of a crystal contains several magnetic terms. The magnetic configuration is the result of the competition between these different energy contributions. We will briefly recall the principal ones displayed in Fig. 1.3 before focusing on the additional energy exchange bias we are interested in.

The *exchange interaction*, strongest among the magnetic interactions (few eV), is at the origin of the ordering of magnetic moments in a material. It arises from the Coulomb interaction between electrons and the Pauli exclusion principle, which requires a total antisymmetric wavefunction ( $\psi_{as}$ ). Assuming that the Hamiltonian does not depend on the electron spin, the total wavefunction ( $\psi$ ) is the product of an orbital ( $\phi$ ) and a spin ( $\chi$ ) wavefunctions. Either one or the other wavefunction is thus antisymmetric.

$$\psi_{as} = \phi_{as} \cdot \chi_s \text{ or } \psi_{as} = \phi_s \cdot \chi_{as}$$

If two electrons are close (low Coulomb interaction), their orbitals overlap. Since the Pauli exclusion separates the similar spins, the spins are aligned anti-parallel. If two electrons are in the same spin state, the spin wavefunction is symmetric. Then the orbital part is antisymmetric, and the probability to find the two electrons close to each other tends towards zero. In summary, two electrons with the same spin cannot lie on the same orbital. [21] This simple reasoning with a two electrons system sets the basis for understanding exchange interaction. Larger systems or strongly correlated electrons are better grasped with methods using for instance the Heisenberg and Hubbard models, than *ab initio* technique such as density functional theory. They take into account the hopping energy of electrons from one atom to the next or the spin-spin interaction.[21] The simple picture presented here has also the advantage to emphasize that exchange interaction is not a direct interaction between magnetic moments but between electrons. Nevertheless it is known as *direct exchange* in opposition to *superexchange* or *indirect exchange*, where the magnetic interaction is mediated respectively by the electrons of a shared neighbor non-magnetic ion or by the conduction electrons.[20]

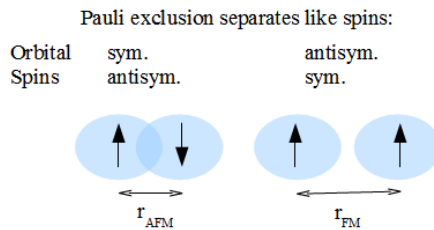


Figure 1.2: An example of exchange interaction

The exchange interaction describes the coupling between neighbor magnetic moments, but lets their orientation completely free. The preferential orientations in magnetic materials, known as easy-axes or easy-directions, are designed by the interplay of different anisotropy sources. An ion embedded in a crystal is subjected to the crystal field resulting from the interaction of its electrons with those of the atoms surrounding it. If the crystal field is too strong, the orbital degeneracy is completely removed and the ground state is an orbital singlet. In this case, the magnetism of the system depends only on the spin and is decoupled from the lattice. The orbital momentum is said quenched.

If the crystal field is not too large, the *spin-orbit interaction*  $\mathcal{H}_{SO} = \lambda \vec{S} \cdot \vec{L}$  (with  $\lambda$  the spin-orbit coupling constant) couples the spin to the lattice.[22] A reduction of the symmetry of the lattice impacts then the degeneracy of the ground state and so the magnetism of the system. The *magnetocrystalline anisotropy*  $\mathcal{H}_{CF} = -e \cdot V(R)$  established (where  $V$  the electrostatic potential created by surrounding charges) is thus related to the spin-orbit interaction. The relation between their energies is not straightforward. The *4f* electrons due to their proximity with the nucleus are less subjected to the crystal field than the *3d* electrons. The magnetocrystalline energy (MCA) is then smaller than the spin-orbit interaction. However in a cubic ionic *3d* compound, the crystal field can be considered as a small perturbation (0.1-1eV) to the Coulomb interaction, significantly larger than the spin-orbit interaction (0.01-0.1eV). Bruno

has shown theoretically that under certain assumptions, the orbital moment is larger along the easy axis and that the difference between the orbital moments along the easy and hard directions is proportional to MCA.[23] The calculation of  $V$ , originally approximated by a collection of point charge (crystal-field theory), focuses now on the bonding between the  $d$ -metal ions and the environment (ligand field theory). MCA is often described by the anisotropy constants  $K_i$ .

Stress at thin film interfaces, caused by the lattice mismatch in an epitaxial growth, deforms the lattice at the interface and so influences the MCA. This additional energy could be considered as a part of MCA or as a different part known as the *magnetoelastic anisotropy*. Magnetostriction, the expansion or contraction of a lattice caused by its magnetization, can also induce magnetoelastic energy.

The last source of anisotropy is the long-range magnetic dipole-dipole interaction, known as *dipolar anisotropy*, *magnetostatic energy* or even *demagnetizing energy*. Each atom is considered as a dipole, source of magnetic field. The interaction between all dipoles gives rise to a spontaneous field, called stray field outside the matter and demagnetizing field  $H_d$  inside. As its name suggests, this self-energy tends to remove the magnetization  $M$  of the material ( $E_{dip} = -\frac{1}{2} \iiint \mu_0 \vec{M}(\vec{r}) \cdot \vec{H}(\vec{r}) dr^3$ ). It plays an important role in structures where the magnetocrystalline anisotropy is expected to vanish due to a negligible spin-orbit interaction such as NiO or MnO,[24] or at macroscopic scale by the creation of uniformly magnetized domains. In this latter case, the magnetization is saturated within each domain, but the directions of the magnetization of each domain are such that the net magnetization of the sample is null.[25] Only the spins in the domain walls experience unfavorable exchange interaction, while the dipolar energy of every spin drops. There the energy is called *shape anisotropy*.

Last but not least, the *Zeeman interaction* corresponds to the action of an external magnetic field  $H_{app}$  onto the spin and orbital angular momentum ( $\mathcal{H}_{Zee} = \vec{\mu} \cdot \vec{H}_{app} = \frac{\mu_B}{\hbar} (2 * \vec{S} + \vec{L}) \cdot \vec{H}_{app}$ ). At the beginning of magnetism, this interaction was used to align iron compass needles. Today, it writes this manuscript on the MRAM of my computer. Most of all, it is used to study the magnetic properties of materials, for instance by the measurement of the magnetization loop.

### 1.1.2 Exchange bias

In 1956 Meiklejohn and Bean discovered that nanoparticles formed by a metallic cobalt core and a cobalt oxide shell show a new magnetic anisotropy, now called *exchange bias* (EB).[26] This effect, qualitatively sketched in Fig. 1.4, appears at the interface shared by a ferromagnetic (FM) and an antiferromagnetic (AFM) layer. It manifests itself by a shift  $H_{EB}$  of the hysteresis loop of the FM layer and an increased coercive field  $H_c$  defined as half of the loop width, after a field cooling process. During this step, the temperature is decreased from a temperature  $T_i$  between the AFM ordering Néel temperature ( $T_N$ ) and the FM ordering Curie temperature ( $T_C$ ) down to a temperature  $T_f$  below  $T_N$  under a magnetic field  $H_{FC}$ . At  $T_i$ , the

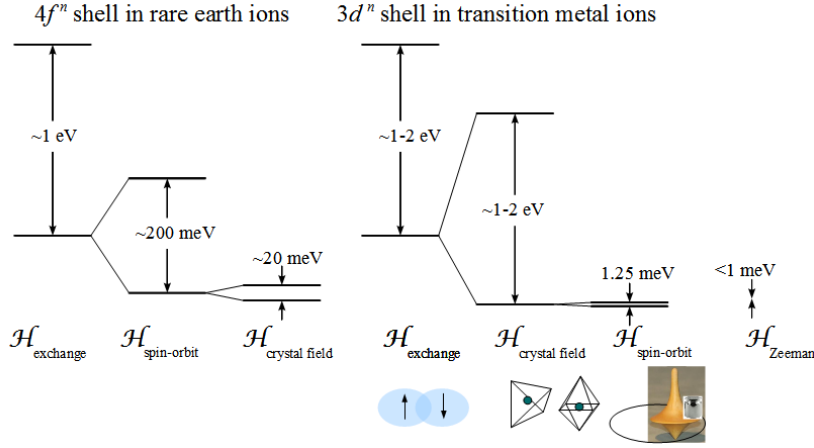


Figure 1.3: The approximate size of four important interactions in solids illustrated by the observed splitting in spectra of the ions in crystals. They are represented for the  $3d^n$  shell in transition metal ions and the  $4f^n$  shell in rare earth ions in single configuration, charge neutral (taken from ref. [21]). One can note the opposite relative size of crystal field interaction and spin-orbit coupling for both systems. I added a useful analogy of effect of spin-orbit coupling: Spinning-top (electron) with a weight in a side (spin) deviates from its usual trajectory (orbital).

FM magnetic moments, ordered, follow the applied field  $H_{FC}$ , while the AFM ones are still randomly oriented (Fig. 1.4a). During the field cooling, the AFM magnetic moments align themselves, taking into account the applied field and above all the interfacial FM moments (Fig. 1.4b). When the field is reversed to describe the hysteresis loop, the AFM moments remain fixed (assuming that AFM have a large enough anisotropy), and exert a torque at the interface on the FM moments, tending to keep them in their original direction (Fig. 1.4c and e). The field needed to reverse the magnetization will be larger in one direction ( $|H_{C1}| > |H_{C2}|$ ) displacing the loop by  $H_{EB} = (H_{C1} + H_{C2})/2$ . [27] The system has to overcome an additional unidirectional interfacial magnetic energy with the density of  $\Delta\sigma$  (erg/cm<sup>2</sup>) (Fig. 1.4d). One says that the AFM layer pins the FM one. The same FM layer would have smaller coercive field and no EB without the coupling with AFM layer (dashed hysteresis in Fig. 1.4). Exchange bias exists up to the blocking temperature  $T_B$  where the AFM is not anymore robust enough to constrain the FM.  $T_B$  is then smaller than  $T_N$ .

The energy per unit area corresponding to such a model is given by the sum of Zeeman interaction, the magnetocrystalline anisotropy energy (supposed here to be uniaxial) and the additional unidirectional anisotropy (corrected from ref. [29])

$$E = -\mu_0 H \cdot M_{FM} \cdot t_{FM} \cdot \cos\theta + K_{FM} \cdot t_{FM} \cdot \sin^2\theta - \Delta\sigma \cdot \cos\theta \quad (1.2)$$

where  $H$  is the applied magnetic field,  $M_{FM}$ ,  $K_{FM}$  and  $t_{FM}$  respectively the saturation magnetization, the uniaxial anisotropy and the thickness of the ferromagnetic film. The angle

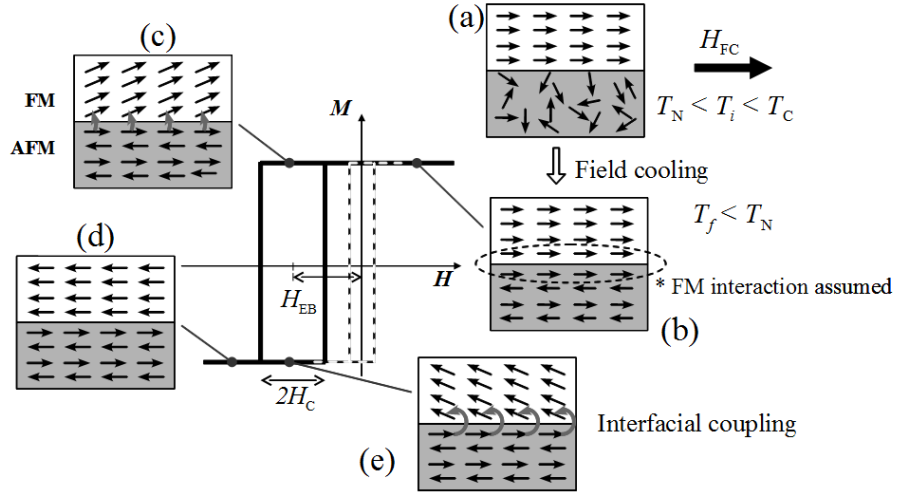


Figure 1.4: Sketch of the exchange bias mechanism for an in-plane anisotropy FM/AFM system with perfectly uncompensated AFM magnetic moments at the interface. The exchange bias field  $H_{EB}$  and the enhanced coercive field are indicated in the hysteresis loop. The dotted line, with smaller  $H_c$  and no EB, corresponds to the hysteresis loop for the FM layer alone, without the coupling with the AFM layer (from ref. [28])

$\theta$  is taken between the magnetization  $M$  and the anisotropy easy axis of the ferromagnet. The bias field is then (by analogy with Zeeman energy)[30]

$$H_{EB} = \frac{\Delta\sigma}{\mu_0 \cdot M_{FM} \cdot t_{FM}} \quad (1.3)$$

and developed for a simple cubic structure

$$H_{EB} = \frac{2 \cdot J \cdot \vec{S}_{FM} \cdot \vec{S}_{AFM}}{a^2 \cdot M_{FM} \cdot t_{FM}} \quad (1.4)$$

where  $J$  is the interatomic exchange across the interface,  $S_{FM}$  and  $S_{AFM}$  the spins of interfacial atoms and  $a$  the cubic lattice parameter. While this qualitative description of the EB mechanism is generally accepted, it is far to explain it quantitatively. Such formula gives values of  $H_{EB}$  two-to-three orders larger than the measured ones. The increase of the coercivity is not explained. This simple ideal model does not realistically represent the FM/AFM interfacial environment. More sophisticated models (well reviewed by Kiwi[31]) have been soon proposed. They insist on the domain walls in the AFM layer, on the random surface roughness (with thus an alternating compensated and uncompensated interface), on the atomic interdiffusion, on the non collinear interface spin configuration or on the extension



of the coupling inside the layers. However none stands for all the experimental results, and the microscopic interfacial interactions involved in EB effect are still controversial.

It must be said that since its discovery, this phenomenon has been observed in a large variety of interfaces and materials (surface oxides, films, nanoparticles, spin glasses, ...) whose a large panorama can be found in the revue from Nogues and Schuller.[27] New features revealing the complexity of the EB effect appeared: vertical shift, positive shift of the hysteresis loop; decreasing of  $H_{EB}$  with the number of hysteresis loop called training effect and highlighting the metastability of the equilibrium after field cooling; non predictable  $T_B$ ... In polycrystalline thin films, results are so widespread that O'Grady and its collaborators developed the York Protocol to reduce the amount of parameters.[32] Here we focus on monocrystalline ultrathin film bilayers, which allow the best control and characterization of the interfaces.

This characterization, essential for the fundamental understanding of the interaction at real FM/AFM interface, is progressively enabled by the availability of experimental and analytical tools such as synchrotron-based techniques. Hence a study using x-ray magnetic linear dichroism (XMLD) directly probed the AFM-compensated spins during the FM-layer magnetization reversal.[33] The results show that two kinds of AFM spins exist: rotatable (unpinned) spins and frozen (pinned) spins. The first ones rotate with the FM spins in contrary to the others. Another study advanced that rotatable uncompensated AFM spins do not completely rotate, but rather cant.[34] A third one dissociated the impact of stoichiometry and roughness on exchange bias features.[35]

### 1.1.3 Surface physics approach

In bulk materials generally (even in a  $1 \text{ mm}^3$  material), the energetic contribution of surface atoms is completely negligible compared to the contribution of volume atoms. During centuries, the specific properties of the surface have been neglected with reason. It is mandatory to take them into account in three physical cases. First, when the volume becomes very small. The ratio of surface atoms under volume atoms increases. Secondly, when the phenomenon considered is an interfacial effect or is strongly influenced by the surface or interfaces. Thirdly, when the transport properties considered concern electrons that passed through the surface and interfaces.[36] The exchange bias effect for spintronics gathers the three situations. Its essential behavior depends critically on the atomic level chemical and spin structure at the buried interface.[30] The structural characterization of the magnetic layers and their shared interface is required for the understanding of the exchange bias mechanism.[37] The elaboration of sharp surfaces/interfaces reduces the complexity of the system, getting it closer to a model sample. Monoatomically flat and clean surface, and well-controlled growth are two conditions of such demand.

The surface of a crystal can be seen as the truncation of an infinite crystal in one direction. Flatness of a surface depends on the cleanness of the substrate and also on the chosen orientation. Kinked surfaces or polar surfaces are unfortunately intrinsically rough. However surface atoms are not inexorably fixed. As in the bulk, the configuration of the surface arises from

the minimization of the total energy. A surface, like any interface, corresponds to a stress field for the material. The calculations developed in ref. [36] show that the strain of a free flat surface describes a modification of the structure known as surface relaxation. Often, the distance between atomic planes reduces, while approaching to the surface. Another kind of modification is the surface reconstruction. Surface atoms reorganize completely to rearrange the dangling bonds between themselves, or to decrease the polarity of the surface. Generally reconstructed surfaces are more densely packed than the volume. Hence close-packed quasi-hexagonal reconstruction are seen in the late  $5d$  metal surface as Pt(001). Magnetite presents also a reconstruction. Both will be described in detail in the next section.

Concerning the samples preparation, high quality ultra-thin films are achieved with the molecular beam epitaxy (MBE) method. Epitaxy refers to the growth of an oriented single crystalline film on a monocrystalline substrate. Two crystals in epitaxy share crystallographic directions within a shared crystallographic plane. An epitaxial growth is characterized by the morphology of the overlayer and by its atomic structure in relation to those of the substrate. For the morphology, three basic growth modes are usually distinguished (cf Fig. 1.5): [36]

- Layer-by-layer (or Franck-Van der Merwe) growth: each monolayer is completed before the next one develops on the top. The adatoms are more strongly bound to the substrate surface than to each other.
- Island (or Vollmer-Weber) growth: small clusters nucleate directly on the surface coalescing then in three dimensional islands. The adatoms are more strongly bound to each other.
- Layer-plus-island (or Stranski-Krastanov) growth: is an intermediate mode. After a formation of an initial atomically flat layer, the layer-by-layer mode becomes unfavorable and islands grow on the top. The thickness of the intermediate flat layer mainly depends on the strain energy which grows with thickness.

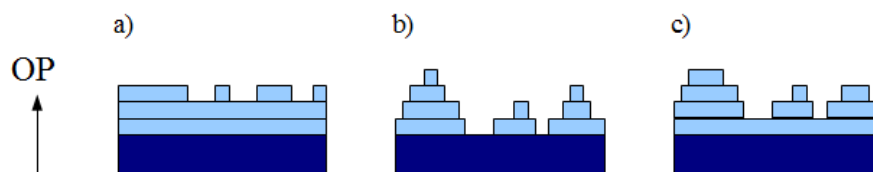


Figure 1.5: Illustration of the different growth modes: a) layer-by-layer, b) island, and c) layer-plus-island growth.

The deposited material of an heteroepitaxy has not the same nature as its substrate. Its structure is thus different, from its symmetries, its lattice parameters or at least from the size of its atoms. It could to some extent accommodate to the substrate lattice. Strictly speaking, a *pseudomorphic* layer has only the same shape as its underlayer. However, it is often used to speak about layers in *coherent epitaxy*, i. e. layers grown with exactly the same in-plane parameters than the substrate. One can also say that the layer is in registry with

the substrate. The disregistry (or mismatch) between the natural lattice parameters of the substrate  $a_s$  and the deposited film  $a_f$  is described by the misfit defined by  $\epsilon = \frac{a_f - a_s}{a_s}$ . [38] Different strategies have been observed to reduce this strain. The film can relax partially or completely to get closer to its natural structure by formation of dislocations or by 3D island growth.

In reality, the growth of a film is a complex phenomenon where many atomic scale processes take place such as adsorption (chemisorption or physisorption), surface diffusion or atoms exchange, and many energies are involved. [39] Successfully predicting the epitaxial relationship between a deposit and a substrate is not straightforward. At least, the most likely possibilities can be drawn from symmetry and lattice matching conditions. [40] Moreover, it is noteworthy that the morphology depends also on the kinematical limitations. Post-annealing lets the atoms diffuse on the surface and sometimes improves the flatness of the films. An active research explores the wide science of growth and surface which already possesses an important literature [38, 36]. Large fields develop with recent technical improvement such as the dynamics of growth with the Video-STM devised by O. Magnussen *et al.* [41]

Historically the development of ultra vacuum technology brought about a revolution in the study of surfaces. The gas in the environment of the sample can alter the growth of an ultra-thin film by two ways: by contaminating the substrate inserting impurities or creating physical defects, or by perturbing the evaporated atoms during their traveling from the evaporator to the surface. The reduction of the pressure in the growth chamber both decreases the probability of contaminant adsorption on the surface (as described in the Langmuir equation) and increases the distance that an atom can travel without meeting another, called the mean free path. Ultra-high vacuum (UHV) environment, corresponding to pressures in the range of  $10^{-9}$  to  $10^{-11}$  mbar, permits both to maintain the cleanness of the substrate longer, and to stabilize the deposition rate. To reach such restrictive condition, the chamber is heated after each opening at  $150^\circ\text{C}$  (320K) during few days (“baking stage”) while turbo-molecular pumps associated to primary pumps are working. The temperature enhances the molecular agitation helping the pump to evacuate all gas molecules. Once cooled down to room temperature, the pressure decreases from one to two orders. The maintain of such pressure needs continuous pumping and a permanent vigilance but is awarded by homogeneous, atomic scale controlled deposition of evaporated atoms and sometimes by sharp interfaces.

## 1.2 Systems of interest

At the beginning of this thesis, we were interested in systems which could present exchange bias associated to a perpendicular magnetic anisotropy. We tackled two different systems. The first one was CoO/Fe bilayer deposited on Ag(001). Ultra-thin Fe layer shows PMA at room temperature for thickness up to 4-6 MLs. CoO is a well-suited antiferromagnetic material for coupling with Fe regarding to the lattice mismatch between the two layers. However the structural study revealed a non negligible oxidation of the Fe layer, which has a tendency to increase with time. Because the coupling between CoO and Fe layers exists through the iron

oxide at the interface, we oriented our research toward a more stable system where the Fe layer was completely oxidized. We replaced then iron by magnetite and achieve an all-oxide CoO/Fe<sub>3</sub>O<sub>4</sub> system. The second system was CoO/FePt deposited on Pt(001). FePt possesses a huge PMA in its chemically ordered phase even in ultra-thin layer. In addition, FePt is more resistant to corrosion than Fe.

In this section, we give a brief review on the features and properties of each material.

### 1.2.1 Ag substrate

Extracted since about 5000 years silver, which can occur naturally in its pure and free form, has long been valued as a precious metal. As a ductile, malleable with a white luster material, it was first exploited for jewelry, silverware or even currency. Its electrical conductivity, considered as the highest of any element and persisting even when tarnished, makes it attracting for electronics and electricity applications. Finally photography consumed a lot of silver in the form of silver nitrate and silver halides for their photosensitivity properties. Although not very abundant, silver has been thus commonly used.

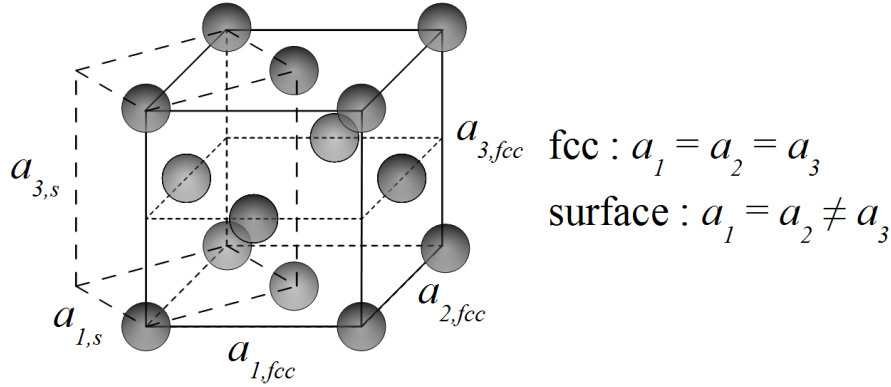
Our own interest in silver is due to its small lattice mismatch with Fe and CoO, which favours coherent epitaxy. Native silver has a *face centered cubic* (*fcc*) structure with lattice constant  $a_{Ag} = 4.0853 \text{ \AA}$ . 45°-rotated *body-centered cubic* (*bcc*) Fe(100) has only a 0.8% of lattice mismatch with Ag(001), while cobalt oxide, *fcc* with lattice constant  $a_{CoO} = 4.261 \text{ \AA}$ , has a lattice mismatch of 4.3% with Ag(001).

The structure of ultra-thin Fe layers on Ag(001) is particularly interesting to study for two reasons. First, the growth and structure at lowest coverage is still in debate. Island formation and intermixing with Ag have a major role in this question.[42, 43] Secondly, ultra-thin Fe layer displays a spin reorientation transition (SRT) as function of thickness. Up to 4-6 MLs, the spins are aligned perpendicular to the sample. Above, the moments lie in the plane of the film.[44] The relation of this reorientation with structural modifications such as relaxation has not been determined. Coupled to CoO, some oxidation at the interface can cause some magnetic disorder in the Fe layer.[45] It could be interesting to determine to what extent the perturbation is in the Fe layer.

In this manuscript the *fcc* (001) substrate structure is represented by the *surface unit cell* instead of the conventional cubic one (respectively in dashed and full lines in Fig. 1.6). For a (001) surface these two unit cells are rotated one from the other by 45° about the surface normal. Surface and cubic lattices are related by:

$$a_{1,s}^{\vec{}} = \frac{a_{2,fcc}^{\vec{}} + a_{1,fcc}^{\vec{}}}{2}, \quad a_{2,s}^{\vec{}} = \frac{a_{2,fcc}^{\vec{}} - a_{1,fcc}^{\vec{}}}{2} \quad \text{and} \quad a_{3,s}^{\vec{}} = a_{3,fcc}^{\vec{}}.$$

During the growth of an adlayer, there is a possible inter-diffusion between the substrate and the deposit, limited usually to some atomic layers close to the surface. When the two elements show a large miscibility gap, they don't mix. The adlayer can either remain at the surface or be buried below some floating substrate monolayers. In the second case the substrate acts as a surfactant climbing through the deposit to the surface. This atomic

Figure 1.6: Surface and *fcc* unit cells

exchange process, called segregation, as well as intermixing are expected with Ag substrate due to its low surface energy ( $\gamma_{SV} = 1.2 \text{ J.m}^{-2}$ )[46] and to the large mobility of its atoms, even at RT.[47, 48]

### 1.2.2 A ferrimagnetic oxide: $\text{Fe}_3\text{O}_4$

The family of iron oxides is composed of three members classified according to the oxidation rate:  $\text{FeO}$ ,  $\text{Fe}_2\text{O}_3$  and  $\text{Fe}_3\text{O}_4$ . These stoichiometries are also often characterized by the charge of the iron ions.  $\text{FeO}$  contains exclusively  $\text{Fe}^{2+}$  ions,  $\text{Fe}_3\text{O}_4$  both  $\text{Fe}^{2+}$  and  $\text{Fe}^{3+}$  ions, and  $\text{Fe}_2\text{O}_3$  only  $\text{Fe}^{3+}$  ions. According to Ketteler *et al.*'s calculations,[49] all oxides may coexist in vacuum as metastable states, because of the kinetic barrier. The oxidation rate depends on both temperature and oxygen pressure.

Wüstite  $\text{FeO}$  phase is not stable under ambient conditions and so is usually in a sub-stoichiometric form:  $\text{Fe}_{1-x}\text{O}$ . It crystallizes in rocksalt structure and is an antiferromagnetic insulator.  $\text{Fe}_2\text{O}_3$  possesses four different phases. The  $\gamma$  phase, or maghemite attracted specially our attention because it crystallizes in the inverse spinel structure and is ferrimagnetic, as the magnetite  $\text{Fe}_3\text{O}_4$ . It can be considered as an  $\text{Fe(II)}$ -deficient magnetite.

Magnetite, although discovered about 1500 BC, remains one of the most intensively studied magnetic compound. Investigations of its transport properties started with Verwey in 1939, who observed a sharp phase transition upon cooling below 120 K, at which the resistivity of magnetite increases by two orders of magnitude.[50] After a long period of doubt due to an under-estimation of the role of crystal preparation and quality control, the transition was characterized as a single first-order transition.[51] Small deviations from the magnetite stoichiometry lead indeed to a broadening of the transition. An accurate control of the oxygen partial pressure even during cooling down to room-temperature is a key to avoid such situation. Because the crystallographic structure at low temperatures remains controversial (orthorhombic, monoclinic or even triclinic), no consensus is established between the many theoretical models proposed for charge ordering.[52]

Above the Verwey transition, magnetite has a cubic structure with a lattice constant  $a=8.394 \text{ \AA}$ . [53] Oxygen anions form a *fcc* lattice. Tetrahedral sites (A type) are occupied by  $Fe^{3+}$  ions, while octahedral sites (B type) are occupied by an equal number of randomly distributed  $Fe^{2+}$  and  $Fe^{3+}$  ions resulting in an average valence value of  $2.5^+$  per  $Fe_B$  cation. [52] Fig. 1.7 illustrates the structure.

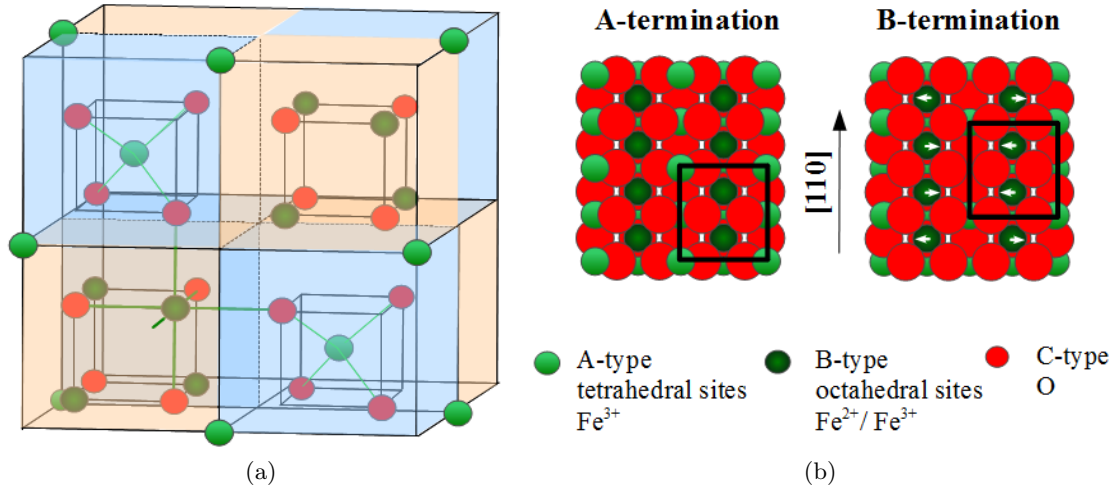


Figure 1.7: Schematic structure of a unit cell of (a) bulk, and (b) the (001) reconstructed surface of  $Fe_3O_4$ . In (a), the iron atoms are green, with octahedral iron atoms (darker) located at the corners of the small cubes (edge length  $2.1 \text{ \AA}$ ), and tetrahedral atoms located at the edges of the large cubes (edge length  $4.2 \text{ \AA}$ ). The entire unit cell is made of 8 small boxes, whose only the atoms in the front half of them are shown. [54] In (b), A-termination and B-termination of  $(\sqrt{2} \times \sqrt{2})R45$  reconstruction. White arrows show the predicted deformation resulting in a *wavelike* structure.

The (001) surface of magnetite typically shows a  $(\sqrt{2} \times \sqrt{2})R45$  reconstruction (cf. Fig 1.7b) which is largely reported in the literature. [55] However, two models supported experimentally and theoretically are still under debate: an A-layer where half of the tetrahedral iron is missing (Chambers *et al.* using x-ray photo-electron diffraction, Rustad *et al.* with molecular dynamics calculation ([56, 57]) and a B-layer with oxygen vacancies (Stanka *et al.* [58]) or hydroxyl groups (Voogt *et al.* with electrostatic considerations [59]). Spiridis *et al.* reconciles both with DFT calculations combined with analysis of high resolution images considering that different preparation conditions -oxygen-rich versus iron-rich- leads to one or the other model. [60] In the case of B-terminated layer, a slight in-plane shift of ions compared to their bulk position forming a *wavelike* structure along the [110] direction is observed. It could be stabilized by lattice distortion or by Jahn Teller mechanism to reduce a surface polarity according to respectively Parkinson *et al.* and Pentcheva *et al.* [61, 62]

Magnetite is a ferrimagnet with a very high order temperature  $T_C = 858 \text{ K}$ . The A- and B-site magnetic moments are coupled antiferromagnetically. Magnetic moment is of  $4 \mu_B$  per  $Fe_3O_4$  formula unit. As shown schematically in Fig. 1.8, magnetite is predicted to have a gap for the majority  $Fe^{3+}$  spin band but the minority spin  $Fe^{2+}$  band crosses the gap.

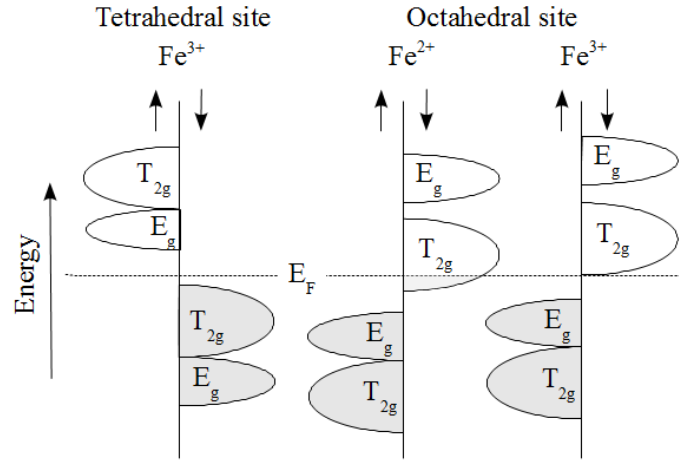


Figure 1.8: Schematic representation of the electronic structure of the Fe-ions in  $Fe_3O_4$  (from ref. [22])

The majority spin electrons exhibit hence insulating or semiconducting behavior, while the minority spin electrons have a metallic behaviour. It leads to an half-metallic ferromagnetic state with a 100% spin polarization at the Fermi energy, making magnetite a promising material for spintronics.

### 1.2.3 Pt substrate

The Pt(001) surface is well-suited to the coherent epitaxial growth of FePt, as Marcio Soares established during his thesis.[28] Pt bulk has a fcc structure with the lattice constant  $a_{Pt} = 3.924 \text{ \AA}$ , close to the a lattice constant of chemically ordered FePt phase ( $a_{FePt} = 3.86 \text{ \AA}$ ).

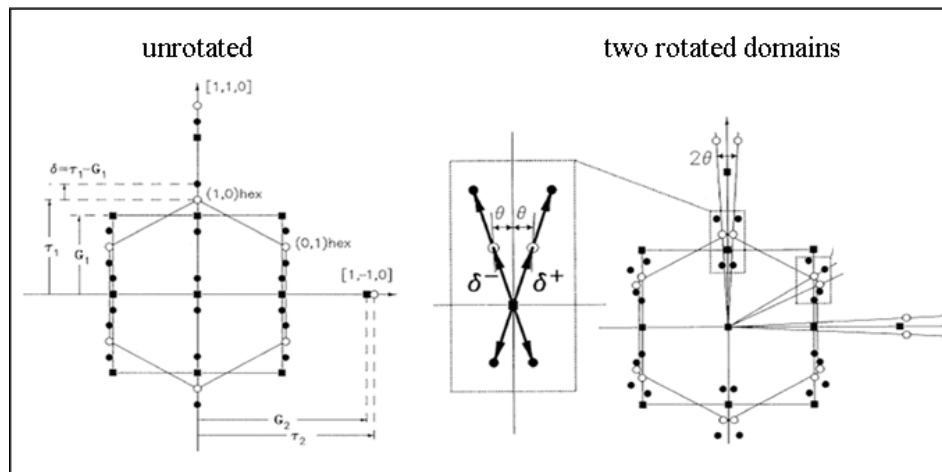


Figure 1.9: Sketch of the diffraction pattern of the hexagonal surface taken from ref.[63].

Pt(001) crystal presents a quasi-hexagonal reconstruction on its surface that has some consequences on the growth of adlayers. The reconstruction, abbreviated  $Pt(001)\text{-hex}$ , differs



depending on the substrate preparation, thermal history and a possible miscut. It is driven by tensile stress imposed on the topmost layer[64]. The surface energy was measured and theoretically demonstrated lower for a reconstructed surface than for an unreconstructed one by about 0.12 eV per (1 x 1) unit cell[65]. Abernathy et al.[63] elaborated its phase diagram. They showed that below 1820 K the rough and disordered surface reconstructs to form a hexagonal monolayer with a high-symmetry direction aligned with the cubic [010] direction. When slowly lowering the temperature below 1685 K, hexagonal overlayer rotates continuously to  $0.9^\circ$  and discontinuously to  $0.75^\circ$  relative to the aligned direction (Fig. 1.9). The two phases still coexist at RT in this case. However, if the sample is heated up to 1000K during 5 min and then cooled down to RT, small domains of the unrotated phase cover the surface with no trace of the rotated domains[63] highlighting the thermal history importance.

A high resolution STM image (Fig. 1.10) taken from Borg et al[66] illustrates the quasi-hexagonal packing of the reconstruction with its characteristic corrugation along the [100] direction. The corrugation comes from the mismatch with the substrate, where one roughly has 6 hexagonal rows each 5 substrate rows, with a periodicity of  $\sim 14 \text{ \AA}$ . One cannot be more precise, because the reconstruction, according to Abernathy et al, is incommensurate in both directions for all its phases, despite its orientational epitaxy. The layer just below the surface keeps the bulk fcc symmetry allowing reconstructed domains, rotated by  $90^\circ$  from each other. A miscut of the surface could favor one domain over another. Our substrate has a miscut smaller than  $0.1^\circ$  and both domains were observed.

Our standard procedure to prepare Pt surface consists in several cycles of 800 V Ar+ sputtering for 40 min (typically  $P_{Ar} = 4 \cdot 10^{-6}$  mbar with sputter current of about 10  $\mu\text{A}$ ) at RT and annealing at 1250 K for 5 to 10 min. The surface which is clean but rough by superficial layers uprooting by argon, gets ordered during the annealing thanks to thermal energy. During the decrease of the ultimate annealing, the sample is exposed to  $3 \cdot 10^{-7}$  mbar of oxygen at 970 K for 5 min to get rid of carbon impurities segregated at the surface followed by a flash annealing at 1250 K for 3 min to enhance CO desorption, before slowly cooling down. The cleanness of the surface is checked by AES. After this procedure the surface usually is flat and a peak of the reconstruction is seen at (1.206 0 0.2) with sometimes  $0.9^\circ$  rotated domains depending on the thermal history and on the number of cleaning cycles applied.

From the position of this reconstruction peak, one can evaluate that the surface reconstruction is 25% denser than the underlying square (1 x 1) plane and 8% denser than the Pt(111) bulk closed-packed planes. The growth of an adlayer or a reactive exposure removes

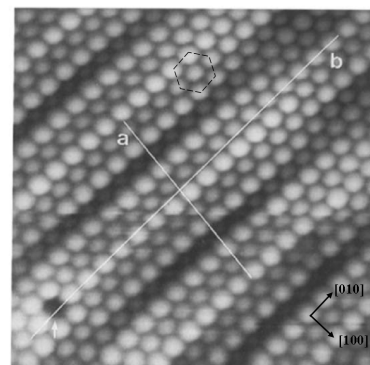


Figure 1.10: Atomic resolution STM image of reconstruction taken from ref. [66] appended with indication of quasi-hexagonal packing (dashed line) and surface orientation convention (arrows)



the reconstruction[67, 68]. During this process, called deconstruction or restructuring, the 25% excess surface atoms become adatoms. They form islands, steps or interfere with the adlayers forming alloys or even acting as a surfactant[69]. In our case, we will use this excess and Pt tendency to segregate to grow FePt alloy.

### 1.2.4 A ferromagnetic alloy: FePt

Ferromagnetic chemically-ordered alloys such as FePt, FePd, CoPt, CoPd, FeNi present a high magnetocrystalline anisotropy. FePt in the  $L1_0$  chemically ordered phase is predicted to possess one of the highest magnetic anisotropy energy with an energy density  $K_u$  of  $16 \times 10^7 \text{ erg/cm}^3$  for complete ordering.[70] Experimentally,  $K_u$  values reaching  $\sim 4 \cdot 10 \times 10^7 \text{ erg/cm}^3$  are reported in ref. [71, 72] making FePt a promising candidate for ultrahigh density magnetic storage media. Moreover, its perpendicular magnetic anisotropy (PMA) allows to increase storage area density and to reduce the spin transfer current.[10, 13, 73, 74] The high uniaxial anisotropy results from the strong hybridization between highly polarized Fe  $3d$  and Pt  $5d$  states inducing a magnetic momentum in Pt atoms, combined with the large spin-orbit coupling of Pt atoms.[75] It depends on the chemical order and probably subtly on the local coordination.[76, 75] Hence, according to its bulk phase diagram, presented in Fig. 1.11, the Curie temperature of stoichiometric FePt ordered alloy is about  $470^\circ\text{C}$ , higher than the disordered one.

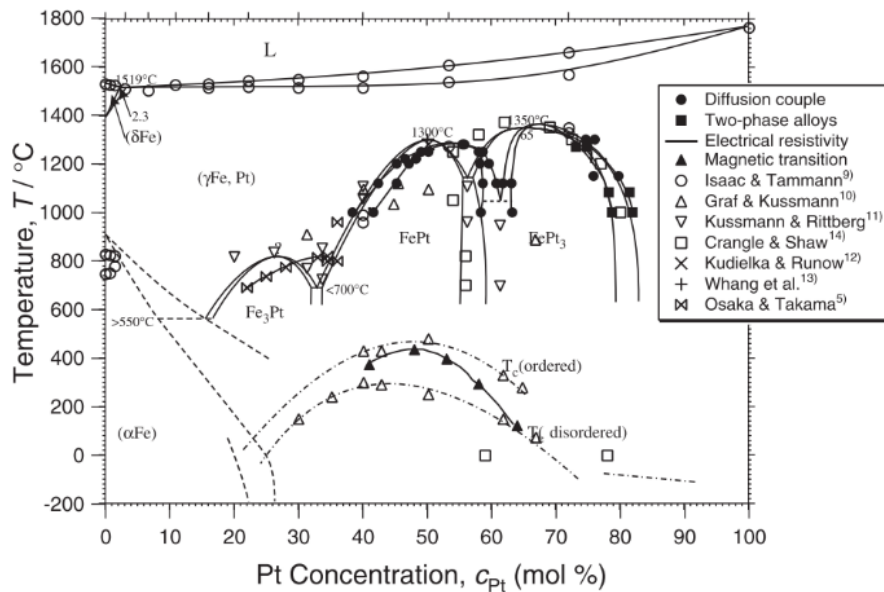


Figure 1.11: Fe-Pt binary alloy phase diagram taken from ref. [77]

The Fe-Pt system exhibits a face-centered cubic ( $fcc$ ) structure at high temperature which organizes in two phases depending on the stoichiometry.[76]  $Fe_3Pt$  and  $FePt_3$  crystallize in  $L1_2$  phase, while  $L1_0$  is achieved in the equiatomic concentration below 1570 K. In the cubic  $L1_2$  structure, the majority atoms occupy the face-centered positions and the minority ones the corners. The cubic  $L1_0$  structure corresponds to the stacking of alternate planes of Fe and

Pt along the tetragonal axis, taken as  $c$ - axis. The powder of this equiatomic phase presents the lattice parameters  $a_{FePt}^{powder} = 3.852 \text{ \AA}$  and  $c_{FePt}^{powder} = 3.720 \text{ \AA}$ . [78] They are slightly different for a nanocrystalline system which is subjected, as epitaxial films, to stress at the boundaries :  $a_{FePt}^{nanocrystal} = 3.86 \text{ \AA}$  and  $c_{FePt}^{nanocrystal} = 3.713 \text{ \AA}$  giving  $(c/a)^{nanocrystal} = 0.962$ . [79]

The tetragonal ratio  $c/a$  arising from the strain from the lattice mismatch influences the ordering of the FePt films. As reported by Ding et al. and explained by Aas and coworkers, a minimum ratio  $c/a$  of about 0.9466 obtained in FePt/ $Cr_{95}Mo_5$ /MgO(001) with 6.33% mismatch coincides with a maximum ordering degree and magnetic anisotropy constant. [80] Aas and coworkers found also by first-principles calculations a linear correlation between the magnetic anisotropy and the chemical order parameters in these layers. According to other electronic-structures calculations led by Brown *et al.* [81] and kept up by Lu *et al.*, [82] the tetragonal distortion as well as the order could stabilize an AFM state in FePt. The antiferromagnetic arrangement can be achieved with a tetragonality ratio of 0.94.

Ferromagnetism as a collective phenomenon is supposed to weaken with thickness. However, FePt layers keep the strong PMA of FePt bulk on the condition that they are well ordered [83] and no additional layer perturbs their structure and electronic environment. [84] Huge coercive fields up to 10 T have been already reported in  $L1_0$  FePt single domains grown on a heated MgO(001) substrate. [85] Perpendicular remanent magnetization at room temperature has been found for FePt film on Pt(001) of only 3 bilayers (BL) (1 nm thick). Authors deduce from this strong anisotropy that  $3d$  Fe states, which are at the origin of PMA, do not depend on the thickness. [86]

### 1.2.5 A unique antiferromagnetic oxide: CoO

The investigations concerning EB boost current research on antiferromagnetic films. For its Néel temperature  $T_N$  close to the room temperature (293 K), its high magnetocrystalline anisotropy, cobalt oxide ranks among the most interesting AFM layers for spintronics devices. [87] A critical issue for competitive CoO-based devices is, however, the preservation of a significant EB effect up to temperatures as close as possible to the room temperature (RT). Nevertheless, so far, all experimental studies in ultrathin (<10 nm) CoO/FM double-layer systems report EB blocking temperatures ( $T_B$ ) smaller than  $T_N$ . [17, 88, 89]

In the paramagnetic phase, bulk CoO crystallizes in the rocksalt structure with  $a=4.261 \text{ \AA}$ . Co and O planes alternate along the [111] direction in an hexagonal mesh with in-plane interatomic distance of  $3.013 \text{ \AA}$  (Fig. 1.12). The antiferromagnetic transition goes along with a cubic-to-monoclinic crystallographic distortion. At 10 K, the monoclinic constants are  $a_m=5.18190(6) \text{ \AA}$ ,  $b_m=3.01761(3) \text{ \AA}$ ,  $c_m=3.01860(3) \text{ \AA}$  and  $\beta=125.5792(9)^\circ$  (instead of  $125.26^\circ$  as at RT), with  $\beta$  the angle between  $a_m$  and  $c_m$ . In the face-centered setting, this corresponds to an angle of  $\gamma=89.962^\circ$  between the two edges of the different lengths. [90] The monoclinic phase results in a tetragonal distortion (along [001] direction) plus a much smaller trigonal one (reducing the angle  $\gamma$ ) to the rock-salt structure.

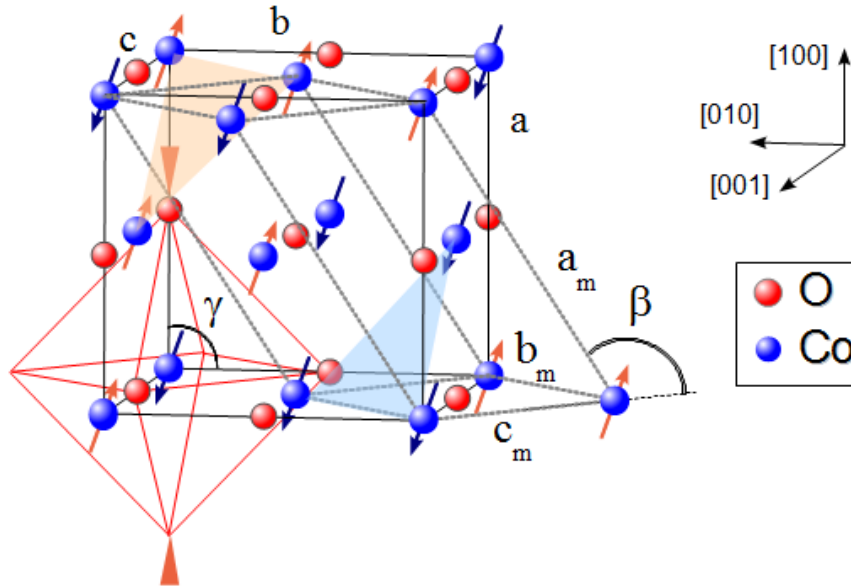


Figure 1.12: CoO rocksalt ( $a$ ,  $b$ ,  $c$ ) and monoclinic ( $a_m$ ,  $b_m$ ,  $c_m$ ,  $\beta$ ) unit cell parameters and low-temperature AFM structure

A detailed description of the electronic structure of CoO, as a transition-metal oxide, should take into account the full multiorbital Coulomb interaction between the electrons of the  $Co^{2+}$  ion and the bonding to the neighboring ions. Fortunately, the localized character of orbitals allows to restrict it within a  $CoO_6$  cluster.  $Co^{2+}$  ions are indeed embedded in an octahedron made of oxygen ions. From group theory, we know that an octahedral symmetry  $O_h$  splits 3d states in two levels, called  $t_{2g}$  et  $e_g$ .  $t_{2g}$  is 3 times degenerated ( $d_{xy}$ ,  $d_{yz}$ ,  $d_{xz}$ ), while  $e_g$  2 times ( $d_{3z^2-r^2}$ ,  $d_{x^2-y^2}$ ). When the crystal distorts in one direction, it loses a symmetry and becomes tetragonal with a local symmetry  $D_{4h}$ .  $t_{2g}$  and  $e_g$  split in two states each. The energy scheme of these levels depends whether if one direction is larger or smaller than the two others. Once the ligand-field energy scheme has been established, the levels can be filled with the 7  $d$ -electrons of  $Co^{2+}$  ion taking into account Coulomb repulsion. In CoO, the ligand field is weaker than Coulomb repulsion. Each degenerate level takes up a single electron, then the two electrons remaining complete two  $t_{2g}$  levels. So two holes reside in the  $e_g$  orbitals and one hole in one of the  $t_{2g}$ .  $Co^{2+}$  is said to have a high spin.[22]

When the crystal is distorted, the  $z$  axis refers usually to the tetragonal axis with the lattice parameter  $c$ , while  $a$  refers to the two equivalent distances.  $c/a$  ratio expresses thus the tetragonal distortion. In the limit that the energy splitting from tetragonal distortion is much larger than the spin-orbit interaction, in strained CoO with  $c/a \ll 1$ , such as CoO bulk at low temperature, the unpaired  $t_{2g}$  electron occupies a linear combination of  $d_{xz}$  and  $d_{yz}$  orbitals. Due to the spin-orbit coupling the orbital moment and the spin tend to be oriented along the tetragonal axis ( $z$ ). In CoO with  $c/a \gg 1$  the unpaired  $t_{2g}$  orbital has  $xy$  symmetry with a quenched orbital momentum. If the distortion is not so important,  $t_{2g}$  splitting is smaller than

the spin-orbit interaction and the orbital momentum is not quenched.[91] Orbital momentum and spin are perpendicular to the tetragonal axis.

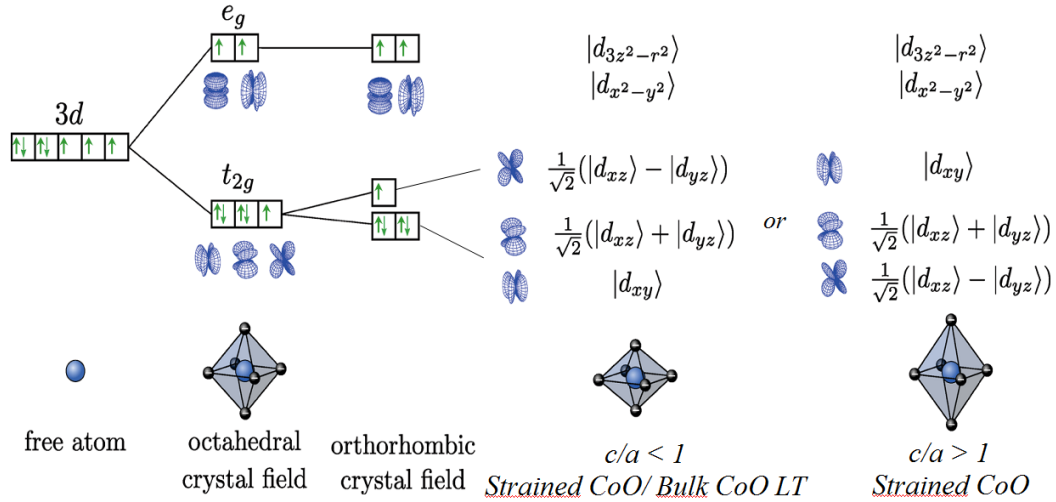


Figure 1.13: Schemes of the level splittings and occupation of the Co 3d states due to the octahedral crystal field with the dominated orthorhombic distortion as function of the ratio  $c/a$  (adapted from ref. [92])

Superexchange is a magnetic interaction between two magnetic ions separated by a non magnetic ion. It is mediated by the electrons in their common nonmagnetic neighbor (here oxygen). As in MnO, FeO and NiO, the superexchange coupling acting via  $180^\circ$  metal-oxygen-metal bonds imposed the magnetic moments of second-nearest neighboring cations  $Co^{2+}$  to be anti-parallel.[93, 94] It results in a stacking of ferromagnetic sheets coupled antiferromagnetically along the cubic [111] axis.[24] This magnetic structure is denoted as a type-II-fcc antiferromagnetic (AFM-II) order and characterized by a propagation vector  $\vec{k} = [1/2, 1/2, 1/2]$ , i.e. along the trigonal axis. The concomitant crystallographic and magnetic phase transitions suggest that distortion and antiferromagnetism are linked by magnetostriction[90] or by Jahn-Teller effect.[95] Nevertheless, Tomiyasu and coworkers found an additional propagation vector  $\vec{k} = [0, 0, 1]$  (along the tetragonal axis) establishing a type-I-fcc AFM order, weaker than the conventional AFM-II. They ascribe then the lattice modulation to magnetic geometrical frustration.[96]

The magnetic moments are all oriented in the monoclinic  $a_m c_m$  plane, pointing close to the cubic [001] axis according to the general consensus. In the Figure 1.12, they are shown oriented along the  $[\bar{1}\bar{1}7]$  direction [90, 97, 92] as shown in Fig. 1.12. It is a compromise between the magnetic dipole forces and the crystal anisotropy which tend to order the moments respectively within the (111) plane and parallel to [001]. Because all are found parallel, spin structure is called collinear. The magnetic moment per atom is evaluated at  $3.98 \mu_B$ . It lies far above the  $3 \mu_B$  value, revealing a large orbital contribution. The strong interaction between spin and orbital magnetic moments through the spin-orbit coupling drives the magnetic anisotropy energy.[92] This view is supported by soft x-ray absorption spectroscopy (XAS) experiments in thin CoO layers grown on different substrates, which revealed significant modifications in

the magnitude and orientation of the magnetic moments induced by epitaxial strain.[\[98\]](#) with the experiments presented in the following, we will try to take a part to this discussion.

# Chapter 2

## Experimental techniques

### Contents

---

<b>2.1 X-rays</b>	<b>24</b>
2.1.1 Electromagnetic waves and photons	24
2.1.2 Synchrotron radiation	26
<b>2.2 X-ray scattering and diffraction</b>	<b>26</b>
2.2.1 X-ray diffraction	28
<b>2.3 Surface X-ray diffraction</b>	<b>30</b>
2.3.1 Pattern of x-rays diffracted by a surface	31
2.3.2 Real surfaces and adlayers	32
2.3.3 Experimental set-up	35
<b>2.4 X-ray specular reflectivity XRR</b>	<b>36</b>
<b>2.5 X-ray Absorption Spectroscopy</b>	<b>38</b>
<b>2.6 X-ray Dichroism</b>	<b>41</b>
2.6.1 X-Ray Magnetic Circular Dichroism (XMCD)	41
2.6.2 X-Ray Magnetic Linear Dichroism (XMLD)	43
2.6.3 Experimental aspects of XMCD / XMLD	45
<b>2.7 Magneto-optic Kerr effect (MOKE)</b>	<b>45</b>
2.7.1 Experimental aspects of MOKE	47
<b>2.8 Preparation and complementary analysis of the surface</b>	<b>47</b>

---

Surprisingly, sight is the sense we trust the most to gauge our surroundings. Yet it is only an indirect probe of reality. It rests on light and its interaction with matter. This said, we obtain in this way precise information on the matter such as its structure, absorption capacity (color), related sometimes to its heating or even roughness... To study matter at micrometer scale and its properties, detectors have been built, based as sight, on the interaction of radiation with matter, enlarging only the field of possibilities. For instance, radiation could

be light but also neutrons or electrons depending on the tested property. Probes of matter can be classified in different ways: according to the sensor (electromagnetic wave, electrons, ions...) in and out, according to the detection mode (spectroscopy, direct space scanning, reciprocal space scanning...) or even according to the phenomenon involved. For probes using radiation-matter interaction alone, scattering (elastic or inelastic, coherent or not), absorption or transmission can take place. Today there is a profusion of techniques to analyze nanomaterials. The choice of one technique against another depends on the desired parameter and the experimental conditions that the sample can support. All the techniques based on x-ray have the great advantages to be non-destructive.

This chapter overviews the main techniques used during this work. The objective is to provide the reader with some essential concepts needed to follow the arguments made in this thesis. We first introduce briefly photon-matter interaction. Then we recall few concepts on x-ray diffraction that will set the basis for the understanding of surface x-ray diffraction (SXRD), also called grazing incidence x-ray diffraction (GIXRD), and x-ray reflectivity (XRR). Afterward, basic principles of x-ray absorption are presented and developed in the case of polarized beam leading to x-ray magnetic circular and linear dichroism (XMCD and XMLD). In the third part we are interested in magneto-optic Kerr effect (MOKE). Finally as a starter of our works, we discuss the surface preparation and the characterization techniques that we used for complementary qualitative analysis of our substrate and adlayers.

## 2.1 X-rays

Any radiation can be seen in two ways. Either as a wave characterized by its intensity, periodicity or wavelength  $\lambda$  and polarization or as an ensemble of particles characterized by their amount, energy  $E$  and spin (equivalent to polarization). It exhibits wave-particle duality. This duality is necessary to fully describe all interactions with quantum-scale objects. All properties of these two paradigms are related.

### 2.1.1 Electromagnetic waves and photons

In this PhD, we will focus mainly on light, which is both electromagnetic radiation or photon particles. Energy  $E$  of photons is linked to wave frequency  $\nu$ , wavelength  $\lambda$  or norm of wavevector  $\vec{k}$  through Planck constant  $h$  equal to  $6.62 \times 10^{-34}$  J.s (or  $4.13 \times 10^{-15}$  eV.s).

$$E = h.\nu = \frac{h.c}{\lambda} = \frac{h}{2\pi}.k.c \quad (2.1)$$

$c$  is the celerity, speed of light. Numerically the relation is given by

$$\lambda = \frac{12.398}{E} \text{ with } \lambda \text{ in } \text{\AA} \text{ and } E \text{ in kiloelectron volt (keV).}$$

The designation of an electromagnetic wave changes in function of its energy: gamma ray, x-ray, ultraviolet light or even radio wave (Fig. 2.1). Because radiation interacts with matter

and generates interferences when its wavelength is comparable to the characteristic size of the studied object, we got interested in x-rays. Typically hard x-rays have a wavelength in the range of 0.01 to 0.1 nm (12 to 120 keV) and so are adapted to interatomic spacing, while soft x-rays have a wavelength between 0.1 to 10 nm (0.12 to 12 keV) are rather sensitive to nanometric structures as orbital or magnetic ordering. The former can penetrate solid objects and is commonly used to image the inside of objects. By contrast, the latter is rapidly attenuated and needs ultra-high vacuum environment to be preserved.

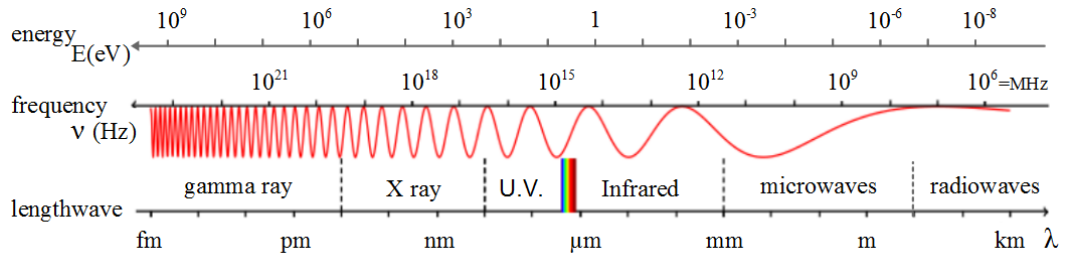


Figure 2.1: Electromagnetic spectrum (adapted from ref. [99])

As its name suggests, an electromagnetic wave has electric and magnetic field components. Both fields oscillate perpendicular to each other and perpendicular to the direction of wave propagation. They are related by the potential vector  $\vec{A}$ . For simplicity, we will consider the electric field only. Orientation of electric field oscillations is called polarization ( $\vec{P}$ ) and can vary with time and space. In a polarized wave, there is a phase relation between the polarization at one space and time position to a polarization at another space and time position. Usually, x-rays are not polarized, except with adapted filters, with a polarized source or after scattering with  $2\theta = 90^\circ$ . Polarization can be linear (electric field oscillates in one direction) or rotate around the propagation direction of the wave. Then polarization is said circular or elliptical. Any linear polarization can be decomposed in two circular polarizations (right and left) with equivalent weight.

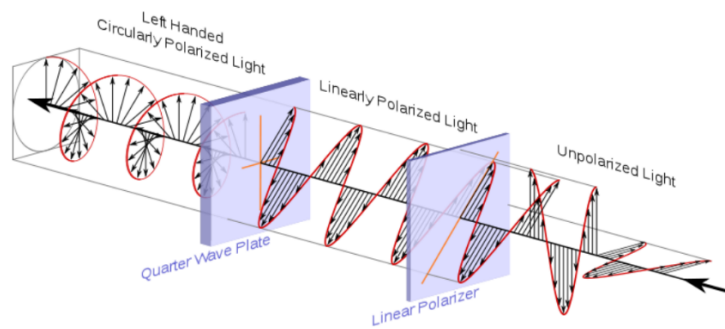


Figure 2.2: Polarization of electromagnetic wave changed by filters. For simplicity, only electric field is represented (taken from ref. [99]).

To describe a monochromatic electromagnetic wave, one needs the wavevector  $\vec{k}$  which gives the orientation and energy of the beam, the polarization  $\hat{\epsilon}$  which is the orientation of



the electric field ( $\vec{\varepsilon} = i\frac{\mathbf{E}_0}{E_0}$ ) and the amplitude of the electric field ( $E_0$ ). All is summarized with the expression of the propagated electric field  $\vec{\varepsilon}$ .

$$\vec{\varepsilon}(\vec{r}, t) = \hat{\varepsilon}.E_0.e^{i(\vec{k}.\vec{r}-w.t)} \quad (2.2)$$

### 2.1.2 Synchrotron radiation

The synchrotron radiation typically ranges from the infrared (IR) to the hard X-ray regions. Consequently, the emitted wavelength turns from micron to fraction of nanometers and the energy from fraction of eV to tens of keV. Wave of such wide spectral band is produced by the acceleration of packets of electrons traveling in a UHV ring on a closed loop. Every time an electron is forced by a magnet to change its trajectory, it is accelerated via Lorentz force to the centripetal acceleration  $a = v^2/R$  where  $v$  is the speed of the particles and  $R$  the radius of the local curvature. As all charged accelerated particles, electrons loose energy by emitting radiation. The radiation emitted by accelerated electron is the typical dipole radiation but, electrons traveling at a relativistic speed, near celerity, it suffers from a relativistic contraction, resulting in a very forward intense peaked beam and the energy shifts to the x-ray region.[100, 91, 101]

Three kinds of synchrotron radiation sources are available now. The *bending magnet*, which is the first and most simple way to extract radiation, is compulsory to make turn electrons on the storage ring. It gives a large spectrum of a linearly polarized light in the plane of orbit of the accelerated charges. Above or below the orbit, a fraction of circularly polarized light is available. The *undulators*, as well as the *wigglers*, are periodic arrays of magnets positioned along the straight section of the ring. Both have higher brilliance and flux. The wavelength of the synchrotron radiation is then related to the vertical distance between the magnets or to the magnetic field function of the flowing currents. Forcing the electron to oscillate in the horizontal and in the vertical plane, the generated light could be circularly polarized.

At the end of each source is designed a beamline containing different experimental set-ups. They develop different environments adapted to the studied sample around several techniques. Three of them are explained here after. They take advantage of the polarization control, the energy selection and the high brilliance of synchrotron radiation.

## 2.2 X-ray scattering and diffraction

In the classical description, electron, which is a charged light particle, is forced by electric field of the electromagnetic wave to vibrate. But a vibrating electric charge acts as a source and radiates an electromagnetic wave with same frequency than its vibration. The scattered wave has hence the same wavelength as the one of the incident beam. The scattering is said elastic. In a quantum mechanical description, energy may be transferred to the electron. Scattered photon has then a lower or higher frequency relative to that of the incident one. The process is said inelastic. In this section, we assume that the x-ray energy is much larger than the

energy of any absorption edges of our sample. Only elastic scattering is taken into account. All the concepts given here have been described in detail in numerous books, reviews, and PhD thesis. [102, 103, 104, 105, 28, 106, 107]

In the case of an incident non polarized wave with electric field amplitude  $E_0$  and wavevector  $\vec{k}_i$ , amplitude  $E_f$  of scattered wave ( $\vec{k}_f$ ) is evaluated at a distance  $R_0$  by [104]

$$E_f = E_0 \cdot \frac{e^2}{mc^2} \cdot \frac{1}{R_0} e^{i(\mathbf{k}_f - \mathbf{k}_i) \cdot \mathbf{r}} \quad (\text{Thompson formula})$$

where  $m$ ,  $e$  and  $\vec{r}$  are respectively the mass, charge and position of the electron.  $R_0$  is far enough from the electron to consider plane wave. The phase difference between the two waves is thus  $(\vec{k}_f - \vec{k}_i) \cdot \vec{r} = \vec{Q} \cdot \vec{r}$ .  $\vec{Q}$  is known as the *momentum transfer*. It is the natural variable to describe elastic scattering processes and is usually expressed in  $\text{\AA}^{-1}$ . When the angle formed by  $\vec{k}_i$  and  $\vec{k}_f$  is the scattering angle  $2\theta$ ,

$$\vec{Q} = \vec{k}_f - \vec{k}_i = \frac{4\pi \cdot \sin(\theta)}{\lambda} \quad (2.3)$$

With the momentum transfer, one usually associates the Ewald sphere. The surface of the Ewald sphere is the site of possible extremities of the momentum transfer.

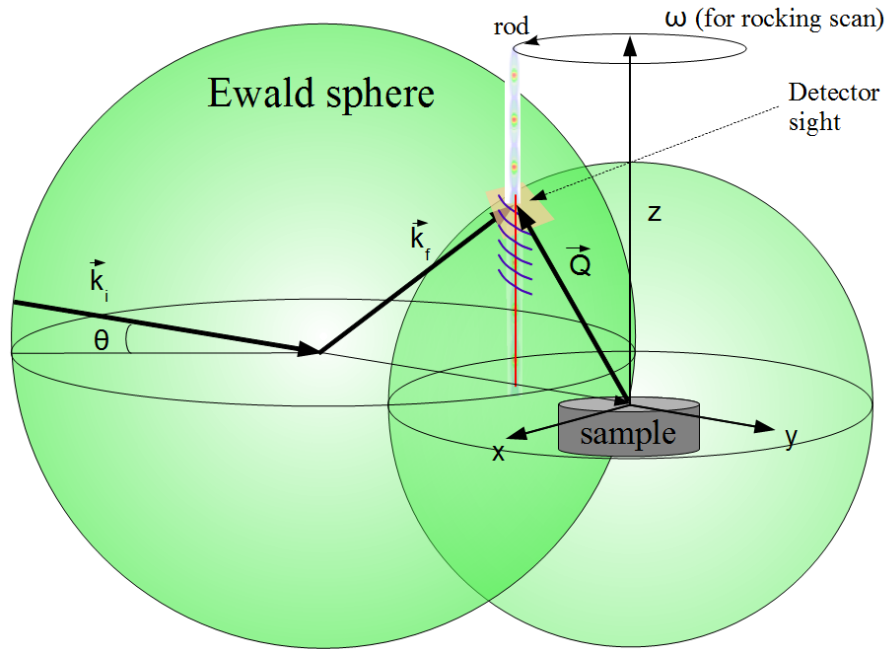


Figure 2.3: Ewald construction

The constant  $r_e = \frac{e^2}{mc^2}$ , known as classic electron radius or Thomson scattering length, is very small ( $3.10^{-15}m$ ). It highlights the weakness of interaction between x-ray and electron. In addition, the nucleus is too heavy to interact with x-ray. Consequently, the probability of x-ray scattered by an atom is so weak that x-ray scattering can be considered as an independent event. It results also that the incoming x-rays are scattered only once and no interaction between the incoming and scattered beams occurs, excluding multiple scattering effects. The

kinematical approximation is valid, and the amplitude scattered by an atom is taken as the sum of the independent contributions from all the individual electrons. Each electron (or atom) represents a scattering center which emits a spherical wave when excited by the incoming plane wave field.

Within this approximation, the amplitude of the electric field of a beam scattered by a single atom is given by

$$E_f = E_0 \cdot \frac{e^2}{mc^2} \cdot \frac{1}{R_0} e^{i \cdot \mathbf{Q} \cdot \mathbf{r}} \cdot f(\mathbf{Q}) \quad (2.4)$$

where  $f$  is the atomic scattering factor, defined as the Fourier transform of the electron density  $\rho$  for a single atom

$$f(\mathbf{Q}) = \int \rho(\mathbf{r}) \cdot e^{i \cdot \mathbf{Q} \cdot \mathbf{r}} d^3r \quad (2.5)$$

For small values of  $\vec{Q}$  it approaches the number of electrons in the atom.

### 2.2.1 X-ray diffraction

X-ray diffraction corresponds to the scattering of x-rays by an ensemble of atoms with periodic arrangement over large distances. They are in general crystals. A diffraction peak is observed when scattered waves interfere then coherently.

A crystal has a repetitive arrangement of atoms along all three directions in space, called unit cell. These directions are defined by three lattice vectors  $\vec{a}_1$ ,  $\vec{a}_2$  and  $\vec{a}_3$  (or  $\vec{a}$ ,  $\vec{b}$  and  $\vec{c}$ ), whose modules give the lattice parameters along the crystal axes. Atoms are referenced according to their nature and coordinates relative to their position in the unit cell. Described space is called direct or real space.

To discuss the x-ray intensity diffracted by a crystal, we suppose that the crystal is small enough to neglect absorption and extinction effects. Else, the scattered intensity is a negligible fraction of the incident beam intensity. Each crystal atom is subjected to the same incident amplitude. For simplicity, we consider a small parallelepiped crystal of size  $N_i a_i$  along each crystal axes. The position of the atom of type  $n$  in a unit cell with coordinates  $(m_1, m_2, m_3)$  is given by the vector  $\mathbf{R}_m^n = m_1 \mathbf{a}_1 + m_2 \mathbf{a}_2 + m_3 \mathbf{a}_3 + \mathbf{r}_n$  with  $\mathbf{r}_n$  the position of the atom in the unit cell. In the kinematical approximation, the total diffracted field corresponds to the summation of diffracted field by all atoms in the crystal. Amplitude of the electric field of the beam scattered far from the crystal can thus be expressed by

$$E_f^{crystal} = E_0 \cdot \frac{e^2}{mc^2} \cdot \frac{1}{R_0} \cdot F_u \cdot \prod_{j=0}^3 S_{N_j} \quad (2.6)$$

with  $F_u$  the unit cell structure factor, which contains all the information concerning the atomic positions in the cell.

$$F_u = \sum_n f_n \cdot e^{i \cdot \mathbf{Q} \cdot \mathbf{r}_n} \quad (2.7)$$

and  $S_{N_j}$  the sum of all unit cells of the crystal in direction  $\vec{a}_j$

$$S_{N_j} = \sum_{m_j=0}^{N_j-1} e^{i(\mathbf{Q} \cdot m_j \mathbf{a}_j)} = \frac{e^{i \cdot \mathbf{Q} \cdot N_j \mathbf{a}_j} - 1}{e^{i \mathbf{Q} \cdot \mathbf{a}_j} - 1} \quad (2.8)$$

We next define vectors  $\vec{b}_1, \vec{b}_2$  and  $\vec{b}_3$  (or  $\vec{a}^*, \vec{b}^*$  and  $\vec{c}^*$ ) such as

$$\mathbf{a}_i \mathbf{b}_j = 2\pi \delta_{ij} \quad (2.9)$$

They form a base in the momentum space, called reciprocal space. We note that the momentum transfer can be written as

$$\mathbf{Q} = h \cdot \mathbf{b}_1 + k \cdot \mathbf{b}_2 + l \cdot \mathbf{b}_3 \quad (2.10)$$

$h, k, l$  are usually called Miller indices when they are integer, but for surface x-ray diffraction we will consider them continuous. Regarding these two expressions, the intensity of the scattered beam given by  $I = \frac{c}{8\pi} \epsilon \cdot \epsilon^*$  results in

$$I = I_e F_u \cdot F_u^* \cdot \prod_{j=0}^3 \frac{\sin^2(\pi h_j \cdot N_j)}{\sin^2(\pi h_j)} \quad (2.11)$$

with

$$I_e = I_0 \frac{e^4}{m^2 c^4 R^2} \cdot \left( \frac{1 + \cos^2(2\theta)}{2} \right)$$

The last term, in brackets, is the polarization factor. It arises from the cross-product of incident and scattered electric field and so depends on their different orientations. The function  $\sin^2(Nx)/\sin^2(x)$  has a maximum value  $N^2$  at integral multiples of  $\pi$ . With a reasonable value of number of unit cell  $N$ , the scattered intensity shows a  $\delta$ -function-like lineshape with strong maxima equal to  $I = I_e F_u \cdot F_u^* \cdot N_1^2 N_2^2 N_3^2$  at the nodes of the reciprocal space ( $h, k, l$  integer) and width proportional to  $1/N_j$ . The scattering intensity is negligible far from the peaks positions. The maxima observed at  $H_{hkl}$  nodes correspond to the Bragg's peaks. At this position, Laue equations are simultaneously satisfied. Rearranged, these equations become the Bragg's law:

$$\lambda = 2 \cdot d_{hkl} \cdot \sin\theta \quad (2.12)$$

where  $d_{hkl}$  is the distance between the scattering atomic planes responsible for the  $hkl$  Bragg peak. They are related by  $|\mathbf{H}_{hkl}| = \frac{2\pi}{d_{hkl}}$ .

Bragg peaks positions correspond then to the reciprocal space lattice, and are obtained by the Fourier transform of the real space crystal lattice. In a qualitative manner, Fourier transform allows to switch from one space to another. As well explained C. Schlepütz in its thesis,[106] Fourier transform ( $FT(f(x)) = \int_{-\infty}^{+\infty} f(x).e^{-2i\pi(x.u)} du$ ) and convolution theorem ( $FT(f.g) = FT(f) \otimes FT(g)$  and vice versa) are appropriate tools to illustrate some properties of the diffraction pattern of a crystal.

The electronic distribution inside a crystal lattice can be seen as a convolution of the crystal lattice ( $\vec{r}$ ) with the electron density of the basis ( $\rho$ ). According to the convolution theorem, the diffraction pattern must be equal to the reciprocal lattice (FT(crystal lattice)) multiplied by a continuous function which falls off with increasing momentum transfer (FT(electron density)). It results in an average fall off of scattering intensities towards higher momentum values. This effect limits the exploration of the diffraction pattern.

We can also examine finite-size effects using this principle. A finite crystal with sharp boundaries corresponds to an infinite real lattice multiplied by a window function giving the size of the crystal. In reciprocal space, it translates into the convolution of the reciprocal lattice with the Fourier transform of the window function. Bragg peaks are broadened and surrounding fringes appear. We find back the results of diffraction by a small amount  $N$  of unit cells. Often small coherent domains compose a crystal. The correlation length  $\zeta$  is thus inferred from the width  $\Delta Q$  of diffracted intensity in reciprocal space.

$$\zeta = \frac{2\pi}{\Delta Q} \quad (2.13)$$

$\Delta Q$  is estimated often with the full width at half maximum ( $F_{whm}$ ) of a lorentzian, gaussian or pseudo-Voigt line shape that best fits the measured profile.

## 2.3 Surface X-ray diffraction

During this PhD, we were interested in ultra-thin films deposited on monocrystalline substrate. To study their growth and atomic structure, we used x-ray diffraction applied to the study of surfaces. The incident angle is chosen grazing, giving name to the technique Grazing Incidence X-Ray Diffraction (GIXRD) in order to reduce the penetration depth of the beam inside the crystal and enhance the sensitivity to atoms close to the surface. However, when the incidence angle of the x-rays is close to the critical angle for total reflection, any deviation of the planeity of the surface shifts the incident angle and induces an important change in intensity. A compromise is found with an incident angle equal to three times the critical angle. This latter depends on the energy of the incident beam and on the atomic species involved. It is therefore chosen at the beginning of all experiments.

### 2.3.1 Pattern of x-rays diffracted by a surface

Similarly as finite crystal, the surface of a crystal can be seen as an infinite crystal truncated in the direction  $z$  perpendicular to the surface. It corresponds to the multiplication of an infinite crystal lattice with a Heaviside step function. The Fourier transform of the abrupt step is a shape function in  $1/q_z$ . The diffraction pattern is therefore the convolution of ideal diffraction pattern with this function. The surface breaks the symmetry in  $z$  direction. Its diffraction pattern is continuous along  $z$  direction with a  $1/(\Delta q_z)^2$  dependence, where  $\Delta q_z$  is the out-of-plane distance away from the Bragg peak. It results in scattering lineshapes sharp in both directions parallel to the surface and continuous in the out-of-plane direction crossing Bragg peaks with same in-plane position. They are known as crystal truncation rods (CTRs) and labeled according to their in-plane position with  $hk$  Miller indices.

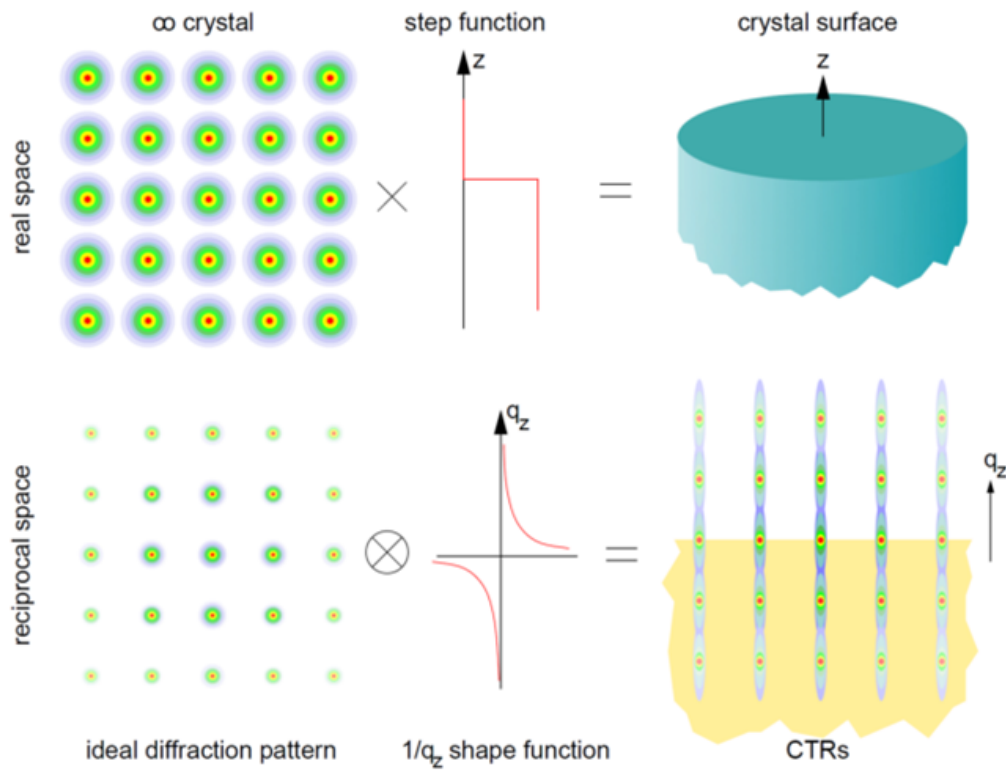


Figure 2.4: The origin of the crystal truncation rods (CTRs), as explained by the convolution theorem (taken from ref. [106])

Another way to see the effect of surface on diffraction pattern is to consider diffraction pattern of a semi-infinite crystal inside  $z \leq 0$  with equation 2.11. The square modulus of  $S_z$  can be approximated by

$$|S_z|^2 = \left| \frac{1}{e^{i\mathbf{Q}\cdot\mathbf{a}_j} - 1} \right|^2 = \frac{1}{2 \cdot \sin^2\left(\frac{1}{2}q_z a_3\right)} \quad (2.14)$$

leading to scattered intensity dependent in the out-of-plane momentum transfer  $q_z$  with

$$I_{CTR} = I_e \cdot F_u \cdot F_u^* N_1^2 N_2^2 \frac{1}{2 \cdot \sin^2(\frac{1}{2} q_z a_3)} \quad (2.15)$$

Nothing has changed in the directions parallel to the surface. Along the surface normal, intensity distribution is continuous with maximum close to Bragg points ( $l$  integer), even this expression is invalid at Bragg peaks. One understands easily that all the information about the surface is contained in the intensity distribution between Bragg peaks.

### 2.3.2 Real surfaces and adlayers

Up to now, we considered surface only as a truncation of a bulk crystal. Real surfaces may relax strain or reconstruct (section 1.1.3). In addition a thin film could be added on the top of the bulk crystal. The slight crystalline deviations relatively to the structure of the substrate and structure of adlayers are the purpose of surface x-ray diffraction (SXRD). Bulk reciprocal lattice becoming the reference, it is then convenient to change the nomenclature from momentum transfer to reciprocal lattice units.

Both substrates we used in this thesis have a *fcc* structure. In a *fcc* (or *fcc*) lattice, each atom with coordinates  $(x_n, y_n, z_n)$  is associated to three identical atoms with coordinates  $(x_n + \frac{1}{2}, y_n + \frac{1}{2}, z_n)$ ,  $(x_n + \frac{1}{2}, y_n, z_n + \frac{1}{2})$ ,  $(x_n + \frac{1}{2}, y_n, z_n + \frac{1}{2})$ . For platinum and silver, a unique atom at  $(0,0,0)$  and its 3 equivalents describe the unit cell. The unit cell structure factor can then be expressed by

$$F_u = f \cdot \left( 1 + e^{i\pi(h+k)} + e^{i\pi(h+l)} + e^{i\pi(k+l)} \right)$$

The sum takes the value 4 when  $hkl$  are unmixed (all odd or all even) and 0 otherwise. This can be easily understood regarding that in the three directions the unit cell is made of two atomic planes. Interatomic distance is thus  $a_i/2$ . In reciprocal space, it translates into reflections separated by  $2 \cdot a_i^*$ . Instead of a conventional *fcc* cell, we represented the substrate structure with the *surface* unit cell described in section 1.2.1. Miller indices of both unit cells are related with

$$h_{fcc} = h_s + k_s ; k_{fcc} = -h_s + k_s ; l_{fcc} = l_s$$

For the (100) and (110) surfaces, there is a rod at each in-plane unit crossing Bragg peaks separated by  $\Delta l = 2$ .

Two cases can be distinguished for an epitaxial film grown at the surface of a crystal. Either the adlayer relaxes, it has in-plane lattice parameters different from those of the bulk. Or the atomic planes of deposited layer are in registry with the interface, in-plane lattice parameters of film and substrate are identical. In the first case, rods and Bragg peaks of the film appear and sharpen during the growth as seen previously for a crystal alone. Film can be considered as crystal growing alone, and the rules previously found for a bulk and its surface are enough to describe it completely. In the second case, film and crystal truncation

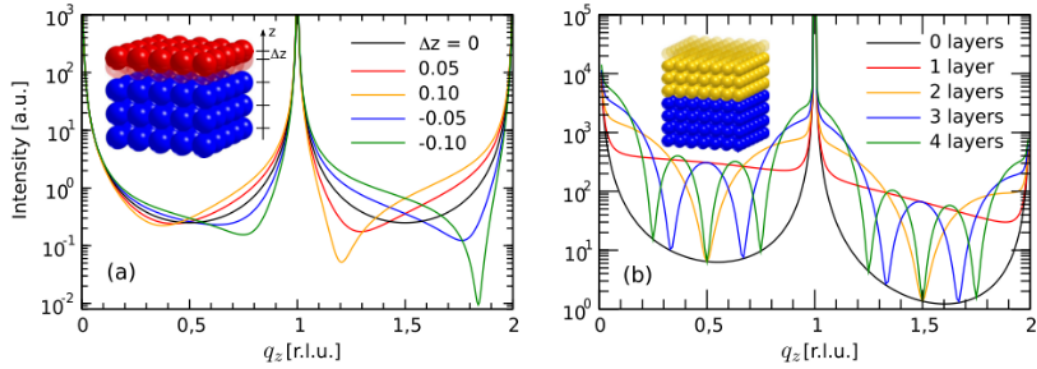


Figure 2.5: Effect on a CTR intensity profile of a displacement of the topmost atomic layer along the  $z$ -direction (a) and of a pseudomorphic growth of adlayer on the top of a bulk crystal (taken from ref. [106]).

rods merge and interfere. While Bragg peaks of deposited film (at often different out-of-plane positions than substrate) stand up, Kiessig fringes marking the interference appear on the rod. Their number and width are directly related to the amount of adlayers (cf Fig. 2.5). The x-ray diffraction pattern of the substrate and of the film has to be considered as a whole. The two contributions cannot be separated. We build then a model of the surface, calculate the structure factor amplitudes from this model and compare them with the experimental values.

A qualitative analysis can be done during the experiment. From Bragg peaks positions and equations 2.9 and 2.10, one can deduce the reciprocal lattice of the crystal and so its direct lattice (distance and symmetry). From width of reflections or periods of Kiessig fringes, one can infer in-plane and out-of-plane correlation lengths. Study of structure factor allows to precise the structure and its deviations with a perfectly periodic arrangement. It is important to keep in mind, however, that in a classical diffraction experiment we only access to the beam intensity, which is proportional to the squared moduli of the structure factor. Phase information is lost.

Experimental structure factors are extracted from the intensity detected at several reciprocal space positions. There are two types of scans: ridge and rocking scans. For the ridge scan, the detector and the sample are rotated simultaneously in such a way that the detector scans along a straight direction in reciprocal space ( $h$ -,  $k$ - or  $l$ -scans). In out-of-plane direction, the detector stays at the maximum of the studied rod (ridge). The scan is repeated with an offset on a side of the rod to find the background (valley). For a well-defined surface, sufficient detector acceptance and not too small polar exit angles, this mode, called stationary mode, quickly gives reliable data.

The maximum intensity depends on the precise alignment of the incident beam and on small deviations of the angle of incidence due to some mosaicity in the crystal. A very good substrate quality is in this case mandatory to get reliable results. In addition, in-plane breadth of a rod is related to the in-plane correlation length of the film. Films with small order present small domain size and so large rods. Detector acceptance can be not sufficient



to collect the whole intensity of the rod. A better suited measurable quantity is the integrated intensity. The Detector is then fixed, while the sample continuously rotates around the Bragg angle at the constant angular velocity about an axis normal to the primary beam (equivalent to out-of-plane axis in grazing incidence diffraction). Rocking scan covers then the whole range of orientation in which there is any contribution to the reflection. To measure a rod, rocking scans are performed at different  $l$  positions. Such a scan measures the total diffracted energy given out from the crystal rather than an intensity. An expression of such total energy diffracted by a small single crystal can be found in [103].

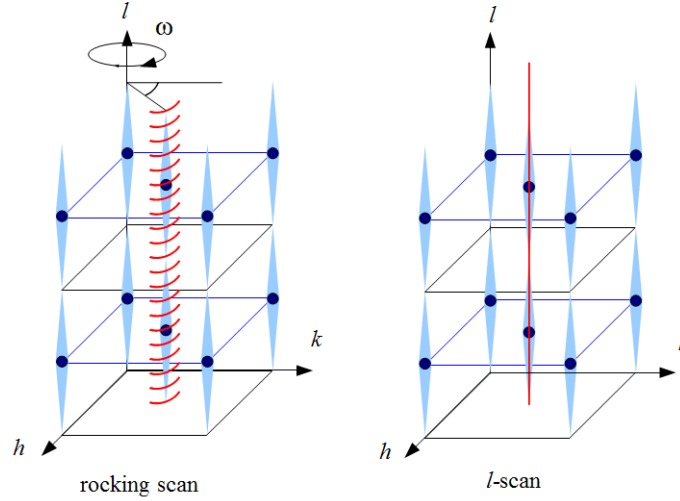


Figure 2.6: Two ways for scanning a rod: rocking scan vs l-scan

Intensity collected is next treated to retrieve structure factors amplitudes. First, background is subtracted and intensity is normalized by the incident beam intensity. Some variations of scattered intensity arise from experimental conditions and not from the structure. Standard correction factors for a z-axis diffractometer are therefore applied to achieve a diffraction pattern independent from measurement conditions.[108] Hence

$$|F|^2 \propto \frac{(I - I_{background})_{normalized}}{P \cdot C_{area} \cdot C_{rod} \cdot C_{det} \cdot L \cdot C_{table}} \quad (2.16)$$

Polarization correction  $P$  accounts for the polarization of the incident and scattered light. Scattered intensity is derived from the cross-product of incident and scattered field and so takes into account the angle between their directions. The area correction  $C_{area}$  normalizes the intensity as a function of the area of the surface participating to the diffracted signal. Width of outgoing slits is constant on the Ewald sphere (angle) but not anymore once projected in the reciprocal space matrix. The integration range  $\Delta l$  along the rod is thus not a constant. The correction  $C_{rod}$  rectifies this point. When a rod shape is so wide that only a portion is integrated by the detector, or in other words, when the in-plane acceptance of the detector is too small, the intensity value can be corrected with  $C_{det}$  thanks to an evaluation of the overall scattered intensity with a rocking scan. Exact corrections vary following the type of scans

and the last two concern only rocking scans. The Lorentz factor  $L$  accounts for the different times spent in the diffraction condition by different reflections. The reciprocal lattice points which are far from the rotation axis cross quicker the Ewald sphere. On our experimental set-up a rotation of our detector for the out-of-plane direction is composed by a translation plus a rotation. The out-of-plane angular acceptance varies then with this angle and should be corrected ( $C_{table}$ ). A correction relative to the shape of the beam can be added. In our case, we consider a uniform incident beam well-defined by ingoing slits.

In this thesis, refinements have been done with ROD program.[109, 110, 111] The structure factor is calculated by the coherent sum of surface and bulk contributions (kinematical approximation).

$$F_{hkl} = F_{bulk} + F_{surface} \quad (2.17)$$

with

$$F_{bulk} = \frac{F_u}{1 - e^{-2i\pi l} e^{-\alpha}} \quad (2.18)$$

and

$$F_{surface} = \sum_n^{surf.cell} f_n \cdot e^{-\frac{B_n \cdot Q^2}{16\pi^2}} \cdot e^{2i\pi(h \cdot x_n + k \cdot y_n + l \cdot z_n)} \quad (2.19)$$

where  $\alpha$  is an attenuation factor allowing that only a finite amount of unit cells contributes to  $F_{bulk}$ , and  $x_n$ ,  $y_n$  and  $z_n$  represent the coordinates of the atom  $n$  in lattice parameter units. A damping term, containing Debye-Waller factor  $B_n$  has been added to take into account the oscillations of the atoms around their equilibrium positions (thermal disorder). Number of layers, coordinates of atoms, interatomic distances, Debye-Waller factor and occupancies at each layer are fitting parameters to reproduce experimental structure factor distribution.

The occupancy parameter evaluates the occupation rate and intermixing in the layer. A layer at the surface is indeed not necessarily fully occupied exhibiting part of previous layers, called terraces. Different occupation profiles are available in an extended ROD program version varying on function distribution of terraces. Roughness always leads to a decrease in intensity. CTR has a much reduced intensity between the Bragg peaks compared to an ideally flat surface.

### 2.3.3 Experimental set-up

The *in situ* and *in real time* SXRD experiments discussed in this manuscript were mainly carried out at European Synchrotron Radiation Facility (ESRF) at the BM32 beamline which belongs to the French Collaborative Research Group on InterFaces (CRG-IF). The x-ray source is a bending magnet delivering an horizontal linearly polarized beam. Photon energies are selected by a Si(111) double crystal monochromator between 7 and 30 keV with an energy resolution  $\frac{E}{\delta E} \simeq 10^4$ . A second crystal is bent to give sagittal focusing on the sample. A mirror at the end of the optics system tilts vertically the beam. Ingoing vertical and hori-

zontal slits cuts the beam in a about  $0.3 \times 0.3 \text{ mm}^2$  spot. The experimental station consists of an ultrahigh vacuum (UHV) chamber, fully equipped for sample preparation, mounted on a Z-axis diffractometer. A complete description of the original set-up is given in ref. [112]. The diffractometer axes are sketched in Fig. 2.7a. The substrate is aligned normal to the azimuthal rotation axis, in vertical position, at the homocenter of the diffractometer. Large in-plane and out-of-plane momentum transfer is accessible. Several evaporation sources can operate in a UHV pressure maintained by several kinds of pumps (ion pump, turbo pump, liquid nitrogen cooled titanium sublimation pump) or under oxygen pressure ( $< \text{about } 10^{-5}$  mbar). Simultaneously, surface can be analyzed by a grazing reflection high energy electron diffraction (RHEED), Auger electron spectroscopic analysis, or x-ray diffraction. The substrate is prepared *in situ* by ion sputtering and annealing. The temperature is monitored by an infrared pyrometer.

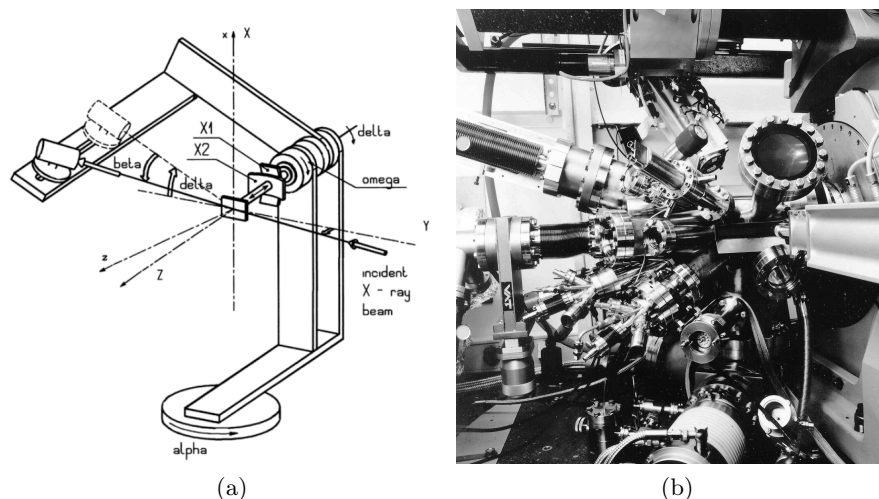


Figure 2.7: (a) Schema of the main movements of the z-axis diffractometer (taken from ref.[112]). (b) Picture of SXR D dedicated experimental set-up at BM32.

## 2.4 X-ray specular reflectivity XRR

Up to now we considered x-ray interaction with atoms. In x-ray specular reflectivity (XRR) technique, ordered atoms in a crystalline structure are “replaced” by thin layers and multilayers on flat substrates. Multilayers can be considered as a succession of continuous flat media with different electron densities. X-rays are reflected at each interface and can interfere constructively giving rise to peaks and Kiessig oscillations. Distances between interfaces being larger than interatomic distances, these oscillations appear at small momentum transfer around reciprocal lattice point (000). Films being considered as planes parallel to the surface, the momentum transfer is kept perpendicular to the surface (specular condition). It means that incident and scattered angles rise together ( $\theta_i = \theta_f$ ). One can see that x-ray reflectivity

corresponds to surface x-ray diffraction with momentum transfer perpendicular and at very low values.

Propagation of light in a homogenous medium is characterized by the refractive index  $n$  of the medium. In the x-ray region,  $n$  can be expressed relatively to the atomic diffusion factors  $f$  with

$$n - 1 = \frac{r_e \lambda^2}{2\pi} \sum_j \rho_j \cdot f_j \quad (2.20)$$

where  $r_e = \frac{e^2}{mc^2}$  is the Thomson scattering length,  $\rho_j$  the mass density of the element  $j$  and  $f_j$  its diffusion factor. This latter can be developed (considering only electronic terms) in

$$f_j \simeq f_0 + f'_j + i f''_j \quad (2.21)$$

$f_0 \propto Z$  is related to the Thomson diffusion,  $f'_j$  and  $f''_j$  are the real and imaginary anomalous dispersion factors.

The wave propagating in the medium can also be described as proportional to  $e^{i(1-\delta)kz} e^{-\beta kz}$ .  $\delta$  (related to  $f_0 + f'_j$ ) represents the dispersion, whereas  $\beta$  (related to  $f''_j$ ) the absorption of the light in the medium.  $n$  is then written as <sup>1</sup>

$$n = 1 - \delta - i\beta \quad (2.22)$$

The specular reflectivity, defined as ratio  $R_\theta = \frac{I_{scattered}}{I_{incident}}$  of scattered intensity over the incident intensity, can be calculated with the Snell's laws. At the interface air/surface, it relates the incident and reflected angles  $\alpha$  and  $\alpha'$  to each other through  $\cos\alpha = n \cdot \cos\alpha'$ . Below the grazing incident angle  $\alpha_c$ , named critical angle, the refracted angle is null. There is a total external reflection ( $R_\theta = 1$ ). Expanding the cosines, previous equation yields to  $\alpha_c = \sqrt{2\delta}$ .

For each wave, the amplitude reflectivity and transmittivity at each interface are described by Fresnel equations derived from Snell's law. Waves interfere inducing thickness oscillations, called Kiessig fringes, in the x-ray intensity as function of angle incidence. Fringe amplitude depends on the surface and interface roughness and the relative electron densities of the materials. The periodicity of the fringes is characteristic of the films thickness. To improve data's quality, the background of the specular reflectivity can be measured with a slight shift of the incident angle compared to the outgoing angle ( $\theta_i > \theta_f$ ). The momentum transfer is then not perpendicular but slightly tilted. The reflected intensity of a stratified medium is widely analyzed with a recursive algorithm based on the recursive method developed by Parratt.[113] The medium is imagined as being composed of N layers sitting on the top of an infinitely thick substrate. Roughness, thickness and electron density of each layer are the fitting parameters.

<sup>1</sup> $n$  decreases after electronic transition edge resulting to a value slightly smaller than unity in x-ray region. However only the phase velocity of light is higher in the material than in vacuum, and not the group velocity, respecting the limit of celerity in vacuum.

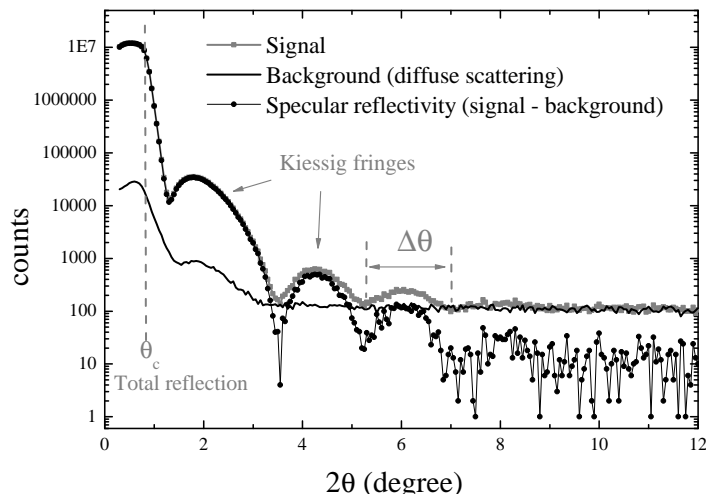


Figure 2.8: X-ray reflectivity profile as function of two times outgoing angle. Below  $\theta_c$ , the reflection is total. Thicknesses are inferred from periods of Kiessig oscillations  $\Delta\theta$ . The background arising from diffuse scattering is measured with an incident angle slightly different than the outgoing angle.

As in diffraction, fluctuations in height due to roughness (uncorrelated interface) increases diffuse scattering leading to a rapid decrease of fringes intensity. If the height fluctuations are bounded, a non-specular diffuse component superimposes along the sharp specular one along  $Q_{in-plane}$  direction. GIXRD at small scattered angle, namely Grazing Incidence Small Angle Scattering (GISAXS), is ideal to explore this component.

The XRR experiments were performed at Néel Institute with a Bruker D8 Discover diffractometer. Göbel multilayer optics select Cu wavelength (1.5418 Å) from a Cu target x-ray tube and make the beam quasi-parallel (divergence  $\leq 0.03^\circ$ ). The beam on the sample is 50  $\mu\text{m}$  large in the incidence plane. Data were collected using a scintillation detector for incident angles up to  $16^\circ$  at maximum. Fits of models to reproduce experimental scans with theoretical curves have been done using Bruker LEPTOS® software.

## 2.5 X-ray Absorption Spectroscopy

When an electromagnetic beam travels through a material, its intensity is attenuated. A part of the beam is absorbed. For an homogenous material, there is a simple exponential decrease of the transmitted beam intensity  $I$  depending on the sample thickness  $t$ .

$$I = I_0 e^{-\mu t} \quad (2.23)$$

where  $I_0$  is the incident intensity. This equation, equivalent to the Beer-Lambert rule, determines  $\mu$  the total linear absorption coefficient.  $\mu$  presents strong and abrupt increases as function of the energy in the x-ray range. At these energies, x-ray is absorbed by an atom, the excess energy is transferred to a core electron which is expelled from its orbital or straight

from the atom, leaving the atom respectively excited or ionized. The energy needed to expel an electron bounded to an atom is characteristic of the element. The more protons in the nucleus, the more core electrons are bounded to the ion and the more energy it will cost to bring a core electron into the valence shell. Each element has therefore its own energy for the core level absorption edge.[102] By selecting the incident energy, one emphasizes the interaction from a specific element in the material and so extracts some information about it. *Element-selectivity* is a great advantage of X-ray Absorption Spectroscopy (XAS) and associated techniques.

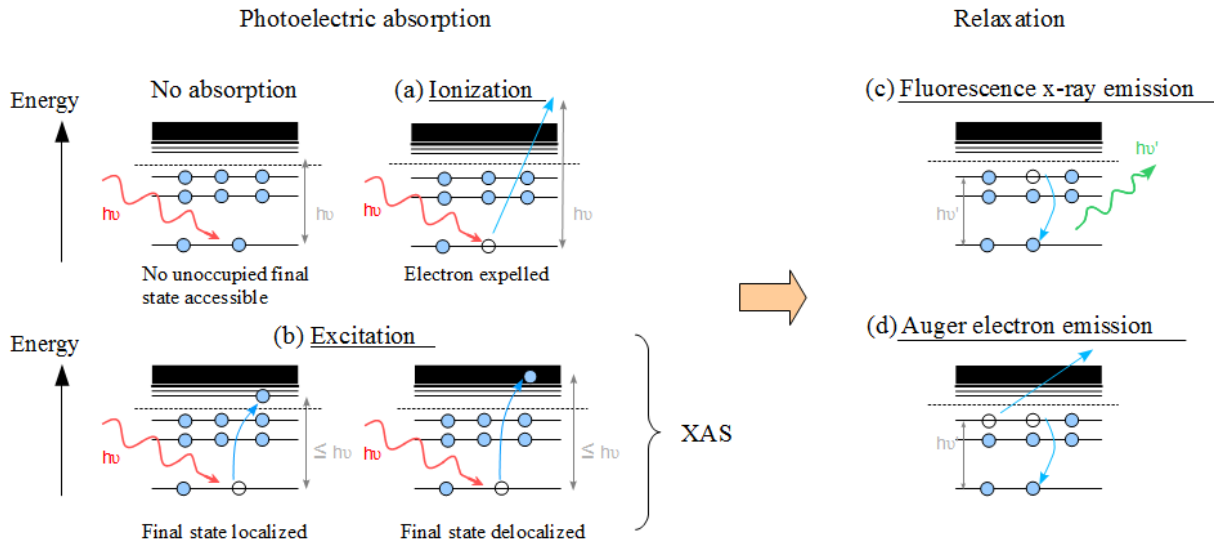


Figure 2.9: Schematic energy level diagram and processes of an atom absorbing a x-ray wave. Depending on energy absorbed, photoelectron is ejected in continuum (a) or localized state (b). Relaxation processes are described in the text.

During the photoabsorption, if the photon energy transmitted to an electron is sufficient to promote it to an unoccupied state, the atom becomes excited. The hole created in the inner shell can be filled by one of the two processes. Either one of the electron in outer shell fills the hole, creating a photon with an energy equals to the energy difference between the two shells (Fig. 2.9c). The emitted photon is then known as fluorescence. Or a process of auto-ionization takes place. Energy released by an electron hopping in a inner shell is used to expel another electron from one of the outer shell (Fig. 2.9d). This electron is then known as Auger electron.

The series of absorption edges give evidence of the existence of the electronic energy levels in the atom, whose binding energy is equal to the energy at the edge. They are labeled by a letter K, L, M, N and O according to the principal quantum number  $n = 1, 2, 3, 4$  or  $5$ . The atomic levels are also split according to the orbital momentum number  $l$  (s, p, d, f, g) and to the total angular momentum  $j = |\mathbf{l} + \mathbf{s}|$ , where  $\mathbf{s}$  is the spin. This last term results in a split when the energy of spin-orbit coupling is not small. It is the case of all  $2p$  core levels, which present two peaks in their XAS spectra. Historically, they are called  $L_3$  and  $L_2$  edges (Fig. 2.10). The  $2p$  shell has an orbital momentum  $l = 1$  and spin  $s = 1/2$  resulting in  $j = 1/2$

or  $3/2$ . The excitations made from the  $2p$  orbital with  $j = 1/2$  to  $3d$  valence band are called the  $L_2$  edge, whereas the excitations made from the  $2p$  orbital with  $j = 3/2$  are called the  $L_3$  edge. Once the atom is excited, there is an effective attractive potential between a  $2p$  core hole and  $3d$  valence electron. One can note that the absorption above the edge is higher than below. This is called the edge-jump and corresponds to excitations from  $2p$  orbital to a state where electrons and hole are non bounded.[114]

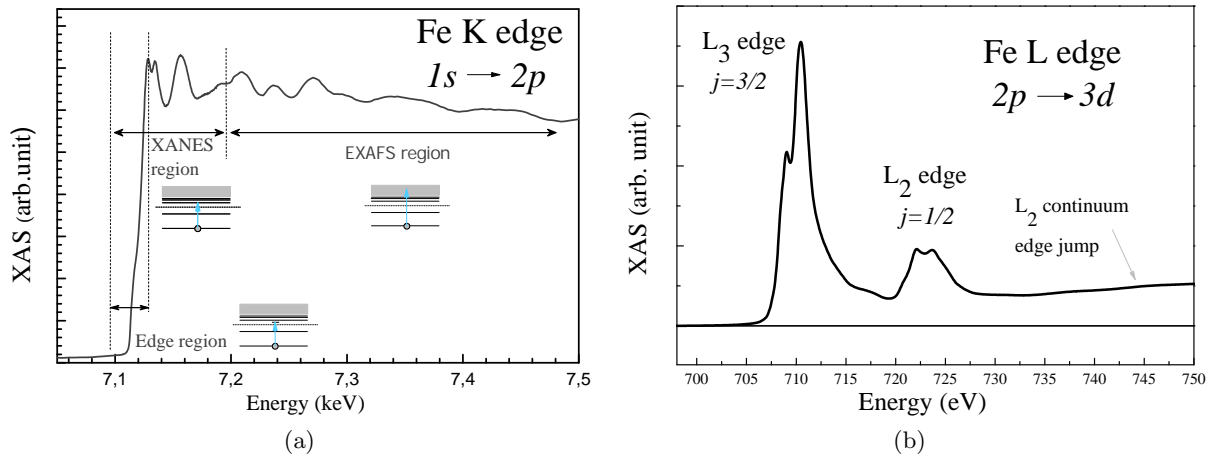


Figure 2.10: X-ray absorption spectrum at the Fe K edge (a) and L edge (b)

In photoabsorption for an inner shell, the initial state of electron is strongly localized on the absorbing atom. Hence photoabsorption probes the value of the final state wavefunction on the absorbing atom. The XANES (X-Ray Absorption Near Edge Structure) range is usually defined from a few eV before to around 60 eV above the edge. The XANES region is sensitive to the electric and magnetic structure of the atom studied. It contains information on local order, orbital hybridization, oxidation state and depends on the crystal field symmetry.

For energies slightly lower than the absorption edge, the energy may be sufficient to bring the electron towards the first empty state of a partially occupied levels, yielding to the emergence of pre-edge structures. For energies from the rising edge up to around 60 eV, the photo-electron has a low kinetic energy. The average distance covered by the electron without energy loss, know as its mean free path, is high. It results that XAS features are dominated by multiple scatterings suffered by photon-electron from its atomic neighbors, explaining the sensitivity to XANES on 3D geometry around absorbing atom. Information on the structural and electronic environment of the studied element can be inferred directly from the comparison between the experimental spectrum and those collected for reference compounds. *Ab initio* simulations using advanced codes, such as FDMNES code,[115] are however mandatory to fully explore the XANES spectrum.

In the wide range from around 60 eV after the edge to several hundredths of eV, the core electron is ejected towards delocalized states of the continuum. Its kinetic energy being large, its mean free path is short and we can consider only the single scattering events. The outgoing wavefunction of the electron propagates as a spherical wave until it reaches one of

the neighboring atoms giving rise to backscattered wave. The interference between the two waves are responsible for the oscillations in the EXAFS region in absorption spectrum (for Extended X-Ray Absorption Fine Structure). The data analysis is performed by comparison with the simulated spectra calculated by superposition of the outgoing and backscattered electron waves by the different shells. It allows the determination of the type and the distance of the atoms in the local environment around the absorbing atom.[91]

## 2.6 X-ray Dichroism

Historically, dichroism is the change in color of a mineral observed at different angles under plane-polarized light. It has been extended to the difference of absorption by rotation, even in x-ray absorption range. Analysis as a function of polarization are often done in the XANES energy range. The dichroism in this region could arise from charge anisotropy or from an anisotropic spin distribution. When the incoming beam is linearly polarized, the spectroscopy is called *linear dichroism*, while *X-ray magnetic circular dichroism* refers to the spectroscopy with an incident circularly polarized beam. In both cases, dichroic signal is the difference between absorption spectra obtained with two different polarizations (left/right or for instance  $\pi/\sigma$ ). These techniques are magnetic probes with the advantages of x-ray spectroscopy techniques. They are both non-destructive and element-specific, even orbital-specific. They couple information of the electronic and structural local environment with the magnetic state of the probed element.

### 2.6.1 X-Ray Magnetic Circular Dichroism (XMCD)

As seen in the previous section, electron can hop from a core level to an empty state with x-ray absorption. The transition probability from initial state  $|i\rangle$  to final state  $|f\rangle$  per unit time follows the Fermi's Golden Rule.

$$P_{fi} \propto \sum_{f,i} M_{fi}^2 \cdot (1 - n(E_f)) \cdot \delta(\hbar\omega - (E_f - E_i)) \quad (2.24)$$

where  $(1 - n(E_f))$  is the density of unoccupied final states and  $M_{if}^2$  the transition matrix element, which relates initial and final states through the hamiltonian of x-ray with matter interaction. The  $\delta$ -function expresses the conservation of energy in the absorption process. For the  $L_{3,2}$  edges of the  $3d$  elements, quadrupolar transition is negligible. The Hamiltonian is approximated as a dipolar operator and is written:

$$H = \vec{\epsilon} \cdot \vec{r} = O \quad (2.25)$$

$\langle i|O|f\rangle$  is equivalent to an integral. As all integrals, it has to be even not to be null. According to the previous equation, the dipolar operator is odd in space. In addition, we



know that  $s$  and  $d$  orbitals are odd, and  $p$  and  $f$  orbitals are even. Using symmetries, we found the selection rules for excitations to be allowed. They imply amongst others that

$$\Delta l = \pm 1 \text{ and } \Delta s = 0$$

Initial  $2p$  states could then hop to a final state  $s$  or  $d$  and the spin of the electron should be conserved during the transition. Since the photon is annihilated in the absorption process, its angular momentum must be transferred to the sample. For right (left) circularly polarized photon, the momentum transfer is  $-1$  ( $+1$ ).<sup>2</sup> It adds a condition on the transition function of polarization of the incident beam. The transition respects, for an atom absorbing a circularly polarized photon,

$$\begin{aligned} \text{right, } \Delta m_l &= -1. \\ \text{left, } \Delta m_l &= +1. \end{aligned} \quad (2.26)$$

This rule is not visible if initial and final states are not differentiable. But spin-orbit coupling, which is by far the largest interaction in  $2p$  orbitals, splits them and introduces a coupling between the spin and orbital of the electron. The proportion of spins up  $\uparrow$  and down  $\downarrow$  (respectively  $m_S = +1/2$  and  $m_S = -1/2$ ) varies in each state. The transition from  $2p$  to  $3d$  is then polarized in spin.

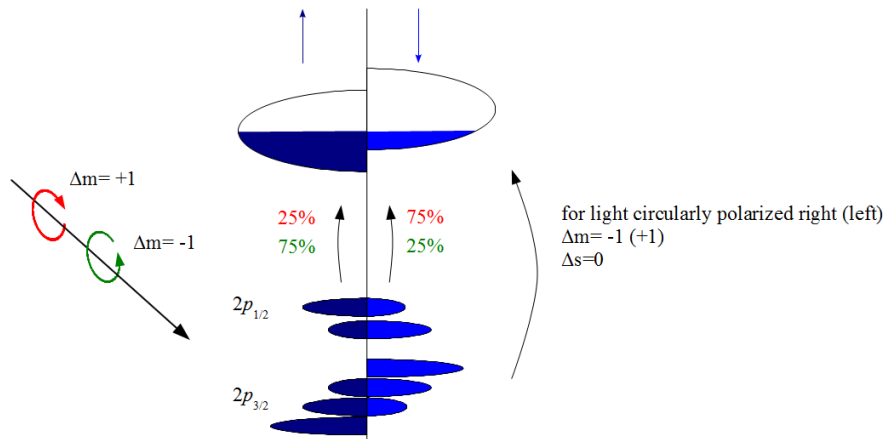


Figure 2.11: Absorption of a circularly polarized x-ray wave by a ferromagnetic material. Proportions of transition from  $2p_{1/2}$  state to  $3d$  state are represented in case of absorption of a wave with a left (right) polarization in red (green).

With a circularly polarized wave, we select the involved states, and thus the proportion of spin up and down. The probabilities of excitation are given by the Clebsch-Gordan coefficients. A photon with helicity  $+1$  has a probability of 62.5% to excite an electron from the  $2p_{3/2}$  state carrying a spin  $\uparrow$  against 37.5% with a spin  $\downarrow$ . From the  $2p_{1/2}$  state, 75% of the excited electrons carry a spin  $\downarrow$  and 25%  $\uparrow$ .<sup>[116]</sup> The results are equivalent with reversed

<sup>2</sup>Linearly polarized wave could be seen as an equally weighted superposition of right and left circularly polarized wave. Its angular momentum is null.

spin orientation for a photon with helicity -1. Since the photoelectrons keep their spin during the transition, we therefore access to a relative quantity of final states with spins  $\uparrow$  and  $\downarrow$ , by comparison of the absorption spectra with the polarized left and right beam.

When the amount of final states with spins  $\uparrow$  and  $\downarrow$  is equivalent, the difference between spectra is null. In ferromagnets, the densities of states above Fermi level (unoccupied states) in the  $3d$  band are different according to spin orientation. The resulting difference between the two XAS spectra is known as X-ray Magnetic Circular Dichroism (XMCD) signal.

XMCD is thus sensitive to the net magnetization of an element. Since its first report in 1987, it has become one of the most important techniques to study localized magnetic moments in thin films and multilayers. The sum rules introduced by Thole *et al.* in 1992 and Carra *et al.* in 1993 contribute to the popularity of XMCD. The former showed that the integral over the XMCD signal at a given edge is related to the ground-state orbital magnetic moment  $L_z$ . The latter introduced an effective spin moment with the spin magnetic moment  $S_z$  and intra-atomic magnetic dipole term  $T_z$  in the ground state. With the sum rules, it is possible to determine separately the spin and orbital magnetic moment from the integrated signals of the dichroism spectrum.

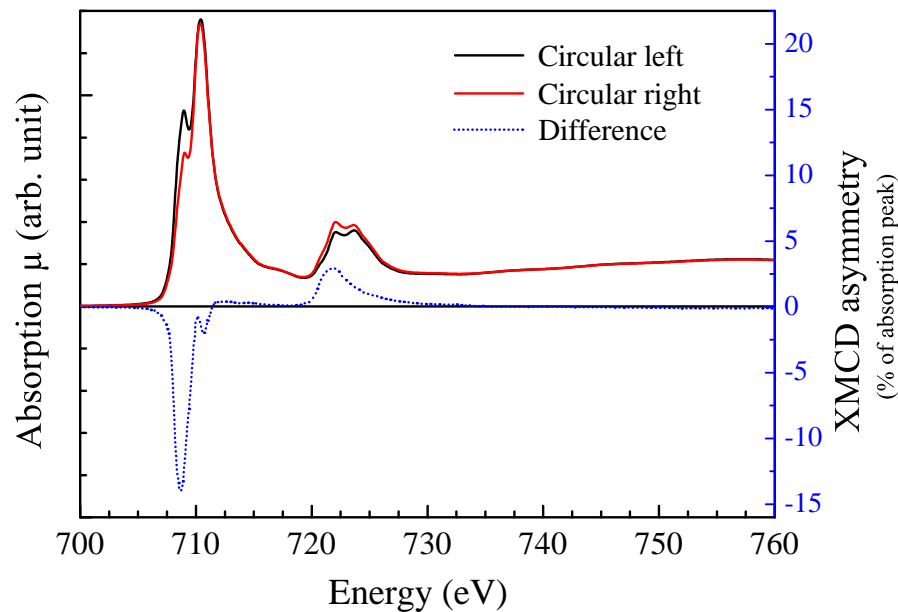


Figure 2.12: Right (red) and left (black) circularly polarized x-ray absorption at Fe L edge. The difference between the two signals gives the XMCD signal (dotted curve).

### 2.6.2 X-Ray Magnetic Linear Dichroism (XMLD)

Linear dichroism is due to a difference in orbital occupation. Haverkort uses a simple example in his thesis to explain this sensitivity.[114] He explains that the difference in a total intensity caused by a non-cubic orbital occupation can be understood in a one-electron picture. Let's start with an excitation from a  $s$  orbital to a  $p$  orbital. Three different orbitals can be excited:

$p_x, p_y, p_z$ . If the light is polarized along  $z$ , the intensity for a  $s$  to  $p_x$  excitation is proportional to the square of  $\langle s|z|p_x \rangle$ .  $s$  and  $p_x$  are even in  $z$ ,  $z$  is odd. The total integrand is thus odd in  $z$ . The integral over an odd function is zero. One understands that only  $s$  to  $p_z$  orbital excitation is possible with  $z$  polarized light. For excitation from a  $p$  to  $d$  shell, it is more complicated, but the basic principle is the same. The absorption of linearly polarized light allows the transition of electron in a specific orbital. However, one should not forget that there are two conditions to have a polarization dependence of XAS spectra. First the unoccupied states distribution should be anisotropic. Secondly energy splitting of orbitals (due to anisotropy) should be larger than the thermal energy of the system, even barely. The huge contrast which exists between two spectra with different polarizations makes XAS a very sensitive tool to study orbital occupations and energy splitting between the orbitals.[100]

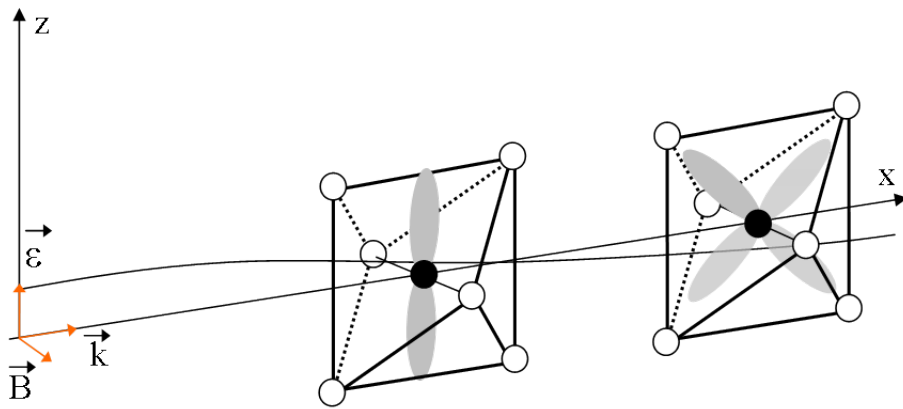


Figure 2.13: An octahedron is surrounding a  $3d$  element. The electric field, here along  $z$ , induces a vibration of the core electron along  $z$ , if we consider the field uniform in the probed zone. The overlap with final states is non zero only for the dipole orbital  $p_z$ , and for the quadrupole orbital is  $3d_{xz}$  if the wavevector is along  $x$  (taken from ref. [91]). In the following, we will neglect the quadrupolar transition.

Atomic magnetic moments could deform charge distribution via spin-orbit coupling inducing energy splitting of orbitals. For some orbitals such as  $2p$  orbital, the spin-orbit is a large interaction and so the splitting is important, larger than thermal fluctuations. When probed matter presents a magnetic order, XAS spectrum depends on the relative orientation of magnetic moments and x-ray polarization. Contrast is then known as x-ray magnetic linear dichroism (XMLD). Because this sensitivity is done through orbital anisotropy, orientations of magnetic moment and x-ray polarization relative to the crystallographic axes must be taken into account for accurate interpretation of XMLD data.[117] Spectral shape and magnitude of XMLD provides then information on magnetic structure relatively to crystalline structure. And this is true whatever the type of magnetic ordering. Hence XMLD is a high-quality tool to investigate magnetic properties of antiferromagnets (difficult to measure by other method), as we will see in this thesis.

X(M)LD signature, as XA spectra in XANES range, can be analyzed directly from the comparison between experimental results and references but is fully explored with simulations using advanced codes based on multiplet calculations.

### 2.6.3 Experimental aspects of XMCD / XMLD

Soft-x-ray absorption spectroscopy measurements were carried out at several experimental conditions in two places. First at the PGM beamline of the Laboratório Nacional de Luz Síncrotron (LNLS, Campinas, Brazil) with a spectral resolution of  $E/\Delta E=6000$  and degrees of linear and circular polarizations close to 100% and 80%, respectively. Second at the ID08 beamline of the European Synchrotron Radiation Facility (ESRF, Grenoble, France) where the beam has a spectral resolution of  $E/\Delta E=6000$  and nearly  $\approx 100\%$  linear and circular polarizations. All spectra were collected using total electron yield (TEY), corrected for electron yield saturation effects[118] and normalized far from  $L_{2,3}$  edges. The sample was allowed to rotate around a vertical axis, with the polar angle  $\theta$  defined as the angle between the surface normal and the x-ray propagation. The maximum magnetic field was  $\pm 9$  Tesla field along the beam,  $\pm 4$  Tesla field perpendicular to the beam generated by a fast-sweeping UHV ( $10^{-10}$  mbar vacuum) split-coil superconducting magnet. Temperature of the sample was varied from 7 K up to 400 K.

## 2.7 Magneto-optic Kerr effect (MOKE)

Magneto-optic Kerr effect (MOKE) is a well-established technique probing the magnetic properties of thin layers.[119] Its wide use is probably due to its sensitivity coupled with its experimental simplicity. Compared to XAS spectroscopies described previously, it allows to study the interaction of polarized wave with matter without requiring synchrotron radiation. Photon energies are within the optical range.

We recall that the electric field of a light propagating through a medium makes its electrons move. The polarization motion drives the motion of the electrons. If an external magnetic field is applied in the direction of the propagation wave, an additional Lorentz force acting on each electron points toward or away from the circle's center for left or right circular motion. It results in the reduction or expansion of the radius of the motion. The difference in radii is at the origin of the different propagating velocities of the two circular modes. This phenomenon, known as Faraday effect, imposed a phase-shift between the two modes yielding a rotation of the polarization plane. Large magneto-optic effects are observed in ferromagnetic materials. Inner magnetic field arises from unbalanced population of electron spins through spin-orbit interaction. This latter couples the magnetic moment of the electron with its motion, and thus with the magnetic and optical properties of the ferromagnet. Actually a second process takes place for light propagating in a magnetized medium. The two modes are absorbed differently because of unbalanced unoccupied densities of states near Fermi level depending on spins. It affects the ellipticity of the beam.

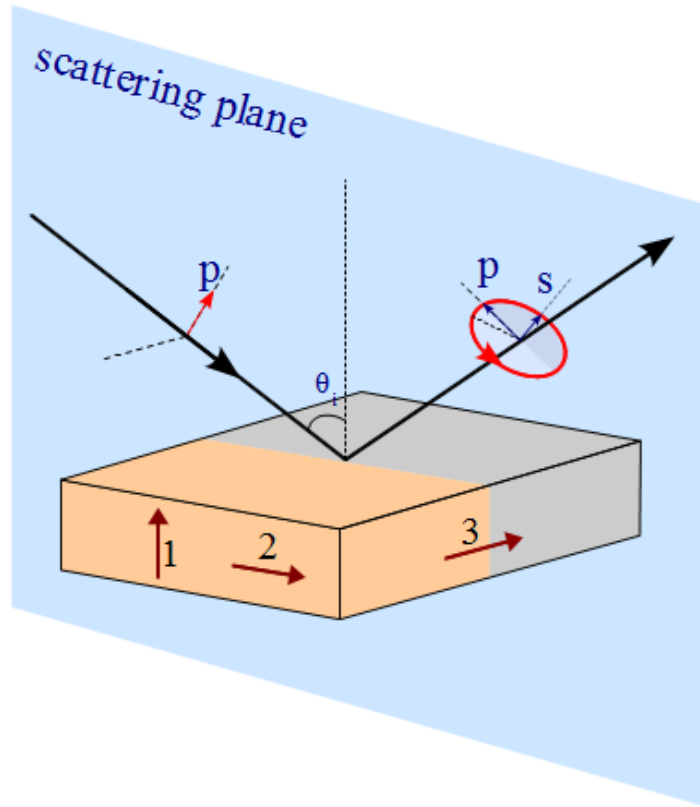


Figure 2.14: Experimental configuration of magneto-optic Kerr effect (MOKE) experiment for an  $p$ -polarized incident plane and a ferromagnetic sample. Polarization of outgoing wave has rotated and changed in ellipticity with apparition of a small  $s$  component. If magnetization is along the brown arrow 1, the configuration is said polar. Along 2, it is known as longitudinal and along 3 as transverse.

Since most magnetic materials of interest are metals, which strongly absorb the light, it is more convenient to measure the reflected light, referring then to Kerr's work. The final reflectivity along different polarization directions can be calculated from Maxwell's equations applied on the multilayer structure and satisfying the boundary conditions at each interface. One deduces that the Kerr rotation  $\phi'$  and ellipticity  $\phi''$  from the reflection coefficients, which are linear functions of the magnetization. Experimentally, the rotation of the light is measured thanks to two polarizers. The first one allows the acquisition of a linear  $p$ -polarized incident light. The second one, placed between the sample and the detector, is slightly shifted from the  $p$ -axis to a small angle  $\delta$ .  $s$  and  $p$  correspond respectively to the polarization perpendicular and in the plane of reflection (Fig. 2.14). If the sample is ferromagnetic, the reflected beam possesses a component  $E_s$  along  $s$ -axis in addition to the main component  $E_p$  along  $p$ -axis. Hence  $E_s/E_p = \phi' + i\phi''$ .

The intensity measured by the photodetector after the polarizer is

$$I = |E_p \cdot \sin\delta + E_s \cdot \cos\delta|^2 \simeq |E_p\delta + E_s| \quad (2.27)$$

$$I = |E_p|^2 |\delta + \phi' + i\phi''|^2 \simeq I_0 \cdot \left(1 + \frac{2\phi'}{\delta}\right) \quad (2.28)$$

where  $I_0$  is the intensity at zero Kerr rotation. The rotation of the light is then measured in function of the field and temperature to access to the relative change of magnetization in the sample. Another way to measure the Kerr effect consists in a modulation of the light in frequency. It allows a synchronous detection, which improves the signal on noise ratio. Three configurations of magnetization and light orientations are possible. In polar MOKE, magnetization is perpendicular to surface plane. Maximal effect is reached at large incidence angles. In longitudinal MOKE, magnetization is in the surface plane and in the incidence plane. Maximal effect is obtained at small incidence angles. In transverse MOKE, magnetization is in surface plane, but perpendicular to incidence plane. In this case, only ellipticity changes from  $p$ -polarized incidence light. In  $s$ -polarized light, magnetization and polarization are collinear, which prevents any Faraday effect.

### 2.7.1 Experimental aspects of MOKE

MOKE experiments were realized during this thesis at INAC (Institut des Nanosciences et Cryogénie) at CEA in Grenoble with Matthieu Jamet and Céline Vergnaud and at the Max Planck Institute of Halle in Germany with Marek Przybylski, Piotr Kuswik, Pedro Gastelois and Maciej Dabrowski. In Halle, a laser diode of wavelength 670 nm with a beam diameter of about 200  $\mu\text{m}$  followed by a polarizer is used as a source of polarized light. The sample is mounted in UHV chamber in the cold-finger holder of a cryostat between the poles of an electromagnet, whose maximum applied field is limited to 5.5 kOe. Temperature could vary from 400 K down to 5 K. The UHV windows usually produce a birefringence, which is compensated by a half-wave plate placed before the analyzing polarizer. Two different MOKE geometries were used, with an incidence angle of  $21^\circ$  for longitudinal MOKE and of  $69^\circ$  for polar MOKE.

In Grenoble, incident light comes from a laser diode of wavelength 632.8 nm. A polarizer and a chopper at a frequency of 921 Hz polarize and modulate the light before the sample. After reflection, a piezoelectric birefringent crystal makes the polarization vary at a frequency of 42 Hz around an equilibrium position of  $140^\circ$ . Sensitivity of detection is enhanced by this synchronous method. The sample is installed vertically in a cryostat, whose temperature can vary from RT down to about 10 K when sample is in a helium bath. Four superconducting coils produce an horizontal magnetic field up to typically 5T, or even 7T.

## 2.8 Preparation and complementary analysis of the surface

The standard procedure to prepare clean and flat single crystal surfaces consists in cycles of noble gas ion sputtering followed by annealing. Low energy  $\text{Ar}^+$  ions removes superficial atoms by collision with simply linear momentum transfer. In our experiments, ion guns emit  $\text{Ar}^+$  ions with an energy of 800 eV under a pressure of about  $P_{\text{Ar}} = 10^{-6}$  mbar. A leakage current due

to ionization of the surface during sputtering is measured typically around  $10 \mu\text{A}$ . The ion bombardment is routinely used to clean contaminated surfaces despite UHV environment, or to remove deposited layers from the surface. A side effect of the sputtering is that it disorders the substrate surface. An annealing flatten the surface. The exact preparation depends on the substrate and will be described for each studied case.

### Deposition by molecular beam epitaxy

One of the most common techniques to grow high-quality epitaxial thin films is molecular beam epitaxy (MBE), also called thermal deposition. The molecular beam is generated by electron-beam heating source. In the source a filament is heated by a current of around 2 A and emits electrons by thermo-ionic effect. High voltage between 800 to 1000 eV is applied between the filament and the rod of the material. The electrons are then projected to the rod. By thermal annealing, atoms evaporate and deposit on the surface. If an oxygen flux is inserted in the chamber during the material evaporation, this technique is called reactive MBE and allows the growth of oxide phases. In UHV pressure, metals quite often evaporate directly from the solid phase. Pt evaporates very close to its melting point at 2040 K and so requires a special attention. The typical rate of Pt deposition is of 30 min/ML, while it is around 4 to 12 min/ML for Fe and Co. The slow deposition rate achieved with this technique should favor the growth of epitaxial films in thermodynamical equilibrium conditions.

Two methods are employed to control the thickness deposited on the surface. First, the deposition rate is calibrated with a quartz crystal micro-balance positioned at the place of the sample. Initially the system oscillates according to a chosen frequency. The particles deposited on the balance increase the weight of the system, producing a slight decrease of the oscillation frequency. The amount of deposited material is calculated from this frequency shift. Second, thickness can be evaluated from the oscillations of the scattered x-ray intensity observed at anti-Bragg position. In the case of layer-by-layer growth, oscillations are periodic and a layer deposition corresponds to one oscillation in case of homoepitaxy.

### Auger electron spectroscopy

Chemical composition of the surface is analyzed at several steps of the growth by Auger electron spectroscopy (AES). A 3 keV primary electron beam ejects electrons from core levels of the atoms close to the surface. The core hole is filled by an electron of an outer shell. The transition energy is used by a third electron (Auger electron) which is expelled from atom with a kinetic energy that depends on the transition. Since the energy levels are specific to each atomic element, the analysis of the amount of Auger electrons depending on the kinetic energy informs on the chemical composition of probed material. Auger electrons considered here have an energy of 5-850 eV and thus a small mean free path in matter. They escape from matter from  $\simeq 1$  nm depth maximum giving AES an extreme sensitivity to surface species. We used AES in derivative mode. In this mode, peaks are not true Auger peaks but rather the maximum of slope. It emphasizes the small secondary peaks surrounding the primary Auger

peaks and allows a better signal on noise ratio. AES is used both to check the cleanness of the substrate surface and to compare the composition of the adlayers.

### **Low energy electron diffraction**

As AES, the low-energy electron diffraction (LEED) draws its surface sensitivity from the mean free path of electrons. The electron diffraction is a direct proof of the particle-wave duality. Electrons emitted in normal incidence with energies between 20 to 500 eV are elastically backscattered by the surface on a screen. If the surface is crystallized, a diffraction pattern appears, whose positions of spots give information on the symmetry of atomic structure on surface. By comparison with the substrate pattern, one can infer lattice constants of adlayers. Our use of this technique was limited to qualitative analysis.

### **Atomic force microscopy**

Last but not least, two scanning probe microscopies were used during this thesis to analyze morphology and typology of the surfaces. The atomic force microscopy is based on attraction/repulsion forces between surface atoms and a tip. The tip is positioned at the extremity of a microlever whose displacements are controlled by a piezoelectric tube. In the tapping mode, the tip oscillates at a frequency with an amplitude which decreases when the tip interacts with the surface. A laser pointing to the tip is reflected. A photodetector analyzes the movement of the reflected beam and so the movement of the tip. Hence the topography of the surface is drawn. The in-plane resolution is limited by the width of the tip (around 7 nm), while out-of-plane resolution is in angström range and so allows the visualization of atomic steps.

### **Scanning tunneling microscopy**

The scanning tunneling microscopy (STM) is based on the quantum tunnel effect. When a conducting tip is brought near to the surface and a voltage is applied between the sample and the tip, a current passes through vacuum from the surface atoms to the tip. This tunnel current is function of voltage, local density of states of the surface and tip position. We worked on constant current mode. The tip scans the sample surface at a fixed voltage while a feedback circuit regulates the vertical position to keep the current constant. A piezoelectric tube controls the height of the sharp tip with a subatomic precision, allowing an in-plane and out-of-plane atomic resolution.

These techniques provide very localized information, helpful for the study of early stages of growth but lack the ability to see below the surface layer. Quantitative LEED has proved to be an invaluable tool in many structure determinations with a nice resolution. The strong interaction of the electrons with the sample is both an advantage by the high scattering efficiency, and a drawback by the reduction of penetration depth. The strain imposed by adlayers



on substrate surface is for example impossible to investigate with LEED. X-rays, which interacts weakly with matter, can penetrate deeper into a sample reaching buried interfaces. Depending on the process taking place, the x-ray characteristic (energy, polarization) and the studied parameter (energy, reciprocal space) techniques based on x-rays are inestimable tools to investigate ultra-thin layers. The drawbacks of such techniques is their requirement of synchrotron light for the measurements. Optical measurements, such as MOKE experiments, are then appreciated to complement them.

In summary, we have now an idea on how our magnetic layers grow, and how to control this growth by surface techniques. The crystalline structure of the layers and their interfaces can be determined by surface x-ray diffraction; the magnetic structure by x-ray absorption dichroism and the magnetic properties by MOKE experiments.

## Chapter 3

# Growth and structure of CoO(111)/FePt/Pt(001)

### Contents

---

<b>3.1 FePt/Pt(001)</b> . . . . .	<b>52</b>
3.1.1 FePt growth . . . . .	52
3.1.2 Modeling the FePt/Pt(001) structure . . . . .	54
<b>3.2 CoO(111) on Pt(001)</b> . . . . .	<b>57</b>
<b>3.3 CoO(111) on FePt/Pt(001)</b> . . . . .	<b>60</b>
3.3.1 Analyzing the CoO diffraction pattern . . . . .	60
3.3.2 Modeling the CoO structure . . . . .	65
3.3.3 Comparison with bulk CoO structure . . . . .	67
3.3.4 Impact on FePt layer . . . . .	69

---

CoO layer structure is extremely influenced by growth conditions, interface chemistry and epitaxial strain. CoO grows epitaxially on Ag(001) with the same (001) orientation. Its structure is bulk-like, except for an in-plane compressive strain (4.2%)[\[120\]](#) which releases with thickness. On Pt(111), CoO films are (111) oriented, and a Moiré pattern can be observed according to the oxidation conditions and thickness of the deposited layer[\[121\]](#). Gagnaniello *et al.*[\[122\]](#) reported a modification of the CoO cristallographic orientation and morphology as function of the coverage on Pd(100). Meyer *et al.* showed the presence of a wurtzite-like CoO bilayer at the surface of CoO(111)/Ir(100) films[\[123\]](#). These differences are likely to strongly influence the magnetic properties of the films, as substrate may induce a spin reorientation according to the nature -compressive or expansive- of the strain.[\[124\]](#).

Unexpectedly , the growth of CoO on Pt(001) has never been reported in literature. Moreover, epitaxial CoO film on Pt(001) opens the way towards a CoO/FePt bilayer on Pt, since Pt-terminated FePt(001) and Pt(001) present rather the same chemical surface. FePt in its chemical ordered  $L1_0$  phase possesses a strong perpendicular magnetic anisotropy

(PMA). The proximity to a FM layer with such PMA can play an important role in the spin orientation of the CoO layer, providing an interesting playground for studying exchange-coupling properties.

### 3.1 FePt/Pt(001)

Fe growth on Pt(001)-hex has been investigated at RT by K. He *et al*[125] using STM, LEED and MOKE for coverages up to 20 monolayers (ML) and as a function of temperature by Soares *et al* using STM and SXRD for coverages up to 13 ML.[28] He and coworkers reported that an atomic site exchange process occurs during the RT deposition between Fe adatoms and Pt substrate atoms. For submonolayer Fe deposition on Pt-hex, no evidence of Fe atoms on the surface was found. Fe atoms have higher surface energy than Pt atoms, and replace them on average. Pt atoms are even observed at the surface in a reconstructed disposition coexisting with unreconstructed regions. Increasing the coverage, the film grows in a quasi layer-by-layer mode with the appearance of a  $c(2 \times 2)$  LEED pattern suggesting a phase transformation from tetragonal  $L1_0$  FePt to  $L1_2$   $Fe_3Pt$ , richer in Fe. A decrease of PMA observed at about 3.3 ML supports this assumption.

The strategy of Soares *et al*[126] to grow FePt on Pt(001) is to reinforce the atomic exchange process by temperature. They studied qualitatively both Fe RT deposition followed by annealing and thermally assisted deposition with the substrate held at different temperatures. According to them, RT deposition gives no trace of order detectable by SXRD. The following annealing at 650 K during 10 hours gives rise preferentially to the  $L1_2$   $FePt_3$  phase, indicating a preference of Fe diffusion into the Pt substrate compared to the Pt diffusion into the Fe layer. This behavior has been already observed by high-resolution TEM in Fe/Pt multilayers under annealing, where formation of  $L1_0$ -FePt starts in the Pt layers and expands over the whole film[127]. Thermally assisted deposition at 600 K maximum leads to the  $L1_0$  FePt ordering. No trace of  $L1_2$  phases was found at any temperature or coverage investigated with this method. In general, the authors found that the higher the temperature, the better the  $L1_0$  order. For high coverage,  $L1_0$  phase could be kept with a long time of annealing, since the Pt segregates more slowly. Alternate thermal deposition of Fe and Pt favors FePt with a high degree of order.

#### 3.1.1 FePt growth

We have grown a 3 bilayers (BL)- FePt layer by thermal deposition of Fe. The Pt(001)-hex substrate was held at 570 K - 600 K during the deposition to reinforce the atom exchange process, and kept at 600 K during half an hour after deposition to improve ordering. Fe was deposited by molecular beam epitaxy (MBE) using a pure rod inserted in a water-cooled electron beam evaporator. The evaporation rate was calibrated with a quartz microbalance at 1 ML per 10 minutes. The base pressure of the UHV chamber was around  $5 \cdot 10^{-10}$  mbar before deposition. The deposition was followed *in situ* and in real time by SXRD at 22 keV

photon energy under a grazing incidence angle of  $0.6^\circ$ , about 3 times the critical angle for total reflection of Pt at this energy ( $\alpha_c = 0.22^\circ$ ). One reconstruction reflection was measured for three different coverages (clean substrate, 1 ML, 3 ML) by rocking scans around its reciprocal space position (1.21 0 0.2), assuming that the  $90^\circ$  turned domains behave in the same way. The amount of reconstruction left is assessed as the ratio between the integrated intensity of the rocking scans before and after Fe deposition. As you can see in Fig. 3.1, the peak has significantly decreased after only 1 ML deposition and almost completely vanished after 3 ML deposition. The deconstruction reached respectively 72% of the reconstructed domains and more than 99.5% at the end of the process. These results express the important intermixing of Fe adatoms with Pt substrate atoms.

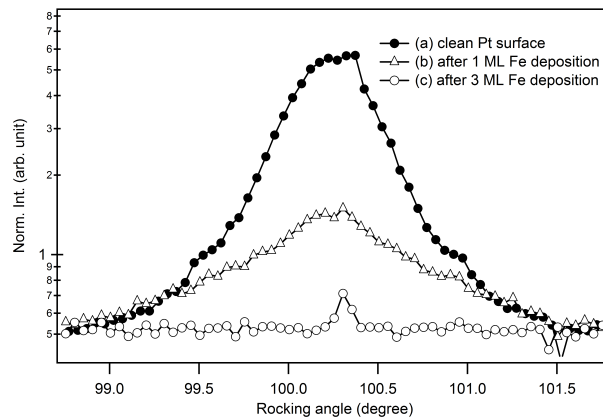


Figure 3.1: Rocking scans around the reconstruction rod (1.21 0 0.2) for the clean Pt surface, after 1 ML Fe deposition and after 3 ML Fe deposition.

FePt grows in registry with the substrate, i.e. with exactly the same in-plane parameter than Pt(001). SXR measurements performed scanning momentum transfer parallel to the surface show no additional rods between the ones of the substrate. FePt contribution shows up in the crystal truncation rods (CTRs - cf section 2.3), giving rise to Kiessig oscillations. Broad peaks close to the anti-phase positions indicate an almost doubling of the electronic density period along the out-of-plane direction. These so-called order peaks express that the layer has the same *fcc* structure than the Pt substrate but with alternate Pt and Fe planes along the *c* direction. It corresponds to the expected  $L1_0$  phase with *c*-axis perpendicular to the surface. Scans of the momentum transfer modulus parallel to the surface (*hk*-scans) at fixed *L* around order peak do not show extra peak or shoulder on the CTRs, preventing any suspicion of relaxation. From the in-plane peak width we estimate the characteristic domain size parallel to the surface about 190 nm. No trace of  $L1_2$  or in-plane  $L1_0$  phases was found.

Qualitatively, the position of the order peak ( $l \approx 1.13$ ) gives a tetragonality of  $c/a = 0.89$  with  $c \approx 3.47 \text{ \AA}$ , suggesting that the layer is Fe rich as the bulk stoichiometric alloy would give a tetragonality of 0.92 for a constant volume. From the out-of-plane peak width we assess that

2.3 BL were grown. The quantitative analysis described just below demonstrate that these results are inexact. Because substrate and layer contributions interfere on the same rods, the order peak can not be taken apart and give such precise values. However the anisotropy revealed here is expected. An out-of-plane compression is required to keep a constant unit cell volume in regards to the expansion of the in-plane parameter.

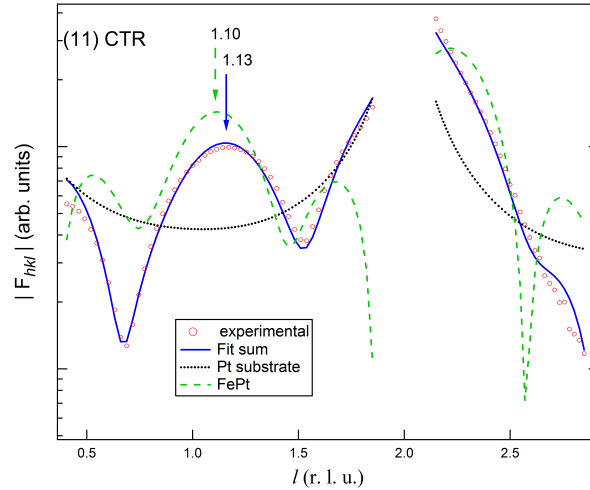


Figure 3.2: (11) CTR of FePt/Pt(001). Intensity distribution results from the interference of the FePt and Pt contributions. The FePt order peak has its maximum at  $l = 1.10$  and not at  $l = 1.13$  as a rapid analysis could let think.

### 3.1.2 Modeling the FePt/Pt(001) structure

To obtain quantitative values, the film structure should be resolved by a model fitted to reproduce the structure factor amplitudes  $|F_{hkl}|$  extracted from  $l$ -scans of 6 CTRs, according to the procedure described in section 2.3. The equivalent rods were averaged in the P4mm symmetry giving (10), (11) and (20) rods presented in Fig. 3.4, with an average agreement factor of 2.7% for 184 non-equivalent reflections. Error bars are calculated from data dispersion of symmetry equivalent rods. Some rocking scans along the 6 rods were measured to check the alignment of the  $l$ -scan along the maximum of intensity of the rods. The best model achieved consists of a central part of FePt alloy, the interface with platinum substrate and the surface, and is summarized in Table 3.1. For each layer  $n$ , the parameters of the fit are the occupation rates ( $occ_{Fe}$  and  $occ_{Pt}$ ) and interplane distances  $d_{n,n-1}$  to the preceding layer. The Debye Waller factor (DW) was considered uniform along the film. Except the surface layer (layer 6), all layers were constrained to be full, i.e.  $occ_{Fe} + occ_{Pt} = 1$ .

The interface is represented by the topmost layer of the substrate with a free and independent distance to the bulk  $d_{1,0}$ . Fe was allowed to interdiffuse into this layer. The layers 1 to 4 compose the main part of the film. A unique interplane distance was considered for them. The occupation rate of the layer 1 was independent from those of the other layers of the film, assuming that the proximity of the substrate has an influence on the mixing. The

surface is composed by 2 ML with free and independent distances. In layer 5, the occupation rate is free with a full occupation while the layer 6 is estimated rough and not full.

layer (n)	region	$d_{n,n-1}$	$occ_{Pt}/occ_{Fe}$
6	Pt site	1.64(3) Å	0.14(5)/0
5	Fe site	1.80(2) Å	0.04/0.96(1)
4	Pt site	1.77(1) Å	0.74/0.26(4)
3	Fe site		0.26/0.74(4)
2	Pt site		0.74/0.26(4)
1	Fe site		0/1(0.1)
0	Pt interface	1.97(1) Å	1/0(0.05)
Bulk		1.96 Å	1/0

Table 3.1: Fitting results of the 3 BL FePt film. Occupation rates ( $occ_{Fe}$  and  $occ_{Pt}$ ) and interplane distance  $d_{n,n-1}$  to the preceding layer are described for each layer.

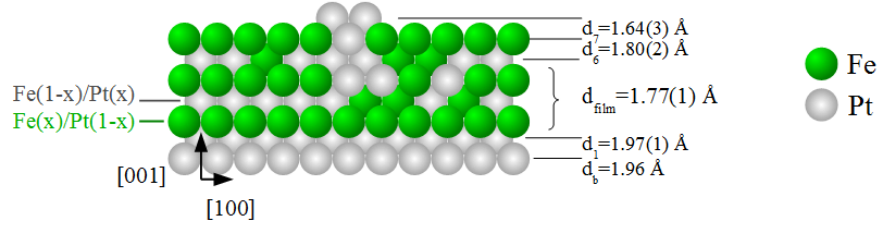


Figure 3.3: Side view of FePt model. The colors are representative of Fe and Pt occupation rates.

The fitting procedure gives alternate Fe and Pt rich layers, characteristic of some degree of  $L1_0$  order. It can be quantified by the order parameter  $S$ , defined in a binary alloy as  $S = r_\alpha - w_\alpha$ , where  $r_\alpha$  and  $w_\alpha$  are the ratio of  $\alpha$ -sites occupied by the right and by the wrong kind of atoms, respectively[103].  $S=0$  ( $S=1$ ) for a completely disordered (perfectly ordered) alloy. Applying this definition for  $n=1$  to 5 we have on average  $S = 0.64(1)$ , which is a high value compared to the literature[126]. Surprisingly, the order is particularly important at the interfaces. The Fe diffusion in the substrate is indeed negligible. Pt occupancy in the last layer of Fe is only about 0.04 %, assuming a complete layer. In the central part of the film, the intermixing is about 26%. The Debye Waller was set equal to the Pt bulk DW (0.31) [128] and was finally fixed. As free, its value had a tendency to decrease, highlighting the important order structuring the film.

The lattice parameter  $c_{FePt} = 3.55 \text{ \AA}$  is compressed by 4.5 % with respect to the FePt bulk, compensating the substrate induced tensile strain. The tetragonality  $c/a = 0.905$  is enhanced compared to the bulk value  $c/a = 0.962$ , but is smaller compared to the value deduced from the preliminary qualitative analysis. The unit cell volume  $V=54.7(4) \text{ \AA}^3$  calculated from  $a_{FePt}$  and  $c_{FePt}$  is smaller than the unit cell volume of both the ordered stoichiometric alloy  $V_{bulk}=55.32 \text{ \AA}^3$ , and even the ordered  $Fe_{55}Pt_{45}$  nano-cristalline alloy  $V_{0.55} = 54.807 \text{ \AA}^3$ . [79]

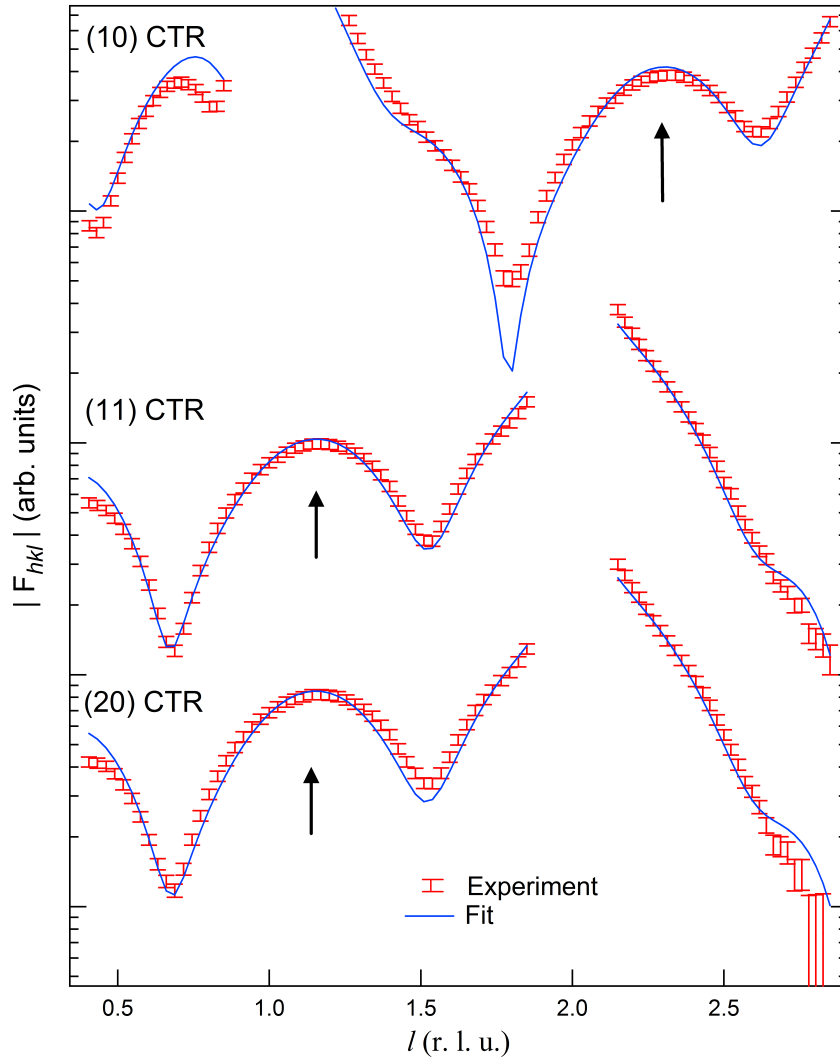


Figure 3.4: Pt rods (CTRs) after 3 ML of Fe thermal deposition. Fitted curves (solid lines) are compared to the experimental structure factors associated to their error bars. Arrows point order peaks.

The surface layer was considered incomplete and modeled as pure Pt layer. This is justified by the tendency of Pt to segregate on Fe. However diffraction data cannot distinguish between a partially occupied Pt layer and a FePt layer with larger occupancy, Fe having a smaller atomic scattering factor than Pt. Another model not presented here, where no Pt but Fe occupying 45% of the surface layer is assumed, obtains almost the same normalized  $\chi^2$  result (6.95 instead of 6.73). All other parameters are unchanged. An intermediate situation with Fe mixed with Pt could also be considered. For the model presented here, 3.2 ML of Fe are distributed into the film against 3.65 ML in the other model. The second solution seems too far from our calibration to be considered as true. Distance of this layer with the previous one is found smaller than those inside the film respecting the general tendency of free-surfaces. In the same way, the second surface layer ( $n=5$ ) can be fitted as partially incomplete, with a larger Pt fraction.

One can note that data are not well fitted in the low region of  $l \leq 0.7$ . This discrepancy can be explained by an overestimation of detector acceptance correction. In stationary geometry the detector acceptance correction diverges at low  $l$ , and the rod size needs to be compared with the projection of the detector acceptance on the surface plane.[108, 121] If the rod size is much smaller than the area integrated, the standard correction is not valid. This configuration happens at low polar angles, as in small  $l$ . Rocking scans can integrate the intensity over a much wider region and should prevent this problem. Since the fitted data are close to the experimental one in other regions with a model coherent with physical expectations and with literature, we considered that new measurements were not mandatory (time consuming).

### 3.2 CoO(111) on Pt(001)

As far as we know the growth of CoO on Pt(001) has surprisingly never been reported. Because Pd has a similar structure to Pt and is in the same column of the periodic table of elements, the growth of CoO on Pd(001) could help us having an idea of what could be expected. The growth on Pd has been investigated by L. Gragnaniello and coworkers [122] using LEED, STM, photoemission and x-ray absorption spectroscopy experiments. They observed different structures as function of the coverage. Up to 2 ML, cobalt oxide atoms are arranged in two quasi-hexagonal structures with different sizes of the surface mesh, and form well-defined wetting layers as an almost (111) oriented rock-salt phase. In the single layer regime, Pd is almost entirely covered and CoO phase is defective. It becomes stoichiometric in multilayers, where a Moiré pattern is observed. At higher coverage (10-20 ML), spinel  $Co_3O_4(111)$  and CoO(100) have been detected.

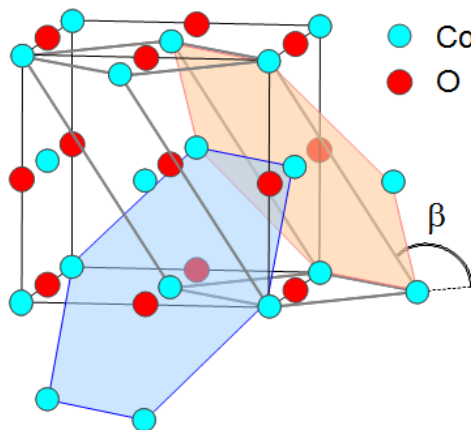


Figure 3.5: (111) planes in CoO bulk structure.

CoO growth on Pt(111) is another judicious base for expectations. This growth is more complex giving a variety of results as function of deposition conditions, but presents in a sense features similar to CoO/Pd(001) growth. M. De Santis and coworkers [121] report from their



LEED and STM experiments that the oxide grows epitaxially as a polar CoO(111) film with a moiré pattern. A deposition of one ML followed by an oxidation at a temperature between RT and 470 K gives rise to a rough surface. Co atoms coming from quasi pseudomorph Co layer on Pt(111) are in excess. With annealing at temperature higher than 570 K or even 740 K under oxygen, these atoms in excess can diffuse into Pt substrate and let a flat and flawless moiré at the surface, while low-temperature annealing creates a zigzag phase, which is oxygen deficient (cf Fig. 3.6). In general, insufficient oxidation leads to defects in the moiré pattern. Dislocation triangles, the zigzag structure or the quasi (3 x 3) structure appear in the moiré pattern with decreasing oxygen content. All these structural changes are a strategy for the system to avoid Co on top of Pt atoms or Pt-Co-O *hcp* stacking. In the single layer regime, the layer has an out-of-plane contraction to reduce dipolar energy at the surface. At higher coverage, films exhibit Stranski-Krastanov growth finding another way to reduce dipolar energy. 3D islands of rock-salt CoO(111) in orientational epitaxy with the substrate form a both rough and well organized surface.

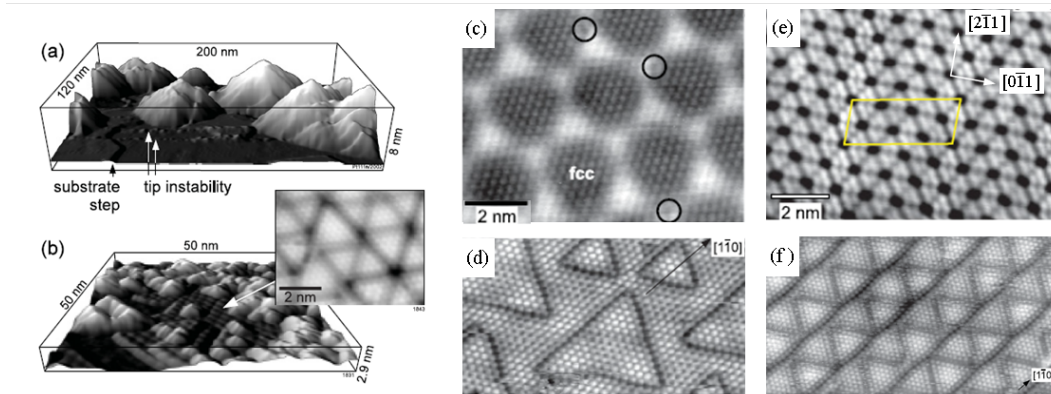


Figure 3.6: STM images of CoO/Pt(111) taken from ref. [121]. 3D islands of epitaxial CoO(111) after 6 ML deposition annealed in oxygen at 740 K (a) with its Moiré pattern (c) or at 450 K (b). Triangular dislocation loops in 1 ML CoO (d), the quasi (3 x 3) structure (e) and the zigzag structure (f) are present in oxygen deficient surfaces.

We have studied qualitatively CoO growth on Pt(001) by GIXRD. Some features are common whatever the deposition conditions. First Pt deconstructs entirely as soon as the first Co layer is deposited (cf Fig. 3.7). Secondly, no trace of pseudomorph or relaxed rocksalt CoO(001) or spinel  $C_3O_4$  was found. Thirdly additional rods appear exhibiting a pattern with roughly six-fold in-plane symmetry. They remind the (111)-rock-salt growth. After about 10 ML Co RT deposition under an oxygen pressure of about  $5 \cdot 10^{-7}$  mbar, the order is so weak that the peaks are almost lost in the diffuse scattering background and are at the limit of detection. Annealing gives rise to order. However the better is not the higher. When the substrate is held at 520 K, intensity of Bragg peaks is higher than that one obtained at 730 K indicating that a too high temperature could destabilize and destroy the film. As seen for FePt growth, Co atoms use more easily thermal energy to reorganize during deposition

than after. Thermally assisted deposition allows to achieve better ordered layers than RT deposition followed by annealing at the same temperature. Thus Co deposition under oxygen pressure of  $2 \cdot 10^{-7}$  mbar with a substrate held at 520 K gives rise to domains with characteristic size of about 8-9 nm in the direction parallel to the surface, compared to about 6 nm for Co RT reactive deposition followed by annealing under oxygen.

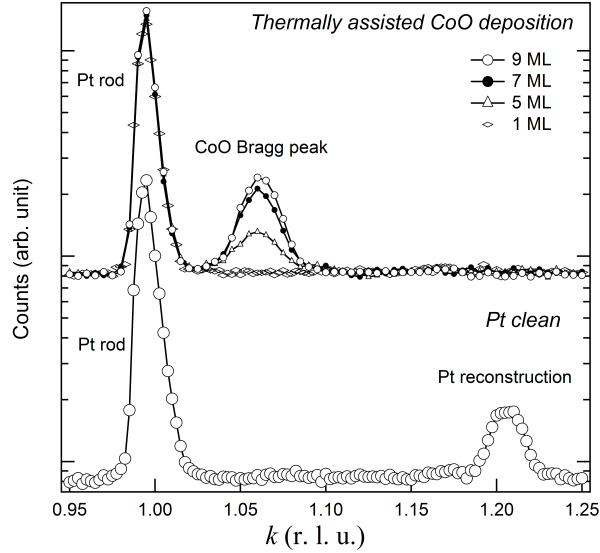


Figure 3.7:  $k$ -scans at ( $h=0, l=0.545$ ) during CoO deposition. Reconstruction rod at ( $0 \ 1.21 \ 0.545$ ) disappears as soon as the first Co layer is deposited. Intensity at ( $1.065 \ 0 \ 0.545$ ) increases with CoO deposition.

In all cases, four growth variants were observed by successive rotation of the sample by  $90^\circ$  around the surface normal. They are due to the fourfold symmetry of the substrate and are almost in same proportion. Because the adlayer is not pseudomorph, in-plane and out-of-plane parameters could be deduced with precision from the positions of the Bragg peaks well separated from CTRs. CoO peaks don't show any oscillations indicating a rough surface. Scanning the momentum transfer parallel to the surface along two directions at  $60^\circ$  from each other, a small but significant anisotropy is clearly detected indicating that the hexagonal mesh is non regular. As can be seen in Fig. 3.8, a shift between the CoO rod position expresses a distortion of the in-plane hexagonal pattern. The in-plane parameters of the CoO pseudo hexagonal mesh are evaluated around  $h_2 = 3.008(3) \text{ \AA}$  and  $h_1 = 3.012(4) \text{ \AA}$  from the position of these rods. While the maxima of the rods are clearly apart, the absolute uncertainty of these estimation values is about  $3 \cdot 10^{-4} \text{ \AA}$ . The measurements were taken before the understanding of the distortion and do not allow to achieve precise values of CoO parameters. In opposite, CoO rods on FePt were precisely measured and show a monoclinic distortion characterized in the next section. Ultra-thin FePt films grown on Pt(001) having the same in-plane parameters as the substrate itself, CoO is subject to the same constraints on Pt(001) and on FePt/Pt(001). That is why we believe that CoO films grown on both surfaces have exactly the same structure. Describing one is describing both.

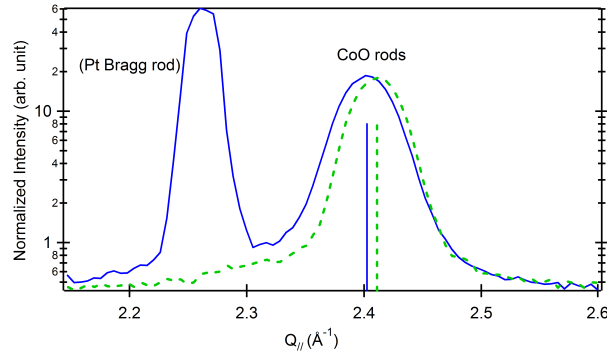


Figure 3.8: Normalized intensity distribution versus the momentum transfer modulus parallel ( $Q_{//}$ ) to the surface at  $Q_z = 0.873\text{\AA}^{-1}$ . The plain (blue) line corresponds to a scan along  $\vec{a}_{Pt,1}$  and crosses both Pt and CoO rods. The dashed (green) line is obtained from a scan along a direction rotated by  $60^\circ$  with respect to  $\vec{a}_{Pt,1}$ . CoO rod positions are pointed by the corresponding plain and dashed marks, highlighting the shift between them.

### 3.3 CoO(111) on FePt/Pt(001)

As seen in section 3.1, the thermal deposition of 3 ML of Fe gives rise to a chemically ordered 3 BL FePt with the topmost layer partially occupied. To obtain a Pt terminated alloy, either the substrate is held longer at 600 K allowing Pt atoms to segregate, or one Pt layer is deposited. To also prevent Fe oxidation during CoO growth, we have chosen to deposit one Pt layer at 610 K and two metallic Co layers at 520 K. The temperature was decreased to limit the highly probable CoPt alloy formation. Co and Pt were deposited by molecular beam epitaxy (MBE), using pure rods inserted in water-cooled electron beam evaporators. The deposition rate, calibrated with a quartz crystal microbalance, was typically 1 ML per 10 minutes for Fe and Co, and 1 ML per 45 minutes for Pt. The deposition was followed by SXRD at 20 keV beam energy with a grazing incidence angle of  $0.6^\circ$  by rocking scan at (1 1 1.12) i.e. close to the FePt chemical order peak and by  $l$ -scan of the (11) CTR. Co grows pseudomorphic on FePt. Its contribution interferes with those of Pt and FePt in the CTRs. The order peak enhance slightly and the Kiessig oscillations have a smaller periodicity. Absence of  $L1_2$  order and Fe spinel was checked.

Additional Co reactive growth, with a molecular oxygen pressure around  $P_{O_2} = 5.10^{-7}$  mbar on a substrate held at 520 K leads to a 4 nm thick CoO. Structure of this film is detailed in next section, while its magnetic properties are described in the next chapter. X-ray absorption spectra at Co  $L_{2,3}$  edges performed at the ID08 soft x-ray beamline of ESRF show no trace of metallic Co component. The first 2 Co ML are completely oxidized during this last step.

#### 3.3.1 Analyzing the CoO diffraction pattern

The analysis of the structure of the CoO film is based on the in-plane position of several rods and their structure factor distribution versus the momentum transfer perpendicular to the surface  $Q_z$  (Fig. 3.12). In-plane  $(h, k)$  positions of 12 rods (4 non-equivalents) were

optimized by scanning the momentum transfer parallel to the surface  $Q_{//}$  (rocking scans and  $hk$ -scans). The intensity distribution along each rod was measured varying the component  $Q_z$  perpendicular to the surface ( $l$ -scans). The beam was set to a grazing incidence angle of  $0.2^\circ$ , smaller than before to obtain a maximum of sensitivity to the CoO film. Structure factor amplitudes along CoO rods were extracted from intensity distribution after background subtraction and standard stationary geometry corrections and symmetry averaged giving the (20), (11), (31) and (02) non equivalent rods reported in Fig. 3.12. They are labeled in the rectangular surface mesh defined below.

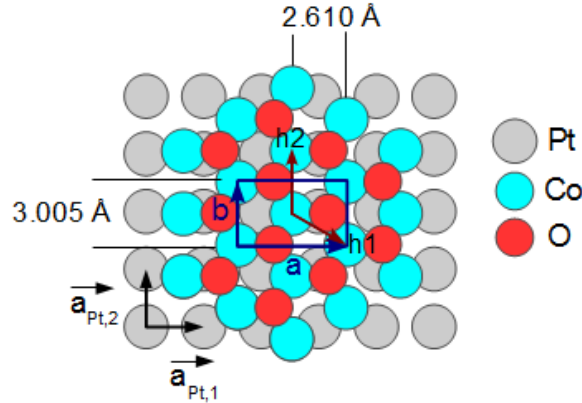


Figure 3.9: Schematic top view of CoO on Pt(001) or FePt/Pt(001). Lengths of  $\vec{h}_1$  and  $\vec{h}_2$  are non-equivalent. The non regular hexagon is easier described using a rectangular surface mesh formed by the in-plane vectors  $\vec{a}$  et  $\vec{b}$ .

As for CoO on Pt(001), the rod pattern exhibits roughly a sixfold in plane symmetry (Fig. 3.11). Scans with the momentum transfer parallel to the surface  $Q_{//}$  along  $\vec{a}_{Pt,1}$  and in the direction rotated by about  $60^\circ$  in-plane show a shift between the two modulus Bragg peak positions (cf Fig. 3.8) indicating that the hexagonal mesh is non regular. A real space schematic view is given in Fig. 3.9. The in-plane parameters are evaluated of about  $h_2 = 3.005(1) \text{ \AA}$  and  $h_1 = 3.012(1) \text{ \AA}$  separated by an angle smaller than  $120^\circ$  (about  $119.93(1)^\circ$ ) from the averaged position of the rods. Due to the larger data set, the accuracy of these values is better than those of CoO on Pt(001). They confirm the in-plane contraction and distortion of the structure. The lost of symmetry leads to describe the non-regular hexagon using a rectangular surface mesh, defined by the vector  $\vec{a}$  parallel to  $\vec{a}_{Pt,1}$  and  $\vec{b}$  parallel to  $\vec{a}_{Pt,2}$  as shown in Fig. 3.9. Both values -slightly for one, clearly for the other- are below the corresponding distance for bulk CoO rock-salt ( $\frac{a_{CoO}}{\sqrt{2}} = 3.013 \text{ \AA}$ ) resulting to a smaller hexagonal surface. The distortion should be related to the anisotropic strain imposed by the mismatch. The epitaxy is indeed characterized by a misfit between the unit-mesh length  $h_2$  and the substrate surface row spacing  $a_{Pt,2}$  ( $\frac{h_2 - a_{Pt,2}}{a_{Pt,2}}$ ) of about  $+8\%$ , and between CoO row spacing  $\frac{1}{2}\sqrt{(2 \times h_1)^2 - h_2^2} = 2.610 \text{ \AA}$  and  $a_{Pt,1}$  of  $-6\%$ .

Due to the substrate symmetry, four variants corresponding to the rotation of the unit cell by the fourfold symmetry axis normal to the substrate are observed, as shown in Fig. 3.10a.

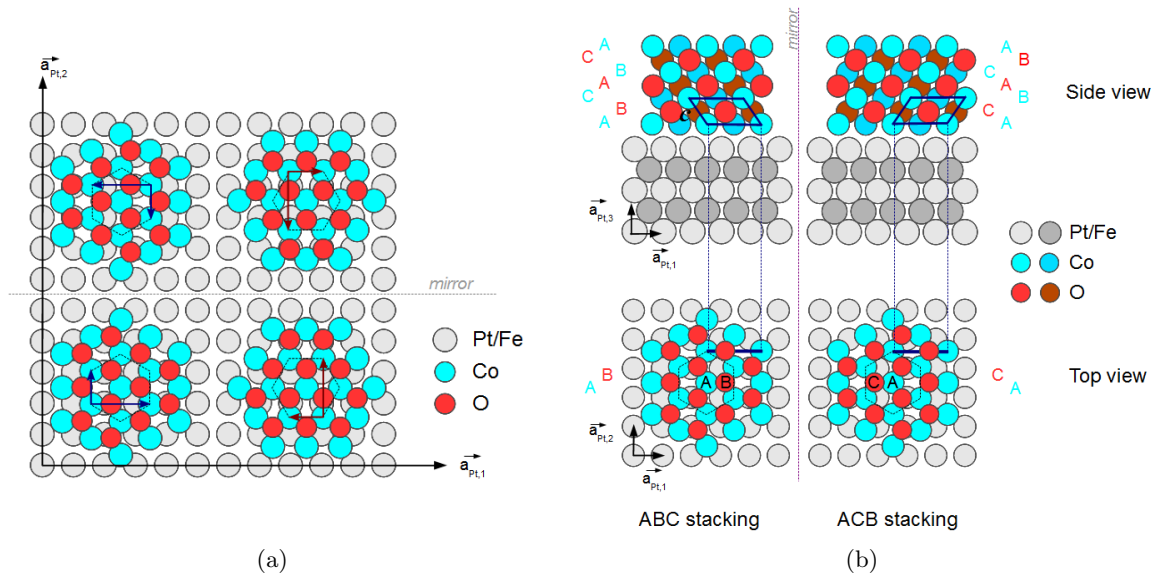


Figure 3.10: (a) Four variants coexist in the film due to the fourfold symmetry of the substrate. (b) The variants related to each other by a  $180^\circ$  rotation are mirror domains. They share the first in-plane layer but have different stacking (ABC or ACB).

For each variant, the positions of the CoO diffraction rods form a non regular hexagonal mesh on the surface plane. The variants rotated by  $180^\circ$  have a special relation. They can be seen as mirror variants. They share the same first in-plane layer (here presented as cobalt layer) but separated from the second one (oxygen layer here). When piling up a close packed structure, A, B or C sites are available (cf Fig. 3.10b). If cobalt is in A sites, oxygen could sit in B or C ones, determining the stacking orientation for the next layers. Hence they correspond to the two ABC and ACB stackings. They are related to each other by an inversion of the coordinate along  $\vec{a}$ . Thus in reciprocal space  $(hk)$  rods of a variant merge with the  $(\bar{h}k)$  rods of its mirror variant. The second set of mirror variants is deduced by  $90^\circ$  rotation of this set. Their rods are clearly separated from those of the first set whose positions are represented in Fig. 3.11.

Each rod is composed by the contribution of the two mirror variants. A clear identification of the diffraction features associated to each of them is required to analyze the out-of-plane part of CoO structure. For a CoO(111) film with cubic rock-salt phase the rods labeled here  $(20)$  and  $(\bar{1}1)$  are equivalent, the surface normal being a three-fold symmetry axis. These rods merge with the  $(\bar{2}0)$  and  $(11)$  ones, respectively, of the mirror variant (also equivalent to each other in the rock-salt structure). In our data a small but clear shift is observed in between the out-of-plane peak positions of the  $(20)$  and the  $(\bar{1}1)$  rods (Fig. 3.12e). A similar shift is observed between the  $(\bar{2}0)$  and  $(11)$  peak positions (3.12f). This shift can only be explained if the  $\vec{c}$  vector of the CoO unit cell is not perpendicular to the surface, but has an in-plane component. Atoms of the fourth Co atomic layer of the oxide film are not exactly above the Co atoms of the first one. The CoO film has a monoclinic distortion. A second experimental observation confirms this statement. The  $(02)$ ,  $(31)$ , and  $(\bar{3}1)$  rods are equivalent in a cubic

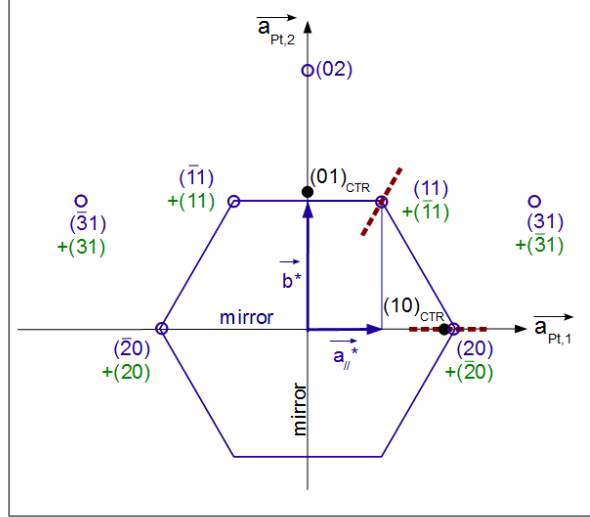


Figure 3.11: In-plane rods positions of CoO film (blue open circles) and Pt substrate (plain circles). The CoO diffraction pattern exhibits roughly an hexagonal symmetry parallel to the surface plane, as in (111)-cubic orientation. The positions show a small in-plane elongation different in the directions parallel to  $\vec{a}_{Pt,1}$  and at roughly  $60^\circ$ . By symmetry inversion,  $(hk)$  rods of one variant (indexed in blue) merge with the  $(\bar{h}\bar{k})$  rods of the mirror variant (indexed in green).

CoO(111) structure, but not in the monoclinic film. In our experiments Bragg peaks observed along the (31) and  $(\bar{3}1)$  rods are wider compared to the ones along the (02) rod (Fig. 3.12c and 3.12d). The (02) rod is located on the inversion-symmetry plane. Only a single component (021) Bragg peak has been measured. Measuring along the (31) rod, a wider peak is observed for the same  $Q_z$  range. It corresponds to the superposition of the (310) peak and the  $(\bar{3}12)$  one of the mirror domain (in the monoclinic cell basis defined below).

The monoclinic unit cell can be described using basis vectors  $\vec{a} = (a, 0, 0)$  (parallel to  $\vec{a}_{Pt,1}$ ),  $\vec{b} = (0, b, 0)$  (parallel to  $\vec{a}_{Pt,2}$ ), and  $\vec{c} = (-c_1, c_2, c_3)$ . As  $\vec{b}$  is in the mirror plane, if  $c_2 \neq 0$  there should be 8 variants instead of the 4 experimentally observed. We have then  $\vec{c} = (-c_1, 0, c_3)$ . If we chose  $\vec{c}$  as the shortest vector joining Co atoms in the Pt (010) plane the lattice pattern is :  $Co(0, 0, 0)$ ,  $Co(\frac{1}{2}, \frac{1}{2}, 0)$ ,  $O(\frac{1}{2}, 0, \frac{1}{2})$ ,  $O(0, \frac{1}{2}, \frac{1}{2})$  and the reciprocal space vectors are  $\vec{a}^* = \frac{2\pi}{a} \cdot (1, 0, \frac{c_1}{c_3})$ ,  $\vec{b}^* = \frac{2\pi}{b} \cdot (0, 1, 0)$ ,  $\vec{c}^* = \frac{2\pi}{c_3} \cdot (0, 0, 1)$ .

The Bragg peak positions for the monoclinic system are given by

$$\vec{Q}(hkl) = 2\pi \cdot \left( \frac{h}{a}, \frac{k}{b}, \frac{1}{c_3} \left( l + h \frac{c_1}{a} \right) \right) \quad (3.1)$$

We can express  $\frac{c_1}{a}$  as

$$\frac{c_1}{a} = \frac{1}{3} + \delta \quad (3.2)$$



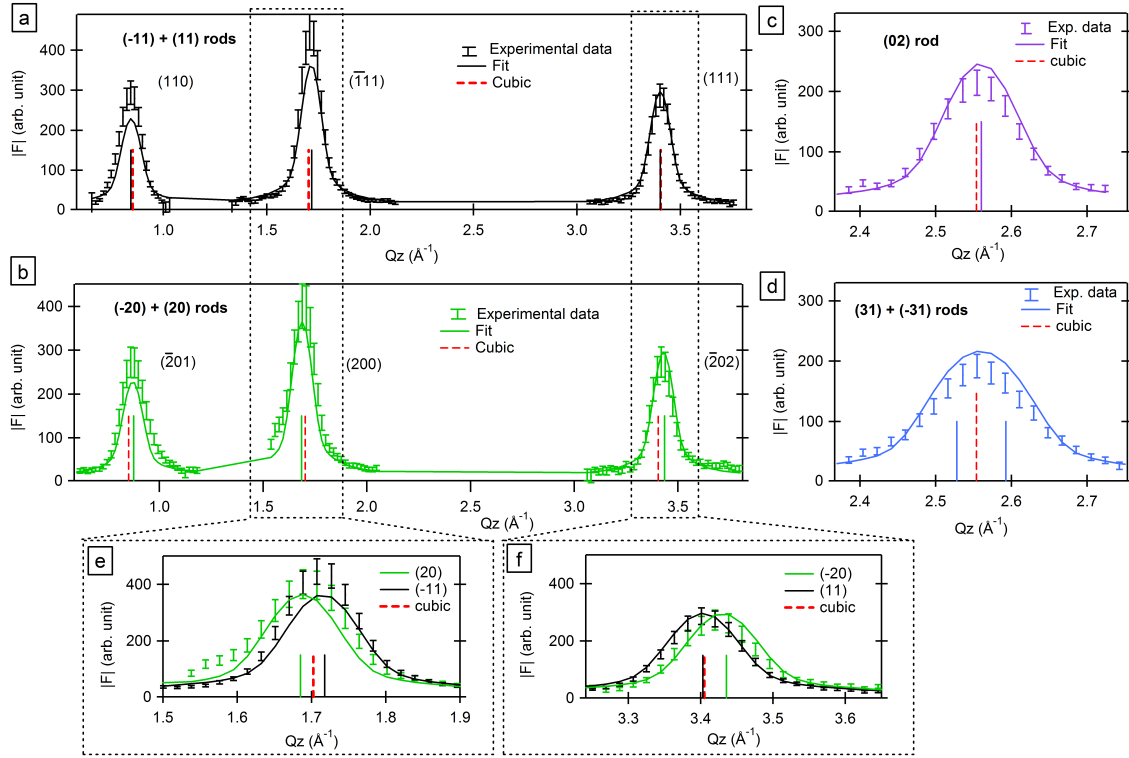


Figure 3.12:  $(\bar{1}1)$  and  $(11)$  (a),  $(\bar{2}0)$  and  $(20)$  (b),  $(02)$  (c),  $(\bar{3}1)$  and  $(31)$  (d) CoO rods. The scattered points correspond to experimental data. They are associated to errors bars obtained from the dispersion of the data in symmetry equivalent rods. The plain lines are obtained by the fitting procedure. Vertical plain lines point the positions of the Bragg peaks. Dashed (red) lines indicate the position of these peaks in a cubic cell, calculated from CoO bulk data from [90] (e) Zoom of  $(200)$  and  $(\bar{1}11)$  Bragg peaks (f) Zoom of  $(\bar{2}00)$  and  $(111)$  Bragg peaks with three vertical lines signaling out-of-plane positions in reciprocal space for these two peaks in monoclinic cell and in cubic cell. In cubic cell, they are merged.

In the Figure 3.14, we give a visual explanation of the link between  $\delta$  and the shift of the peak positions in a schematic view of  $(11)$ ,  $(20)$ ,  $(\bar{1}1)$  and  $(\bar{2}0)$  rods of two mirror variants projected in Pt(010) plane. The blue color refers to one variant, the green color to its mirror variant. For comparison, the positions of the cubic structure are in red. Higher is  $|\delta|$ , closer to the surface is  $a^*$ , smaller is the out-of-plane position of peaks in  $(11)$  and  $(20)$  rods and higher is the position of peaks in  $(\bar{1}1)$  and  $(\bar{2}0)$  rods. Because in each rod appear the peaks of  $(hk)$  and  $(\bar{h}k)$  rods, some peaks get closer while other go away from each other. Since they come from different variants, the peaks in  $\langle 11 \rangle$  rod act in the opposite way as peaks in  $\langle 20 \rangle$  rod with the same  $l$  positions creating the shift observed in our measurement.

For the rock-salt cubic structure  $\delta=0$ . Thus  $(200)$  and  $(\bar{1}11)$  reflections have the same  $Q_z$ . For a monoclinic lattice these two reflections are shifted by

$$\Delta Q = Q_z(2, 0, 0) - Q_z(\bar{1}, 1, 1) = \frac{2\pi}{c_3}(3 * \delta) \quad (3.3)$$

From Fig. 3.12e  $\Delta Q < 0$  then  $\delta < 0$  and  $c_1 < \frac{a}{3}$ .

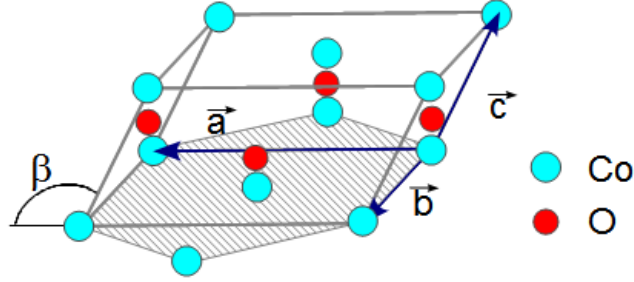
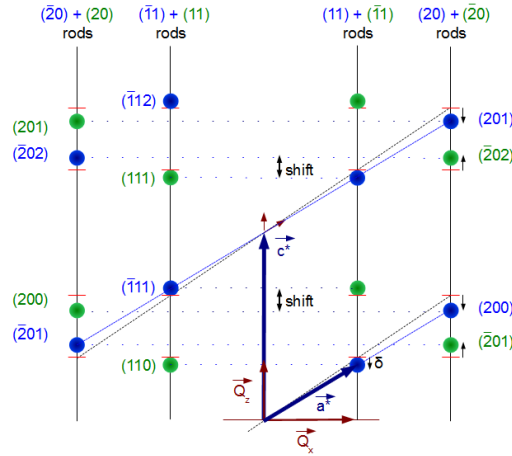


Figure 3.13: Monoclinic CoO unit cell in perspective

Figure 3.14: Schematic view of (11), (20),  $(\bar{1}1)$  and  $(\bar{2}0)$  rods of two mirror variants projected in Pt(010) plane.

### 3.3.2 Modeling the CoO structure

Once the monoclinic distortion is qualitatively described, the structural parameters of the CoO films should be obtained. The first step is the calculations of precise in-plane parameters  $a$  and  $b$  from a collection of  $Q_{//}$  -scans.

As explained in the previous section, the positions of the rods  $Q_x$ ,  $Q_y$  were evaluated by fitting the in-plane line-shape of 12 rods belonging to different variants. Equivalent positions were averaged to get the inequivalent couples reported in Table 3.2. Errors bars were obtained from the dispersion of the data in symmetry equivalent rods.  $a$  and  $b$  lattice constants were derived from the  $\vec{Q}(hkl)$  formula through a weighted mean of these values. Their values are  $a = 5.220(2)$  and  $b = 3.005(1)$  in agreement with  $h1$  and  $h2$  values given before.

Then the structure factor amplitudes as function of the momentum transfer perpendicular to the surface ( $Q_z$ ) were simulated using a model of the CoO film with monoclinic structure with the ANA-ROD package [110] (extended version) to reproduce the rods reported in Fig. 3.12.

The interlayer spacing was taken uniform over the full thickness. The measured signal decreases quickly along the rods moving away from the CoO Bragg peaks, which is a sign of a



rod	$Q_x(\text{\AA}^{-1})$	$Q_y(\text{\AA}^{-1})$	$Q_{//}(\text{\AA}^{-1})$
(11)	1.207 (2)	2.092(1)	2.415(2)
(20)	2.4069(7)	0	2.407(1)
(02)	0	4.180(1)	4.180(1)
(31)	3.614(3)	2.087(1)	4.173(2)

Table 3.2: In-plane CoO peaks positions  $Q_x$ ,  $Q_y$  and  $Q_{//} = \sqrt{Q_x^2 + Q_y^2}$ . In each couple ((11)/(20) and (02)/(31)) a small shift reveals the in-plane distortion of the film.

strong surface roughness. This latter was simulated by introducing an occupancy value  $Occ(n)$  for each atomic layer  $n$  of the oxide film. Different models of occupancy have been tested. Data are well reproduced with a complementary error function  $\text{erfc}(z)$ . This model is based on the assumption that the distribution of the terraces' width is described by a gaussian centered at  $z_0$  and with a variance  $\sigma$  ( $\text{\AA}$ ). In this second step of the structural analysis, interlayer spacing parameter  $c_3$  and occupancies were obtained through a fit of the (02) rod, which is insensitive to the monoclinic distortion, or more exactly to the  $\delta$  parameter.

Occupancies are then fixed. The fit of the ensemble of rods is performed to optimize  $c_3$  and determine the component along  $x$  of the third unit cell vector ( $-c_1$ ). As  $(hk)$  and  $(\bar{h}k)$  rods of the two mirrors variants are merged, the diffracted intensity is calculated for these two domains and added with identical weight.. The parameters  $c_1$  and  $c_3$  obtained from the best fit are reported in Table 3.3. The corresponding curves are plotted in Fig. 3.12. The values of  $\delta$  (deduced from  $\frac{c_1}{a} - \frac{1}{3} = \delta$ ),  $\beta = 180^\circ - \arctan(\frac{c_3}{c_1})$  and  $c$  are also reported in Table 3.3. In the cubic system  $\beta = 180^\circ - \arctan(\sqrt{2}) = 125.264^\circ$ . The lower value of  $\beta = 125.05^\circ(7)$  expresses the deviation from cubic unit-cell.

$a$ ( $\text{\AA}$ )	$b$ ( $\text{\AA}$ )	$c_1$ ( $\text{\AA}$ )	$c_3$ ( $\text{\AA}$ )	$c$ ( $\text{\AA}$ )
5.220(2)	3.005(1)	1.721(3)	2.454(3)	2.998(4)
$\delta$	$\beta$ (deg)	$z_0$ ( $\text{\AA}$ )	$\sigma$ ( $\text{\AA}$ )	$\chi^2$
-0.0036(7)	125.05(7)	43(9)	21(4)	2.3

Table 3.3: Best-fitted parameters of the CoO film structures. The first line concerns the unit cell vector lengths and their projections along the Pt crystallographic axes. In the second line, the monoclinic distortion is highlighted with  $\delta$  and  $\beta$ .  $z_0$  and  $\sigma$  are linked respectively to the thickness and the roughness of the films.  $\chi^2$  marks the quality of the fit.

The best fit gives an average thickness  $z_0 = 4.3$  nm, while the variance  $\sigma = 2.1$  nm results in a r.m.s. roughness of about 1.8 nm. This should be considered only as a rough estimation. Repeated fits give a large dispersion (represented in the Figure 3.15) around these values. The error bars are evaluated from the dispersion. However this estimation is in fair agreement with the thickness and roughness of the CoO layer obtained from complementary measurements by x ray reflectivity ( $z_0 = 3.5(6)$  and  $\sigma = 0.8(3)$  nm) and atomic force microscopy AFM (surface roughness rms = 1.0(2)nm). The AFM results has to be considered as a lower limit reflecting its resolution. Such strong roughness was expected for a growth of CoO in (111) orientation

as explained in section 3.2. A Stranski-Krastanov growth mode with pyramidal islands was observed for such polar surface in the case of CoO/Pt(111) or CoO/Pd(001) (cf section 3.2).

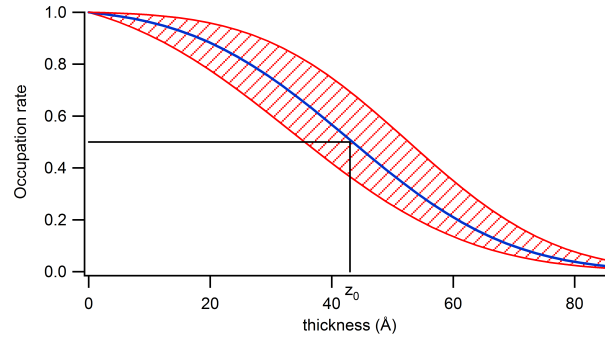


Figure 3.15: Occupation rate in function of the thickness in our best fitted model of CoO on FePt/Pt(001).

### 3.3.3 Comparison with bulk CoO structure

The quite anisotropic epitaxial mismatch with the substrates leads to a stress that deforms the hexagon. Such anisotropy is at the origin of the monoclinic distortion when the layer develops. All the structures can be easily compared within the distorted cubic cell, taking as lattice basis  $\vec{a}' = \vec{b} - \vec{c}$ ,  $\vec{b}' = \vec{b} + \vec{c}$ , and  $\vec{c}' = \vec{a} + \vec{c}$ , as shown in Fig. 3.16. In the cubic structure, Co atoms (resp. O) are embedded in a regular octahedron formed by its first neighbors O atoms (resp. Co) and drawn in the Figure 3.16.

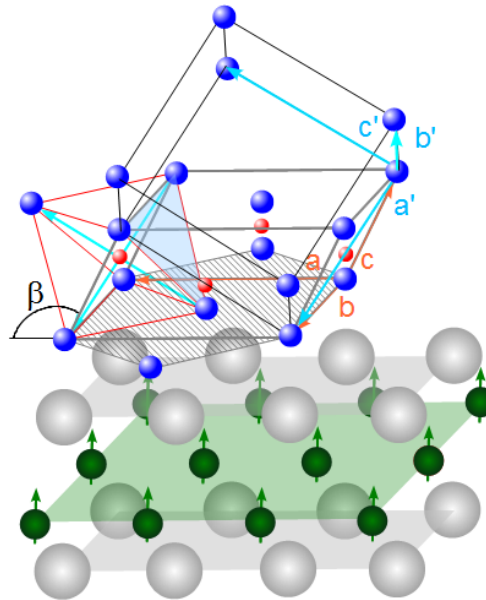


Figure 3.16: Illustration of CoO layer on FePt in perspective.  $(\vec{a}, \vec{b}$  and  $\vec{c})$  lattice basis of the monoclinic cell and  $(\vec{a}', \vec{b}'$  and  $\vec{c}')$  of the distorted cubic cell are represented.  $c'$  and  $a'$  axes of tetragonal elongation are indicated in the  $CoO_6$  octahedron (red lines).

Compared to the rocksalt structure, the surface formed by the non regular hexagon in the plane of the layer is contracted of about 0.24%. Distance  $a$  is barely affected (5.22 Å instead of 5.219 Å) but  $b$  reduces significantly (from 3.013 Å to 3.005 Å) getting closer to the substrate distance of 2.775 Å, as a result of the compressive constraint exerted by the substrate along this direction. If the layer had a cubic symmetry, each oxygen atom belonging to the second plane would be localized at equidistance of the three Co atoms of the first plane, on the top of a regular pyramid. This position defines the  $c$  distance and the  $\beta$  angle between the surface and the plane formed by  $\vec{b}$ ,  $\vec{c}$ . Since the distance  $b$  is smaller than in cubic bulk structure, the overlap of orbitals between oxygen and cobalt atoms in this plane slightly increases. This is amplified by the reduction of  $c$  distance. To keep an equidistance with all the surrounding Co atoms, the O atom should approach to the last Co atom, localized in the center of the hexagon. It would results into a reduction of the  $c'$  distance and an enhancement of the  $\beta$  angle and induce a decrease of the angle  $\alpha'$  between  $\vec{c}'$  and the plane formed by  $\vec{b}$  and  $\vec{c}$ . We observed that it is not the case. The plane formed by  $\vec{b}$  and  $\vec{c}$  stays perpendicular to  $\vec{c}'$ . This latter instead of reducing enhances from 4.261 Å to 4.273 Å, strengthening the distortion. The octahedron is asymmetric. The results are not easy to interpret. The elongation in the octahedron might be related to the splitting of the  $t_{2g}$  orbitals. Is the tetragonal distortion a consequence of this splitting caused by the instability produced by the mismatch ? Usually it is considered more at the origin of a splitting of the  $t_{2g}$  orbitals by the orthorhombic crystal field. Finally the mechanism driving the out-of-plane distortion is difficult to determine, all the more so as the in-plane distortion in the surface plane comes clearly from the anisotropic epitaxial mismatch.

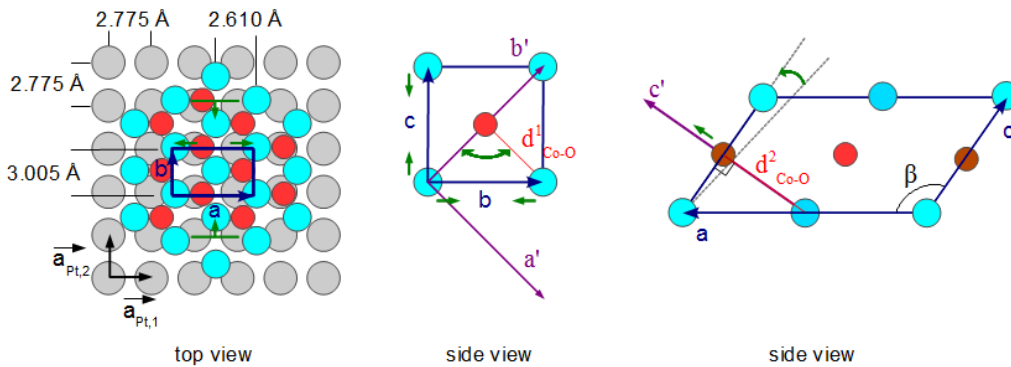


Figure 3.17: Structure of the CoO layer. Green arrows describe the changes compared to a CoO(111) rocksalt structure.

Interestingly, this distortion, obtained at room temperature, is of the same order of magnitude as those observed in the bulk CoO phase at low temperature. All the lattice parameters of the reference cell are reported for both structures in Table 3.4, together with the cell volume and the Co-O first neighbor distances. In the cubic structure, Co atoms (resp. O) are embedded in an regular octahedron formed by its first neighbors O atoms (resp. Co) and drawn in Fig. 3.16.

	CoO film (this work)	CoO bulk values at 10 K (from Jauch <i>et al.</i> [90])
$a' = b'$ (Å)	4.245(2)	4.2682
$c'$ (Å)	4.273(5)	4.2145
$\alpha'$ (deg)	90.00	90.038
$\beta'$ (deg)	90.00	89.962
$\gamma'$ (deg)	89.866	90.018
$c'/a'$	1.007(2)	0.987
$V$ (Å <sup>3</sup> )	77.0(2)	76.77
$d_{Co-O}^1$ (Å)	2.137	2.1073
$d_{Co-O}^2$ (Å)	2.122	2.1341

Table 3.4: Comparison of CoO monoclinic phases in a distorted unit cell.

The monoclinic phase results as a tetragonal distortion plus a much smaller trigonal one to the rocksalt structure. The first striking difference between the bulk and the film phase is the opposite and of the same order  $c'/a'$  ratio, reflecting the tetragonal distortion. As a result, the apical oxygen distance  $d_{Co-O}^1$  in the film is larger than the in-plane distance which deforms the octahedron. The overall film structure is almost tetragonal. However the symmetry is broken by the slight decrease in the in-plane angle  $\gamma'$  in the film, giving the trigonal distortion. In low temperature bulk structure, the apical Co-O interatomic distance  $d_{Co-O}^1$  is shorter than the distance  $d_{Co-O}^2$  to the four in-plane oxygens. The unit cell volume of the film is in between the bulk room temperature rocksalt value ( $77.36 \text{ \AA}^3$ ) and the low temperature one. The main tetragonal distortion in the bulk can be explained within the Jahn-Teller effect. In the film, the structure is measured at room temperature and the driving force at the origin of the monoclinic distortion is the epitaxial stress. To perfectly compare the two structures, the evolution of such a distortion with the temperature has to be investigated. An experiment of surface x-ray diffraction as function of the temperature on this sample is scheduled for the end of October.

### 3.3.4 Impact on FePt layer

The oxidation of Fe at the proximity of an oxide interface is expected owing to the high oxidation potential of Fe [118]. To precisely evaluate the impact of cobalt oxide deposition despite our protection layers, 6 crystal truncation rods were measured at the end of the deposition by rocking scans around HKL nodes along each CTR. The intensity of each (hkl) reflections were integrated after subtraction of the background composed by the thermal diffuse scattering. The amplitudes of the structure factors were then extracted applying the standard corrections (ref section 2.3). The equivalent rods were averaged in the P4mm symmetry giving the (10), (11) and (20) rods presented in Fig. 3.4, with an average agreement factor of 2.5% for 133 non-equivalent reflections. The error bars are calculated from the data dispersion of symmetry equivalent rods. The film structure has been resolved by a model fitted to reproduce the structure factor amplitudes  $|F_{hkl}|$ .

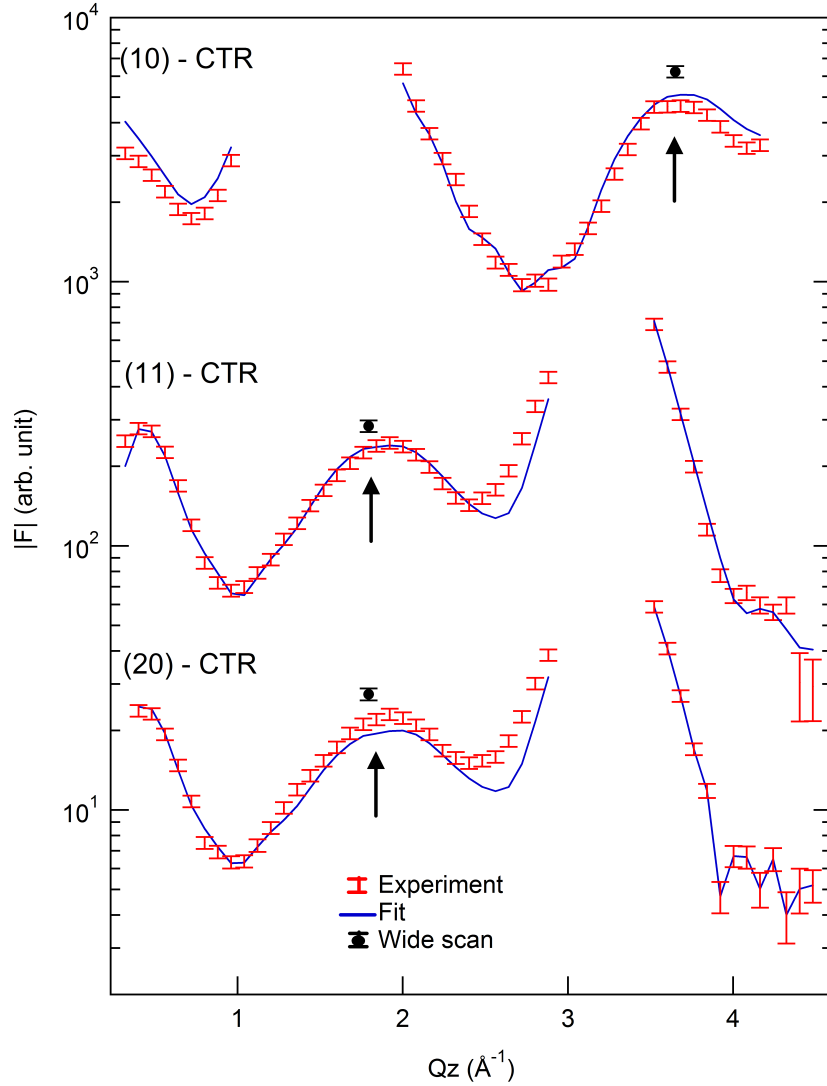


Figure 3.18: Pt rods (CTRs) after iron and cobalt oxide deposition. The experimental data (scattered marks) are associated to errors bars calculated from data dispersion of symmetry equivalent rods. Simulated structure factor amplitudes are in solid lines. The broad peaks associated to the doubling of the electronic density in PtFe are pointed by arrows. Black circles represent structure factor amplitudes extracted from wide angular scans, highlighting an underestimation of the order peaks amplitude.

As for FePt before CoO growth, the model consists of a central part of partially ordered FePt film and its two interface regions. As the data come from rocking scans around reflections regularly spaced on the rod and not from  $l$ - scans, they are more reliable. The film could be here modeled in more detail. For each layer  $n$ , the parameter of the fit are the occupation rates ( $occ_{Fe}$  and  $occ_{Pt}$ ) and interplane distance  $d_{n,n-1}$  to the previous layer. The Pt interface is formed by 2 atomic layers. Layer 1 contains only Pt ( $occ_{Pt}=1$ ). Fe is allowed to diffuse in the layer 2 -topmost layer of the substrate-. The distance  $d_{1,0}$  and  $d_{2,1}$  are free and independent. The layers 3 to 6 correspond to the FePt film. A unique interlayer distance  $d_{film}$  was considered for these 4 layers. Fe and Pt occupation rates were fitted with constraint

of a complete filling on each layer. For the CoO interface region ( $n > 6$ ), the distances of each layer are free and independent. Fe and Pt occupation rates were adjusted independently, with the only constraint of  $occ_{Fe} + occ_{Pt} < 1$ . The structural parameters given by the best fit are summarized in Table 3.5. They correspond to the fitting lines in Fig. 3.18.

layer (n)	region		$d_{n,n-1}$	$occ_{Pt}/occ_{Fe}$	$(occ_{Pt}/occ_{Fe})_{est}$
1			1.97 (1) Å	1/0	
2	Pt interface		1.99 (1) Å	0.7(1)/0.3	
3	FePt film	Fe site	1.804(5) Å	0.10(5)/0.9	0.1/0.9
4		Pt site		0.7(1)/0.3	0.8/0.2
5		Fe site		0.2(1)/0.8	0.1/0.9
6		Pt site		0.7(1)/0.3	0.8/0.2
7			1.93(2) Å	0.5(1)/0	
8	CoO interface		1.80(4) Å	0.4(1)/0	
9			1.97(2) Å	0.15(5)/0	

Table 3.5: Fitting results of a 4 ML FePt film and its interfaces after cobalt oxide deposition. Occupation rates ( $occ_{Fe}$  and  $occ_{Pt}$ ) and interplane distance  $d_{n,n-1}$  to the previous layer are described for each layer. In a second step, Fe and Pt occupancies were adjusted to reach a better estimation of the film order, giving the values of the last column.

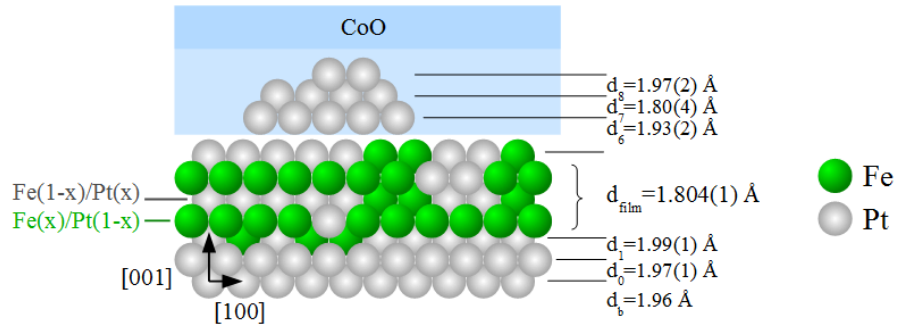


Figure 3.19: Side view of FePt model at the end of the sample growth. The colors are representative of Fe and Pt occupation rates.

The lattice parameter  $c = 2d_{film} = 3.60(1)$  Å is compressed by 3.0% with respect to the FePt bulk and slightly expanded compared to the previous FePt model. It perfectly compensates the substrate induced in-plane strain allowing the unit cell volume to get back to its ordered stoichiometric alloy value. The tetragonal distortion of this pseudomorphic layer  $c/a = 0.917(3)$  is still enhanced compared to the bulk value  $(c/a)_{bulk} = 0.962$  and gets closer to a value previously measured on a 2.0 nm thick FePt film grown by alternate deposition on Pt(001).[126]

The Debye Waller factor (DW) was considered uniform along the film and was fitted to 0.96. This value is far from the bulk values for Fe and Pt (resp. 0.39 and 0.31) and so from the model before deposition. It indicates that the structural disorder dominates. The order parameter  $S$  for the central part of the film ( $n = 3$  to 6) is on average  $S = 0.5(1)$ , smaller than

for FePt alone (cf section 3.1.2). CoO deposition has perturbed the film. This perturbation is explicit in Fig. 3.20 that shows rocking scans around the order peak at (1 0 2.2).

After 1 ML of Pt and 2 ML of Co deposition, the reflection has grown in intensity and presents a larger baseline. Two reasons could explain the enhancement of the order peak. First, we complete the last layer of Pt of the film. So the film is thicker. Secondly, Co grows pseudomorph on FePt. It probably creates a CoPt alloy with almost the same out-of-plane parameter as FePt. Its contribution adds up with those of FePt. These additional layers form an ordered phase with smaller domain size. The intensity coming from small ordered domains is scattered over a larger angular range. Here they wide the baseline of the order peak which is not anymore fully integrated by a conventional rocking scan. After the reactive Co deposition, a wide angular scan was performed to recover the large part. The final shape could be fitted with two lorentzian distributions. Sharp and large components have a different evolution. The large part coming from the small ordered domains has apparently not decreased during this step. In opposite, the sharp component has decreased more than before Co deposition, indicating that Co layers are completely oxidized and that a part of FePt is affected by the reactive deposition. Probably some oxide nucleate in the FePt layer reducing the lateral size of  $L1_0$  domains.

In first conclusion, one can say that FePt film was slightly laterally disordered and partially oxidized during CoO deposition.

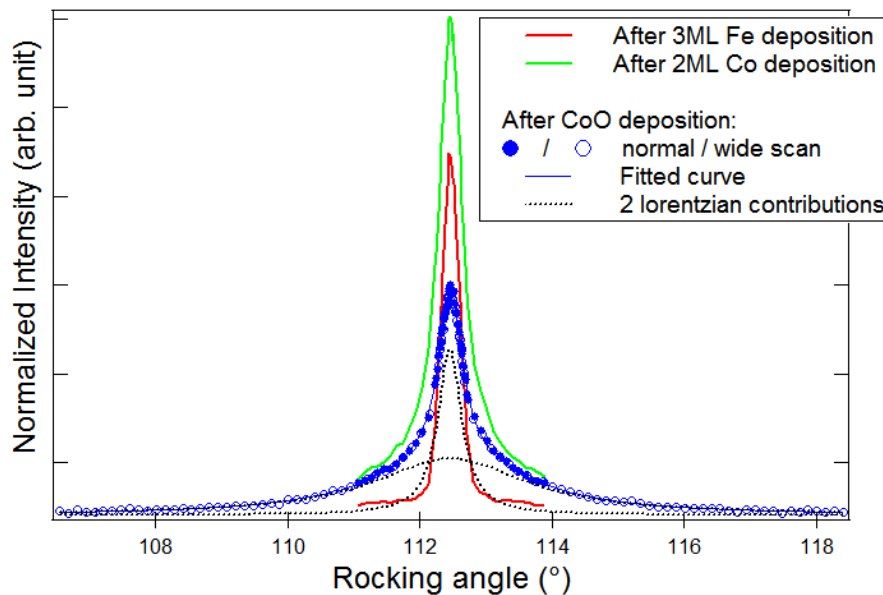


Figure 3.20: Rocking scans around the Fe order peak at (1 0 2.2). Peak increases with Co deposition and presents a larger baseline. After Co deposition under oxygen, peak decreases whereas baseline is kept constant. A wide angular scan allows to recover the large part. Final shape was fitted with two lorentzian contributions.

Actually the value of the order parameter  $S$  is based up to now only on the sharp component, and so is largely underestimated. Scattered intensity over the wide angular scans performed at the maximum of the order peaks was integrated and corrected resulting to the

structure factors reported in Fig. 3.18. Pt and Fe occupations for layers 3 to 6 have been adjusted to match the new structure factors, all other structural parameters being unchanged. The fit results in new Fe and Pt occupancies written in the last column of Table 3.5. The order parameter calculated from these values is  $S = 0.7(1)$ . Thus the order could be considered kept constant after CoO growth even if the layer has smaller in-plane domains.

Concerning the oxide interface, the model has its limitations, essentially for two reasons. First only ordered layers with enough correlation length contribute to the coherent scattering signal under thermal scattering background. Secondly a full layer of Fe-Pt is hard to differentiate from a partial layer of lonely Pt, which has an higher atomic scattering factor. Moreover Co and Fe cannot be distinguished due to their similar atomic scattering amplitudes. A part of Fe atoms could be spread in the CoO film. However the SXRD data are satisfactorily described as Pt islands embedded in the oxide layer, suggested by the large interplan distance of these layers. Coexistence of pseudomorphic Pt islands and relaxed CoO has been already reported in literature[121]. A mixture of metallic iron covered by Pt, relaxed or disordered Co and Fe oxide domains, and Pt islands could be expected at such interface. Anomalous SXRD could help to discriminate Co and Fe atoms and help to interpret these data.

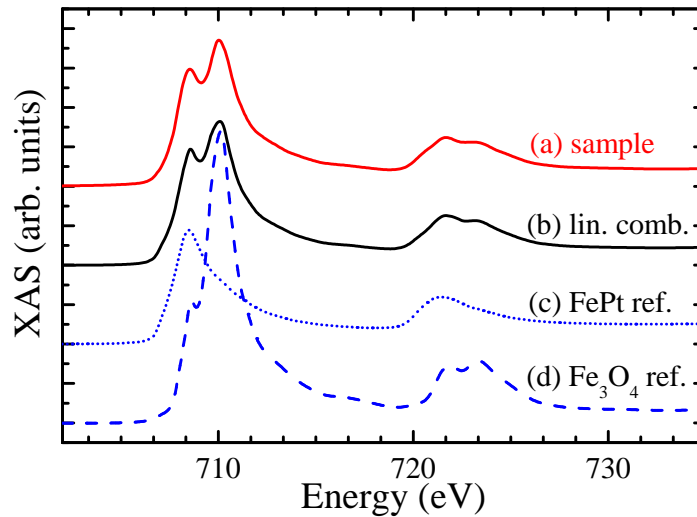


Figure 3.21: Comparison of sample XAS (a) with linear combination (b) of two reference spectra: metallic FePt (c) and  $Fe_3O_4/CoO$  (d). The linear combination spectrum is obtained with the following coefficients:  $\mu_{lin.comb} = 0.65\mu_{FePt} + 0.35\mu_{Fe_3O_4}$ .

The total Fe content summed over the metallic alloy film ( $n=1$  to  $6$ ) is 2.6 ML smaller than the nominal 3 ML value highlighting a partial oxidation of Fe. The extent of Fe oxidation is estimated by comparing the XAS spectrum of the CoO/FePt/Pt(001) sample with those of the metallic FePt and Fe oxide (Fig. 3.21). An *ex-situ* prepared  $Fe_3O_4(2\text{ nm})/CoO(4\text{ nm})$  bilayer was used as Fe oxide reference. Figure 3.21 shows a linear combination (black full line) of the two reference spectra with a factor 0.35 for the Fe oxide (dash) and 0.65 for the pure metallic Fe (dot). It gives very good agreement over the entire spectrum, including the peak ratio in the  $L_2$  edge. This corresponds approximately to 1/3 of Fe in oxide environment.



Although the majority of them are  $Fe^{2+}$  in octahedral site, we can't really consider Fe spinel when Fe is in sub-monolayer regime.

Reactive CoO deposition on pure Fe oxidizes at least about 2 ML of Fe at 340 K.[45] Our Pt-terminated high-quality FePt(001) layer shows a smaller oxide contribution, corresponding to only 1 Fe ML even if the deposition was performed at 520 K. This oxide contribution is likely related to the Fe atoms dispersed within the CoO layer or from Fe-O bounds at the interface and shows the good resistance to corrosion of FePt.

## Conclusion

We reported in this chapter the growth and structure of ultrathin CoO/FePt layers on a metal Pt(001) substrate. The syntheses were followed *in situ* and *real time* by SXRD and special care has been taken in a deep structural analysis.

We have grown a 3 BL- FePt film by thermal deposition of Fe on a substrate held at 570 K - 600 K. The ferromagnetic layer grows in coherent epitaxy with the substrate in  $L1_0$  phase, with  $c$  direction out-of-plane. A large chemical order structures the film suggesting a strong perpendicular magnetic anisotropy despite its thinness.

The novel epitaxial growth of antiferromagnetic CoO on a metal Pt(001) substrate was studied first qualitatively. We found that thermally assisted deposition allows to achieve better ordered layers. The structure of ultrathin layer of CoO is identical on the Pt(001) and on PtFe/Pt(001) substrates. It shows an in plane hexagonal pattern corresponding to CoO(111) planes. The slight distortion of this hexagonal pattern is associated to a tetragonal distortion of the cubic unit cell and so to the octahedron formed by the first neighbors around Co atoms ( $c/a = 1.007$ ). A detailed analysis revealed an additional out-of-plane component of distortion. The structure is monoclinic like its bulk low temperature phase. However, the growth of such a phase is driven by the epitaxial stress and the monoclinic strain tensor is different from the bulk one. In particular, the tetrahedral contribution results in a  $c/a > 1$ , at the opposite of the bulk phase. Both the presence and the strain tensor elements of this monoclinic phase suggest that epitaxy can be exploited to tune both the onset of the magnetic transition and the magnetic moment orientation in ultrathin films.

After CoO growth, the in-plane domain size has decreased in FePt layer, but the order remains constant. The proportion of FePt oxidized has been evaluated by comparing the XAS spectrum with references. Approximately 1 ML of Fe is in oxide environment, which shows the good resistance to corrosion of FePt. Both layers of this CoO/FePt system show a large structural anisotropy that we determined with precision. In the light of the structure properties, the magnetic properties of this bilayer are very promising.

## Chapter 4

# Magnetism of exchange coupled CoO(111)/FePt

### Contents

---

<b>4.1 FePt magnetic properties</b> . . . . .	<b>76</b>
<b>4.2 CoO magnetic properties</b> . . . . .	<b>80</b>
4.2.1 Considerations from structural anisotropy . . . . .	80
4.2.2 XLD angular dependance . . . . .	82
4.2.3 XLD features . . . . .	84
4.2.4 XLD temperature dependance . . . . .	86
<b>4.3 Exchange coupling</b> . . . . .	<b>87</b>
<b>4.4 CoO magnetic anisotropy</b> . . . . .	<b>90</b>
4.4.1 Strength . . . . .	90
4.4.2 Structural anisotropy . . . . .	93

---

A direct measurement of the magnetic properties of ultra-thin antiferromagnetic layers is quite challenging. Néel temperature and spin configuration are routinely measured on bulk crystal thanks to neutron diffraction, in which the magnetic contribution is relatively large compared to the electronic one. However due to the neutron flux available on actual experimental set-up, it is not possible to perform such experiments on ultrathin films. In contrary, magnetic contribution is relatively small compared to electronic one in x-ray diffraction. Therefore, the cross section of magnetic scattering by neutrons is strongly higher by neutrons than by x-ray.[129] M. Blume calculated a ratio in  $10^{-4}$  range.[130] Using high flux 3rd generation x-ray beamline and resonance effect at an absorption edge, it becomes however possible to measure x-ray magnetic diffraction on ultra-thin films.

We performed such measurements on ID03 at ESRF. Following Tomiyasu and coworkers's experiment,[96] we looked for the pure magnetic  $(\frac{3}{2} \frac{3}{2} \frac{3}{2})$  reflection at low temperature,

which results from the antiferromagnetic order along the [111] direction. Photon energies were chosen below the Co K edge (7.709 keV) and close to it to have contribution from both resonant and non resonant magnetic scattering. Unfortunately we could not detect any magnetic peak. Beside the thickness of the film, the peak intensity is weakened by the small domain size parallel to the surface and by the probably even smaller size of the magnetic domains, which spread the magnetic diffraction intensity in the reciprocal space. Magnetic peaks cannot then be distinguished from the background.

In the chapter that follows we will inquire *ex situ* the magnetic properties of CoO/FePt bilayer on Pt(001), using both soft x-ray absorption spectroscopies through linear and circular magnetic dichroism (XMCD and XMLD) at Fe and Co  $L_{2,3}$  edges, and experiments based on magneto-optic Kerr effect (MOKE). XMLD gives a direct measurement of the magnetic properties of the AFM film itself, while MOKE allows to deduce the magnetic ordering of the CoO thanks to the exchange bias with the ferromagnetic film.

## 4.1 FePt magnetic properties

Bulk FePt alloy in the chemically-ordered  $L1_0$  phase exhibits one of the strongest magnetic anisotropy (see section 1.2.4). Since ferromagnetism is a collective phenomenon, one could expect a magnetization decrease and possibly vanishing when the thickness is reduced, leading to lower Curie temperature ( $T_C$ ) in thin films. Imada and coworkers reveal that FePt perpendicular magnetic anisotropy (PMA) persists down to the thinnest limit. A Fe ML sandwiched by Pt(001) has a remanent magnetization until 160 K[86]. These authors report that  $T_C$  is above RT for only two FePt BLs under 1.4 T and at remanence for 3 BLs. Their layers were fabricated by alternate deposition at 500 K. They estimated the order parameter at  $S=0.6(1)$  for the 10-BLs film and assumed it would be similar for thinner layers.

Initially FePt film of our sample was made of 3 chemically ordered BLs ( $S=0.64$ , cf previous chapter). Referring to the study just cited it might keep a perpendicular remanent magnetization close to RT. However CoO growth impacts the FePt layer, oxidizing a part of the film evaluated at almost one ML according to x-ray absorption spectra analysis. Only the central part of the film was considered as chemically ordered  $L1_0$  phase. These 2 BLs have a general order parameter  $S=0.5(1)$  even  $0.7(1)$  considering domains with small structural correlation length. Fe spin orientation and ferromagnetic order were determined by XAS and XMCD measurements performed at experimental conditions described in the section 2.5.

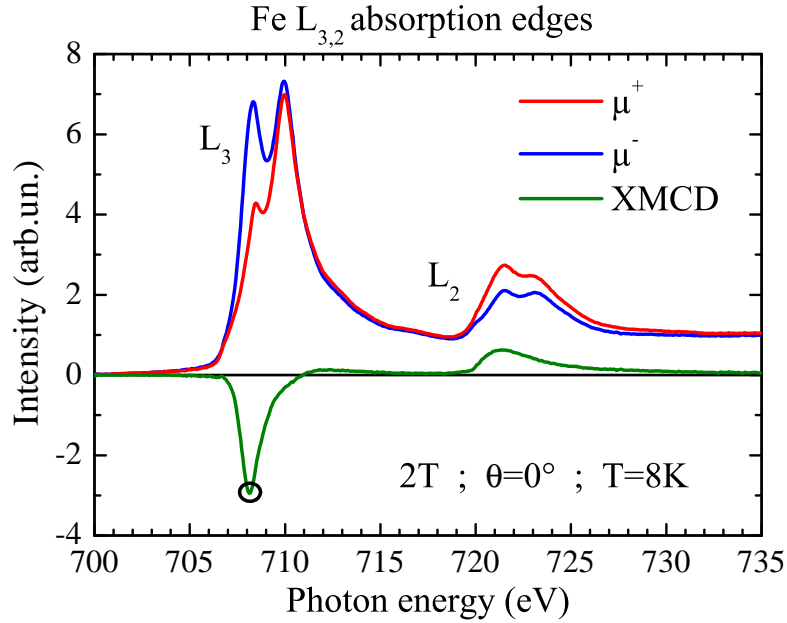


Figure 4.1: Fe XAS spectra ( $\mu^+$  and  $\mu^-$ ) at Fe  $L_{3,2}$  absorption edges collected in TEY mode by flipping the circularly polarized light at an applied magnetic field of +20 kOe (2T) and at 8 K. The difference of the two XAS spectra gives the XMCD signature.

Figure 4.1 shows two XAS spectra collected in mode with incident light circularly polarized right or left ( $\mu^+$  and  $\mu^-$ ), with the sample surface aligned normal to the beam ( $\theta=0^\circ$ ) in the photon energy range of Fe  $L_{2,3}$  absorption edges (700-735 eV). X-ray magnetic circular dichroism (XMCD) spectrum also presented in Fig. 4.1 is calculated as the difference  $\Delta\mu$  of the two normalized (to 1 far from the edge) spectra. The sample was set to 5 K after a field cooling from 350 K down to 5 K under +5 kOe applied field. Fe  $L_{2,3}$  XMCD signal is very large. At 5 K under 2 kOe, the maximum of XMCD signal corresponds to about 40% of the maximum of the average spectra at the  $L_3$  edge ( $\frac{(\Delta\mu)_{max}}{\mu_{max}} = \frac{(\mu^+ - \mu^-)_{max}}{((\mu^+ + \mu^-)/2)_{max}} \simeq 0.4$ ). XMCD shape is characteristic of metallic  $L1_0$  FePt and is not notably affected by the small Fe oxide content [131]. No trace of ferromagnetic contribution from Fe oxide has been detected in XMCD spectra whatever the incident angle or the temperature.

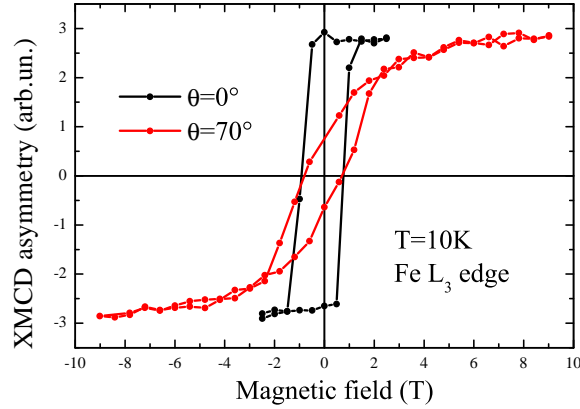


Figure 4.2: Fe hysteresis loop at 10 K from XMCD spectrum with the beam perpendicular ( $\theta = 0^\circ$ ) and almost parallel ( $\theta = 70^\circ$ ) to the surface sample.

Fe hysteresis loop is drawn by reporting the maximum amplitude of the XMCD (highlighted by a circle in Fig. 4.1) for each value of the applied perpendicular magnetic field and is shown in Fig. 4.2. At low temperature, the loop is shifted towards negative values and yields a magnetization at zero field (remanence) close to the saturation magnetization. Such 100% remanence indicates the PMA character of the FePt layer. It has been confirmed by a hysteresis loop measured at  $\theta = 70^\circ$  and presented in the same figure. XAS spectrum can not be measured at higher angle, where incident beam reaches the side of the sample perturbing the measurement. The small hysteresis loop appearing at  $\theta = 70^\circ$  is reminiscent of the out-of-plane component. From this curve, we can deduce that about 6 T are required at 10 K to completely rotate Fe spins to the surface plane, demonstrating the strength of the perpendicular anisotropy of FePt layer.

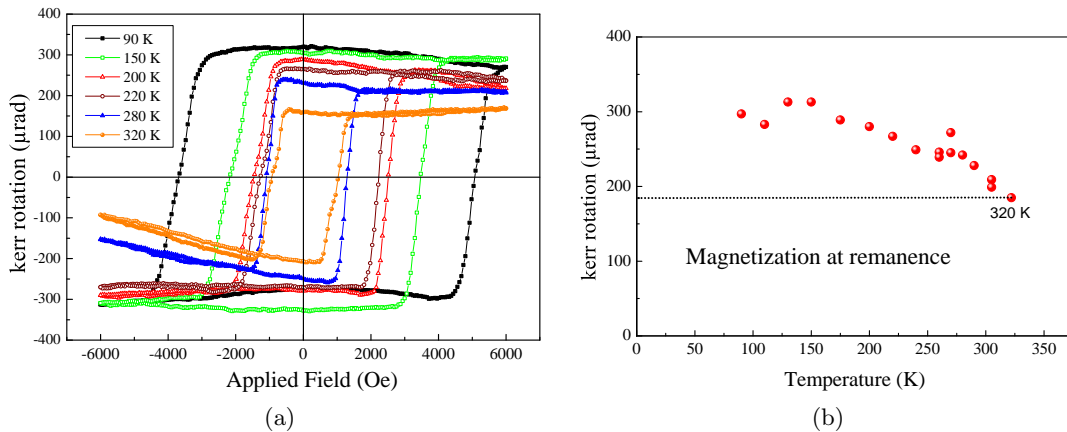


Figure 4.3: Polar MOKE measurements of the CoO/FePt double-layer at different temperatures after a field cooling at -3500 Oe: Hysteresis loops (a) and remanent magnetization deduced (b).

Hysteresis loops reported in Fig. 4.3 come from MOKE experiments in polar configuration (with an incidence angle of  $69^\circ$  to the sample normal) performed in Halle<sup>1</sup> after a field cooling of the sample from 320 K down to 5 K at an applied field of - 3500 Oe perpendicular to the surface. Fluctuations in the absolute Kerr rotation at saturation are due to instabilities in optical alignment. The loops are shifted towards the positive values, in opposite to the direction of the field applied during the cooling. The loops from MOKE and XMCD at Fe  $L_3$  edge show then similar features and behavior with temperature. It indicates that the ferromagnetism of the system comes essentially from the Fe atoms in metallic environment.

It was shown by Imada *et al.*[86] that PMA in FePt films remains until RT for 3BLs at minimum. Here we observe the decreasing of remanent magnetization with temperature, but the slope of the loops are still sharp at 320 K (see Fig. 4.3). PMA in the layer is hence maintained. The Curie temperature stays above 320 K, higher than the finding of Imada for 2 BL. Either FePt thickness is in-between 2 and 3 BLs, or our layer has a better structural order. Imada's assumption about the value of S in thin layers is indeed strong. As seen in section 1.2.4, the chemical order is considered as essential for the magnetic anisotropy energy in FePt alloy. Another explanation based on the work of Antoniak and collaborators could be raised.[84] These authors are interested in a detailed understanding of the magnetism of FePt nanoparticles in the idea to design it. They conclude that three rules are compulsory to obtain the desired magnetic properties, drawing three key parameters. One of them underlines the importance of the capping layer, which introduces structural modifications and changes in the electronic environment. Although Co spins are not organized at this temperature ( $T > T_N(\text{CoO, bulk})$ ), their presence could have an impact on the FePt electronic environment.

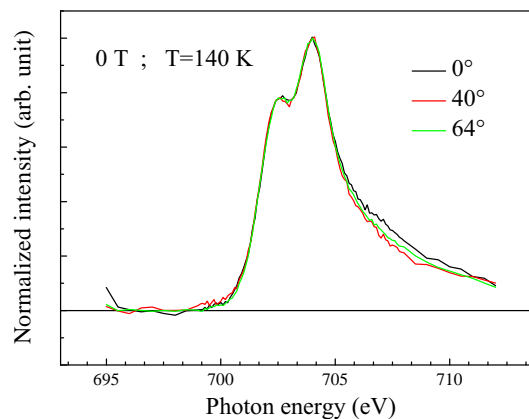


Figure 4.4: XAS spectra at Fe  $L_3$  absorption edge with linearly polarized light and different incident angles at remanence at 140 K.

To conclude the study of Fe magnetic properties, we looked for an antiferromagnetic component coming from Fe oxides. XAS spectra with linear polarization have been measured as function of the incident angle in the photon energy range of the Fe  $L_3$  absorption. The difference of two XAS spectra with linear polarization giving the XMLD signal is sensitive to

<sup>1</sup>Max Planck Institute in Germany, in collaboration with M. Przybylski

charge anisotropy. This latter concerns the more localized charges of the oxide, where orbitals shape is more dependent on both the local crystal field and the local exchange field through the spin-orbit coupling. Even if metals, with delocalized electrons, can show anisotropic effects in the local environment, generally oxides (insulators) give larger effects because they are more sensitive to final state (core-hole coulomb interaction) and multiplet effects. All spectra collected look similar. Three of them are presented in Fig. 4.4. The difference between them is within the noise. We can conclude that no anisotropy of charges in Fe oxide orbitals is detected.

## 4.2 CoO magnetic properties

CoO thickness was chosen around 4 nm, close to the onset thickness for frozen spins, according to J. Wu and coworkers.[132] These authors determine the amount of rotatable and frozen CoO spins as a function of the CoO film thickness by XMLD measurements. They characterize the  $L_3$  ratio ( $R_{L3}$ ), defined as the ratio of the XAS intensity at 778.1 and 778.9 eV and used to quantify the XMLD effect[117] in Co spins as a function of polarization angle in two situations. First, right after the field cooling, to determine the total amount of AFM compensated spins. Then, after rotating the applied field by  $90^\circ$ , to observe spins orientation changes. If no Co spin is rotatable, curves are identical. If all Co spins are rotatable, curves are inverse. They establish that the CoO spins are rotatable below 2.2 nm CoO thickness, become partially frozen between 2.2 nm and 4.5 nm and totally frozen above 4.5 nm.

4 nm of CoO ensures a FePt layer protection from external contamination despite the important surface roughness keeping a CoO thickness in a partially frozen spin regime .

### 4.2.1 Considerations from structural anisotropy

In a rocksalt CoO crystal, cobalt ions are high spin  $Co^{2+}$  with 7 electrons in  $3d$  level. In octahedral symmetry,  $d$ -level split into a threefold degenerate  $t_{2g}$  ( $d_{xy}$ ,  $d_{xz}$ ,  $d_{yz}$ ) and a twofold degenerate  $e_g$  ( $d_{3z^2-r^2}$ ,  $d_{x^2-y^2}$ ) orbitals by ligand field (or crystal field). The 7 electrons fill each state at least once. In the independent electron picture, there is one hole in the  $t_{2g}$  level and two in the  $e_g$  level (cf section 1.2.5). The degeneracy can be lifted by the  $3d$  spin-orbit coupling, lower symmetry ligand field and exchange field. This latter is mainly responsible for the temperature dependance of the levels in magnetic materials.

In the low-temperature bulk CoO, the monoclinic distortion is essentially driven by the Jahn-Teller effect due to the partial filling of the  $Co^{2+}$   $t_{2g}$  orbitals.[92] It can be seen as the result of a main tetragonal plus a small trigonal distortion. The monoclinic distortion breaks the cubic symmetry along the [111] axis, setting what was the (111) plane apart. The moments are coupled ferromagnetically within this plane. Since the magnetic dipole-dipole interaction is minimized when the ferromagnetic spins have the same direction, it tends to align Co spins in the (111) plane. The crystal field energy, arising from the compressive ( $c'/a' < 1$ ) tetragonal deformation, favors rather the [001] direction.[97] As a consequence, the CoO

spin structure is collinear with the spin axis, making a small angle with the [001] direction of the rocksalt lattice [97, 90] (cf section 1.2.5).

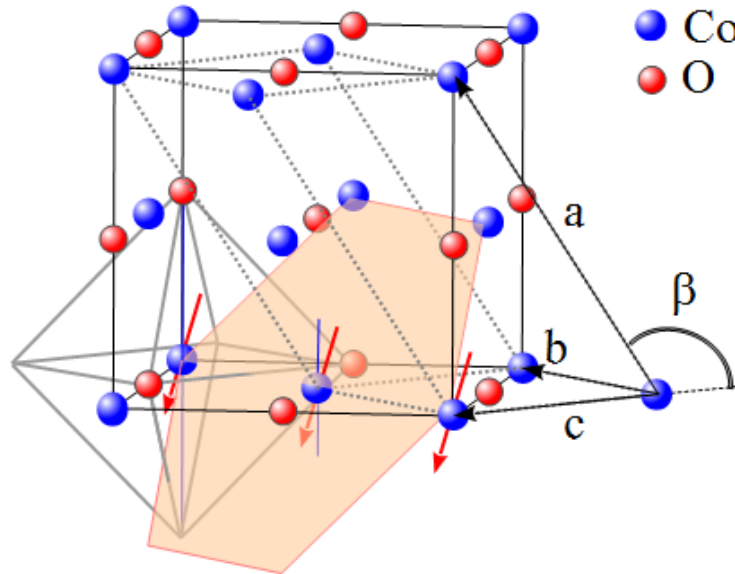


Figure 4.5: Bulk CoO structure showing the Co(111) FM plane (in orange) coupled antiferromagnetically along the [111] direction. A  $CoO_6$  octahedron is shown. The [001] direction is highlighted in blue.

In epitaxial thin films the strain drives the anisotropy. Csiszar and coworkers[98] have demonstrated the relationship between the orientation of the magnetic moments and the sign of the crystal field effect. They have shown that an ultrathin CoO layer sandwiched by MnO layers on Ag(001) shows an out-of-plane magnetization axis along [001], while in direct epitaxy the Ag(001) substrate shows an in-plane magnetization axis orthogonal to the [001] direction. The main structural difference between the two cases lies in the CoO(001) epitaxial strain, which is tensile on MnO(001) and slightly compressive on Ag(001), generating respectively a compressive ( $c'/a' < 1$ ) and a slightly extensive ( $c'/a' > 1$ ) tetragonal deformation.

The slightly anisotropic strain imposed by the PtFe/Pt(001) surface on the CoO layer leads to a monoclinic distorted lattice that resembles the CoO bulk lattice at low temperatures. However, while the tetragonal deformation is compressive in the bulk ( $c'/a' = 0.988$ ), it is extensive in the film ( $c'/a' = 1.007$ ) (cf. section 3.3.3). In this particular situation, the crystal field favors the  $t_{2g}$  hole to occupy the  $d_{xy}$  orbital. The spins are then aligned in the plane containing  $\vec{b}$  and  $\vec{c}$  (hatched plane in Fig. 4.6).

Our CoO layer has a strain induced monoclinic distortion that reminds the one of bulk at low temperature. We can then assume that the FM plane in our film has the same relation with the distortion, i.e. consider that the FM plane is the (111) plane. The dipole-dipole magnetic energy is minimized when the AFM Co spins are within the (111) FM plane (full blue planes).[24] Only one direction is at the crossing of the two planes: the  $\vec{b}$  direction ( [1 $\bar{1}$ 0]



direction in the rocksalt lattice). Such AFM configuration resembles the model predicted by DFT calculations for a single CoO overlayer on Ir(001).[133]

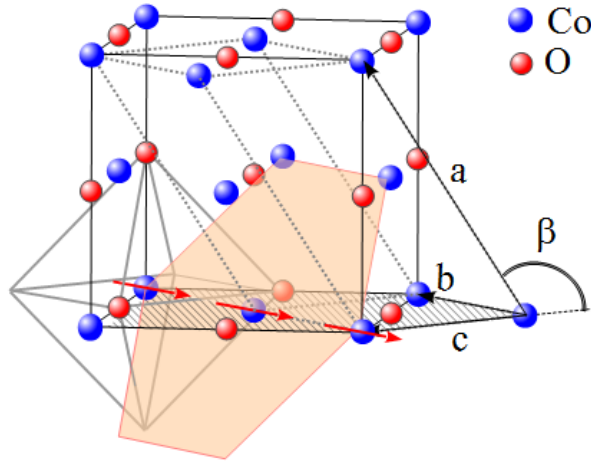


Figure 4.6: Illustration of CoO spins orientation as a compromise of two interactions:  $t_{2g}$  orbitals might be lifted due to the tetragonal distortion getting the lowest level unpaired electron lying in the  $d_{xy}$  orbitals, i.e. in the hatched plane. Magnetic dipole-dipole interaction tends to align spins in the (111) plane (full orange plane). The direction of the spins is at the intersection of these two planes, along the **b** direction.

#### 4.2.2 XLD angular dependance

As for the Fe XMCD measurements, the sample was cooled down with an applied magnetic field of 5 kOe perpendicular to the surface plane. All XAS spectra presented in this section were collected at remanence, i.e. with the magnetic field set to zero. The sample was allowed to rotate about a vertical axis, with the polar angle  $\theta$  defined as the angle between the surface normal and the x-ray propagation (inset in Fig. 4.7a). In this experimental geometry, the variation of the escape length of the electrons as a function of  $\theta$  should be corrected in order to recover the real x-ray absorption signal. This has been systemically corrected using the standard procedure for electron yield saturation effects. To check this correction, the x-ray absorption spectrum collected with vertical polarization was used as a reference for each  $\theta$ . Vertical polarization is in the surface plane whatever the  $\theta$  angle. Hence associated XAS spectrum is insensitive to  $\theta$ . At each angle, the x-ray linear dichroism (XLD) is obtained by two ways: (1) from the difference between the absorption with the horizontal and vertical x-ray polarizations and (2) with the horizontal x-ray polarization, from the difference between the absorption at  $\theta$  and at  $\theta = 0^\circ$ . The two methods give the same signals, within the accuracy of the measurements.

Figure 4.7a shows the Co  $L_3$  edge XAS spectra at 10 K for four  $\theta$  values from the polarization vector in the surface ( $\theta=0^\circ$ ) towards the surface normal ( $\theta=70^\circ$ ). The spectra, normalized far from the  $L_{2,3}$  edges, show a clear linear dichroism. Four main features (labeled from A to D) are observed in the XAS and XLD signals. They correspond to the transitions

towards orbitals of different symmetries and then show distinct variations as a function of  $\theta$  (Figure 4.7, inset). Taking the  $\theta=0^\circ$  spectrum as reference, the feature D at higher energy is almost constant, feature B increases with  $\theta$ , while A and C decrease.

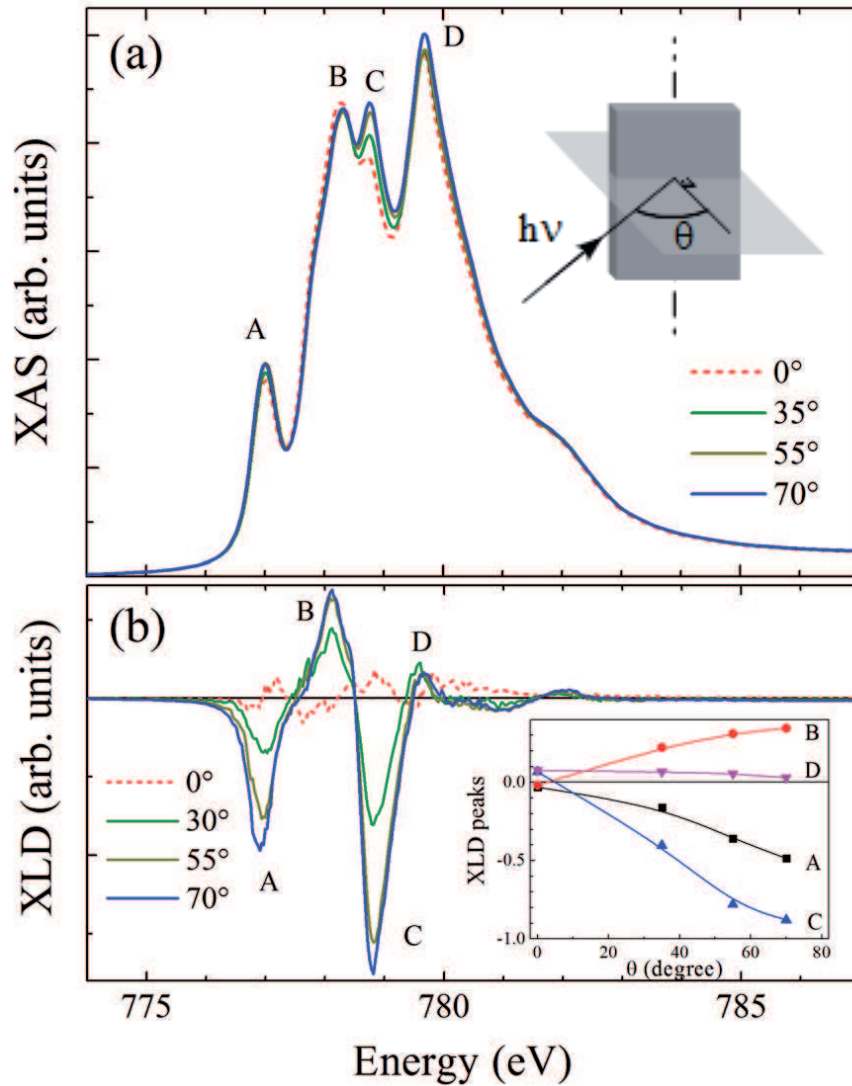


Figure 4.7: (a) Co  $L_3$  edge XAS as function of  $\theta$  after field cooling in a +5kOe magnetic field. Inset: experimental geometry. (b) XLD as function of  $\theta$ . XLD is the difference between the absorption at  $\theta$  and at  $\theta = 0^\circ$ . Inset: angular variation of the intensity of the four main XMLD features.

Following Wu and coworkers we used the  $\theta$  dependence of the intensity ratio  $R_{L3}$  between the peaks at C (778.74 eV) and B (778.26 eV) as a measure of the overall anisotropy. The XLD signal essentially measures the charge anisotropy associated with both the local crystal field and the local exchange field through the spin-orbit coupling. Relatively to the magnetic axis, the anisotropy due to local exchange fields and spin-orbit coupling is given by:[21]

$$I_{XMLD} \propto |\vec{m} \cdot \vec{E}|^2 \quad (4.1)$$

with  $\vec{E}$  the electric field polarization and  $\vec{m}$  the magnetic axis. A  $\cos^2\theta$  dependence is then expected for the magnetism-sensitive transitions. The intensity ratio  $R_{L_3}$  fits well with a  $\cos^2\theta$  function, with a minimum at  $\theta = 0^\circ$ . From multiplet calculations it has been demonstrated that the situation when the polarization vector is perpendicular to the magnetic axis ( $\vec{m} \perp \vec{E}$ ) corresponds to the  $R_{L_3}$  maximum.[117] This is obtained for  $\theta = 90^\circ$ , within an accuracy of a few degrees. We can then conclude that the Co spins are essentially parallel to the surface plane. This is in the line with the result deduced in the previous section, that indicated that the Co spins are along the  $\vec{b}$  axis. As the FePt spin axis is perpendicular to the layer, the coupling between Co and Fe spins at the interface is orthogonal.

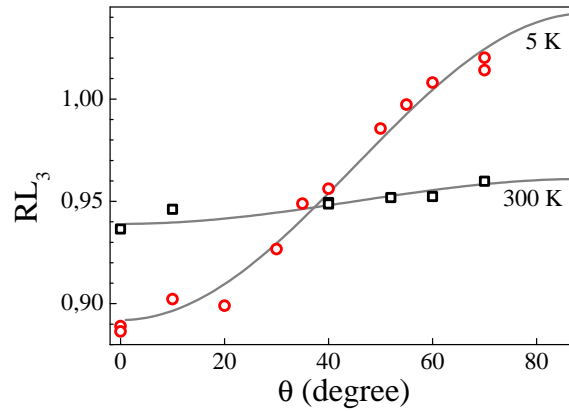


Figure 4.8: Angular dependence of intensity ratio  $R_{L_3}$  defined by the C over B peak contrast and characterizing Co anisotropy. Experimental results at 5 K (red circles) and at 300 K (black squares) are fitted with a  $\cos^2\theta$  function (grey lines).

### 4.2.3 XLD features

Atomic multiplet calculations performed by van der Laan and coworkers[117] show that quite different features could be obtained for XAS and XLD spectra with same relative orientation of  $\vec{E}$  and  $\vec{m}$  but different Co magnetization axis with respect to the crystalline axis. The relative variations of  $L_3$  and  $L_2$  features and from those of  $L_3$  A and C peaks can differentiate for example when the spin axis  $\vec{m}$  is along the  $\langle 110 \rangle$  or along the  $\langle 100 \rangle$  direction (cf Fig. 4.10). In the first case, A and C features (at 777.0 eV and 778.74 eV, respectively) have the same variation with  $\theta$ .

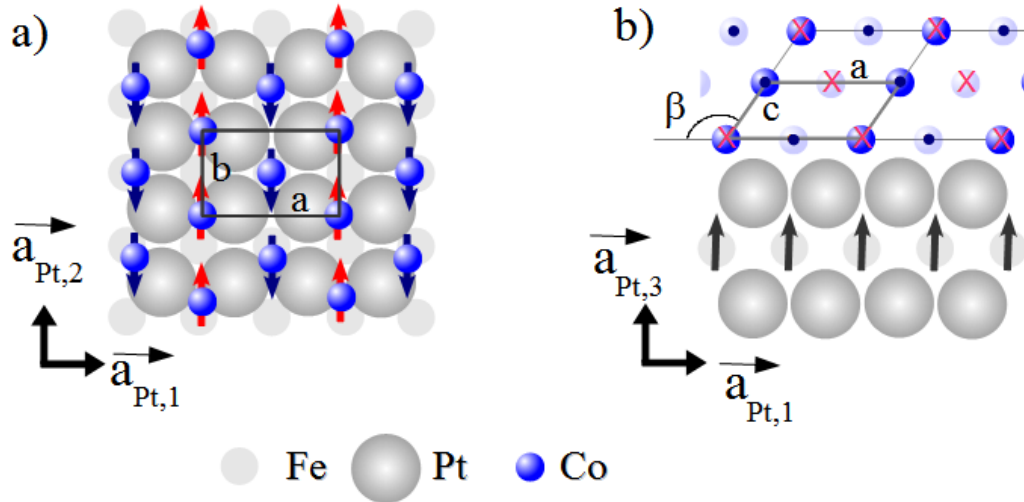


Figure 4.9: Illustration of the magnetic structure of the sample S8 composed of CoO layer on PtFe/Pt(001). Spin orientation and relation between the CoO monoclinic ( $a$ ,  $b$ ,  $c$ ,  $\beta$ ) and Pt ( $a_{Pt}$ ) parameters. (a) Top view: Co AFM spin structure projected onto the surface, with spin axis along the Pt  $[1\bar{1}0]$  direction. (b) Side view: Fe spins are perpendicular to the surface and the projected Co AFM spins point forward ( $\bullet$ ) or backward ( $\times$ ).

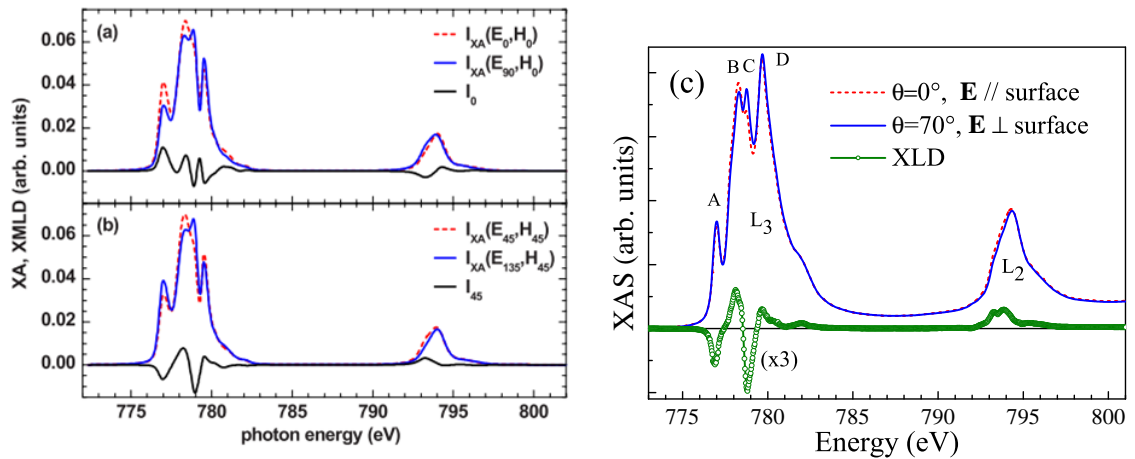


Figure 4.10: Comparison of calculated (a and b) and experimental (c) Co  $L_{3,2}$  XAS spectra. Calculated spectra are taken from ref. [117]. A detailed description can be found in the text.

In Fig. 4.10a and b are presented the XAS spectra calculated in octahedral crystal field from van der Laan and collaborators with two different orientations of magnetic moment relatively to the crystallographic axes.[117] In Fig. 4.10a, the magnetic moment  $\vec{m}$  is along the  $\langle 100 \rangle$ , while the electric field  $\vec{E}$  of the x-ray beam is parallel (dashed red line) or perpendicular (solid blue line) to the magnetic moment. The difference of the two spectra gives  $I_0$  (solid black line). The rotation of  $\vec{E}$  can be in any plane-of-orientation containing  $[100]$ . In Fig. 4.10b, the magnetic moment  $\vec{m}$  is along the  $\langle 110 \rangle$ , with  $\vec{E}$  parallel (dashed red line) or perpendicular (solid blue line). The difference of the two spectra gives  $I_{45}$  (solid black

line). The rotation of E is here in the (001) plane. The experimental Co  $L_{3,2}$  XAS spectra (Fig. 4.10c) were obtained at 5 K after cooling in a + 5kOe magnetic field with linear polarization parallel to the surface plane (red dashed line) and towards the surface normal (blue solid line). The XLD (green dot line) is the difference between them.

The experimental XLD signal in Fig. 4.10c matches perfectly the calculated one in Fig. 4.10b. A and C peaks vary also in the same way. We deduce that Co spins are along a  $\langle 110 \rangle$  direction of the CoO bulk structure. It points in the direction of the first Co atom neighbour. The [001] axis mentioned by van der Laan *et al* is not perpendicular to the surface in our CoO layer, but tilted by  $\varphi=54.74^\circ$  in relation to the normal surface. Six axes belongs to the  $\langle 110 \rangle$  directions (cf Fig. 4.11). Half of them are in the plane of our layer ( $[\bar{1}\bar{1}0]$ ,  $[10\bar{1}]$  and  $[01\bar{1}]$  directions).  $\vec{b}$  axis is amongst them. It confirms our previous statement. Co spins are along  $\vec{b}$  axis.

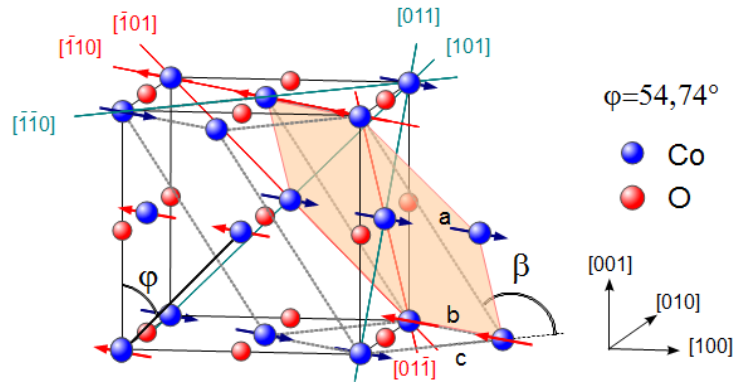


Figure 4.11: CoO rocksalt ( $[100]$ ,  $[010]$  and  $[001]$ ) and monoclinic ( $a, b, c, \beta$ ) structures. The orange hexagon indicates the plane lying on the FePt layer. The black large line is perpendicular to the plane and gives the out-of-plane direction of our layer. It is at  $54.74^\circ$  of the  $[001]$  direction. Colored lines represent the possible Co orientation according to XLD features. The blue directions are out-of-plane of our layer. The red ones are in-plane. It confirms that CO spins are along  $\vec{b}$  direction.

Because the  $\vec{b}$  axis is fourfold degenerated in the surface layer, it would have been hard to evaluate the in-plane anisotropy with in-plane angular dependence XLD analysis. By XLD features analysis, we determined that the Co spins point in the direction of a second neighbour. This example shows that XLD measurements associated with multiplet calculations provide a sensitive and powerful probe to determine the orientation of the spin axis with respect to the crystalline axes.

#### 4.2.4 XLD temperature dependance

XLD measures essentially the charge anisotropy associated with both the local crystal field and the local exchange field through the spin-orbit coupling. Magnetic and structural contributions mixed up in the  $R_{L3}$  ratio can be disentangled by a full temperature dependence study of the anisotropy amplitude. The anisotropy amplitude is experimentally defined as  $\Delta R_{L3} =$

$R_{L3}(70^\circ) - R_{L3}(0^\circ)$  and its variation is presented in Fig. 4.12.  $\Delta R_{L3}$  decreases following a Brillouin-like function up to  $T_N \approx 293$  K and then stabilizes, when the magnetic contribution to the anisotropy has vanished. This unambiguously confirms that the AFM order is preserved up to about 293 K. It also proves that the Néel temperature of the CoO film is very close to that of the bulk CoO crystal. Above  $T_N$  only the nonmagnetic crystal field contribution to the anisotropy still remains. This explains the small residual anisotropy observed at 300 K (Fig. 4.12), where no magnetic contribution is expected. The curve also confirms that the XLD signal at 10 K then measures principally the magnetic dichroism and validates the precedent analysis.

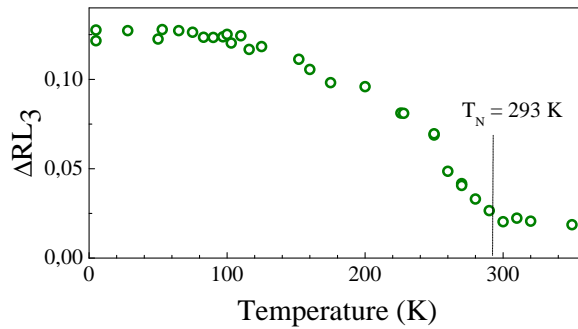


Figure 4.12: Temperature dependance of the anisotropy

Such high magnetic order seems surprising for an only 4 nm CoO layer. As ferromagnetism, antiferromagnetism is expected to weaken with a decrease of the thickness leading to a smaller Néel temperature  $T_N$ . Because antiferromagnetic layers are often studied for their coupling with ferromagnetic ones, it is widely believed that exchange bias blocking temperature ( $T_B$ ) follows the ordering temperature  $T_N$ , and knowing one of them is knowing both. Since a lot of experiments found that blocking temperature decreases with thickness, nothing contradicted this assumption. Up to an article published by van der Zaag and his collaborators.[17] They found an ordering temperature ( $T_N$ ) of CoO in  $Fe_3O_4/CoO$  exchange biased systems larger than the bulk one for small CoO thickness whose  $T_B$  is reduced. They explained the enhancement of  $T_N$  in CoO layers above the bulk  $T_N$  for layer thicknesses  $\lesssim 10$  nm by the proximity of magnetic  $Fe_3O_4$  layers. An analogous argument could be raised in our CoO layer in proximity with FePt layer which has an higher ordering temperature.

### 4.3 Exchange coupling

Before focusing on the interaction between the two layers, let's recall all the results on each layer. FePt layer has a strong perpendicular magnetic anisotropy persisting up to at least 320 K. Co spins are essentially in-plane, aligned along the  $\vec{b}$  direction up to 293 K. Therefore Co and Fe spins are at  $90^\circ$ . At first sight, the reversal of Fe spins should not influence Co spins orientation, suggesting that the layers won't be coupled.

Amongst the four equivalent (111) planes of the rocksalt bulk CoO, only one becomes completely non compensated, when the temperature is below  $T_N$  and the monoclinic distortion takes place. The spins are coupled ferromagnetically within what was the (111) plane of the cubic lattice. The other planes are fully compensated (cf Fig. 4.5). The monoclinic distortion of our CoO layer, as the bulk, sets what should be the (111) plane in rocksalt lattice apart. We can consider that it is the FM plane. The hexagonal plane, which sits on the PtFe(001) surface, is formed by **a** and **b**. It is then expected that the Co sheets parallel to the surface contain fully compensated spins. In this plane rows of Co spins are coupled ferromagnetically along **b** and antiferromagnetically along **a** (respectively  $[1\bar{1}0]$  and  $[11\bar{2}]$  directions in the rocksalt structure). Atomic and magnetic structures at the interface are illustrated in Fig. 4.13.

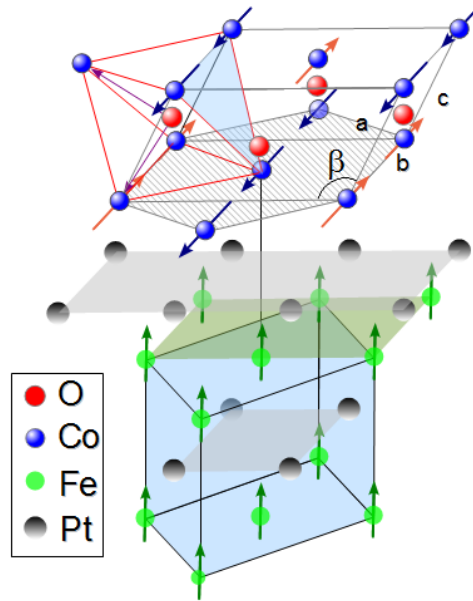


Figure 4.13: Sketches of the spin orientation in the CoO/PtFe bilayer in perspective. The  $[001]$  axis of tetragonal elongation is indicated in the  $CoO_6$  octahedron.

Exchange coupling between FM and AFM layers is mainly identified by an increase of coercive field ( $H_C$ ) and a shift ( $H_{EB}$ ) of the FM hysteresis loop at low temperatures after field cooling (cf section 1.1.2). Polar MOKE measurements of this sample after a field cooling of the sample from 320 K down to 5 K under an applied field perpendicular to the surface present a shift in the hysteresis loops towards negative values at low temperatures. The exchange bias shift is about  $H_{EB} = -0.75$  kOe at 5K. The enhancement of coercive field observed at low temperature compared to RT is around one order of magnitude. The two layers are well coupled.

Such orthogonal coupling is not so unusual. It has been predicted theoretically by N. C. Koon [134] in thin films with a fully compensated AFM interfacial spin configuration interacting with the exchange field of the FM layer. A minimum of energy is reached for such frustrated interface when spins are at  $90^\circ$  from each other. T. C. Schulthess and W. H. Butler extended the microscopic Heisenberg model developed by N. C. Koon adding magnetostatic



energy.[135] They found that the spin-flop coupling - name they introduced to describe this type of effective exchange coupling - does not lead to an exchange bias as N. C. Koon proposed, but rather gives rise to an uniaxial anisotropy which in turn causes the large coercivities observed in exchange biased films. Larger coercivity and strong exchange bias are both present in our film, preventing to decide between the two theories. Spin-flop coupling has been experimentally observed in other systems as for instance CoO/Fe on Ag(001) [132] or Fe/NiO bilayers grown on Ag(001)-stepped surface.[136]

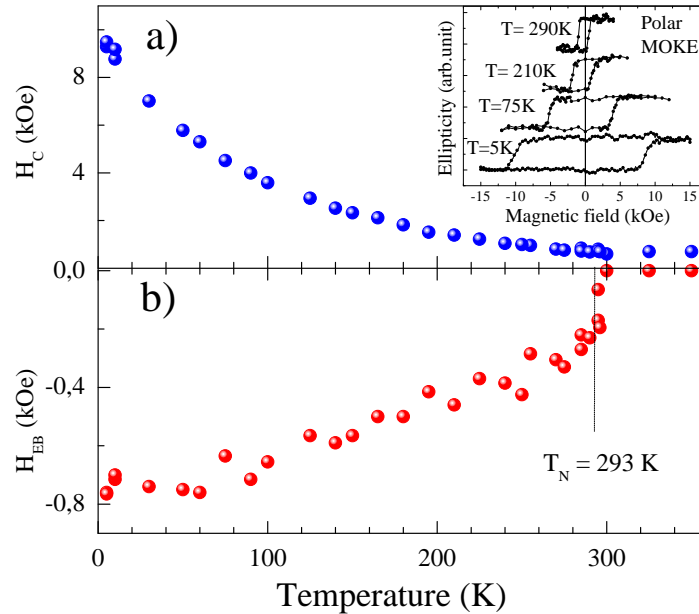


Figure 4.14: Temperature dependence of the (a) coercive field and (b) exchange bias after cooling the sample in a +5 kOe perpendicular magnetic field. Polar MOKE hysteresis loops at a few selected temperatures are shown in the inset.

The temperature dependence of the coercive field ( $H_C$ ) and the exchange bias field ( $H_{EB}$ ) are identical whether the field during the cooling is at + 3.5 kOe, + 5 kOe or + 10 kOe . When the field during the cooling is at -3.5 kOe, exchange bias is positive, and shows the same behavior in function of temperature (cf Fig. 4.3). As shown in Fig. 4.14, they decrease with temperature up to the nominal bulk Néel temperature. As far as we know, this is a unique example where the blocking temperature  $T_B$  is identical to Néel temperature  $T_N$  for an ultrathin CoO layer and matches the bulk Néel temperature.

Many experimental studies report that to reach the blocking ( $T_B$ ) temperature close to  $T_N$ , CoO thickness should be at least about 10 nm [137, 17, 138, 139]. In most cases, the blocking temperature measured from the onset of the exchange bias shift is smaller than the expected  $T_N$ . Films with a thickness around 3–5 nm display  $T_B$  typically around 200–240 K. In contrast, our CoO layer sustains an EB shift up to  $T_N \approx 293$  K. This exceptional behavior must be related to the stable spin configuration at the interface and to the good crystalline quality of the layers. A detailed study on the CoO/Fe bilayers led by G. Nowak



and his collaborators shows indeed that the blocking temperature is strongly influenced by the stoichiometry of the CoO layer, while the morphology of the interface acts more on the magnitude of the characteristic fields.[35] Nevertheless in the PtFe layer the high magnetic anisotropy relies on the strong spin-orbit coupling of the Pt site and hybridization between Fe  $3d$  and Pt  $5d$  states.[140] Exchange coupling of Co and Fe moments through Pt  $5d$  states at the interface are likely to contribute to the preservation of the EB shift up to the AFM phase transition.

Exchange coupling properties are largely determined by the direction and strength of the anisotropy in the FM and in the AFM layers. The large blocking temperature of this layer demonstrates that AFM order as robust as in the bulk may be established in CoO films as thin as 4 nm. It confirms the results of Van der Zaag and coworkers.[17] The thickness effect, which reduces the ordering temperature, is not an intrinsic property.

## 4.4 CoO magnetic anisotropy

In this section, some experiments in progress are developed. Our understanding is not as complete as for the previous ones. We are interested in the evaluation of the strength of the magnetic anisotropy in the CoO layer compared to the other energies in play.

### 4.4.1 Strength

As seen in section 4.2, CoO spins are essentially aligned in-plane. At a first sight, one could envisage two main reasons imposing such an in-plane alignment: either orthogonal exchange coupling with FePt or the structural anisotropy induced by epitaxy. Even when a strong out-of-plane magnetic field is applied, Co spins remains almost unchanged. We tried to force Co spins to turn with a field of 9 T (90 kOe) applied perpendicularly to the sample at 10 K and at 300 K. XLD signal does not present any change and only a small perpendicular FM component shows up. At low temperature, exchange interaction between Co spins is most likely too strong to hope a reversal and breaking of the AFM couplings. At RT, the paramagnetic Co spins have still their anisotropy axis in plane and much larger field would be needed to taken them out-of-plane. The experiment does not allow to conclude precisely, but is compatible with that the effective in-plane anisotropy is strong.

As the Co spins are pointing along the  $\mathbf{b}$  direction related to the CoO structure, and four structural variants coexist, two Co spin orientations rotated by  $90^\circ$  are present in the film plane. Therefore, no in-plane anisotropy is expected. One can try to create an anisotropy by the application of a strong magnetic field in the sample plane. We tried to do that by the application of a magnetic field of 4T at 10 K. At these conditions, the Fe spins are forced to be almost (even if not completely) oriented in-plane along the field direction. However, as the precedent experiment, no in-plane anisotropy has been detected. XAS with polarization horizontal (parallel to the field) and vertical (perpendicular to the field) were measured but the shape of XAS signal does not change significantly. Because the orthogonal coupling is

not perturbed by an in-plane rotation of Co spins and the structural distortion is small, we could have expected that a part of the Co spins would flip by  $90^\circ$  along the field direction. Such an evidence would indicate that the interaction with the exchange coupling interaction with FePt film were strong enough to overcome the anisotropy and rotate the Co spin axis. Probably, the sample temperature was too low and the exchange interaction between Co spins is likely too strong to be overcome by 4T. No rotatable Co spins have been detected. This experiment has to be done as function of temperature to be more conclusive. Then, the results should be compared to distinguish the exchange interaction contribution to the magnetic anisotropy contribution.

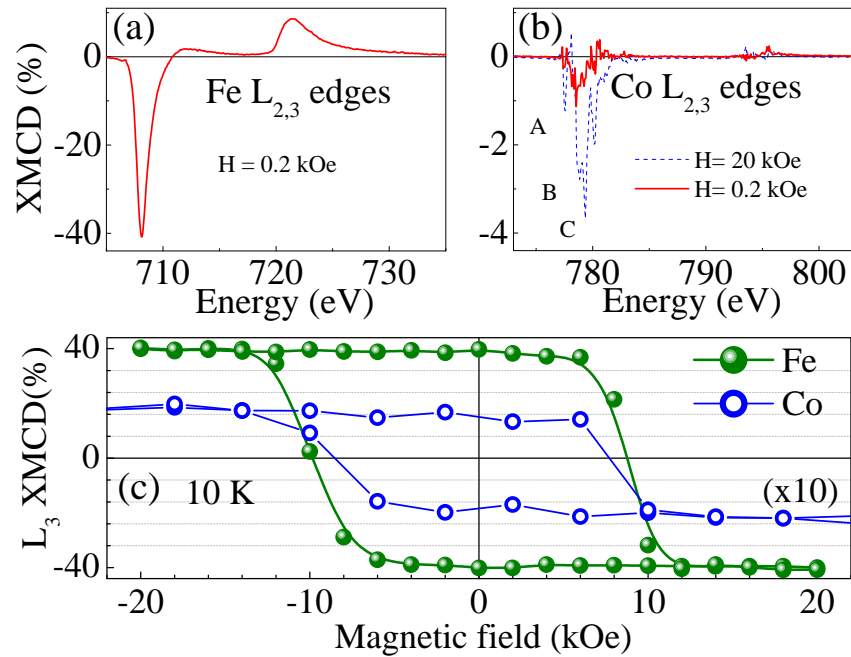


Figure 4.15: (a) Fe  $L_{2,3}$  and (b) Co  $L_{2,3}$  XMCD: Solid (red) lines are close to remanence; dashed (blue) line is at 20 kOe. Note the factor of ten between scales. (c) Element-selective hysteresis loops at Fe and Co  $L_3$  edges.

As a small out-of-plane contribution of interface Co spin cannot be ruled out from the only XMLD, we went on performing XMCD measurements at Co  $L_{2,3}$  edges. Element-selective hysteresis loops were drawn by reporting for each value of the applied perpendicular magnetic field the maximum amplitude of the XMCD at the Fe and Co  $L_3$  edges in Fig. 4.15. At the Co  $L_3$  edge, we observe a weak XMCD signal due to the Co spin component not compensated (Fig. 4.15b). It shows the CoO characteristic multiplet features[141, 117]. The maximum amplitude of this XMCD signal is roughly proportional to the applied magnetic field but shows a weak hysteresis opening with a remaining contribution of about 0.5(3)% close to remanence and coinciding with the Fe hysteresis loop (Fig. 4.15c). Two contributions to the field dependent Co XMCD should then be considered. The linear contribution is a bulk-like effect, arising from the coupling of the whole set of Co spins in the CoO layer to the external

magnetic field. On the other hand, the weak hysteresis, following the Fe hysteresis loop, results from an interface exchange coupling with Fe. This small contribution originates from an uncompensated Co spin component perpendicular to the surface, as shown in Fig. 4.16.

It is worth noting that the Co hysteresis loop shows an downward shift of about 11%. The ferromagnetic Co component can be divided in two categories: the rotatable moments, which rotates with the FePt and might take a part in the enhancement of the FePt coercivity; and the frozen moments, which stay in the same direction whatever the direction of Fe moments. In the Figure 4.16, the spins at the interface are shown rotatable and the spins in the layer are shown frozen. The downward shift could be related to the frozen spins. Indeed, they stay in the direction of the field cooling whatever the direction of the applied field. In this case, they give a negative contribution to the whole loop. It leads to a vertical shift of the loop.

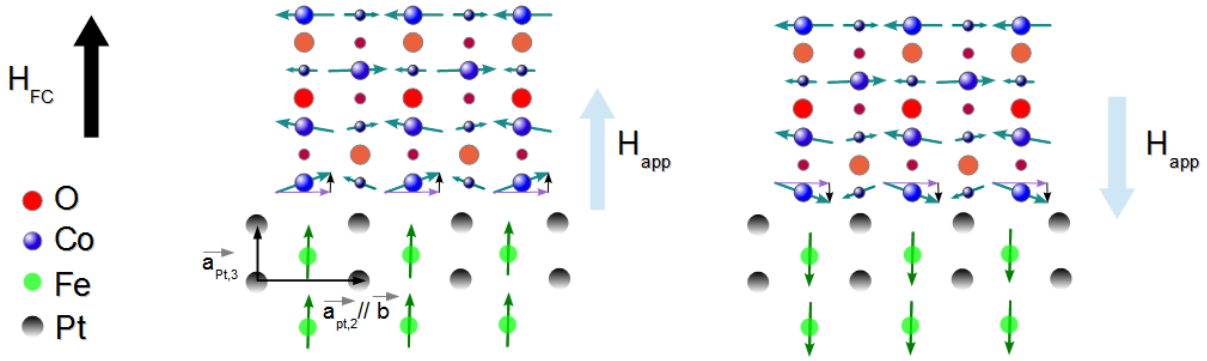


Figure 4.16: Illustration of CoO spin canting in the plane ( $\vec{a}_{Pt,2}/\vec{b}$ ,  $\vec{a}_{Pt,3}$ ). Black arrows, representing the uncompensated Co spin component perpendicular to the sample, are exaggerated compared to the compensated in-plane component. Rotatable moments are drawn near the surface, while the canting in the rest of the layer is supposed frozen.

The uncompensated Co spin component may refer to the small canting of the AFM moments located at the interface flipping with the direction of the FM ones that N. C. Koon introduced in its model to explain the exchange bias. According to him, the canting decreases rapidly as a function of the distance from the interface. This view is supported by experiments carried out by Y. Shiatsu and coworkers [34] under Pt/Co(FM)/ $\alpha$ -Cr<sub>2</sub>O<sub>3</sub>(AFM)/Pt perpendicular-exchange-biased system. They observed a vertical shift of the element-specific magnetization curve of Cr. According to pinned spin model, 75% of the uncompensated Cr spins should be pinned. Such amount is too large for the vertical shift of the hysteresis loop observed. They consider then a model in which the interfacial AFM spins are supposed only to cant. The spin canting extends into the bulk site of the AFM layer and is enough to be responsible for exchange bias.

The hysteresis loops we measured by MOKE after in-plane field cooling are in line with this idea. During the cooling, the FePt spins are aligned with the field of about +50 kOe applied in the plane of the sample. It imposes an in-plane exchange field at the interface that acts on the Co spins while they get to the AFM order state. Once at low temperature, the

applied magnetic field is set to zero. The FePt spins get back to their out-of-plane direction. The perpendicular hysteresis loops present their enhanced coercivity but they do not show any exchange bias shift. Two possible scenarii are conceivable. Either a canting develops but is randomly distributed in domains or there is no canting at all or just at the interface.

The first case means that the out-of-plane component is intrinsic to Co spins. When the field is applied perpendicularly to the sample during the cooling, this component aligns with. The canting has one preferential direction. It results in a non-zero magnetization and an effective exchange coupling with the FePt layer. When the applied field is in-plane during the cooling, there is no preferential direction. The perpendicular component is randomly distributed in upwards and downwards domains.

The second case means that the canting develops due to the exchange coupling with FePt or to the interaction with the magnetic field. It extends in the layer during the cooling if the applied magnetic field is perpendicular. Once at low temperature, the exchange between Co spins is too strong to allow a canting in the all layer. At maximum it develops at the interface with FePt. However the canting at the interface probably rotates with FePt, creating the enhancement of coercivity. The rest of the layer has no canting. It probably corresponds to the frozen moments, which might be responsible for the exchange bias (cf Fig. 4.16). Further measurements would be necessary to properly check this interesting preliminary result.

#### 4.4.2 Structural anisotropy

As all 3d transition-metal (TM) compound CoO has a final state well described within a  $CoO_6$  cluster. In the  $CoO_6$  octahedron the elongation of the distances along the  $c'$  axis ( $c'/a' > 1$ ) goes along with a splitting of the  $t_{2g}$  orbitals.[142] The low lying  $t_{2g}$   $d_{xz}$  and  $d_{yz}$  orbitals are filled and the  $t_{2g}$  hole will occupy the higher  $d_{xy}$  orbital. We should note that in our film the tetragonal distortion is weak ( $c'/a' \approx 1.007$ ) and that its influence on the orbital occupancy may be called into question. The integrated intensity of the XAS spectra may provide a direct experimental verification of the orbital occupation.[98] We have calculated the integral  $I$  over the entire  $L_{2,3}$  spectral region (775eV to 801eV) for the different angles and plotted in Figure 4.17 the ratio  $(I_\theta - I_0)/I_0$ . The increase of this ratio gives clear evidence of the increase of accessible  $t_{2g}$  holes as  $\theta$  increases. In a simple experimental geometry of CoO(001) on Ag(001), where the film plane would also be the  $d_{xy}$  orbital plane, we could straightforward conclude about the preferential orbital occupancy. In the case of CoO(111) on PtFe/Pt(001), however, the normal of the planes containing  $d_{xy}$  orbitals are tilted by an angle of  $\theta_0 = 54.74^\circ$  in relation to the surface normal (see Fig. 4.13) and the growth proceeds in fourfold equivalent domains. Instead of a simple  $\cos^2(\theta)$  angular dependence, the intensity  $I_{xy}(\theta)$  of the transition towards  $d_{xy}$  orbitals should be geometrically derived and averaged over the four domains. We found that  $I_{xy} \propto \cos^2(\theta - \theta_0) + \cos^2(\theta + \theta_0)$ . This function shows a maximum for  $\theta = 90^\circ$  and minimum at  $\theta = 0^\circ$ . The experimental results (Fig. 4.17) confirm then a preferential localization of the  $t_{2g}$  holes with  $d_{xy}$  symmetry. With the spin-orbit coupling tending to align the spin in this same plane, we can expect the spin along the common direction of the  $d_{xy}$  planes and

the surface plane ( $\bar{1}\bar{1}1$ ), i.e. the Co spins must be along the  $[1\bar{1}0]$  direction (Fig. 4.13). This is in full agreement with the conclusions drawn from the study of the multiplet features.

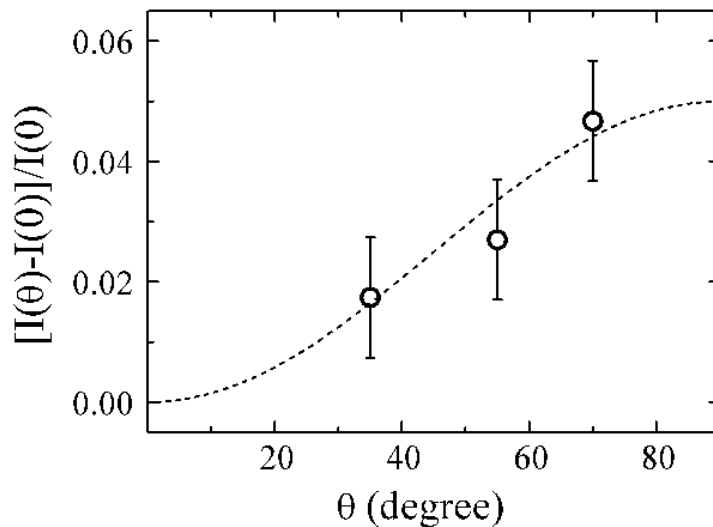


Figure 4.17: Experimental angular variation of the integrated intensity of the XAS spectra (dots). The dotted line corresponds to the calculated  $I_{xy}(\theta)$  function.

## Conclusion

We performed *ex situ* x-ray absorption spectroscopies, with linear and circular polarization at Fe and Co  $L_{2,3}$  edges to determine the spin orientation and the magnetic order of each layer of the CoO/FePt system. The Fe spins are oriented out-of-plane until at least 320 K. This high Curie temperature value reflects the chemical order of the only 3BLs FePt film. The perpendicular magnetic anisotropy (PMA) is strong since kept until at least 320 K with a remanent magnetization identical to saturation magnetization. The Fe oxide layer found at the interface between FePt and CoO layers by XAS analysis doesn't contribute to ferromagnetism. X-ray magnetic circular dichroism is indeed characteristic to a FM metallic spectrum.

According to the effects of magnetocrystalline and dipolar energies in the Co magnetic structure, we estimated that Co spins should be along the  $\vec{b}$  direction, pointing towards the first Co neighbour. We measured the intensity ratio  $R_{L3}$  of XMLD signal at Co  $L_3$  edge in function of incident angle to determine Co spins orientation. Co spins are found in the plane of the surface, which is compatible with the previous result. The latter is also nicely confirmed by the analysis of the features of XMLD asymmetry compared to the results from multiplet calculations. Fe and Co spins are then at  $90^\circ$ . With the temperature dependance of the  $R_{L3}$  ratio, we demonstrated that the AFM order is preserved up to about 293 K. Therefore, the Néel temperature of the CoO film is very close to the one of the bulk CoO crystal.

Hysteresis loops of FePt, measured mainly by MOKE experiments, show an increase of coercivity and a shift after field cooling. The two layers are well coupled. A small hysteresis

loop can also be drawn by XMCD at Co  $L_{2,3}$  edge. We attribute it to a small out-of-plane canting of CoO layer. Exchange bias is maintained up to RT, asserting the steadfastness of the CoO/FePt exchange interfacial coupling, and also the AFM order of the CoO layer. This is a unique example where the blocking and Néel temperatures for an ultrathin CoO layer are identical and match the bulk Néel temperature. It demonstrates that the thickness effects on the ordering temperature  $T_N$  and on the blocking temperature ( $T_B$ ) are not intrinsic properties of these double layers. Such exceptional behavior shares a close relationship with the strain-induced distortion of the oxide layer.



# Chapter 5

## Growth, structure and exchange coupling of CoO(001)/FePt/Pt(001)

### Contents

---

<b>5.1 (001) oriented CoO on Pt(001)</b> . . . . .	<b>98</b>
5.1.1 Growth . . . . .	98
5.1.2 Structure . . . . .	100
<b>5.2 CoO(001)/FePt grown on Pt(001) (Sample S19)</b> . . . . .	<b>104</b>
5.2.1 Growth . . . . .	104
5.2.2 CoO structure . . . . .	106
<b>5.3 Magnetic studies of CoO(100)/FePt(100)/Pt(100)</b> . . . . .	<b>108</b>
5.3.1 Magnetic studies by MOKE . . . . .	108
5.3.2 Magnetic study by XMCD and XMLD . . . . .	111

---

Recently, Heinz, Hammer and coworkers investigated intensively the epitaxial cobalt oxide growth on Ir(100). They showed a way to tune CoO growth orientation on Ir(100) by interface chemistry. Co reactive deposition on clean Ir(100) gives rise to CoO(111) film. CoO(100) film is realized by deposition of a buffer layer of pseudomorphic  $1\frac{3}{4}$ - $5\frac{3}{4}$  MLs Co on the clean unreconstructed substrate. After a moderate oxidization at  $5 \times 10^{-9}$  mbar for about 1 min at 320 K followed by annealing at 670 K, a well-ordered  $c(4 \times 2)$  superstructure, precursor of  $Co_3O_4$  spinel, develops in the top layer. This phase is a precursor for the growth of CoO(100) obtained by further Co reactive deposition in oxygen.[143, 144]

Platinum and iridium are neighbours in periodic table. They share the same crystalline structure with almost the same lattice constant (3.924 Å and 3.839 Å respectively). We can expect similar growth on both surfaces. Indeed, the CoO layer we obtained on Pt(001) by reactive deposition and presented in chapter 3 reminds that one obtained on Ir(001) by Meyer et al.[123] Both are (111) oriented with a slight distortion. The proximity of Pt(001) and Ir(001) and the tuning of the CoO growth mode on this last surface calls us to study such a



phenomenon on Pt(001). The magnetic properties of the CoO(111)/FePt(001) system convinced us to build CoO(001)/FePt(001) system on Pt(001) and see the impact of orientation and anisotropy on magnetic properties.[24]

## 5.1 (001) oriented CoO on Pt(001)

### 5.1.1 Growth

Several attempts of CoO(001) growth on Pt(001) were studied by GIXRD at the BM32 beamline at ESRF. Oxygen pressure and temperature were optimized to avoid hexagonal phase development and obtain Bragg peaks from cubic phase as sharp and intense as possible. The growth conditions described here gave the best results and are the last one tested.

Pt(001) substrate was cleaned following our standard procedure (see chap.3) exhibiting at the end two reconstructed domains rotated by  $90^\circ$ . The domains turned up to be different, with one of them showing the well-known splitting into two directions rotated by  $0.9^\circ$  from the main axis, while the other one didn't split. The reconstructed domain size was around 58 nm. They reflect the cleanness of the surface. As shown in the chapter 3, the reconstruction disappears as soon as the first Co monolayer is deposited. The growth was followed by SXR at 22 keV photon energy under a grazing incidence angle of  $0.65^\circ$  for Pt CTR, or at an angle of  $0.22^\circ$ , to be more sensitive to the surface layer, in the case of the CoO study. Co was deposited by molecular beam epitaxy (MBE) using a pure rod inserted in water-cooled electron beam evaporator. The evaporation rate was calibrated with a quartz microbalance at around 1 ML each 6 minutes. The base pressure of the UHV chamber was around  $2 \times 10^{-10}$  mbar before deposition.

The CoO(111) growth was realized directly by reactive deposition of Co on a Pt(001) substrate held at 520 K, with a molecular oxygen pressure in the chamber of about  $5 \times 10^{-7}$  mbar during evaporation. The CoO(001) growth requires four fundamental steps.

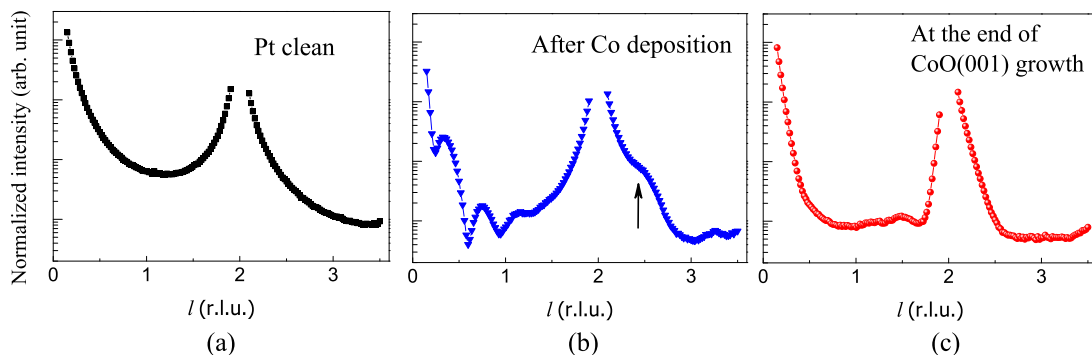


Figure 5.1: Evolution of intensity measured by  $l$ -scans along the (1 1) CTR for clean Pt (a), after Co deposition (b) and at the end of the process (c).

In the first step, about 5 MLs of Co are deposited on Pt surface. A deposition with the substrate held in temperature or an annealing following the deposition leads to the formation

of  $L1_0$  CoPt phase. Then a broad peak in (1 1 1.06) stands up in the rod. To avoid the growth of this phase, the first Co layers are deposited at room temperature (RT) and are not annealed.

Co bulk has an hexagonal close-packed structure with the shorter distance between two atoms of 2.497 Å.[20] However, in thin films, it was shown that Co can take a structure close to  $bcc$  with a lattice constant  $a = 2.827$  Å.[145] In this case, the misfit between Co and Pt is only 2%. Kiessig fringes settle along Pt CTRs as shown in Fig. 5.1 indicating that Co grows in registry with the substrate. The pseudomorphic layer has thus the same in-plane parameter as the bulk ( $a_{Co} = 2.775$  Å). (1 1 2) Pt Bragg peak shows a shoulder at high  $l$  outlining the starting of Co order peak around  $2.4 \pm 0.1$ . It gives an out-of-plane interplanar distance of 1.64(7) Å. This value is intermediate between the interplanar distance of  $fcc$  Co(100) planes (1.77 Å) and  $bcc$  Co(100) planes (1.41(3) Å).[145] These results are in agreement with the study led by S. M. Valvidares during his thesis on the growth of Co on Pt(001) by scanning tunnel microscopy (STM) and SXRD. Valvidares and coworkers found that Co grows pseudomorph in a layer-by-layer mode on a Pt surface completely deconstructed after 1ML of Co deposition.[69] Because they found a vertical interplanar distance of about 1.485(5) Å for a thickness of 2.6(2) nm, they analyze the Co structure of the film as a  $bct$  structure, tetragonally distorted with respect to the  $bcc$  phase, with the lattice constant  $a_{Co} = 2.82$  Å.[69] The in-plane pseudomorphism imply a compressive strain in the Co film of -1.8% ( $(2.775 - 2.82(5))/2.82(5)$ ), while out of the surface plane, the strain is tensile,  $((1.485 - 1.41)/1.41 = 5.1\%)$ . It is noticeable that this yields a unit cell volume differing from that of the  $bcc$  by only 1.4%. Our structure seems to be closer to the  $fcc$  structure, with a unit cell volume of  $12.63 \text{ \AA}^3$ . However a precise determination of the out-of-plane lattice constant would require a quantitative analysis based on rocking scans derived structure factors, which was not performed here. From the periods of the oscillations, we can deduce the film thickness as described in chapter 2. A value of  $1.12 \pm 0.02$  nm corresponding to about 7 ML is obtained, which is larger than the nominal thickness of 5 ML. Unfortunately, the deposition rate had increased during the growth in this first step.

In the second step, still at RT to avoid CoPt formation, oxygen at a rather small average pressure of  $9 \times 10^{-9}$  mbar is introduced in the chamber for about 1 min 30 s followed by an annealing at 500 K for 30 min. At this step, no peaks from cobalt oxide in spinel or stoichiometric phase have been detected. In the CoO growth on Ir(001), at similar conditions, a layer of a precursor of  $Co_3O_4$  spinel develops at the topmost surface. This layer is probably enough locally ordered to be seen by STM but not by GIXRD. In the third and fourth steps, the sample is annealed and oxidized as described in Fig. 5.2. Temperature is increased before a second oxidation to promote the ordering of the surface spinel precursor layer and reach the thermodynamical stabilization of the surface chemistry.

Right after the first 5 minutes under oxygen pressure at  $5 \times 10^{-7}$  mbar, a Bragg peak from CoO in (001) phase appears abruptly, in a partially relaxed structure. The following oxidations at higher temperatures sharpen and enhance the peaks indicating an ordering of the layer as can be seen in Fig. 5.3. No traces of hexagonal or spinel phases are visible. Crystal truncation

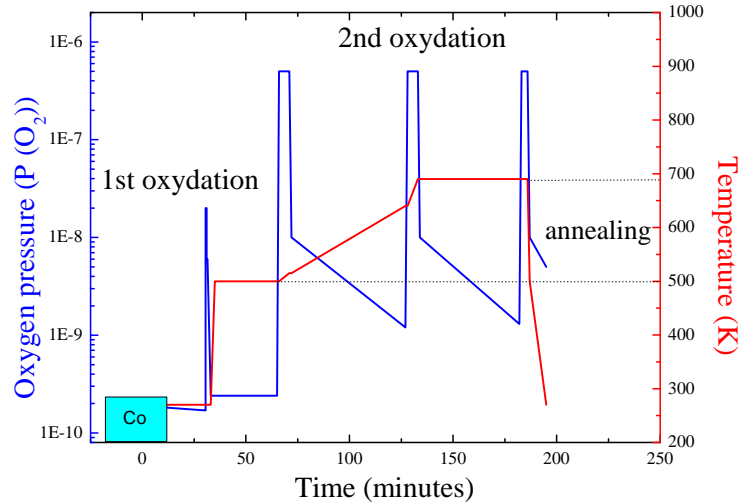


Figure 5.2: Temperature of the sample and oxygen pressure in the chamber during the CoO(001) growth on Pt(001).

rods lose mainly their Kiessig oscillations (cf Fig. 5.1c). Intensity between Bragg peaks in the CTR is very small indicating a rough interface between Pt and CoO.

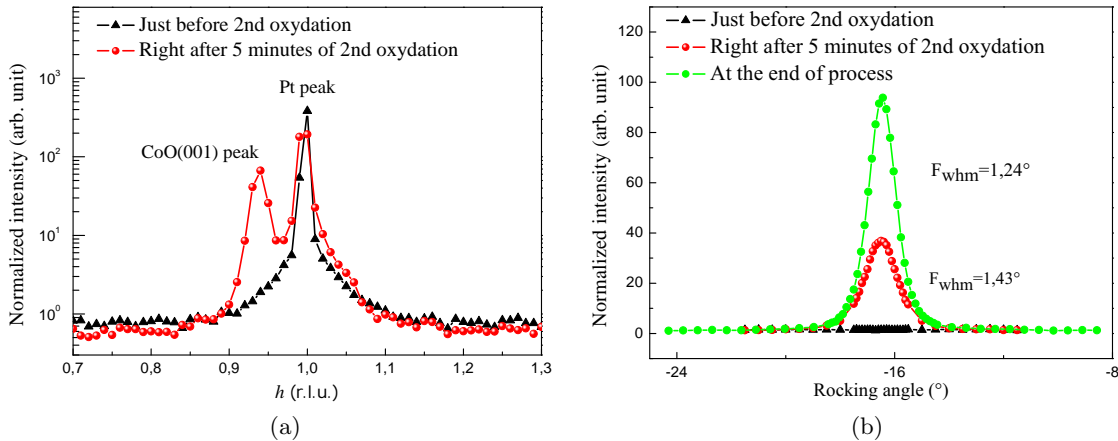


Figure 5.3: Growth of CoO(001) peak at (0.942 0.942 0.1) observed in  $h$ -scan and rocking scans measured at different steps.

### 5.1.2 Structure

After cooling down to RT the CoO layer, a set of 39 scans in-plane ( $h$ -scans,  $k$ -scans or rocking scans) and out-of-plane ( $l$ -scans) around CoO peaks were collected to a total of 6 non equivalent CoO peaks. Despite the profusion of scans, the determination of the only two lattice constant values could not be done with a high precision. A pattern of a superstructure with the same in-plane position of CoO perturbs the assessment.

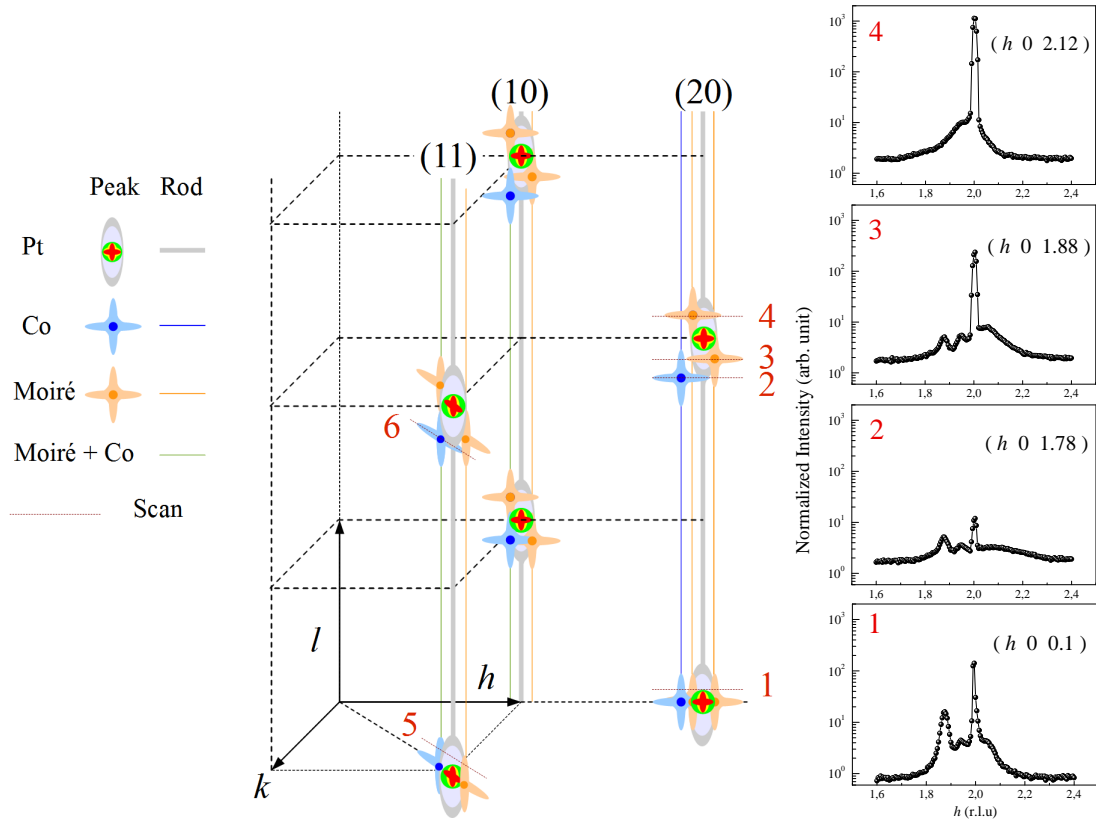


Figure 5.4: Diffraction pattern of CoO(001) overlayer on Pt(001) with 4 normalized intensity distributions parallel to the surface around (20) Pt rod at four out-of-plane positions. Peaks from Pt (multicolors), CoO (blue) and the superstructure (orange) and their rods associated are drawn for the three first non equivalent rods.

Figure 5.4 shows the diffraction pattern of the sample. The diffraction by CoO shows peaks at positions multiple of  $\frac{c_{Pt}}{c_{CoO}}$  or  $\frac{a_{Pt}}{a_{CoO}}$  ratio. The separation between Pt and CoO rods and Bragg peaks increases proportionally to  $h$ ,  $k$  and  $l$ . On the contrary spots coming from the superstructure keep the distance with Pt rods. Therefore  $(10)_{CoO}$  and  $(11)_{CoO}$  rods<sup>1</sup> are superimposed with the superstructure ones, in contrary to  $(20)_{CoO}$  rods. The in-plane scans 1 to 4 present the evolution of the intensity around (20) Pt CTR at different out-of-plane positions (Fig. 5.4). For  $l=0.1$ , Pt CTR with its two satellites rods and CoO rod are well distinguishable. The two satellites rods have the same intensity and are localized at  $\pm\Delta h$  from Pt rod.

A comparison of intensity diffracted along  $(11)_{CoO}$  and  $(20)_{CoO}$  rods is presented in Fig. 5.5. The two rods cross Bragg peaks at same  $l$  positions and so have usually the same shape. Here it is not the case. The complex peak shape around  $l=2$  is composed of three peaks of different origins and illustrates well the complexity of analysis. A CoO peak at  $l \simeq 1.77$  is followed by the bottom of Pt peak at  $l \simeq 1.95$  and by a superstructure peak at  $l \simeq 2.12$ . Scans parallel to the surface performed at the positions indicated in the figure are presented

<sup>1</sup>In this chapter, for reason of clarity, I will use a special notation.  $(hkl)_{CoO}$  means  $(hkl)$  in the CoO base, i.e.  $(0.937*h \ 0.937*k \ 0.886*1)$  in the Pt base.

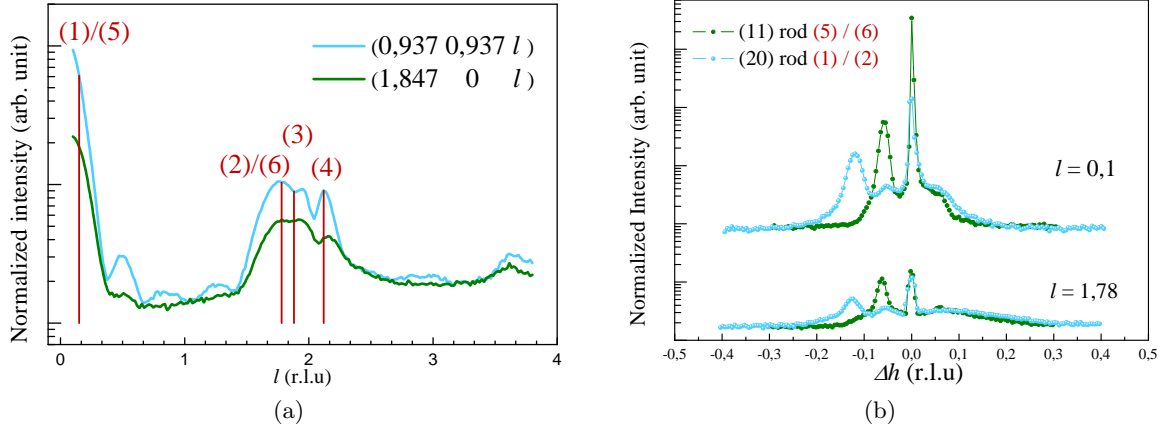


Figure 5.5: CoO rods (a) and normalized intensity distribution versus the in-plane lattice constant  $h$ , centered on the Pt rod (b).

in Fig. 5.5b. They show clearly that the superstructure and CoO rods, merged in  $(11)_{CoO}$  rod in one broad and intense peak, are separated in  $(20)_{CoO}$  rod.

The superstructure comes from the stress between CoO layer and Pt surface. CoO relaxes laterally inducing a network of defects or dislocations in the layer. The strain generates an atomic elastic displacement field originating from the surface and attenuated in the substrate as can be seen in Fig. 5.6. Analytical calculations made by G. Prévot and coworkers[147] show that for periodic distribution of defects, the force distribution can be decomposed into Fourier series with wavevector  $\vec{q}_{||}$  parallel to the surface in

$$\mathbf{F} = \mathbf{f}_0 \cdot e^{i\mathbf{q}_{||} \cdot \mathbf{r}_{||}} \quad (5.1)$$

and results into atomic displacements  $\mathbf{u}$

$$\mathbf{u} = \mathbf{u}_0(q_z) \cdot e^{iq_z \cdot z} \cdot e^{i\mathbf{q}_{||} \cdot \mathbf{r}_{||}} \quad (5.2)$$

with  $\mathbf{r}_{||}$  the component of  $\mathbf{r}$  parallel to the surface,  $q_z$  a complex number related with  $\mathbf{q}_{||}$  by  $q_z = k \cdot q_{||}$ . It is associated with an elastic displacement mode which behaves similarly to a vanishing wave in the bulk. It expresses that the perturbation concerns not only the interface layer but propagates inside the substrate. The physical solutions have  $Im(q_z)$  negative to be attenuated in the substrate. According to G. Prévot and collaborators, the total displacement must be real. When an elastic mode corresponding to  $\Delta h = q_{||}$  is considered, the elastic mode corresponding to  $-\Delta h$  is also present, with the same amplitude in order to have  $e^{i\mathbf{q}_{||} \cdot \mathbf{r}_{||}}$  real. Maxima of amplitude on the rods appear for  $Q_z = Q_{Bragg} - Re(q_z) = Q_{Bragg} - Re(k) * q_{||}$  with  $Q_{Bragg}$  the position of the bulk Bragg spot. It explains why maxima of the two rods surround the bulk Bragg peak as can be seen in Fig. 5.6 for structure factors of O overlayer on Cu(110).[146]

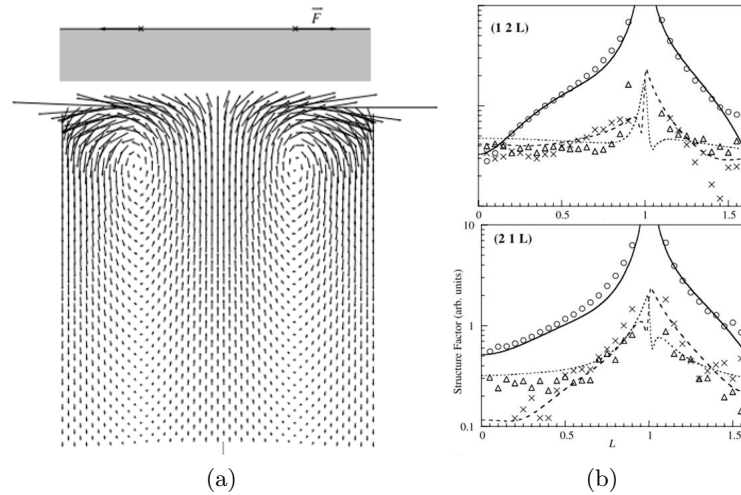


Figure 5.6: Illustration and curves taken from ref. [146]. (a) Transverse section of the atomic relaxations near the Cu(110) surface on which a periodic distribution of lines forces  $\vec{F}$  is applied in a O/Cu(110) system. The atomic displacements (arrows) are amplified by a factor of 200. (b) Structure factors along  $(2\ 1\ l)$  and  $(1\ 2\ l)$  of oxygen on Cu(110). Experimental data are represented by symbols, simulated results by lines. Circles and full line correspond to Cu CTR; triangles and dotted lines to  $h - \delta Q$  satellite; crosses and dashed line to  $h + \delta Q$  satellite.

The separation between dislocations can be obtained dividing the Pt lattice parameter by the distance between the satellites and the Pt rod ( $a_{dislocations} = a_{Pt}/\Delta h$ )[148]. Here  $\Delta h$  is evaluated at 0.056(5) from 8 positions (2 inequivalents) with maxima amplitude. It corresponds to a period of about 49(4) Å ( $5 \pm 0.5$  nm), i.e. around 1 domain boundary each 18 atoms.

As we told before, CoO Bragg peaks move away from Pt Bragg peaks and its satellites increasing  $h$ ,  $k$  or  $l$ . Therefore a way to study CoO rods without be perturbed by the superstructure is to measure at high  $h$ ,  $k$ ,  $l$ . However CoO layer is rough and intensity decreases rapidly when one of these parameters increases. A good compromise is nevertheless obtained with  $(20)_{CoO}$  CoO rods (and equivalents) for in-plane parameter and with  $(113)_{CoO}$  CoO peaks (and equivalents) for out-of-plane parameter. Peaks have been fitted with area gaussian and positions deduced have been averaged.

The CoO structure on Pt(001) is tetragonal with lattice constants  $a_{CoO} = 4.19(1)$  Å and  $c_{CoO} = 4.41(3)$  Å. The in-plane parameter  $a_{CoO}$  is compressed by 1.8% with respect to the bulk rocksalt CoO (4.261 Å) revealing an only partial relaxation. The substrate induced in-plane strain reduces the (001) plane atomic density by 3.5(2)%. It is compensated by the extension of the out-of-plane lattice parameter  $c_{CoO}$  by 3.1(8)%. Hence lattice volume in the film is equivalent to that one in bulk ( $V=77.3(8)$  Å<sup>3</sup>). The tetragonal distortion of this layer  $c/a = 1.05(1)$  is extensive and slightly enhanced compared to the CoO(111) layer on Pt(001) in the previous chapters. Considering the relation between strain and orbital filling as discussed

in section 4.2.1, this result could have an important impact on the magnetic properties of this layer.

## 5.2 CoO(001)/FePt grown on Pt(001) (Sample S19)

### 5.2.1 Growth

#### 5.2.1.1 FePt

The same procedure as for the sample presented in chapter 3 was applied to grow the 3 BL of FePt on Pt(001). The growth of FePt films on Pt(001) is discussed in section 3.1. Before Fe deposition, the cleanliness of the surface has been checked by Auger spectroscopy. SXRD shows large terraces of the typical Pt(001) quasi-hexagonal reconstruction, with equivalent domains rotated by  $90^\circ$ . The width of the reconstruction peaks corresponds to a terrace size of about 23 nm.

After Fe deposition on the substrate held at 600 K, oscillations and broad peaks identical to the FePt layer grown in the precedent sample (cf section 3.1) appear along Pt CTRs (11) and (10) (Fig. 5.7). Previous oscillations were more emphasized along (10) rod due to a misalignment of the scan along the rod. It doesn't follow exactly maximum of intensity in the rod. However it reports faithfully width of order peak (pointed by arrows) and oscillations which characterize the thickness and order of FePt layer. Since they are identical to the previous one, we can rely on the previous analysis. This layer can be considered as a chemically ordered FePt film grown in registry with Pt(001). The thickness of FePt layer evaluated from period of oscillations at  $9 \text{ \AA}$ , corresponding to 2.5 BL. Its structure was not analyzed quantitatively but has been assumed very close to that one of the previous sample, including its tetragonal distortion.

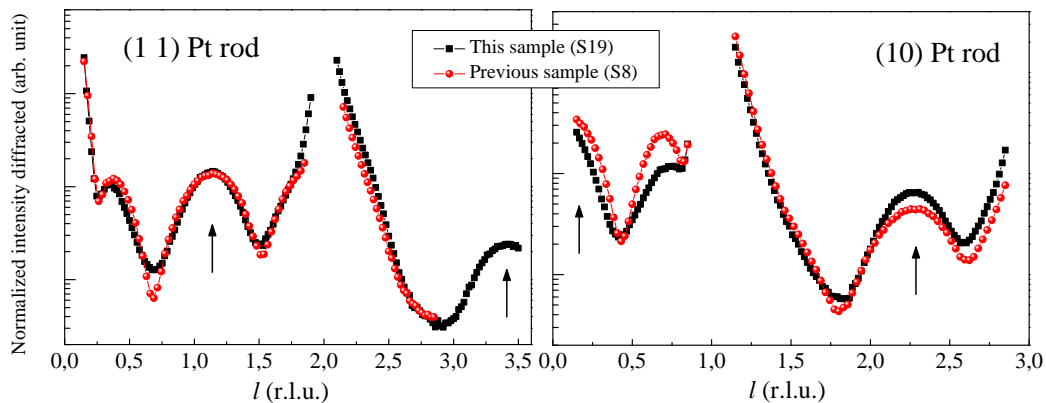


Figure 5.7: Pt rods after Fe deposition and before Co deposition of this sample and the precedent one. Arrows point order FePt peaks.



### 5.2.1.2 Co

As for the growth of CoO directly on Pt(001), a few MLs of Co have been deposited on the FePt surface at room temperature. Intensity diffracted along (11) Pt CTR present additional oscillations as shown in Fig. 5.8. Co grows in registry with FePt. An additional broad peak (pointed by an blue arrow) appears around  $l = 2.4$ , while FePt order peak (pointed by an orange arrow) doesn't grow. The intensity distribution along (11) Pt rod after Co/FePt growth on Pt(001) looks like the interference of the intensity distributions after FePt growth and after Co growth on Pt(001). The order peak does not enhanced. A CoPt phase can thus be excluded. From the period of oscillations, a total thickness of  $18.5(1) \text{ \AA}$  is assessed. About  $9(1) \text{ \AA}$  corresponding to about 6 ML of Co have been added.

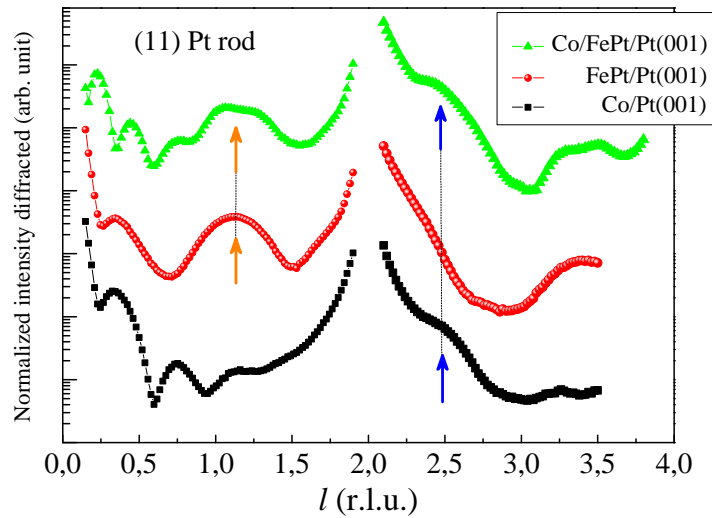


Figure 5.8: Comparison of the intensity distribution along the (11) Pt rod after FePt growth on Pt(001), after Co growth on Pt(001) after Co/FePt growth on Pt(001).

### 5.2.1.3 Oxidization

The first oxidization of the Co layer on FePt/Pt(001) is identical to the one of the Co layer on Pt(001). A partial oxygen pressure of  $9 \times 10^{-9}$  mbar is introduced in the chamber for about 1 min 30 s at RT followed by an annealing at around 500 K for 40 min. The annealing is intended to help the growth of the spinel precursor at the surface of the Co film, like in the case of Ir(001) substrate. The second oxidization is made at once in only 10 minutes with an oxygen pressure  $P_{O_2} = 5 \times 10^{-7}$  mbar at a temperature comprise between 500 K and 600 K. The following annealing doesn't exceed 630 K. These precautions have been taken to limit Fe oxidation. At the end of CoO growth, Pt rods show the same oscillations than after FePt growth and before Co deposition indicating that FePt layer is mainly preserved (cf Fig. 5.10). Order peaks (pointed by arrows) are however smaller and larger. FePt layer has been destabilized during CoO growth and its order has decreased.



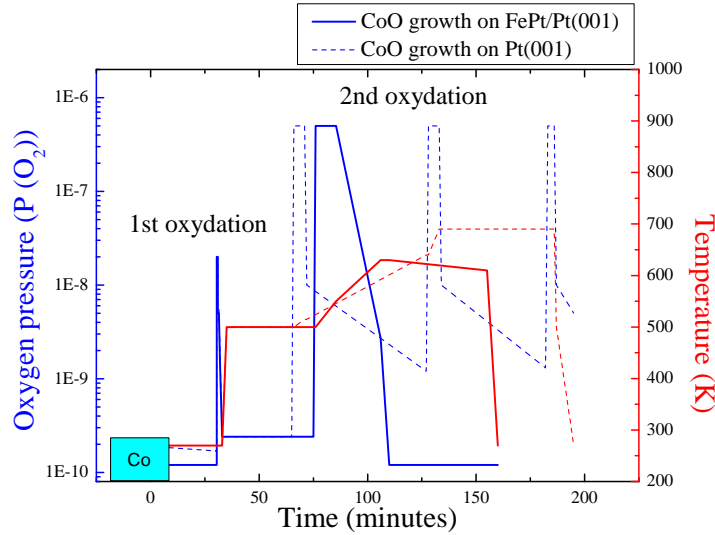


Figure 5.9: Temperature of the sample (red solid line) and oxygen pressure (blue solid line) in the chamber during the CoO(001) growth on FePt/Pt(001). By comparison, conditions of growth of CoO(001) on Pt(001) are represented in dashed lines.

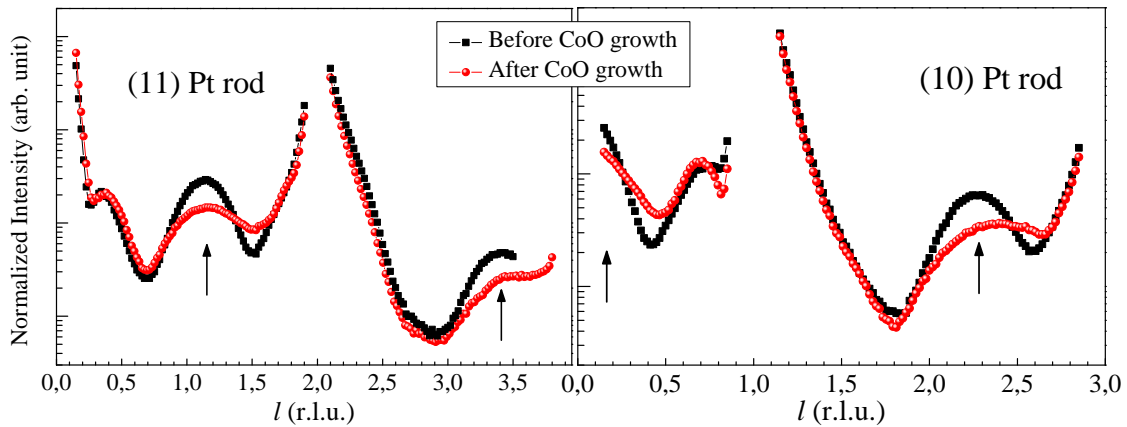


Figure 5.10: (11) and (10) CTRs before and after CoO growth (black and red dots respectively)

### 5.2.2 CoO structure

The CoO structure on FePt/Pt(001) has been determined using a set of 40 in-plane ( $h$ -scans,  $k$ -scans or rocking scans) and out-of-plane ( $l$ -scans) around CoO peaks to a total of 8 non equivalent CoO peaks. The superstructure rods are still present, with the same features. CoO peaks separated from the superstructure have been fitted with a gaussian. The results weighted by a confidence coefficient have been averaged. Error bars come from the standard deviation between all fitted values.

Only peaks from the tetragonal structure have been detected. No traces of spinel  $Co_3O_4$  phase or hexagonal CoO (111) have been detected. This oxide layer is more relaxed than on Pt(001), with lattice parameters  $a_{CoO} = 4.213(5)$  Å and  $c_{CoO} = 4.36(2)$  Å. The (001) plane atomic density reduced by 2.2(3)% by substrate in-plane strain is exactly compensated by the

extension of the out-of-plane lattice constant. It keeps the volume constant ( $V=77.3(4) \text{ \AA}^3$ ). The tetragonality of the layer  $c/a = 1.03(1)$  decreases compared to CoO(100) on Pt(001) but still remains enhanced compared to the CoO(111) layer on FePt/Pt(100).

The in-plane averaged domain size in CoO layer are evaluated from the width of the peak around 6 nm through 4 rocking scans. The thickness of the layer is deduced around  $15(5) \text{ \AA}$  from  $l$ -scans collected at high values to separate CoO peaks to the superstructure and Pt ones. The weak intensity of these peaks prevents to obtain a better accuracy. This thickness corresponds to about 7 ML of CoO.

Furthermore, Auger electrons spectroscopy shows a ratio of oxygen on cobalt larger than usual indicating a large concentration of oxygen atoms at the near surface. In Fig. 5.11 are plotted Auger electron spectra in derivative mode. We used the ratio of strongest Co and O peaks  $R(O/c_o)$  in this mode to follow oxygen rate in the near surface. If we compare to our reference  $R(O/c_o)=2.73$  of 1 ML of stoichiometric CoO on Pt(111), the layer of CoO(001) on Pt(001) was barely oxygen deficient with  $R(O/c_o)=2.55$  while oxygen in the top of the layer of CoO(001) on FePt/Pt(001) with  $R(O/c_o)=3.66$  is clearly in excess.

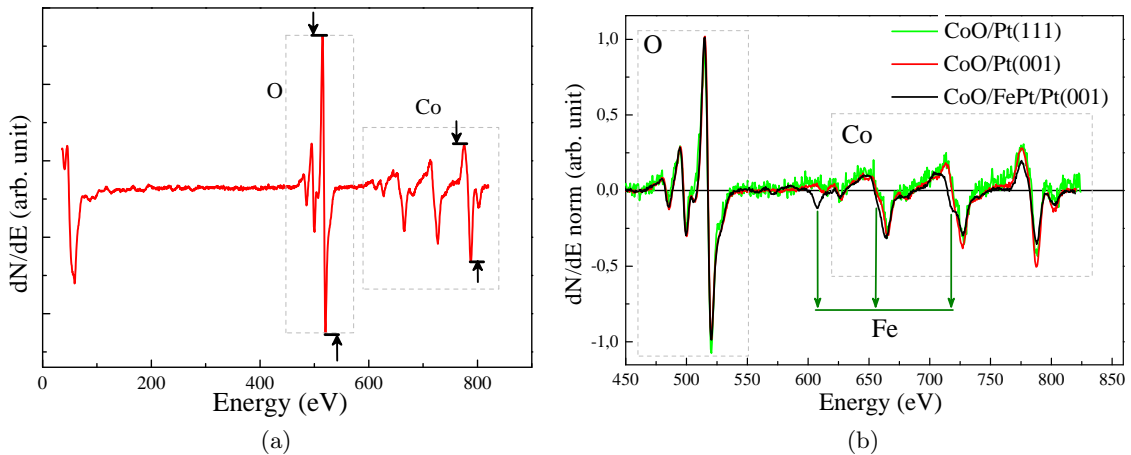


Figure 5.11: Auger electron spectra of the two samples studied in this chapter - CoO/Pt(001) and CoO/FePt/Pt(001) - and our reference CoO(1ML)/Pt(111) in derivative mode. (a) Large spectra of CoO/FePt/Pt(100) studied here. (b) Zoom on the region of Co and O peaks. Peaks are normalized by the more intense oxygen peak.

In Figure 5.11b are displayed Auger electrons spectra of three samples normalized by the maximum of intensity of highest oxygen peak (at 517 eV). Co peaks of this sample are reduced compared to the others and also deformed. Three small peaks underlined by green arrows coming from iron transition interfere. Hence, this high ratio arises from a lack of cobalt rather than an excess of oxygen. It is worth to note that despite our effort a small amount of Fe migrates to the surface and is oxidized.

X-ray absorption spectroscopy experiments performed at ID08 beamline at ESRF confirms that structure of this sample is more complicated than expected. X-ray absorption spectra (XAS) at the Fe and Co L edges have been recorded at 270 K with an incident beam perpen-

dicular and at  $20^\circ$  to the surface of the sample. Partial oxidation of Fe and partial reduction of Co are clearly observed. The extent of Fe oxidation is estimated by comparing the XAS spectrum of this sample with a linear combination of two others. XAS of metallic FePt and of ex-situ prepared  $Fe_3O_4(2\text{ nm})/CoO(4\text{ nm})$  bilayer were used as references as for Fe oxidation assessment in previous sample. For Co oxidation estimation, references of XAS and XMCD of metallic Co were used. All XAS have been normalized after background removal. To compare XAS of layers with different oxidation rate, spectra are normalized by the edge step and not by the maximum of absorption. The step of an absorption peak is related to the number of atoms taking part in the absorption process and is less sensitive to the local atomic environment compared to the peak.

Figure 5.12a shows linear combination (red full line) of the two reference spectra for energies where Fe absorbs. The data are well reproduced with a factor 0.57 for the Fe oxide (dotted line) and 0.43 for the pure metallic Fe (dash line). It gives very good agreement over the entire spectrum of the XAS sample around Fe edge energies, including the peak ratio in the  $L_2$  edge. Approximately one half of Fe is in oxide environment.

$L_3$  features of CoO are very sensitive to structural anisotropy (especially D feature). It is difficult and even sometimes tricky to obtain a linear combination of two references fitting another spectrum. We need a reference of CoO with the same orientation and strain to compare correctly. Since Co XMCD spectra is characteristic to a metallic ferromagnetic signal, we can estimate Co oxidation rate comparing XMCD maximum with a reference. In Co metallic, maximum of dichroism corresponds to about 59% of the maximum of the XAS signal which is compatible with values reported in literature.[149] Maximum of XMCD of this sample is evaluated at 8% of the maximum of absorption. Assuming that each Co atoms in metallic environment contributes to the signal dichroism, we estimate that 14% of Co atoms are metallic.

Considering the high potential of oxidation of Fe compared to that one of Co,[150] the large amount of Fe in oxide environment could have been expected. It confirms that Pt layer deposited after Fe in the growth of the previous sample protected the metallic layer decreasing the Fe oxidation from one half to one third. The presence of cobalt metallic is more embarrassing. How can be Fe oxidized before Co ? A plausible scenario consists in an exchange of Fe and Co atoms during the first annealing. Some Co atoms are hence inserted in the FePt / CoPt matrix, while some Fe atoms used temperature energy to get closer to the already oxidized surface. Fe and Co having almost the same electronic density, they can not be distinguished by surface x-ray diffraction.

## 5.3 Magnetic studies of CoO(100)/FePt(100)/Pt(100)

### 5.3.1 Magnetic studies by MOKE

Magnetic measurements on the CoO(001)/FePt/Pt(001) film (sample S19) were performed using the MOKE facilities installed in the ultra-high vacuum (UHV) multi-chamber system

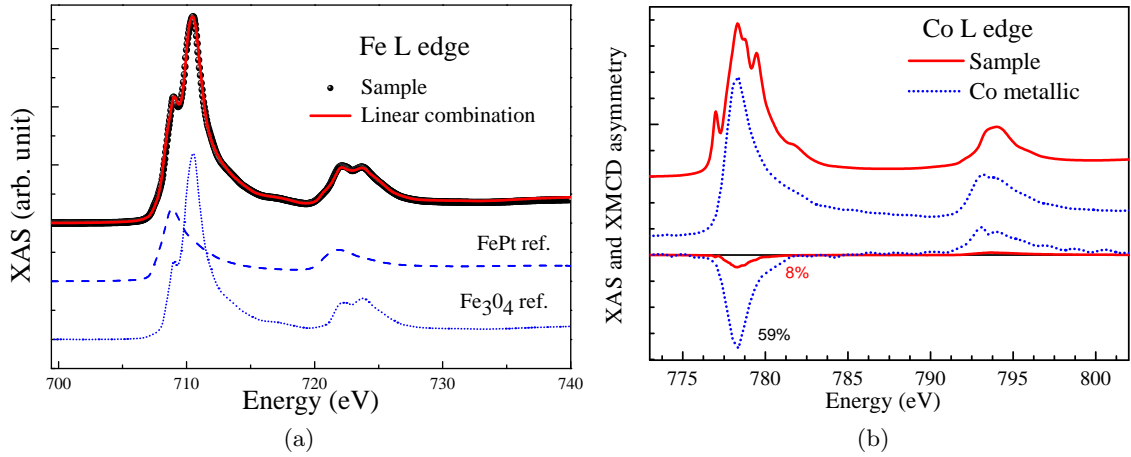


Figure 5.12: (a) Comparison of sample XAS (black dots) with linear combination (solid red line) of two reference spectra at Fe L edge. XAS of metallic FePt (dashed line) and  $Fe_3O_4/CoO$  (dotted line) are combined with  $\mu_{lin.comb.} = 0.55\mu_{Fe_3O_4} + 0.45\mu_{FePt}$  to reproduce sample XAS. (b) Comparison of sample XAS and XMCD (red full lines) at Co L edge with a reference of pure metallic Co (dotted lines). Maximum of dichroism is evaluated at 8%. Compared to the 59% of dichroism from the reference, it corresponds to 14% of Co atoms in metallic environment.

at Max Planck Institut of Halle in Germany and at Institut des Nanosciences et de la Cryogénie in Grenoble in France. The experimental conditions were similar to those reported for sample S8 (CoO(111)/FePt/Pt(001)).

Different field cooling experiments have been done. With a field perpendicular to the surface, the sample has been cooled three times: from 400 K to 5 K under + 5 kOe and from RT to 10 K under + 10 kOe and + 50 kOe. During the cooling the AFM moments order taking into account the FM moments, aligned with the field. To ensure a paramagnetic state of the CoO spins at the beginning of the process, the initial temperature is taken equal or higher than the Néel temperature of CoO (290 K). Then, from low temperature to RT, temperature is increased by step. At each step, we stabilized the temperature and magnetic loops are drawn looking for coercive field ( $H_C$ ) and exchange bias ( $H_{EB}$ ).

Whatever the field during the cooling, the coercive field is enhanced by one order of magnitude at low temperature compared to at RT (Fig. 5.13). This effect comes from exchange coupling between FM (FePt) and AFM (oxides) layers. Below the ordering temperature of the antiferromagnetic layer ( $T_N$ ), the reversing field has indeed to overcome the additional energy coming from the coupling. And the coupling is more stable that the temperature is low. Above  $T_N$ , the coercivity depends less on temperature. Hence the transition temperature of the oxides (largely AFM) is evaluated from the intersection of the two behaviors at  $T_N \approx 220$  K. The coercive fields at 5 K of this sample and previous (Sample S8) one are similar, but then  $H_C$  decreases more rapidly for this sample. An exchange bias shift is clearly observed at low temperatures after a field cooling. At 10 K, the value of  $H_{EB} \approx -120$  Oe. Exchange bias shift decreases rapidly and vanishes around  $T_B \approx 110-140$  K. AFM order of this layer and exchange

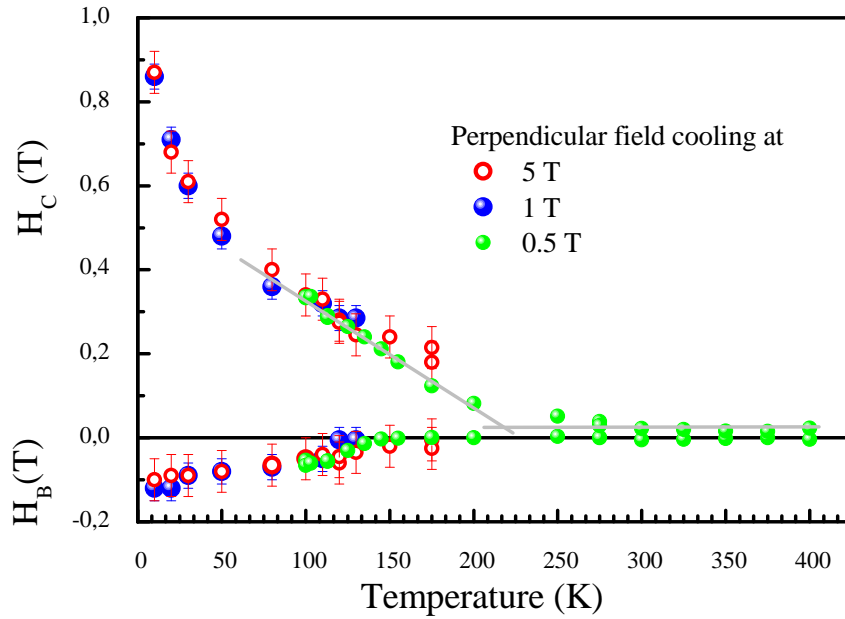


Figure 5.13: Evolution of coercive field  $H_c$  and exchange bias field  $H_B$  with temperature after different perpendicular field cooling.

coupling are less robust than in the previous sample as illustrated by magnetic loops and coercivity evolution in Fig. 5.14. No training effect have been seen during the hysteresis loops measurements.

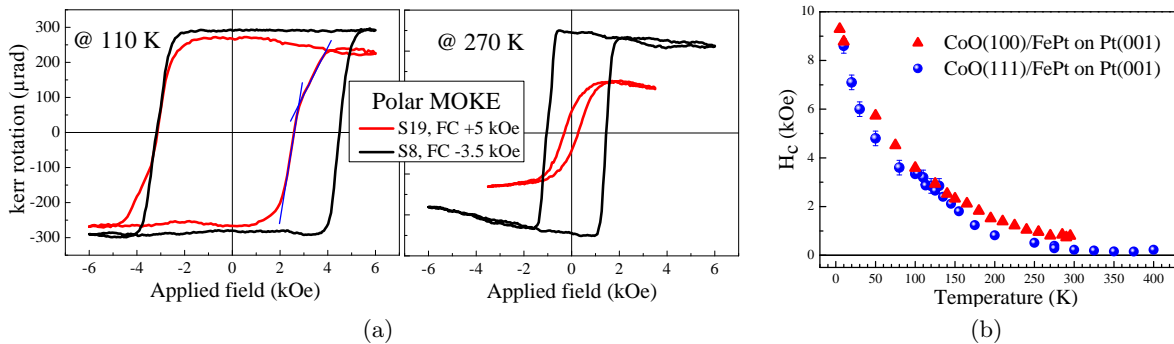


Figure 5.14: Comparison of magnetic results measured by polar MOKE from the sample presented here (sample S19) and in the precedent chapter (sample S8). (a) Hysteresis loops at 110 K and 270 K. (b) Evolution of the coercivities with the temperature.

The shape of the loops is a striking difference between hysteresis loops of this sample and those of the previous one. Even at low temperature, the slope - and so the anisotropy of the FM layer - is not as strong as we could expect from FePt in its chemically ordered  $L_{10}$  phase. Total perpendicular magnetic anisotropy of the sample is not characteristic to this phase. Moreover the shape evolves with temperature. A few loops are shown in Fig. 5.15. At low temperatures, the loops present two components difficult to interpret. The first part of

each reversal decreases abruptly, while the second one has a slight slope, as emphasized by the two lines in Fig. 5.14. One component disappears between 200 K and 250 K.

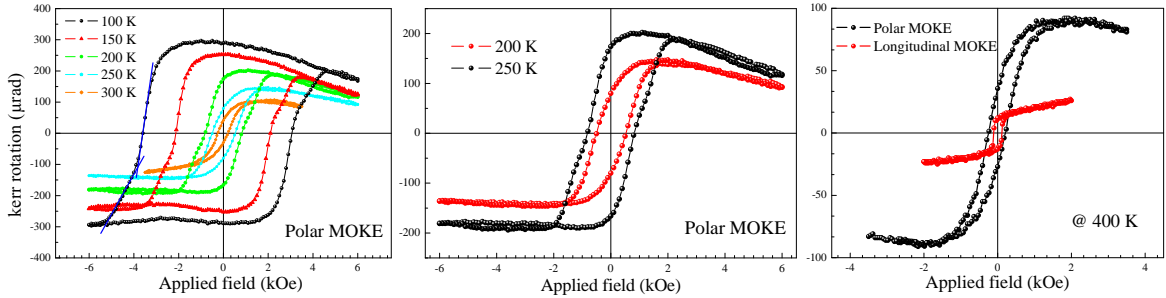


Figure 5.15: Hysteresis loops at different temperatures in polar and longitudinal MOKE configurations after a +5 kOe perpendicular field cooling.

Magneto-optic Kerr effects measured in longitudinal geometry show hysteresis loop for temperature above 250 K as displayed in Fig. 5.15. The intensity of the signal is always smaller in this geometry even if the amount of ferromagnetic atoms would be the same. It is also more difficult to measure because more sensitive to instabilities. Therefore, the coercive field could be evaluated only above 290 K. It is invariant between 290 K and 400 K and is equal to 110 Oe.

In summary, there are two out-of-plane ferromagnetic components below 250 K. Above 250 K, there are one out-of-plane and one in-plane components. The component, which stays out-of-plane, comes probably from FePt layer. The other components might correspond to only one component, which suffers a spin reorientation transition around 250 K. It might arise from other ferromagnetic contributions, that we will present in the next section.

### 5.3.2 Magnetic study by XMCD and XMLD

We carried out XMCD measurements at the Fe and Co  $L_{2,3}$  edges on the ID08 beamline at ESRF with Márcio Soares to separate magnetic moments of each element and XLD measurements at Co  $L_{2,3}$  edges to determine Co spin orientation. All the absorption spectra were recorded in total electron yield mode (TEY) at 270 K under a field of 10 kOe. Average of spectra circularly polarized right and left ( $\mu^+$  and  $\mu^-$ ) are presented in Fig. 5.12. XMCD asymmetries corresponding to the difference between the two spectra are displayed in Fig. 5.16. The XMCD signal at the Co  $L_3$  edge confirms that a part of Co atoms have a metallic environment and play a non negligible role in the ferromagnetism of the sample. The XMCD asymmetry is in absolute as large as those at Fe  $L_3$  edge. However XAS spectra at Co edges are higher than at Fe edges, because Fe atoms are buried under the CoO layer. The relative difference  $\frac{(\Delta\mu)_{max}}{\bar{\mu}_{max}} = \frac{(\mu^+ - \mu^-)_{max}}{((\mu^+ + \mu^-)/2)_{max}}$  is still larger at the Fe edge. At Fe  $L_3$  edge, the XMCD signal reaches 20% of the maximum of the XAS, while at Co  $L_3$  edge, it reaches 9.3% of the XAS maximum. Nevertheless, the signal at Co edge is important compared to the signal obtained from sample S8. A spin canting is not enough to explain its presence.

Moreover, the XMCD signals at Fe edge show an additional feature compared to those of FePt. The  $Fe_xO_y$  atoms takes part to the ferromagnetism of the sample. In conclusion, the ferromagnetism of the sample is made of three components : Fe atoms in metallic environment, Fe atoms in oxide environment and Co atoms in metallic environment. All of them follow a field of 1 T at 270 K. Measurements with the magnetic field aligned close and perpendicular to the sample surface demonstrate that the Fe oxide and Co contributions are more easily aligned along the surface. They probably correspond to the in-plane ferromagnetic component observed by MOKE experiments at 270 K.

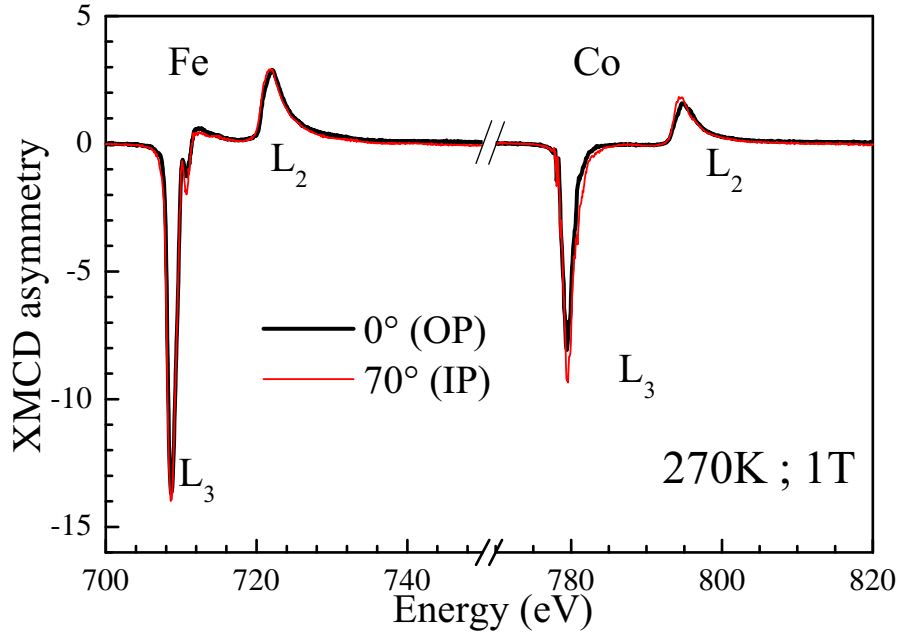


Figure 5.16: XMCD signals at the Fe and Co  $L_{2,3}$  edges with the beam incidence at  $0^\circ$  and at  $70^\circ$  to the normal to the sample. Each XMCD has been normalized by the maximum of the associated peak.

Figure 5.17 shows Co  $L_{2,3}$  XAS spectra with linear polarization of the beam parallel to the surface (the sample is perpendicular to the incident beam,  $\theta = 0^\circ$ ) and towards the normal to the surface (the surface of the sample is at  $\theta = 70^\circ$  of the incident beam). The XLD signature is the difference between the two XAS spectra. Four main features, labeled A to D, are observed in the  $L_3$  absorption peak. As seen in section 2.6, they are associated to electron transitions towards orbitals with different symmetries and show different behavior with the  $\theta$  angle. Taking the  $\theta = 0^\circ$  spectrum as reference, features C and D at higher energy are almost constant, while features A and B increase. As previously, we based on the intensity ratio  $R_{L3}$  between the peaks at C (778.74 eV) and B (778.26 eV) as function of  $\theta$  to measure the overall anisotropy. According to multiplet calculations the ratio  $R_{L3}$  is maximum when the polarization vector is perpendicular to the magnetic axis. Here the ratio is higher at  $\theta = 70^\circ$  when the polarization is out-of-plane. The Co magnetic moments are essentially in-plane. This result is in agreement with the discussion about the relationship between strain and orbital filling (cf section 4.2.1). Since the  $c/a$  ratio, characterizing the tetragonal distortion,



is  $>1$ , crystal field favors the lowest unpaired level to be in the  $d_{xy}$  orbital. The  $d_{xy}$  orbital is in the plane of the film. As the FePt spin axis is perpendicular to the layer, the coupling between Co spins and Fe spins in metallic environment at the interface is orthogonal.

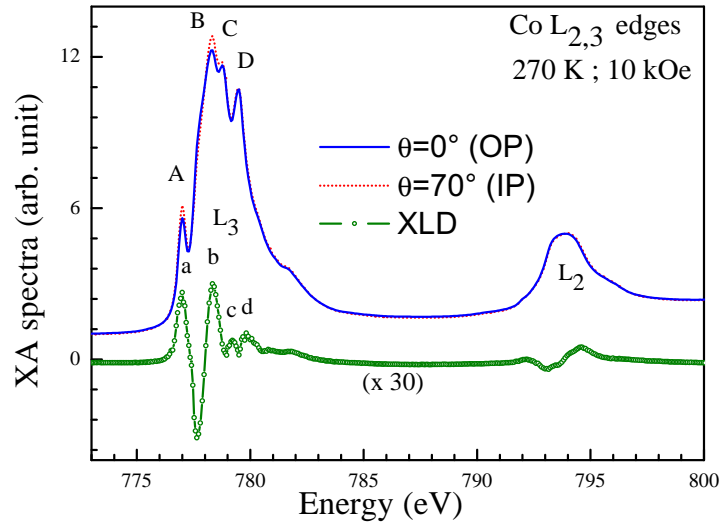


Figure 5.17: XAS and XMLD signal at Co L edge at 10 kOe

Van der Laan and coworkers described in ref. [117] Co  $L_{2,3}$  XLD signature in a crystal field for cubic and tetragonal point-group symmetries. They demonstrate by multiplet calculations that for cubic symmetry, the XMLD is a linear combination of only two fundamental spectra  $I_0$  and  $I_{45}$ .  $I_0$  is the spectrum obtained when the Co magnetic moment is along  $\langle 100 \rangle$  direction, while  $I_{45}$  spectrum corresponds to Co magnetic moment  $\vec{m}$  along  $\langle 110 \rangle$  plane. Both come from the difference of two XAS with polarization of the incident beam  $\vec{E}$  parallel and perpendicular to  $\vec{m}$ . In the first case, the rotation of the polarization related to the crystal axes can be in any plane-of-orientation containing  $[100]$ . In the second case, it is in the  $(001)$  plane. For tetragonal symmetry, four XLD spectra are required to reproduce any XLD results.

To compare the experimental data to these calculated results, we assume that the tetragonal distortion of CoO layer is small enough to consider an octahedral crystal field. The experimental XLD signal in Fig. 5.17 does not match perfectly a calculated one reported in Fig. 4.10 but gets close to  $I_0$  spectrum especially in the energy region of  $L_2$  transition. Features observed at  $L_3$  edges and labeled a to d might be identical but in different proportion. The XLD signature is a linear combination of  $I_0$  and  $I_{45}$  with an important weight for  $I_0$ . Therefore Co spins might point near the  $(001)$  and  $(010)$  equivalent directions in the CoO(001) layer, i.e. towards O atoms in the plane.

## Conclusion

We succeeded to grow a CoO oriented (100) on Pt(001) and FePt/Pt(001) by tuning the interface chemistry. The layer is partially relaxed and imposes a field of strain on the substrates.



It gives rise to a field of atomic displacement in the substrate expressed by satellites peaks surrounding Pt Bragg peaks. They disturb the measurement of the CoO diffraction pattern. Growth and structure have been studied *in situ* and *in real time* by SXRD. The CoO layer presents an important tetragonal distortion with  $c/a = 1.05(1)$  on Pt(001) and  $1.03(1)$  on FePt. Its interface with substrate is rough.

During the CoO growth on FePt, a portion of Fe and Co atoms likely exchange their sites due to the high potential of Fe oxidation. According to XAS and XMCD comparison around one half of Fe atoms are in oxide environment, while about 14% of Co atoms are in metallic environment. It might be interesting to add 1 ML of Pt at the interface to increase the resistance to corrosion of the FePt layer.

We carried out MOKE, XMCD and XMLD experiments to investigate the magnetic properties of CoO(100)/FePt(100) bilayer. The two layers are coupled after a perpendicular field cooling up to 110-140 K. Below 250 K, there are two out-of-plane components. Above, one is in-plane and another one is out-of-plane.

XMCD has been measured at 270 K at Fe and Co L edges. It shows three contributions to the ferromagnetism of the system: Fe atoms in metallic environment, Fe in oxide environment and metallic Co atoms. The Fe oxide and Co contributions are more easily aligned along the surface at 270 K. The Fe metal spins are aligned out-of-plane. Probably the FePt layer keeps its perpendicular anisotropy whatever the temperature, while the Fe oxide and Co contributions experiments an out-of-plane reorientation transition at around 250 K from out-of-plane to in-plane.

According to XMLD angular dependance, Co spins are oriented in-plane, which is in agreement with its tetragonal distortion. From the features of the XLD signature, Co spins might point near the (001) or (010) directions, towards oxygen atoms in the surface plane.

In conclusion, the system is more complicated than expected and could probably be improved by the addition of 1 ML of Pt at the interface between the FM/AFM layers. It should avoid Co and Fe site exchange and so the presence of Fe oxide and Co metal. The magnetic results are however promising, since the two layers are coupled. The coupling is once again orthogonal. We have determined the spin orientation of each wished layer and have an idea of the behavior and the origin of the non expected contributions. Last but not least, we demonstrate that the orientation of CoO epitaxial film can be tune on Pt(001) by the appropriate interface chemistry.

## Chapter 6

# Fe/CoO - $Fe_3O_4$ /CoO systems on Ag(001)

### Contents

---

<b>6.1</b>	<b>CoO/Fe/Ag(100) system</b>	<b>116</b>
6.1.1	Fe/Ag(001)	118
6.1.2	CoO/Fe/Ag(001)	120
<b>6.2</b>	<b><math>Fe_3O_4</math>/Ag(100)</b>	<b>123</b>
6.2.1	Growth	123
6.2.2	Structure	127
6.2.3	Distinction between magnetite and maghemite	129
6.2.4	Mosaicity	133
<b>6.3</b>	<b>CoO/<math>Fe_3O_4</math>/Ag(001)</b>	<b>133</b>
6.3.1	Growth and structure of CoO on $Fe_3O_4$ /Ag(001)	134
6.3.2	X-ray absorption (preliminary) study	135
<b>6.4</b>	<b>CoO/Ag(100)</b>	<b>138</b>

---

The CoO/Fe bilayer on Ag(001) is a widely studied exchange biased system. First of all, many authors used it to explore the behavior of the antiferromagnetic CoO layer, when it is coupled to a FM layer. Secondly, thickness effects are important in Fe layers deposited on Ag(001), whether concerning their magnetic or structural properties. In addition, they are difficult to determine experimentally and so are still in debate. Thirdly, the coupling of the two layers is made through an iron oxide, which develops at the interface.

In the same framework, we were interested in the CoO/ $Fe_3O_4$  bilayer on Ag(001). Magnetite is a half-metallic ferrimagnet predicted by local spin density approximations (LSDA) calculations to possess 100% spin polarization (SP) at the Fermi level (cf section 1.2.2). It is

thus a good candidate for spin injection and a very attractive electrode in tunnel magneto-resistance (TMR) devices. Nevertheless experimental studies of  $Fe_3O_4$  epitaxial thin films have shown limited SP.[151] Using spin and angle-resolved photoelectron spectroscopy at RT, Fonin *et al.* observe that the maximum of SP depends on the surface orientation.[52] The measured SP of  $Fe_3O_4(001)$  is about -55%, even much lower than the -80% obtained for  $Fe_3O_4(111)$ . It points out the importance of structure and interface in magnetic properties of thin films.

$Fe_3O_4$ /CoO bilayer exhibits exchange bias effect even with a CoO layer as thin as 5 Å.[17] It has been proposed as a component in all-oxide spin-valves or TMR devices. Although the two oxides do not have the same crystal structure, a good epitaxy with small strain is expected thanks to the matching of the lattice parameters:  $a_{CoO} = 4.261$  Å,  $a_{Fe_3O_4} = 8.396$  Å. The size of the primitive unit cells of the O sublattices differs only by 1.5%.[152]

## 6.1 CoO/Fe/Ag(100) system

The CoO/Fe bilayer on Ag(001) has been widely studied for its exchange bias properties. One of the striking results concerning this system was the observation of a small amount of uncompensated spins on cobalt atoms detected by XMCD measurements. Among them, only a small amount is pinned (frozen).[153] The interface between iron and cobalt oxide is quite complex. Although the frozen and rotatable spins are found uniformly distributed in the film, a larger fraction of the rotatable spins occurs for thinner CoO films, while for larger thicknesses the spins are mainly frozen.[132] The role of frozen and rotatable spins in the exchange coupling in FM/AFM system is a burning issue. Ji *et al.* separate the magnetic anisotropy in a unidirectional component due to the exchange bias, a uniaxial one linked to the field cooling

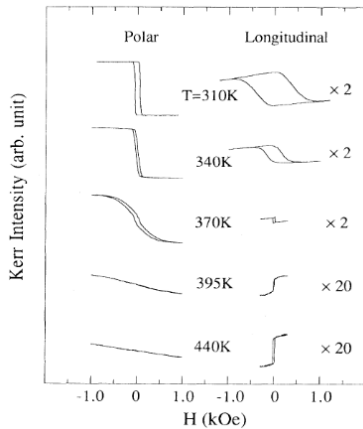


Figure 6.1: The hysteresis loops for (left panel) perpendicular (labeled polar) and (right panel) in-plane (longitudinal) magnetic field configurations for a 6.0 MLs Fe films at different temperatures. (taken from ref.[154])

direction, and in the 4-fold magnetic anisotropies of the Fe film. They used the dependence of CoO frozen spins with thickness to establish that only the uniaxial magnetic anisotropy follows them.[155] Exchange bias and coercive field have been found to have very different and complicated dependence on the AFM-layer thickness.[132]

As regards the FM Fe layer, ultrathin Fe layers on Ag(001) present two main interests from the magnetic point of view. First theoretical calculations predict an enhanced magnetic moment up to 2.98-3.01  $\mu_B$  for Fe layers in contact with Ag due to the broken symmetry of the interface. Wooten *et al.* observed indeed indirectly a 20%-30% enhancement in the first 2-3MLs by comparing with

the bulk moment. Jal *et al* confirmed this result recently, using x-ray resonant magnetic scattering.[19, 156] Second, Fe films exhibit two spin orientations depending on the Fe thickness. The spins are oriented out-of-plane up to about 4-6 MLs. Above, a spin reorientation transition (SRT) takes place (Fig. 6.1). In thicker Fe films, the moments lies in-plane with easy axes along Fe  $\langle 001 \rangle$ . [154, 44] In addition, in thin Fe films, according to Pappas *et al.* the magnetic moments switch from perpendicular to in-plane as the temperature increases. Only 1-2 annealing cycles to 300 K is sufficient to stabilize the switching.[16] Although Fe/Ag(001) films have been extensively studied, the causes of such a reorientation remain unclear. Schaller *et al.* observed by STM measurements that after an annealing at 470 K, an initial 4.5 MLs rough surface is transformed into island with single atomic steps.[157] But uncertainties of the structural parameters and discrepancies of the exact thickness where the reorientation occurs makes the comparison of the experimental data with theory difficult.

In the ultra-thin regime ( $<6\text{ML}$ ) accurate determinations of these parameters are scarce. For instance, while a *bcc* Fe structure for a thickness  $t > 6$  MLs is clearly identified,[42] the stabilization of the *bcc* Fe for the thinnest layers is not assessed. Canepa *et al.* found a slightly larger out-of-plane distance than expected for *bcc* Fe and Hahlin *et al.* observed strong deviations in their simulation of Fe structure.[42, 158] Intermixing and distortion have been suggested as explanation. The morphology in the first steps is also controversial.[159] According to RHEED experiment of Egelhoff *et al.*, a layer-by-layer growth is installed up to 5 to 6 layers for samples grown at room temperature, in contrary to STM measurements where Fe film morphology gradually deviates from the island growth towards the two-dimensional (2D) growth.[43, 158] Moreover, these parameters are strongly influenced by substrate quality, deposition rate or annealing procedure, which are rarely properly addressed.

Last but not least, the interface between iron and cobalt oxide is a warm subject. The direction of the anisotropy, either in the FM or in the AFM layers,[141] and the morphology of the interface are among fundamental parameters determining the exchange coupling. Full coverage with CoO causes the formation of a mixed  $Fe_2O_3 - Fe_3O_4$  interfacial oxide layer. The amount of iron-oxide varies with the layer thickness below 8MLs of Fe. Above, it reaches a constant value of about 2 ML.[45] Even a reduction of CoO has been observed.[150] Mlynczak *et al.* followed three recipes of CoO/Fe bilayers growth on MgO to vary the amount of oxide at the interface and identify their impact on magnetic properties. EB value is largest for the over-oxidized interface, while coercivity shows different temperature dependencies following the oxidation rate.[160]

With the experiments presented here, we first aimed at investigating the correlation between structure, morphology and magnetic behaviour of ultra-thin Fe layers on Ag(001). In particular, we wanted to verify the limit of the pseudomorphic growth and determine inter-layer spacing to see if there is any relation with the magnetic reorientation. Else, we intended to shed some light on the growth mode and the Fe structure in the 0-6 MLs range. Secondly, we would like to well-characterize a CoO/Fe/Ag(001) sample grown under well-controlled UHV conditions, and couple several advanced experimental techniques (*ex situ* MOKE, *in*

*in situ* GIXRD, reflectivity and polarized XAS) to probe structural organization, morphology and magnetism.

### 6.1.1 Fe/Ag(001)

The first steps of Fe growth on Ag(001) were studied *in situ* by surface x-ray diffraction at 22 keV photon energy. At this energy, Ag critical angle is about  $0.16^\circ$ . The measurements, except when it is precised in the text, have been performed at  $0.48^\circ$ , three times the critical angle.

Ag substrate was cleaned following the standard procedure of cycles of ion sputtering ( $P_{Ar^+} = 4.10^{-6}$  mbar, 800 eV) and annealing at 800 K during about 10 minutes. Auger electron spectroscopy measurements allow to check chemical composition of the surface. To reduce intermixing, Fe atoms were deposited at room temperature. Fe deposition rate was calibrated with a quartz balance at 1 ML per 4, 6 and 11 min depending on the experiment. Then a moderate annealing of about 30 minutes up to 470 K was done to improve the film order. The growth was followed in real time scanning along the (1-1) CTR to track the perpendicular lattice parameter  $c$ . The momentum transfer was also scanned parallel to the surface to cross this same (1-1) rod at  $l = 2.7$  and  $l = 2.8$  and check the pseudomorphism of the layer.

We found that Fe grows in registry with Ag(001) substrate up to at least 14 MLs. It keeps the in-plane lattice parameter of silver  $a_{Ag}$  even after annealing at 470 K. In the surface cubic cell, the lattice parameter is  $a_{Ag} = 2.889 \text{ \AA}$ , larger than the bulk *bcc* Fe ( $a_{Fe} = 2.8665 \text{ \AA}$ ) by only 0.8%. This result excludes the relaxation as an explanation for the SRT with thickness.

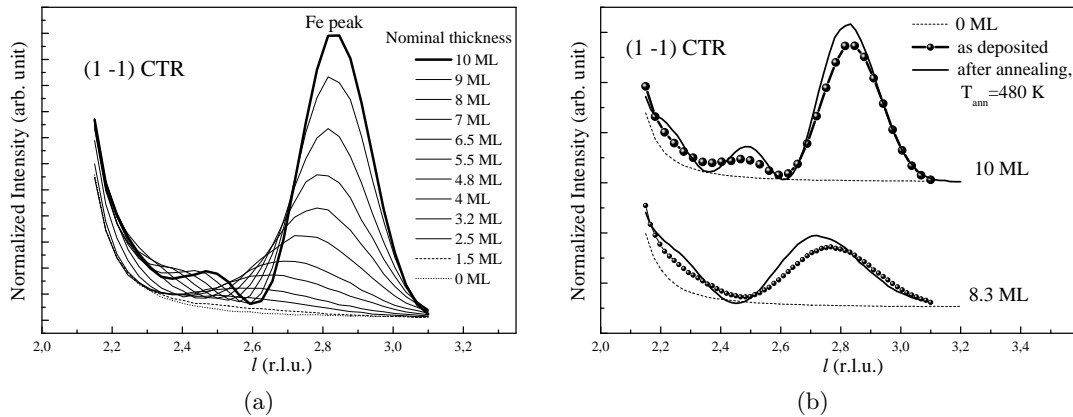


Figure 6.2: Fe/Ag(001): (a) Real time evolution of the  $(1\bar{1})$  CTR during Fe deposition. (b)  $(1\bar{1})$  CTR before and after annealing of 8.3 MLs and 10 MLs Fe films on Ag(001)

Interestingly the out-of-plane parameter  $c$  is not those expected for a growth at constant volume as often in a metal growth. Considering a *bcc* Fe bulk cell volume of  $23.55 \text{ \AA}^3$ ,  $c$  should be around  $2.822 \text{ \AA}$ . It even evolves during Fe on Ag(001) deposition without reaching such value as can be seen in Fig. 6.2a. The position of the peak increases from about 2.6 to

2.8 in reciprocal lattice units, leading to a decrease of the out-of-plane lattice constant to 2.9 Å. The tetragonal distortion characterized by the  $c/a$  ratio decreases with thickness.

For films grown on Ag, annealing is a process subtle to manage. It could improve the morphology of the surface, reducing the surface roughness but also induce intermixing and segregation due to the high mobility of the Ag atoms.[48] If the annealing is too long or the annealing temperature too high, Fe atoms are buried in the substrate.[158]

In Fig. 6.2b, we show the effect of the annealing on the  $(1\bar{1})$  CTR for the 8.3 ML and 10 ML films. On the one hand, Fe peaks sharpen and Kiessig oscillations assert themselves with the same in-plane positions. It indicates that the roughness reduces, while the layer stays pseudomorphic. The thickness gets closer to the nominal value. It seems that some Ag atoms segregate on the top of the layer. On the other hand, the Fe peak position move back towards the Ag Bragg peak. The  $c$  lattice parameter increases as if the Fe film contains more Ag atoms. If we consider naively that the layer is made of an alloy of Ag-Fe, the fraction  $x$  of the Ag atoms in the Fe layer can be deduced from Vegard's law assuming volume conservation:

$$(1 - x) * c_{Fe} + x * c_{Ag} = c_{experimental}, \text{ or } x = \frac{c_{exp} - c_{Fe}}{c_{Ag} - c_{Fe}}.$$

For 8.3 MLs,  $c_{Fe}$  is evaluated at 2.94 Å corresponding to 10% of Ag atoms before annealing and 14% after annealing. Moreover, Auger electron spectroscopy presents a slight increase of Ag signal compared to Fe after the annealing, which accentuates the role of Ag atoms but does not close the discussion. These structural changes should be taken into account to understand the SRT with temperature.

These qualitative and remarkable outcomes on Fe growth deserves a quantitative study. We intended to analyze complete sets of 5 CTRs measured for some particular coverages (4, 8 and 10 MLs) using the model layer procedure as seen before.

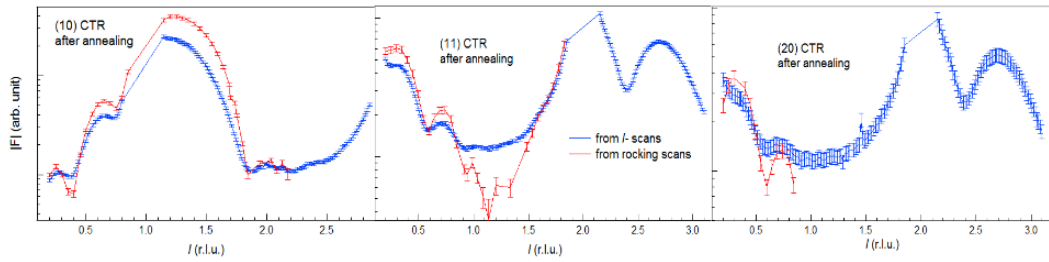


Figure 6.3: Fe/Ag(001): (10), (11) and (20) Ag rods after annealing. Structure factor amplitudes extracted from rocking scans are precise but scarce in contrary to those from  $l$ -scans.

Most of the data were collected through  $l$ -scans. Rocking scans performed on the same regions than  $l$ -scans show that the Fe rod is too wide to be properly integrated through  $l$ -scan and the background is not correctly evaluated (Fig. 6.3). It results that intensity collected with  $l$ -scans clearly underestimate features of the rod. Between sample and detector, slits are used to decrease the background. This time, slits were chosen too thin and cut a part of the reflected beam. It expresses that the rods are particularly large in-plane due to a small size of the coherent domains.

In addition, the portion of the rod integrated with rocking scans is too narrow to allow a full structural resolution of the deposited layer. Nevertheless, we tried to resolve the film structure by a model fitted to reproduce the structure factor amplitudes. None of tested model fitted well. Uncertainties are too important. Generally, models accept well a Fe/Ag intermixing and have a tendency to a non-constant out-of-plane interplanar distance. This is compatible with the idea that intermixing between Ag and Fe is important at the interface and is smaller for planes away.

### 6.1.2 CoO/Fe/Ag(001)

As next step, CoO was grown on the surface of Fe(8MLs)/Ag(001). To avoid Fe oxidation during growth, 2 MLs of Co were first deposited on the surface at RT. The evaporation rate was calibrated with a quartz microbalance at 1 Å per 7 minutes. As we expected owing to the small lattice mismatch (2%) between the Co *bcc* and Ag surface unit cell,[145] Co grows in registry with Fe/Ag(001). Subsequently, the sample was exposed to an oxygen pressure of  $5 \times 10^{-7}$  mbar during 10 minutes. Finally, a reactive Co deposition under the same pressure followed.

Co oxide layer is partially relaxed with the in-plane and out-of-plane lattice constants  $a = 4.207(3)$  Å and  $c = 4.28(2)$  Å. These values have been determined using a set of 33 scans in-plane (*h*-scans, *k*-scans) and out-of-plane (*l*-scans) around CoO peaks to a total of 9 non equivalent CoO peaks. The important proximity of CoO peaks with those of Ag substrate complicates the determination of their exact positions. It forces to the analysis of high order reflections in the reciprocal space, more separated from the Ag substrate ones. Normalized intensities have been fitted with gaussian curves. The results have been averaged. Standard deviation between all fitted values gives error bars. Compared to the bulk CoO, there is a small reduction (-2%) in the unit cell volume:  $V = a_{CoO}^2 * c_{CoO} = 75.8 \text{Å}^3$  relatively to  $4.261^3 = 77.36 \text{Å}^3$  for the bulk crystal. No hexagonal peak coming from a CoO (111) phase has been detected. In conclusion, CoO grows (001) on Fe/Ag(001) with a slight tetragonal distortion characterized by a  $c/a$  ratio of about 1.017.

From the in-plane rod width, we estimate the characteristic in-plane domain size about 2-3 nm, which is relatively small. From out-of-plane rod width or from the period of Kiessig fringes, we estimate the thickness of the deposited film. For each growth, the calculated thickness is in good agreement with the nominal one, expressing that all Co atom deposited is a part of CoO layer.

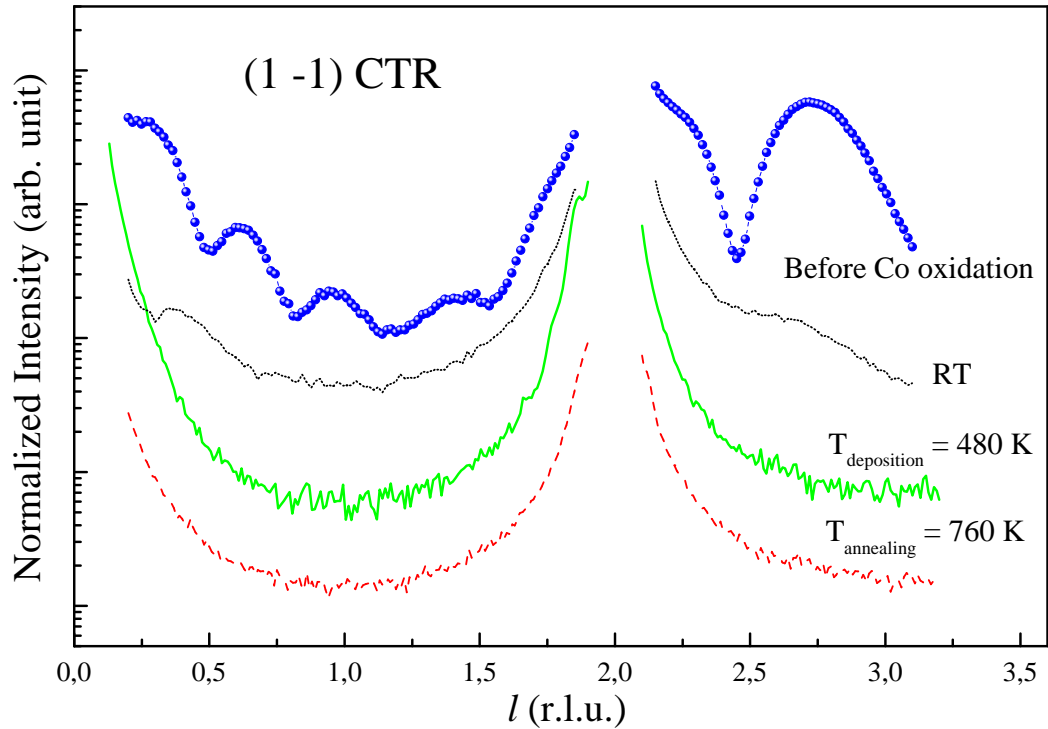


Figure 6.4: CoO/Fe/Ag(001):  $(1\bar{1})$  CTR before and after CoO growth on Fe (8 MLs)/Ag(001) with different conditions: at RT, at 480 K during the reactive deposition, after annealing at 760 K.

Crystal truncation rods change completely with CoO deposition. Fe peaks are drastically reduced and Kiessig oscillations mainly disappeared. Fig. 6.4 shows  $(1\bar{1})$  rod after CoO growth in different conditions. Impact depends clearly on the temperature of the substrate. Dotted (black) lines represent  $(1\bar{1})$  rod after CoO growth entirely at RT. A small bump can still be observed at the previous Fe peak position as well as some residual thickness oscillations. By comparison with the rod before oxidation (blue circles), one can be confident that the whole Co layer is oxidized and a part of the Fe layer is oxidized, too. The Fe peak vanishes after a Co deposition with the sample held at 480 K (solid line). Dash lines correspond to a CoO growth followed by an annealing at 760 K. At this temperature, CoO rods sharpen expressing an order improvement in the oxide layer. However neither Fe order peaks nor oscillations survived. Fe is probably completely oxidized.

This iron oxide at the interface between Fe and CoO films, which stands up even for a room temperature oxidation preceded by a 2 MLs Co deposition, may play a major role in the exchange coupling and should be deeply studied. We looked for diffraction peak of the different Fe oxides. Small peaks of  $Fe_3O_4$  spinel have been detected on a sample with CoO growth at RT. The maximum of diffracted intensity at these reflections is around 600 counts, compared to CoO peaks about 3000 counts. The amount of such phase is small. It is well ordered .



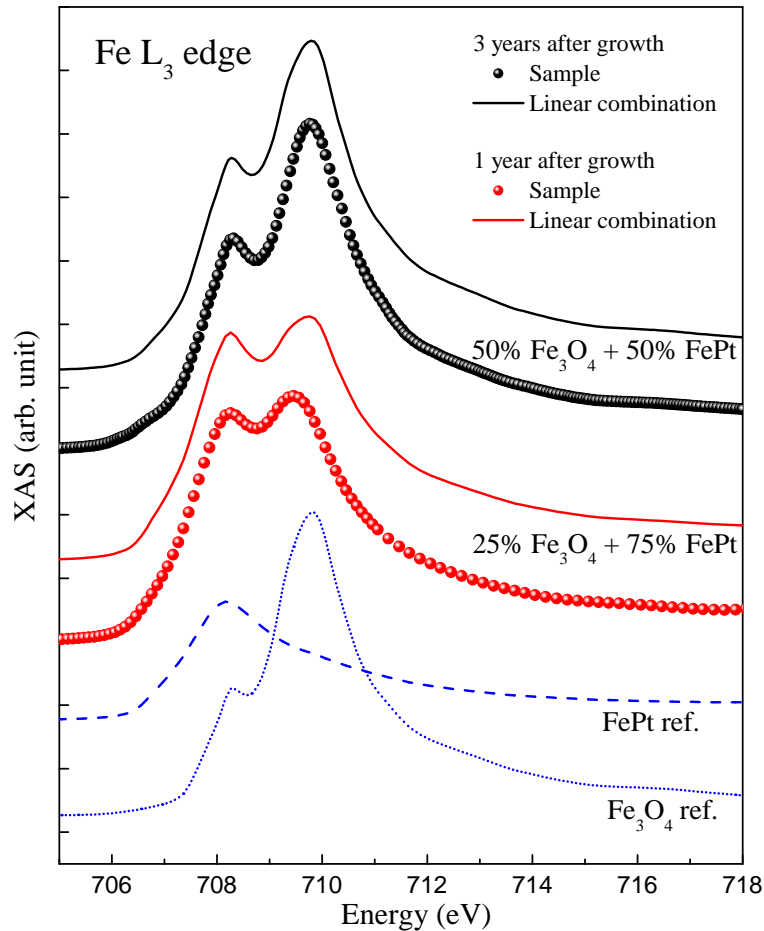


Figure 6.5: CoO/Fe/Ag(001): Comparison of sample XAS (dots) with linear combination (solid lines) of two reference spectra at Fe absorption  $L_3$  edge absorption. XAS of metallic FePt (dashed line) and  $Fe_3O_4$ /CoO (dotted line) are combined to reproduce sample XAS. Sample spectrum is different whether it is collected 1 (red) and 3 (black) years after growth. Oxidation rate increased in the film.

X-ray absorption spectroscopy measurements at Fe  $L_3$  edge have been performed *ex situ* at PGM beamline at LNLS to assess the oxidation rate of Fe layer on the sample in which CoO was grown at room temperature. According to diffraction results a part of ordered Fe layer should be non oxidized. A linear combination of spectra from the metallic FePt layer and an *ex-situ* prepared  $Fe_3O_4$ (2 nm)/CoO(4 nm) bilayer has been fitted to reproduce experimental spectrum of this sample. All spectra are displayed in Fig. 6.5. Data are well reproduced with a factor 0.25 for the Fe oxide (dotted line) and 0.75 for the pure metallic Fe (dash line). The equivalent of 2 MLs of Fe are in oxide environment. This is much less of what would be expected at first sight from the intensity decrease of the Fe peak in Fig. 6.4. This last one can be explained with a lost of lateral coherence of metallic iron domains, which widen the related diffraction peaks in reciprocal space.

This experiment was repeated almost two years later. Surprisingly the absorption peak changed. New data are well reproduced with a factor 0.5 for the Fe oxide and the pure

metallic Fe (Fig. 6.5). This result indicates that Fe layer oxidizes with time. 3.8 nm of CoO (approximately 18 MLs of CoO(001)) is not enough to protect Fe layer. Such a unstable and uncontrolled oxidation oriented our research toward a more stable system where the Fe layer is already completely oxidized.

## 6.2 $Fe_3O_4/Ag(100)$

We have elaborated magnetite layers on Ag(001) by molecular beam epitaxy in UHV chamber whose base pressure is about  $1 \times 10^{-10}$  mbar. Growth and structure have been investigated *in situ* in two chambers. One is at BM32, the other one is at Néel Institute and is dedicated to surface analysis with a scanning tunnel microscope (STM) and low-energy electron diffraction (LEED) set-up. Both possess also Auger electron spectroscope (AES) which is the chemical counterpart of the other structural equipments. X-ray beam was set at 22 keV photon energy.

### 6.2.1 Growth

Growth of some characteristic samples are detailed in Table 6.1.

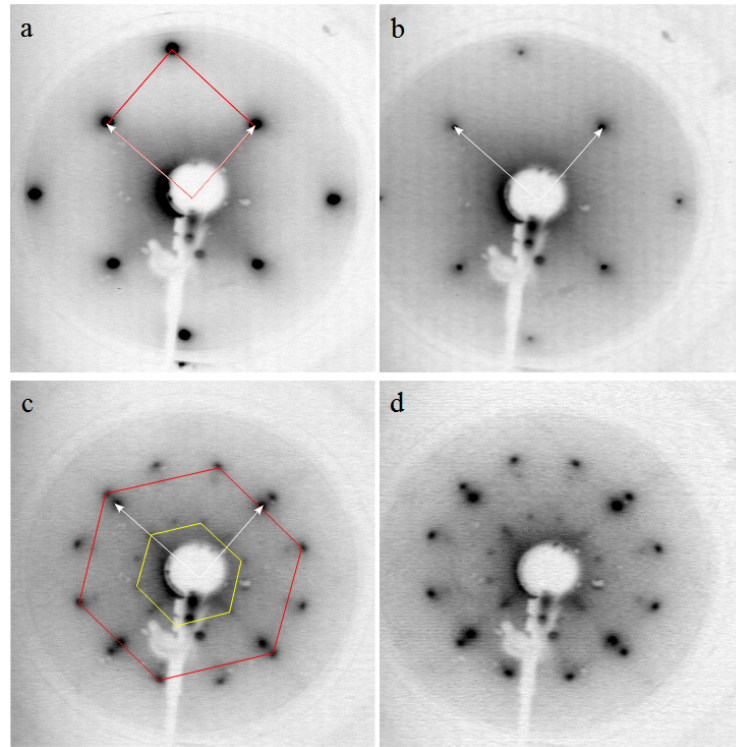


Figure 6.6:  $Fe_3O_4/Ag(001)$ : LEED patterns for (a) clean Ag(100) substrate; (b) 1 ML of Fe oxide on Ag(100); (c) 5 MLs of Fe oxide annealed at 620 K and (d) 5 MLs of Fe oxide additional annealed at 500 K. The electron energy of the LEED pictures is 60 eV. Red square and hexagon highlight unit cell of Ag(001) and Fe oxide overlayer. White arrows refer to [001] and [010] directions in Ag reciprocal lattice.

In the first attempt, one ML of Fe was deposited at room temperature followed by 5 min of oxidation under a pressure of  $P_{O_2} = 1.8 \times 10^{-6}$  mbar. Islands of about 4 nm long and 1 nm thick are observed in STM measurements, although only spots referring to Ag substrate pop up in the LEED pattern. Subsequently, 4 MLs of Fe were deposited under oxygen pressure of  $P_{O_2} = 2 \times 10^{-6}$  mbar followed by an annealing made of three stages. The temperature was increased by steps of 10 minutes at 320 K, 570 K and 620 K. Nothing appear on LEED images before annealing at 620 K. We can conclude that this temperature is a minimum to order the layer. The LEED pattern is composed of two nice crowns corresponding each to two hexagons rotated by  $90^\circ$ . One of them is marked with red solid lines in Fig. 6.6. Fe oxide achieved is textured (111). Substrate remains visible with the four supplementary spots forming a square. Then 5 MLs have been added under the same oxygen pressure followed by 20 minutes of annealing at 500 K. The spots in the LEED image become brighter and thinner (Fig. 6.1d). New layers are oriented regarding previous ones, i.e. (111).

From distance between spots in the small yellow hexagon, we evaluated the in-plane lattice constant of Fe oxide in the surface unit cell at around 6 Å. The larger red hexagon refers to the oxygen-sublattice surface unit cell with an in-plane distance of about 2.98 Å. These values are in agreement with the lattice constants of  $Fe_3O_4$  (111) surface described in literature.[52]

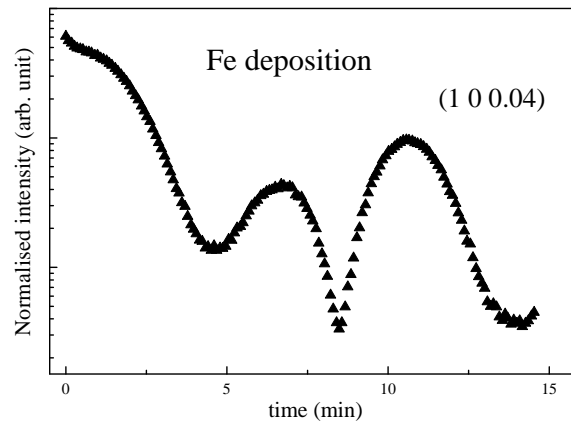


Figure 6.7: Fe/Ag(001): Growth-oscillations for Fe on Ag(001) at RT around (1 0 0.04).

To growth the wanted  $Fe_3O_4(001)$  orientation, we followed a different method. A pseudomorphic Fe(001) layer was deposited previously to the oxidation, in the hope to keep the orientation despite insertion of oxygen atoms. We thus deposited 6 MLs of Fe at room temperature. Fe deposition was followed in real time on the anti-Bragg position (1 0 0.04) as shown in Fig. 6.7. For a layer-by-layer growth mode, the oscillations are regular. It is clearly not the case. It may arise a large intermixing of iron and silver in the first steps.

Then we introduced an oxygen flux during 5 min leading to a pressure of  $P_{O_2} = 1 \times 10^{-7}$  mbar. After, a small peak appears at (0,48 0 1,48) where we expect the strongest spinel peak ((113)<sub>spinel</sub> peak).<sup>1</sup> The layer is ill ordered and we did not observe other diffraction

<sup>1</sup>The relationship between Ag reciprocal space and spinel peak positions is given in 6.2.2 and detailed in the appendix A.

peaks. Thus the sample was annealed under an oxygen pressure of  $P_{O_2} = 1.5 \times 10^{-7}$  mbar to let the layer orders with oxygen. The temperature shut down before oxygen pressure to avoid Fe reduction.[161] Complete set of spinel peaks is then detected.

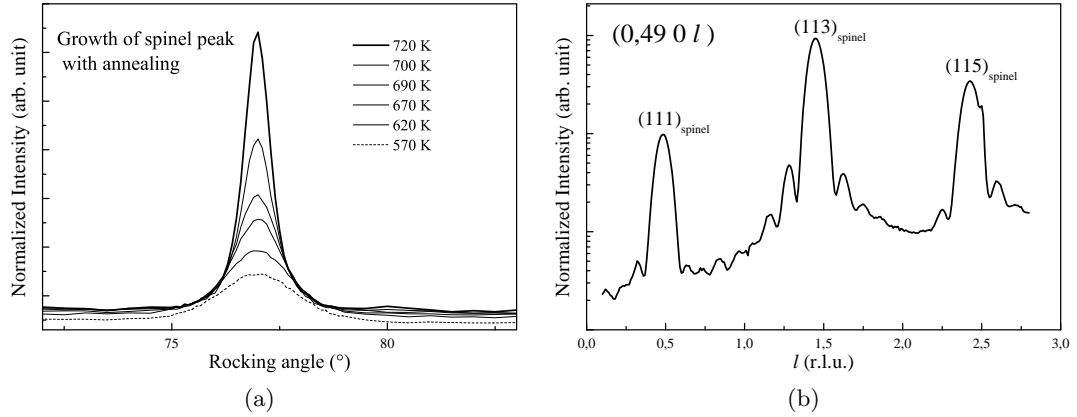


Figure 6.8:  $Fe_3O_4/Ag(001)$ : Spinel peaks. (a) Growth of  $(111)_{spinel}$  during annealing of 4 MLs of Fe oxide and (b)  $(11)_{spinel}$  rod of 8 MLs of Fe oxide after annealing at 725 K.

The temperature is a key parameter in the growth of spinel film. During the annealing in oxygen, the higher the temperature (in the range spanned during the experiment), the better the order. Fig. 6.8a presents the  $(111)_{spinel}$  peak, characteristic of the spinel, scanned during the annealing in oxygen of a further sample obtained by the deposition of 4 Fe MLs. The peak increases and sharpens with temperature, while Kiessig oscillations rise. The presence of these nice fringes ensures that the layer is well-ordered with a sharp interface with Ag. High potential of Fe oxidation might favor demixing between Fe and Ag at the interface.

The Fe/O AES peaks ratio is almost constant showing that oxygen content in the layer is stable with annealing under oxygen pressure. It remains to be seen whether this content corresponds to the expected magnetite  $Fe_3O_4$  or to maghemite  $Fe_2O_3$ , which has a close lattice constant, as seen in section 1.2.2. The presence of other Fe oxide phases or orientations in this film can be excluded. No peak coming from  $Fe_3O_4$  hexagonal phase or  $\alpha - Fe_2O_3$  (hematite) phase have been detected.

In one attempt (A3), Fe was deposited with substrate held at 475 K. We observed a segregation of silver at the surface. A thin Ag layer seems floating on the surface even after Fe oxidation, annealing and CoO growth. Several pieces of information well match this assumption. First, Fe/Ag peaks ratio in AES spectra is smaller in this sample compared to in the others whatever the step of Fe growth (Fe deposition, oxidation, annealing). After Co oxide deposition, no Fe can be detected by AES. But O/Ag peaks ratio is still of the same order of magnitude, and is smaller than in the other preparations. Second, we detected by SXRD peaks of low intensity with hexagonal in-plane symmetry (Fig. 6.9a). Intensity collected by scan with momentum perpendicular to the surface ( $l$ -scan) is almost continuous (Fig. 6.9b). It means that the layer at the origin of these peaks is almost 2D. When we reduced the grazing

angle to be more sensitive to the surface, these peaks became more intense. One monolayer of hexagonal is on the surface. It is probably made of silver.

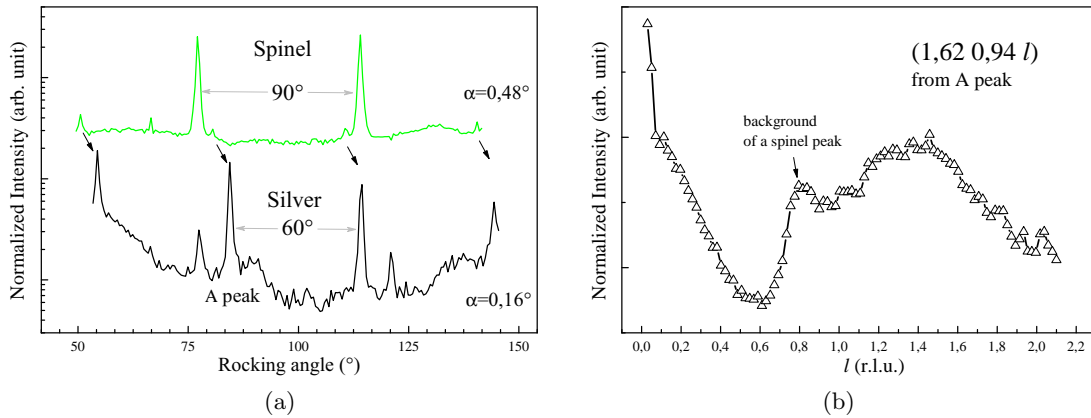


Figure 6.9:  $Fe_3O_4$ /Ag(001): Intensity diffracted by an hexagonal layer on the surface with momentum transfer parallel (a) and perpendicular (b) to the surface. Peaks appearing each  $60^\circ$  are more intense when incident angle  $\alpha$  decreases, i.e. when detection is more sensitive to the surface.

This view is also confirmed by atomic force microscopy experiments led *ex situ* at Néel Institute. Scans on this sample and a counterpart are displayed in Fig. 6.10. The surface is covered by flat terraces with holes instead of islands as in our other CoO(001)-terminated samples. The holes between the terraces are rather rectangular and around 1nm deep.

This special morphology resemble to results imaged by Schaller *et al.* using STM of a 4.5 MLs-thick Fe film grown at RT on Ag(001) and annealed at 420 K.[157] Coinciding with this morphology change, they found also an increase of the ratio Ag 3d peak area to the Fe 2p peak area measured by x-ray photoelectron spectroscopy (XPS). They attributed at this time these observations to a flat Fe surface with holes exposing the Ag substrate. Considering also our results, we assume that the flat layer is rather composed of silver atoms segregated at the surface.

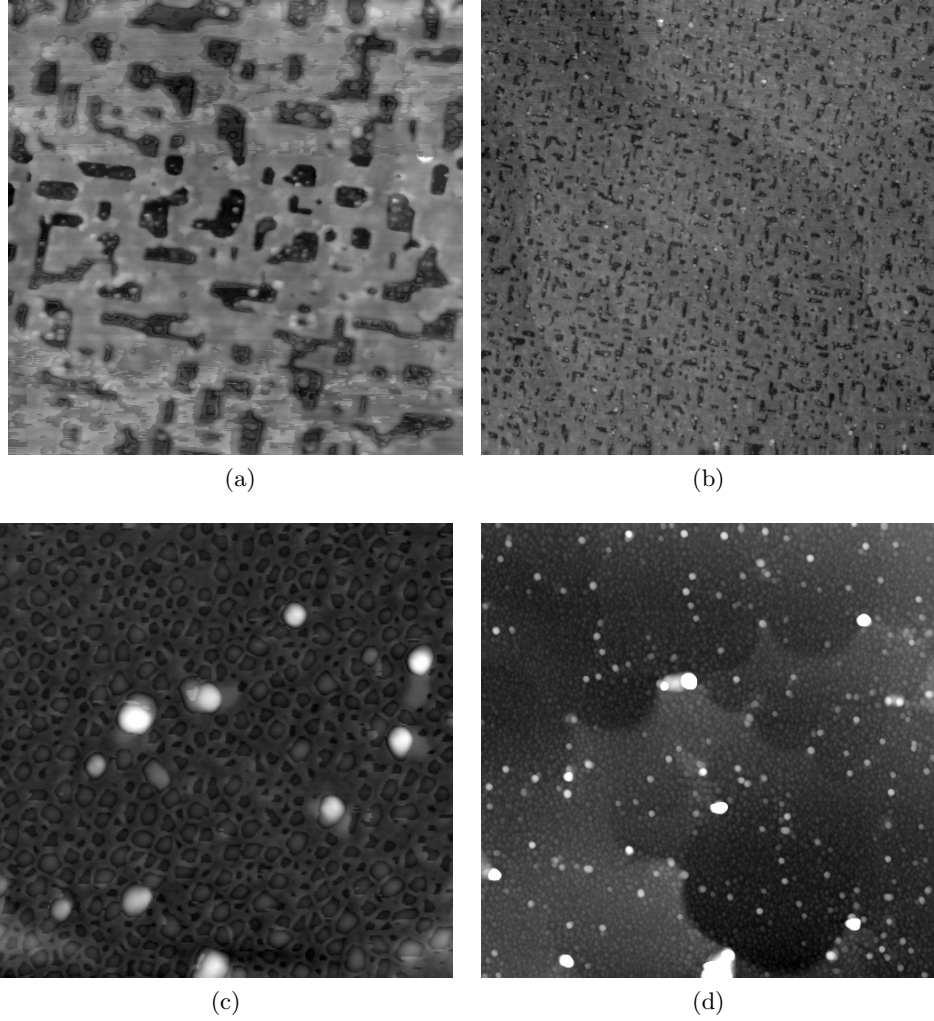


Figure 6.10: Atomic force microscopy images of sample A3 (a and b) and A2 (c and d) as reference. Fe was deposited at  $T = 475$  K and not at RT in sample A3. (a) and (c) are  $1\mu\text{m} \times 1\mu\text{m}$  large, (b) and (d) are  $4\mu\text{m} \times 4\mu\text{m}$  large. Flat surface in (a) and (b) is attributed to a silver layer floating at the surface.

### 6.2.2 Structure

For each growth, a set of in-plane ( $h$ -scans,  $k$ -scans or rocking scans) and out-of-plane ( $l$ -scans) scans around 30 to 44 spinel peaks have been collected for a total of 5 non equivalent peaks. Reciprocal space positions and widths of each reflections were measured by a fit with gaussian function. The spinel grows with the  $\langle 100 \rangle$  axis along the  $\langle 100 \rangle$  axis  $fcc$  Ag substrate or along the  $\langle 110 \rangle$  axis of Ag surface unit cell. The  $(h_{spinel}, k_{spinel}, l_{spinel})$  spinel peaks appear in Ag reciprocal lattice in  $h_{Ag}$ ,  $k_{Ag}$  and  $l_{Ag}$  positions according to

$$h_{spinel} = n_1 * (h_{Ag} - k_{Ag})$$

	A1	A2	A3	A4
Fe deposition (1)	5 ML	6 ML	4 ML	4 ML
reactive deposition	Yes	No	No	No
oxygen pressure	$1.8 \times 10^{-6}$			
temperature	RT	RT	475 K	RT
time	30'	16'	16'	16'
Oxidization at RT				
pressure $P(O_2)$		$1 \times 10^{-7}$	$1.5 \times 10^{-7}$	$3 \times 10^{-7}$
time		5'	7'	10'
Annealing				
pressure $P(O_2)$ (mbar)		$1.5 \times 10^{-7}$	$1.5 \times 10^{-7}$	$2 \times 10^{-7}$
temperature $T_{max}$	620 K	575 K	725 K	665 K
time at $T \geq 575$ K	20'	20'	~1h35	~30'
Fe deposition (2)	5 ML			4 ML
pressure $P(O_2)$ (mbar)	$1.8 \times 10^{-6}$			$2 \times 10^{-7}$
temperature	RT			665 K
time	30'			16'
Annealing				
pressure $P(O_2)$ (mbar)				$2 \times 10^{-7}$
temperature	610 K			775 K
time at $T \geq 575$ K	20'			1h20
CoO deposition	15 ML	11 ML	14 ML	10 ML
pressure $P(O_2)$ (mbar)	$2 \times 10^{-6}$	$1.3 \times 10^{-7}$	$1.3 \times 10^{-7}$	$1.7 \times 10^{-7}$
temperature	580 K	525 K	525 K	~450 K
time	45'	71'40"	97'	76'15"
Comments	Hexagonal $Fe_3O_4$	Large $Fe_3O_4$ peaks	Silver on surface	

Table 6.1: Four different growths of  $CoO/Fe_3O_4$  bilayers on Ag(001)

$$k_{spinel} = n_1 * (h_{Ag} + k_{Ag})$$

$$l_{spinel} = n_3 * l_{Ag}$$

Expected reflections positions in the Ag reciprocal lattice are tabulated in the appendix A. Average  $n_1$  and  $n_3$  values were deduced from a linear regression of all these results at around 0.4886 and 0.4848 respectively. The lattice constants are calculated from the relations  $a_{spinel} = \frac{a_{Ag} * \sqrt{2}}{n_1}$  and  $c_{spinel} = \frac{c_{Ag}}{n_3}$ . Because they are almost identical whatever samples A2 to A4, they have been averaged and standard dispersion gives error bars. The inferred lattice parameters are  $a_{spinel} = 8.363(3) \text{ \AA}$  and  $c_{spinel} = 8.434(4) \text{ \AA}$ . Magnetite bulk value  $a_{spinel}^{bulk} = 8.396 \text{ \AA}$  is between the two values. The spinel film is partially relaxed ( $2 * a_{Ag} = 8.17 \text{ \AA}$ ) with a tetragonal distortion at almost constant volume (-0.3%, smaller than uncertainties).  $c/a$  ratio is about 1.008.

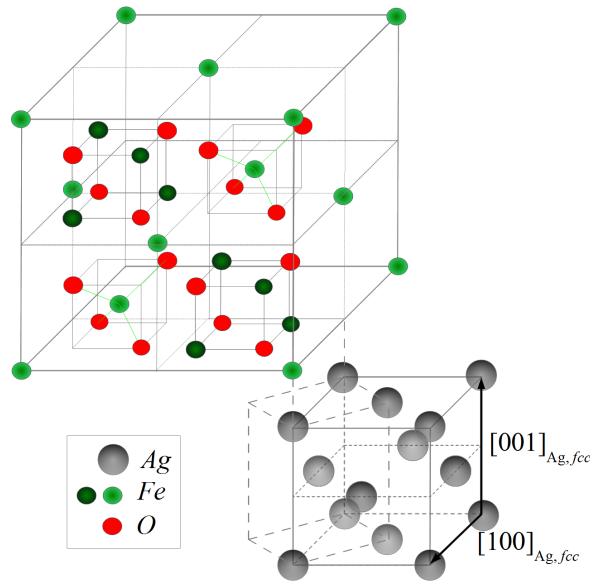


Figure 6.11: Spinel Fe oxide over Ag substrate

### 6.2.3 Distinction between magnetite and maghemite

The maghemite is the  $\gamma$ - phase of  $Fe_2O_3$ , while the magnetite is the pure phase of  $Fe_3O_4$ . They both have a spinel structure with very similar lattice parameters (8.34 Å instead of 8.396 Å). In layer, structures are partially relaxed. The differentiation between magnetite and maghemite is virtually impossible considering only the lattice constant values, even if the volume of our film is close to the magnetite film.[162] The maghemite is a semiconductor with a bandgap of around 2 eV. The magnetite is metallic above Verwey transition. The electronic behavior could differentiate the phases, but needs an important experimental set-up on the layer. Both are ferrimagnetic with different transition temperatures. But the transition temperature can change with the thickness. It is not a sufficient criterion. Oxidation rate could be one.  $Fe^{2+}$  are absent in maghemite and not in magnetite. The issue is to have one fail-safe reference because differences between AES spectra or XAS spectra are subtle and often smaller than experimental uncertainties. However we have found two ways to distinguish the two phases. First,  $\gamma - Fe_2O_3$  and  $Fe_3O_4$  have different structure factors. Second, the magnetite possesses a surface reconstruction in contrary to maghemite.[56]

#### From diffraction data

References of bulk structure factor of maghemite and magnetite have been calculated from data of powder diffraction published in American Mineralogist. The Bragg peak intensity was divided by correction factors (Lorentz and polarization corrections) and multiplicity. The corrections factors are in agreement with the results proposed by Diamond software. We then inferred the bulk structure factor  $F_{bulk}$ . For each peak, we thus have



$$F_{bulk} = \sqrt{\frac{I_{powder}(Am..Min.)}{(Correction*Multiplicity)}} \text{ with } Correction = \frac{1+\cos(\theta)^2}{\sin(\theta/2)*\sin(\theta)}$$

and  $\theta$  the diffraction angle.

During the surface x-ray diffraction experiment, we collected the intensity diffracted around 5 peaks and their symmetry equivalents. In the spinel reciprocal lattice, they correspond to (111), (202), (311), (422) and (511). To avoid scale factor issues between measurements, each structure factor presented is normalized by the structure factor of the (311)<sub>spinel</sub>. The (311)<sub>spinel</sub>, as most intense peak, is a good reference to comparison. The diffracted intensity has been corrected as explained in section 2.3.

Initially, the structure factors of the equivalent peaks in a simple spinel structure have been averaged. However, (131), (242) and (151) peaks are equivalents to (113), (224) and (115) respectively in the bulk structure but not in the films, due to epitaxial growth. Peaks with different out of plane momentum transfer need to be considered apart. This question will be developed next after. We thus averaged the data of 8 non-equivalent Bragg peaks. The results are displayed in Fig. 6.12. The experimental values are not exactly equivalent to those of spinel powder, regardless whether they come from magnetite or maghemite data. However we find almost the same results whatever the growth. Fortunately (111)<sub>spinel</sub> gives the clearest structure factor to differentiate magnetite to maghemite, and is the Bragg peak with smallest uncertainties. We observe that the best agreement is reached for peaks with the same out-of-plane momentum transfer, and that thicker is the film, better the agreement. This is why the bulk structure factor neglects the surface reconstruction. The worst agreement of sample A2 is also related to its peak width. From this original study, we can establish that we achieved to grow well-ordered and stable magnetite films on Ag(001).

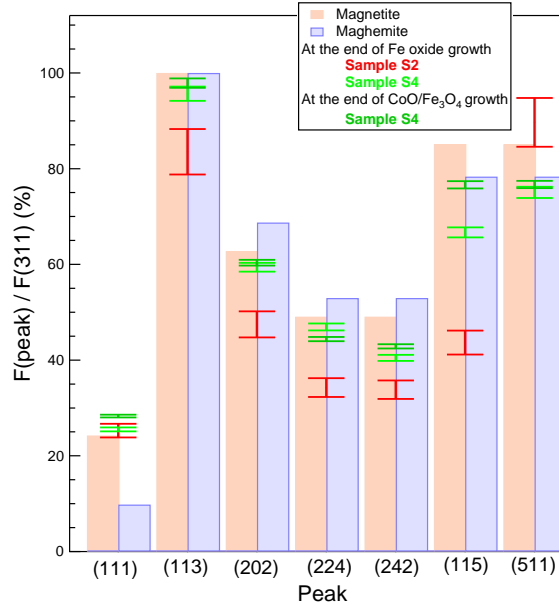


Figure 6.12:  $Fe_3O_4/Ag(001)$ : Ratio of structure factor of several peaks on those of  $(311)_{spinel}$ . Experimental results are compared with magnetite and maghemite ratio calculated from literature (detailed in the text). Note that the  $(111)_{spinel}$  intensity agrees with the intensity from the magnetite and is more than twice the expected value for the maghemite.

This result is confirmed by STM and LEED measurements carried out at Néel Institute. The Fe oxide was grown on clean Ag(001) using the same recipe of sample A4 (sample A5) and studied *in situ*. A surface reconstruction has been observed in both techniques. Magnetite surface reconstruction is either  $(1 \times n)$  or  $(\sqrt{2} \times \sqrt{2})R45^\circ$  depending on its oxidation rate. One can transform the surface from one state to the other by heating between 530 K and 770 K in oxygen or in UHV.[58] The LEED pattern we measured shows clearly a  $(\sqrt{2} \times \sqrt{2})R45^\circ$  reconstruction with respect to the  $Fe_3O_4(001)$  non reconstructed surface unit cell. This symbol means that the superstructure has a lattice unit equal to  $\sqrt{2}$  times the lattice of the spinel surface unit cell with axis rotated by  $45^\circ$ . Spinel and Ag surface unit cells are rotated by  $45^\circ$  compared to *fcc* Ag or spinel unit cell. The axis of the spinel reconstruction is then parallel to the Ag bulk unit cell.

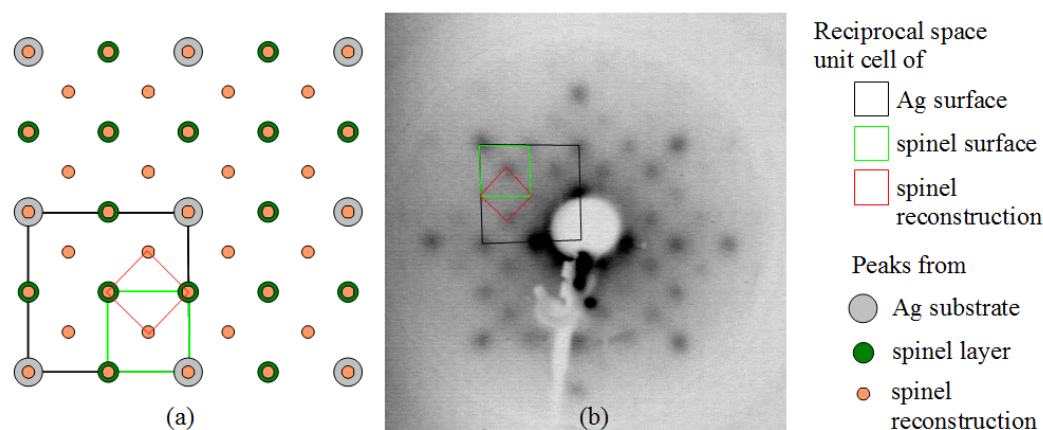


Figure 6.13: Experimental (b) and scheme (a) of LEED pattern for  $(\sqrt{2} \times \sqrt{2})R45^\circ$  reconstructed  $Fe_3O_4$  on Ag(100). The electron energy of the LEED picture is 70 eV. Black, green and red square underline respectively surface Ag, spinel layer and spinel reconstruction reciprocal space unit cell.

In the high-resolution STM image, a *wave-like* surface structure is visible. Two domains rotated by  $90^\circ$  due to cubic spinel symmetry show rows of protrusions. Pairs of protrusion are alternatively shifted perpendicularly to the rows, resulting in this *wave-like* structure. Similar square-lattice structure types were also observed in STM measurements by Stanka *et al* and Fonin *et al.* [52, 58]

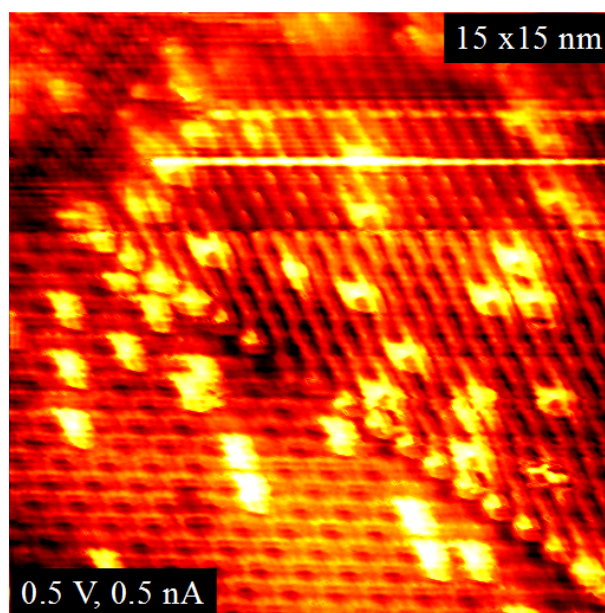


Figure 6.14: High-resolution STM image of  $Fe_3O_4$  surface of the epitaxial magnetite film on Ag(001). Rows of protrusions run along two directions rotated by  $90^\circ$  showing wave-like structure associated to  $(\sqrt{2} \times \sqrt{2})R45^\circ$  reconstruction. Bright spots are considered by Parkinson *et al.* coming from adsorbed hydroxyl groups at antiphase domain boundaries.[61] Note that the surface reconstruction slightly modifies the intensity of magnetite peaks, which could explain some small discrepancies with bulk values.

### 6.2.4 Mosaicity

Usually the width of Bragg reflection is related to the averaged size of domains. It should be unique for each growth whatever the observed peaks. Here it increases with the momentum transfer  $Q$ . For out-of-plane  $Q \geq 4.61 \text{ \AA}^{-1}$ , peaks are even separated in three, as can be seen in Fig. 6.15. This effect arises probably from mosaicity of the layer. Two domains slightly tilted from one to the other diffract at slightly different angles. Peaks from each domain are always separated by the same angle and merge at small momentum transfer perpendicular to the surface, if domains are tilted with respect to the surface plane. This kind of tilt was observed for CoO/Ag(001).[148]

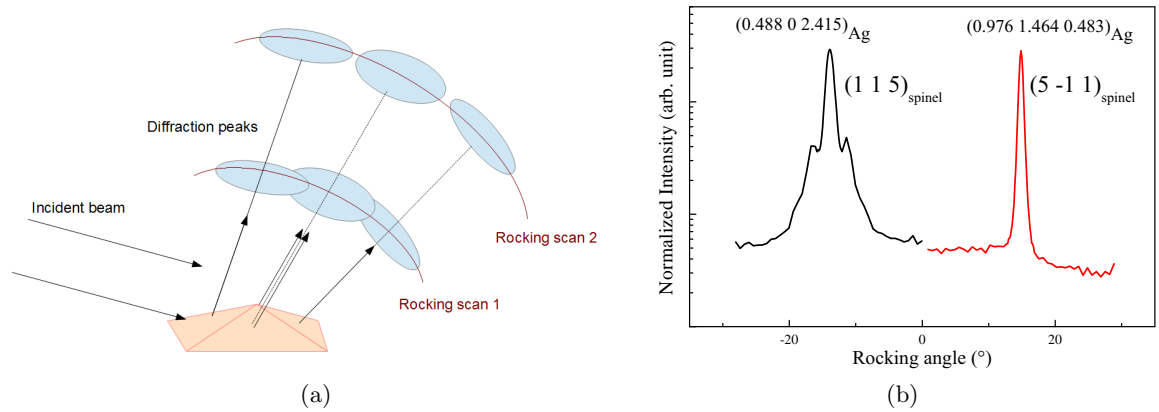


Figure 6.15:  $Fe_3O_4$ /Ag(001): (a) Schematic illustration of diffraction of mosaic domains. Each domain diffracts in one direction slightly tilted compared to the others, resulting in different Bragg peak positions. Here we can assume four directions corresponding to the facets of a cubic pyramid. (b) Normalized intensity around  $(115)_{spinel}$  and  $(5\bar{1}1)_{spinel}$  peaks as example of mosaicity.

It explains why the structure factors of supposed equivalent Bragg peaks, as for instance  $(115)_{spinel}$  and  $(511)_{spinel}$ , are so different. To calculate the peaks area of triple peaks, we had to add the three areas and not only the main peak. The accuracy of the data was then reduced.

## 6.3 CoO/ $Fe_3O_4$ /Ag(001)

$Fe_3O_4$ /CoO bilayer is a widely studied system, especially in multilayers.[163] It exhibits exchange bias effect even for CoO layer as thin as 5 Å.[17] It has been proposed as a component in all-oxide spin-valves or TMR devices. Although the two oxides do not have same crystal structure, a good epitaxy with small strain is expected thanks to the matching of the lattice parameters:  $a_{CoO} = 4.261 \text{ \AA}$ ,  $a_{Fe_3O_4} = 8.396 \text{ \AA}$ . The size of the primitive unit cells of the O sublattices differs only by 1.5%.[152] It probably favored the insertion of magnetite at the interface between Fe and CoO in the CoO/Fe/Ag(100) sample described previously. We stud-

ied the growth, structures and coupling of this bilayer in the idea to then add other material such as MgO or  $Al_2O_3$  to form a magnetic tunnel junction.

### 6.3.1 Growth and structure of CoO on $Fe_3O_4$ /Ag(001)

To grow CoO film on  $Fe_3O_4$ /Ag(001), Co was deposited with the substrate held at 450 K or 525 K under oxygen pressure. We have demonstrated previously that the order of Fe spinel oxide is enhanced with temperature. There is no risk to destroy this layer by heating. The oxygen pressure was maintained around  $1.3 - 2 \times 10^{-7}$  mbar to ensure the good stoichiometry of the Fe and Co oxides. If enough oxygen is in the chamber, interface should be fairly chemically inert during the growth. We followed the CoO reactive deposition by SXRD.

We observed that after CoO deposition, spinel peaks are not at all destroyed but in contrary enhanced, and the surrounding Kiessig oscillations have a smaller periodicity (Fig. 6.16a). It indicates a growth and maintain of ordering of the spinel film. The first layers of cobalt oxide seem to adopt a spinel structure. We evaluate the additional layer to around 8.5 Å, i.e. 1 unit cell of spinel for a growth at 525 K (sample A2) and to only 1.76 Å at 450 K (sample A4). The temperature increases the reactivity and favours the intermixing. The growth at 450 K is thus preferable to obtain a net interface between Fe spinel oxide and Co rocksalt oxide. Peaks referring to rocksalt CoO have also been detected and analyzed.

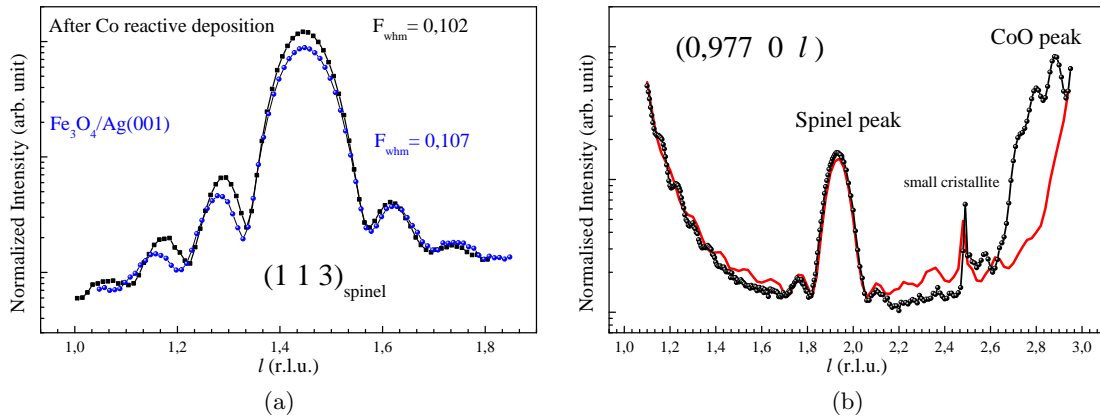


Figure 6.16: CoO/ $Fe_3O_4$ /Ag(001): Growth of spinel (113) peak (a) and rocksalt CoO (103) peak (b) with Co reactive deposition.

CoO grows with (001) orientation. We looked for the hexagonal pattern coming from CoO(111) growth but no peaks were found. The determination of the CoO peak positions is difficult because they are very close to those coming from the Ag substrate and the spinel layer. The in-plane lattice parameter is evaluated at 4.18(1) Å and the out-of-plane at 4.25(1) Å from a linear regression of positions deduced from 7 in-plane and 11 out-of-plane scans. It is pseudomorph with spinel. Compared to the bulk CoO, there is a moderate reduction in the unit cell volume. We found  $V_{layer} = 4.25 * 4.18^2 = 74.3 \text{ \AA}^3$  instead of  $77.3 \text{ \AA}^3$  giving a reduction of -4%, as on Fe. CoO layer is tetragonally distorted with a  $c/a$  ratio of about 1.017, which

could influence its magnetic properties. In-plane domain size is assessed at 20 nm, expressing a well-ordered layer.

Regarding to the fringes, the interfaces in the CoO/ $Fe_3O_4$ /Ag(001) system are particularly abrupt in contrast to other systems, such as CoO(111)/FePt for instance. Sharpness of interfaces is an essential feature in exchange coupled system. Intermixing and roughness may give rise to a random field acting on the interface spin and explain exchange bias according to Malozemoff's theory.[164]

### 6.3.2 X-ray absorption (preliminary) study

Initially we intended to combine MOKE experiments and polarized XAS to study magnetic properties of CoO/ $Fe_3O_4$  system. We didn't succeed to obtain results by MOKE. Hysteresis loops have been measured at 270 K from x-ray magnetic circular dichroism (XMCD) signal at Fe  $L_3$  edge at ID08 beamline in ESRF. All the results presented here concern sample A2, which unfortunately is rougher than the others. The latter has been made after the beamtime we obtained to lead XAS experiment.

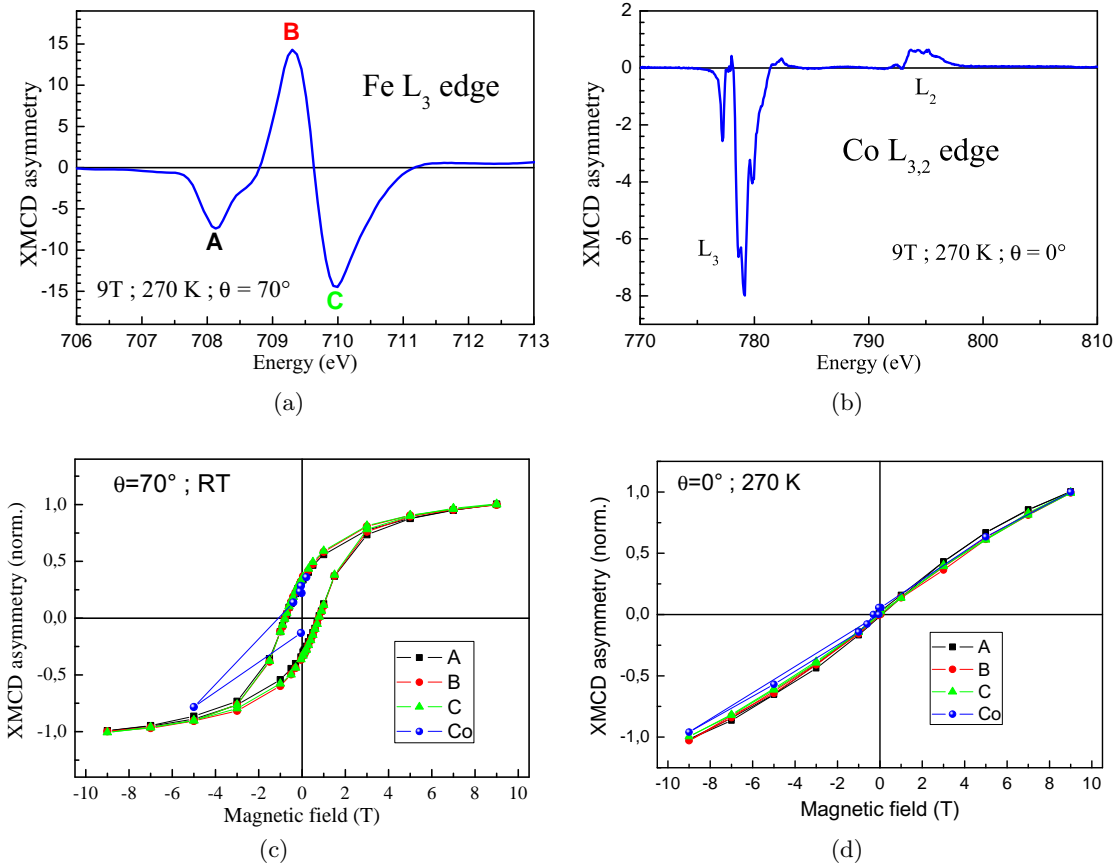


Figure 6.17: CoO/ $Fe_3O_4$ /Ag(001): XMCD signal at Fe  $L_3$  edge (a) and Co  $L_{3,2}$  edges (b) normalized respectively by the first Fe peak and the Co step. Three features labeled A, B, C are distinguished in Fe XMCD asymmetry. Behavior of each feature and of the maximum Co signal versus applied field gives hysteresis loops presented in (c) and (d) after normalization (grazing and normal incidence, respectively). They are equivalent whatever the feature. Fe magnetic moment and ferromagnetic Co component are aligned parallel to the surface.

Coercivity is evaluated about 0.6 T (Fig. 6.17). This high value cannot be reached with the electromagnet in the MOKE set-up we used, and so Fe spins cannot be reversed. Such high anisotropy could come from CoO coupling. Even if bulk CoO is supposed to be paramagnetic at RT, van der Zaag and coworkers have found an enhancement of CoO Néel temperature in contact with magnetite.

Another explanation comes from our observation of the spinel Bragg peak enhancement during CoO growth. Few Co atoms would insert inside Fe oxide matrix occupying Fe ions sites. The presence of  $Co^{2+}$  ions inside the ferrimagnetic layer increases its magnetic anisotropy. Co ferrite ( $CoFe_2O_4$ ) has indeed the highest values of magneto-crystalline anisotropy and magnetostriction. Its structure is identical to the one of magnetite with  $Co^{2+}$  ions replacing  $Fe^{2+}$  ions. Hence octahedral B sites are occupied in equal number by  $Co^{2+}$  and  $Fe^{3+}$  and tetrahedral A sites by remaining  $Fe^{3+}$  cations.[165] We can assume to have a mixed  $Co_xFe_{3-x}O_4$  spinel at the interface between magnetite and CoO. This idea is supported by Lee and collaborators who found by Mössbauer analysis that  $Co^{2+}$  ions replace Fe ions located

at the octahedral site.[166] They observe also that relative intensity of (1 1 1) to (311) reflection increases with the addition of  $Co^{2+}$ . We verified it also in our X-ray diffraction data. However the difference is so small compared to the uncertainties that it should be put into question.

In addition, XAS spectra at Co  $L_{3,2}$  edges show a dichroic signal. XMCD is characteristic of ferromagnetic Co atoms in oxygen environment. It behaves as Fe spins as function of the applied magnetic field. This argument goes for both explanations. Either ferromagnetic Co atoms are inside spinel and Co spins follow their neighbours, or exchange coupling at the interface is so large that it influences the coercivity of magnetite and induces a net magnetic moment at the interface with rotatable CoO spins.

In the literature, each feature of XMCD signal at Fe  $L_3$  edge are identified to a particular electronic environment in magnetite. The peak A refers to  $Fe^{2+}$ , B to  $Fe^{3+}$  in tetrahedral sites and C to  $Fe^{3+}$  in octahedral sites. In a stoichiometric magnetite, A peak is slightly enhanced compared to C peak. In our case, A peak is smaller. It is coherent with the idea that a part of  $Fe^{2+}$  is replaced by  $Co^{2+}$  cations.[167] Simulations are mandatory to have quantitative results and could be interesting to explore.

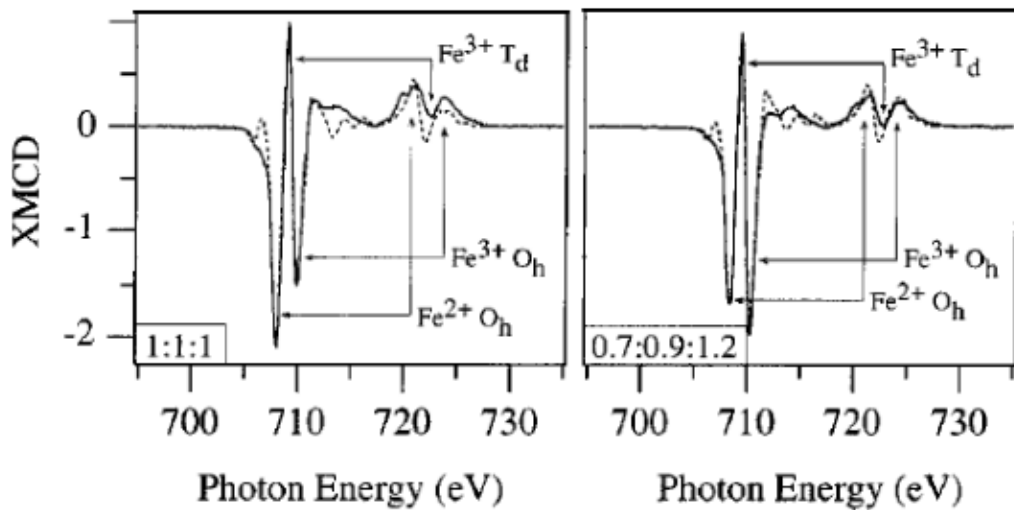


Figure 6.18: XMCD spectra taken from ref.[167]. The insets show the relative ratio of the ions of the calculated dichroism, in the order  $Fe^{2+}$ ,  $Fe^{3+}$  in tetrahedral and octahedral symmetry, each normalized to the value for stoichiometric  $Fe_3O_4$ .

Whatever the magnetic moments of Fe ions or the Co component, all turn together with the same field and are oriented in-plane. Following Wu and coworkers,[132] we looked at the ratio between the peaks C (778.74 eV) and B (778.26 eV) of Co XAS spectra. When this ratio is maximum, the polarization vector is perpendicular to the magnetic axis of the layer. Polarization being perpendicular to the beam, beam direction is parallel to the magnetic axis. If we compare XAS spectra at two angles, ratio is higher when the beam gets closer to the surface. We can assume that Co AFM spins are in-plane, in consistence with the literature results.[98]



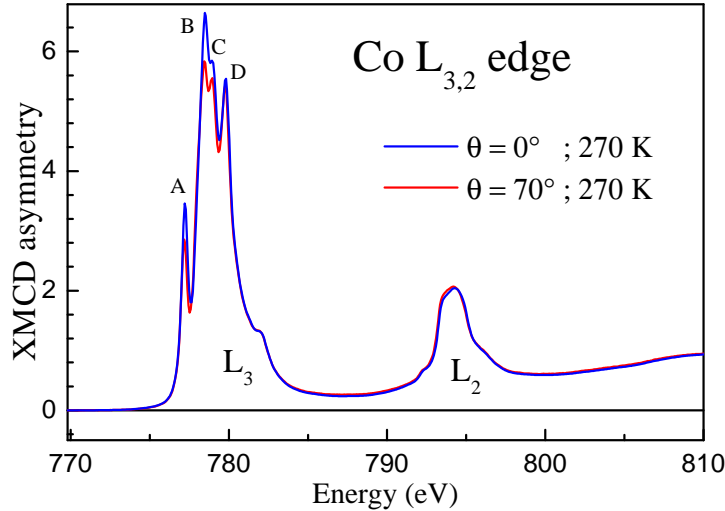


Figure 6.19: CoO/ $Fe_3O_4$ /Ag(001): X-ray absorption spectra at Co  $L_{3,2}$  edges with beam perpendicular to the sample ( $\theta = 0^\circ$ ) and almost in-plane ( $\theta = 70^\circ$ ) after normalization and background subtraction.

The magnetic properties of these bilayers are promising. It can be deepened with temperature dependent XAS measurements to determine whether an exchange coupling takes place between the two layers. With X-ray linear dichroism experiments at Co  $L_{2,3}$  edges, the exact direction of magnetic moments could be determined.[168] Co anisotropy could be compared to the anisotropy of the layers obtained in others samples, allowing to relate magnetic anisotropy with layer orientation or distortion.

## 6.4 CoO/Ag(100)

A magnetic tunnel junction (MTJ) is composed of two FM layers separated by a thin insulator. The tunnel magnetoresistance effect (TMR) is observed in a MTJ when the spin configuration of the two FM layers can be switched from parallel to antiparallel. This can be achieved by pinning one of them through the exchange coupling with an AFM layer, as in the  $Fe_3O_4/CoO$  bilayer system. A good candidate for an all-oxide MTJ would be the  $Fe_3O_4/MgO/Fe_3O_4/CoO$  multilayer, where the MgO is the barrier. A good epitaxy is expected owing to proximity of all lattice parameters ( $a_{MgO} = 4.212 \text{ \AA}$ ). Ag(001) as a metal with lattice parameters close to those of all layers is an ideal substrate for such MTJ. To realize this multilayer, we first grew CoO on Ag(001). Mastering growth of CoO on Ag(001) could be interesting to study CoO/Fe system too. Deposition of Fe on CoO(001) induces indeed less Fe oxidation than CoO growth on Fe(001).[141]

To prevent intermixing with Ag segregation, Co was deposited at room temperature. 1 ML alone first, then oxidized at  $1 \times 10^{-6}$  mbar, followed by 21 MLs of Co deposition under oxygen pressure ( $P_{O_2} = 1 \times 10^{-6}$  mbar). No diffraction peak is then visible. The layer is not enough ordered to diffract. In addition, Ag CTRs indicate a particularly rough interface.

Subsequently, the layer was annealed at maximum temperature of 750 K during around one hour. Peaks corresponding to CoO(001) develop during the annealing. They enhance and their in-plane position shifts slightly. Interface with silver remains rough according to the low intensity between Bragg peaks in CTR.

The structure of this layer has been analyzed using a set of in-plane and out-of-plane scans of 15 reflections corresponding to 7 non-equivalent reflections. The determination of the out-of-plane positions is particularly difficult due to the proximity of CoO reflections with Ag Bragg peaks. We found that CoO grows at almost constant volume (less than -2%) with lattice parameters  $a_{coO} = 4.215(5) \text{ \AA}$  ( $h=n_i*0.969$ ) and  $c_{coO} = 4.27(1) \text{ \AA}$  ( $l=n_i*0.957$ ). The layer is thus partially relaxed. Measured thickness is equivalent to nominal one (22 MLs) indicating that all CoO atoms finally organized and participate to diffraction. Indeed, no peak from hexagonal CoO(111) has been detected.

In the literature, CoO is rather deposited at 470 K on Ag(001). First MLs grow pseudomorph in a nearly layer-by-layer mode. Schindler and collaborators investigated by LEED curves compared with multiple scattering calculations the atomic structure of four layer of CoO on Ag(001) substrate.[120] They observed that two outermost layers of CoO relax outward. This slight deviations compared to the bulk surface are supposed driven by the in-plane compressive stress imposed on CoO film by the lattice mismatch. Torelli and coworkers follow the same line using SXRD, XPS and LEED of 1ML to 23 MLs thick CoO on Ag(001).[148] They found that CoO relaxes gradually after 4 MLs, releasing progressively the small residual strain. The lattice constants of our and their experiments are in consistence, despite of the different growth conditions. They also observed the presence of a dislocation network at the interface thanks to satellites spots surrounding Ag Bragg peaks. Their absence in the diffraction pattern of our layer expresses probably a smaller degree of order.

Finally they recorded LEED images for different CoO coverages and found satellites spots aligned along the  $\langle 110 \rangle$  directions around each normal spot. The position of these peaks move as a function of energy. They ascribe them to the formation of mosaics tilted from the surface normal referring to the work of Wollschläger *et al.* on MgO films on Ag(001) substrate.[169]

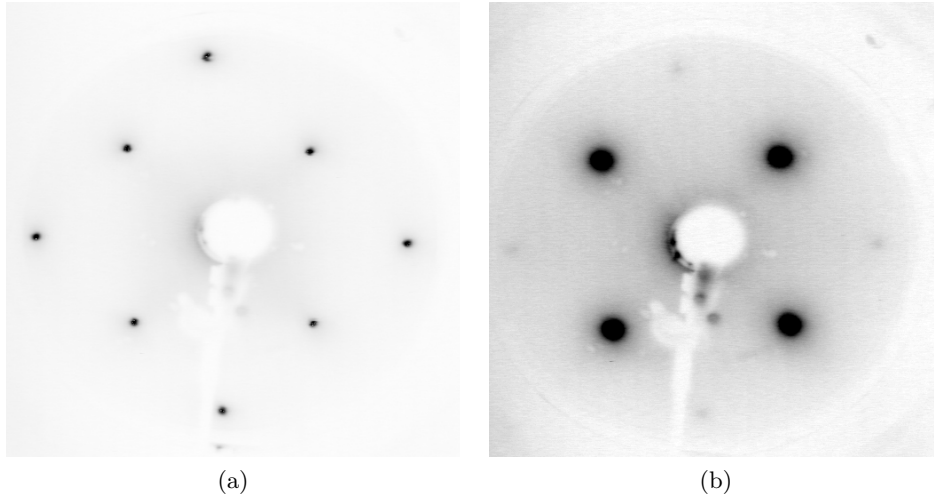


Figure 6.20: CoO/Ag(001) LEED pictures of (a) clean Ag substrate and (b) 4 MLs of CoO(001) on Ag. Electron energy is at 60 eV in both cases.

Fig. 6.20 displayed LEED pattern a film of 4 MLs of CoO on Ag(001) deposited at 470 K assisted by oxygen pressure of  $P_{O_2} = 1 \times 10^{-6}$  mbar. The distance between two CoO spots compared to the distance between two silver spots gives a ratio of 0.97, identical than those found in surface diffraction. CoO spots are large compared to those of Ag substrate reflecting a small in-plane correlation length. Satellite peaks are not visible.

However we noted that out-of-plane positions of Bragg peaks of CoO change slightly between equivalent peaks. We assigned this shift to domains tilted off the surface normal. One orientation seems to be preferential. A small miscut of the surface of Ag substrate could have influenced the orientation of mosaics.

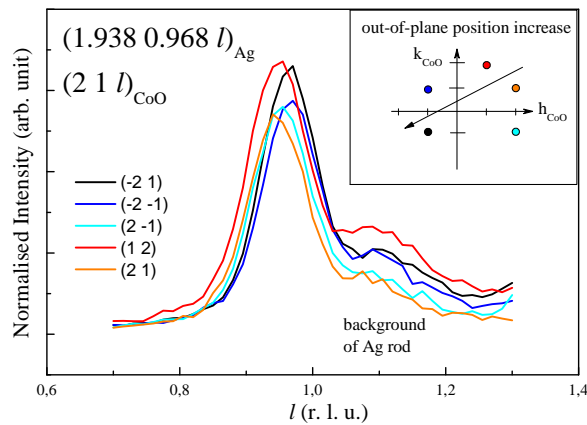


Figure 6.21: CoO/Ag(001): Reciprocal out-of-plane positions shift as function of in-plane positions of equivalent  $(211)_{CoO}$  peaks. Position increases following black arrow in the illustration of in-plane peak positions (inset).

## Conclusion

We investigated by surface x-ray diffraction (SXRD) the growth and structure of the first Fe layers deposited on Ag(001), in the idea to shed some light on the correlation between their structural and magnetic properties and on their growth mode. We found that the spin reorientation transition (SRT) occurring in the Fe layer at 4-6 MLs cannot be explained by a structural relaxation. Fe grows in registry with Ag(001) up to at least 14 MLs. Nevertheless, we observed a large variation of the out-of-plane lattice parameter with thickness and temperature, which could be at the origin of the SRT. We tried to understand the cause of such variation by models of the structure at different coverages. The data quality was unfortunately insufficient to obtain quantitative results. We however noticed that the intermixing with Ag atoms is crucial.

We then follow the growth of CoO on Fe/Ag(001) to build an exchange coupled CoO/Fe system. The CoO growth clearly impacts the Fe layer even at RT, reducing strongly the order in the layer. 25% of the initially 8 MLs of Fe are in oxide environment after the growth. This oxide is at interface and so may play a major role in the exchange coupling of the bilayer. However XAS measurements repeated two years after on the very same sample show a large increase of Fe oxidation with 50% of Fe atoms in oxide environment. To control the oxidation rate in the ferromagnetic layer, we replaced the Fe layer by a magnetite  $Fe_3O_4$  layer.

We have elaborated magnetite layers on Ag(001) by MBE in UHV chamber. The growth and the structure have been investigated *in situ* by SXRD, AES and STM. Reactive Fe deposition leads to a magnetite textured (111). (001) orientation is achieved by the deposition of 4 to 6 MLs of Fe at RT before oxidation. The layer orders well with annealing under oxygen pressure showing nice Kiessig oscillations surrounding its Bragg peak. The annealing must be after the first oxidation to avoid a floating silver layer on the surface.

A tricky issue in magnetite growth is the determination of the phase compared to the maghemite  $Fe_2O_3$ . By comparison of the experimental values of structure factors with those found in literature for powder, we verified that we have grown magnetite. This results was confirmed by STM images, which display the *wave-like* reconstruction characteristic of the magnetite. We establish then an original way to differentiate the two phases.

The spinel grows with  $\langle 100 \rangle$  axis along  $\langle 100 \rangle$  axis *fcc* Ag substrate or along  $\langle 110 \rangle$  axis of Ag surface unit cell. The lattice parameters are in-plane  $a = 8.363(3)$  Å and out-of-plane  $c = 8.434(4)$  Å showing a partial relaxation. The layer present an important mosaicity with slightly tilted domains. This behavior has also been observed in the CoO layer grown on Ag(001).

The first layers of CoO grown on  $Fe_3O_4$ /Ag(001) adopt the spinel structure. Then the film becomes rocksalt, oriented (001) and in coherent epitaxy with the spinel. The magnetic properties of the CoO/ $Fe_3O_4$  system have been studied by MOKE and XAS spectroscopies. The coercivity of ferromagnetic layer is evaluated about 0.6 T. Such high value could come from the coupling with the CoO layer or from an intermediate layer, composed of  $Co_xFe_{3-x}O_4$ . This idea is in coherence with the XMCD results, where some spins of a ferromagnetic Co

oxide reverse with Fe spins. According to XMLD and XMCD signals, all the spins are in-plane whatever the spins from Fe oxide or ferromagnetic and antiferromagnetic Co oxide. The elaboration of the CoO layer on Ag(001) followed by the magnetite to a  $Fe_3O_4$ /CoO /Ag(001) system should prevent the development of the intermediate layer. However such ultra-thin hard phase could also be interesting for spintronics applications.

# Conclusions and Outlooks

During this thesis, we investigated four AFM/FM bilayer systems to better understand the mechanism of the exchange coupling at their interface. The exchange coupling in a AFM/FM bilayer is characterized by an enhancement of the coercivity of the FM layer and a shift of its hysteresis loop, known as exchange bias. Several aspects of this phenomenon, despite its scientific relevance and its widespread use in magnetoelectronic applications, are still not elucidated.

Our strategy was to carefully synthesize and deeply characterize exchange coupled systems. First, we elaborated bilayers at a very fine control. The growth was optimized to form ideal model systems. Second, we characterized their crystalline and magnetic properties as completely as possible. This allowed us to report their real structures, which could help to the development of exchange bias theory. For that, we exploited the ability of molecular beam epitaxy to grow ultra-thin epitaxial films and multilayers. We then combined structural and element-selective probes available in synchrotron light sources with other surface techniques, such as experiments based on magneto-optic Kerr effect (MOKE).

Surface x-ray diffraction (SXR) at the French CRG BM32 Beamline at ESRF in Grenoble was an invaluable tool in the precise determination of the crystallographic structures of the ultra-thin layers. X-ray absorption spectroscopy (XAS) at ID08 Beamline at ESRF and at PGM Beamline at LNS in Campinas (Brazil) gave pieces of information on the local environment of the atomic species. Using linearly or circularly polarized beam (XMCD and XMLD) at Fe and Co  $L_{2,3}$  edges, we got access to the local magnetic moments and anisotropy of selected atomic species, and so ascertained the spin orientation and magnetic order of FM and AFM layers. MOKE experiments complemented XAS results.

Initially, we were especially interested in systems presenting a perpendicular magnetic anisotropy (PMA). At the starting, we tackled two different systems: CoO/FePt on Pt(001) and CoO/Fe on Ag(001).

The first one relies on CoO/FePt deposited on Pt(001). 3 BL of FePt were grown by thermal deposition of Fe. The FePt layer is in registry with Pt(001) in a highly ordered  $L1_0$  phase with  $c$ -axis perpendicular to the surface. Reactive Co deposition leads to the same oxide structure on Pt(001) and on FePt(001) substrates. The epitaxial films have an in-plane hexagonal pattern which resembles the cubic CoO(111) one. The detailed analysis revealed a slight monoclinic distortion induced by the anisotropic stress at the interface. The

distortion, stable at room temperature, reminds the magnetically driven distortion in the low temperature antiferromagnetic bulk phase. Unlike this latter, the tetragonal contribution to the distortion results in a  $c/a$  ratio  $>1$ . Part of this work can be found in ref. [170].

The FePt keeps a strong PMA until at least 320 K. This Curie Temperature value is high for a FePt film of only 3 BL, reflecting a high chemical order in the layer. The Co spins are in the plane of the surface, pointing towards the first Co neighbour. The AFM order is preserved up to about 293 K. A strong exchange bias stands up in the FM loops, while the AFM layer shows a small ferromagnetic component attributed to a spin canting. The two layers are perpendicularly coupled up to RT. The Néel temperature  $T_N$  of this 4 nm CoO film is identical to the one of the bulk CoO crystal, and matches the blocking temperature. It asserts the robustness of the interfacial coupling and of the AFM order in the CoO layer. Such exceptional behavior shares a close relationship with the strain-induced distortion of the oxide layer. It also demonstrates that the thickness effects on the ordering temperature  $T_N$  and on the blocking temperature ( $T_B$ ) are not intrinsic properties of these double layers. Part of this work has been published in ref [171, 172].

The nice results of this bilayer makes one want to know more. Such CoO layer is a perfect playground to the study of the relationship between the structural and magnetic anisotropies. The distortion of the CoO bulk with the temperature below the Néel temperature results in a  $c/a$  ratio  $<1$ . It asserts that the structure is sensitive to the temperature via the magnetic ordering. Our monoclinic layer possesses the opposite distortion at RT. The structure might evolve with temperature. Using SXRD we could resolve the structural modifications of the layer as function of temperature. In addition, the CoO layer has the same structure on FePt and on Pt(001). The study of its spin orientation on the bare substrate would also allow to disentangle the effects of exchange interaction with the FM layer and of magnetocrystalline anisotropy. In particular, the ferromagnetic component should be absent in this layer, if it is really related to a spin canting. Finally, the preliminary results of in-plane field cooling of this sample are promising to compare the relative energies of the different magnetic interactions.

By tuning the interface chemistry, we have successfully grown a CoO film oriented (001) on Pt(001) and FePt/Pt(001). The layer is partially relaxed, has a large tetragonal distortion ( $c/a$  ratio about 1.03) and a network of periodic dislocations. Some Fe and Co atoms might exchange their sites during the growth. Hence half of Fe are atoms in oxide environment and 14% of Co atoms are metallic. The addition of few ML of Pt at the interface, as in the growth of the precedent sample, should stabilize the FePt film and prevent this effect. Nevertheless, the two films are coupled below 110-140 K. At low temperatures, the perpendicular FM loops present two components difficult to interpret. One comes from an hard phase, probably the FePt phase. The other is soft. One component reorients itself from out-of-plane to in-plane at around 250 K. It comes probably from Fe oxide or Co metallic. The AFM Co spins are oriented in-plane, pointing near the (001) or (010) directions, towards oxygen atoms in the surface plane. Therefore the system is a bit more complicated than expected, but the causes of

the non-expected contributions are identified. The bilayer gives promising results with a clear orthogonal coupling. Further measurements would allow to explore more deeply its magnetic properties. By comparison with the results of the precedent sample, we could investigate the relationship between the exchange coupling of the FM/AFM bilayer and the strain and structure of the AFM layer.

The third system has been CoO/Fe double-layer deposited on Ag(001). Fe layer presents a PMA on Ag(001) up to 4-6 ML. Then the spins lie in the plane. Fe grows pseudomorphically up to at least 14ML. The spin reorientation transition, taking place at 6 ML, seems to be related to a change in the unit cell volume, rather than to a relaxation of the in-plane lattice parameter. The CoO growth clearly impacts on the Fe layer even at RT, with one fourth of the initially 8 ML of Fe atoms in oxide environment and a dramatic decreases of the Fe domain size observed in diffraction. This oxidation, which plays a major role in the coupling at the interface, has a tendency to increase with time. Such an unstable and uncontrolled oxidation oriented our research toward a more stable system where the Fe layer was completely oxidized.

(001) and (111) oriented magnetite  $Fe_3O_4$  layers have been grown on Ag(001) substrate. A tricky issue in magnetite growth is the determination of the phase compared to the maghemite  $Fe_2O_3$ . By comparison of the experimental values of structure factors with those found in literature for powder, we verified that we have grown magnetite. This result was confirmed by STM images, which display the *wave-like* reconstruction characteristic of the magnetite. We establish then an original way to differentiate the two phases.

The first layers of CoO grown on magnetite adopt the spinel structure. Then the film becomes rocksalt, (001) oriented and in coherent epitaxy with the spinel. The high coercivity of the FM layer comes either from the coupling with the CoO layer or from an intermediate layer, made of  $Co_xFe_{3-x}O_4$ . Some Co atoms insert then in the magnetite layer. This idea is in coherence with the XMCD results, presenting ferromagnetic Co oxide spins of Co oxide reversing with Fe spins. All the spins are in-plane at 270 K. Further measurements with the application of high magnetic field would determine the coupling of the system.

Two ways are then opened with this system. First, ultra-thin layer with such high coercivity has promising applications. A better control of its growth on Ag(001) could be deeply investigated before foreseeing a coupling with an AFM layer. Second, the layer of  $Fe_3O_4$  provides an interesting playground to study magnetic transitions of magnetite and confinement effects changing magnetic properties and transport. The better should be then to deposit magnetite on top of CoO/Ag(001). In both cases, these systems, coupled with for instance  $MgO$  layer, could be a part of all-oxide spin-valves or TMR devices.

One can notice that, during this thesis, we particularly worked on the ultra-thin CoO layer. We explored its growth on different surfaces: Ag(001), Pt(001), FePt/Pt(001), Fe/Ag(001),  $Fe_3O_4$ /Ag(001). We precisely determined its monoclinic distortion after reactive Co deposition on Pt(001) and on FePt/Pt(001). We then demonstrated that the orientation of CoO



---

epitaxial film can be tuned on Pt(001) by the appropriate interface chemistry. Different spin orientations, AFM orders and FM components have been found according to the growth and strain. This manuscript contributes to a better understanding of ultra-thin CoO layers and of the relationship between the orientation of the magnetic moments and the crystal field effect.

## Appendix A

# The spinel pattern in Ag(001) lattice

In this appendix are referenced Bragg peaks of a spinel structure. Only the 20 first at low angles are presented. The associated Miller indices in the spinel reciprocal lattice unit are  $h_{spinel}$ ,  $k_{spinel}$  and  $l_{spinel}$ . In the Ag reciprocal lattice unit, they are  $h_{Ag}$ ,  $k_{Ag}$  and  $l_{Ag}$ . To move from one lattice unit to the other, one uses the  $n_1 = \frac{a_{Ag}}{a_{Fe_3O_4}}$  and  $n_3 = \frac{c_{Ag}}{c_{Fe_3O_4}}$  ratios and the following relations

$$\begin{array}{ll} \text{Ag} \rightarrow \text{Spinel} & \text{Spinel} \rightarrow \text{Ag} \\ h_{spinel} = n_1 * (h_{Ag} - k_{Ag}) & h_{Ag} = \frac{h_{spinel} + k_{spinel}}{2 * n_1} \\ k_{spinel} = n_1 * (h_{Ag} + k_{Ag}) & k_{Ag} = \frac{k_{spinel} - h_{spinel}}{2 * n_1} \\ l_{spinel} = n_3 * l_{Ag} & l_{Ag} = \frac{l_{spinel}}{2 * n_3} \end{array}$$

As  $n_1 \simeq 2$  and  $n_3 \simeq 2$ , we decided to write in the following Table the closer half-value of  $h_{Ag}$ ,  $k_{Ag}$  and  $l_{Ag}$ .

Of course, some peaks are equivalents in cubic symmetry and not in tetragonal symmetry. For instance, (0 2 2) Bragg peak is not equivalent to (2 2 0) Bragg peak in tetragonal symmetry. As the d-spacing and the structure factor are almost identical, we do not separate them and let the reader do it if necessary.

All the intensity and structure factor values have been calculated by Diamond software for a spinel powder and are given without the Lorentz and polarization corrections.

N°	$2\theta$ (°)	d-spacing (Å)	Intensity	Structure Factor	$h_{spinel}$	$k_{spinel}$	$l_{spinel}$	Multiplicity	$h_{Ag}$	$k_{Ag}$	$l_{Ag}$
1	6,665	4,8476	26409,54	57,46	1	1	1	8	0.5	0	0.5
2	10,894	2,9685	344686,49	169,48	0	2	2	12	0.5	0.5	1
3	12,781	2,5316	1,75045E6	270,07	1	1	3	24	0.5	0	1.5
4	13,352	2,4238	116435,67	120,64	2	2	2	8	1	0	1
5	15,429	2,0991	596257	315,24	0	0	4	6	0	0	2
6	16,823	1,9262	22948,68	30,92	1	3	3	24	1	0.5	1.5
7	18,926	1,7139	448876,36	136,76	2	2	4	24	1	0	2
8	20,086	1,6159	355178,29	210,71	3	3	3	8	1.5	0	1.5
9	20,086	1,6159	1,3438E6	236,63	1	1	5	24	0.5	0	2.5
10	21,888	1,4843	2,90584E6	492,09	0	4	4	12	1	1	2
11	22,904	1,4192	74695,14	39,45	1	3	5	48	1	0.5	2.5
12	23,233	1,3994	29,14	1,1	2	4	4	24	1.5	0.5	2
13	24,509	1,3276	320001,2	115,47	0	2	6	24	0.5	0.5	3
14	25,426	1,2804	883398,05	191,85	3	3	5	24	1.5	0	2.5
15	25,725	1,2658	396458,14	128,53	2	2	6	24	1	0	3
16	26,89	1,2119	316513,81	198,91	4	4	4	8	2	0	2
17	27,734	1,1757	15626,81	25,52	1	1	7	24	0.5	0	3.5
18	27,734	1,1757	44741,75	43,18	1	5	5	24	1.5	1	2.5
19	29,09	1,122	502430,74	102,31	2	4	6	48	1.5	0.5	3
20	29,877	1,0931	751532,58	176,96	3	5	5	24	2	0.5	2.5

# Bibliography

- [1] Richard P. Feynman. Plenty of room at the bottom. *Available on wikipedia*, 1959. [1](#)
- [2] G Binnig and H. Rohrer. In touch with atoms. *Reviews of Modern Physics*, 71(2):324–330, 1999. [1](#)
- [3] M. N. Baibich, J. M. Broto, A. Fert, F. Nguyen Van Dau, F. Petroff, P. Eitenne, G. Creuzet, A. Friederich, and J. Chazelas. Giant Magnetoresistance of (001)Fe/(001)Cr Magnetic Superlattices. *Physical Review Letters*, 61(21):2472–2475, 1988. [1](#)
- [4] C. Chappert, A. Fert, and F. Nguyen van Dau. The emergence of spin electronics in data storage. *Nature Materials*, 6:813, Nov 2007. [1](#)
- [5] B. Dieny, V. S. Speriosu, S. S. P. Parkin, B. A. Gurney, D. R. Wilhoit, and D. Mauri. Giant magnetoresistive in soft ferromagnetic multilayers. *Physical Review B*, 43:1297–1300, Jan 1991. [1](#)
- [6] E. Du Trémollet de lacheisserie, D. Gignoux, and M. Schlenker. *Magnetism*. Springer, 2005. [1](#)
- [7] J F Gregg, I Petej, E Jouguelet, and C Dennis. Spin electronics – a review. *Journal of Physics D: Applied Physics*, 35(R121), 2002. [1](#)
- [8] S Tsunashima. Magneto-optical recording. *Journal of Physics D: Applied Physics*, 34(R87), 2001. [1](#)
- [9] M R J Gibbs, E W Hill, and P J Wright. Magnetic materials for MEMS applications. *Journal of Physics D: Applied Physics*, 37(22):R237–R244, November 2004. [1](#)
- [10] A. Chernyshov, D. Treves, T. Le, C. Papusoi, H. Yuan, A. Ajan, and R. Acharya. Measurement of Magnetic Properties Relevant to Heat-Assisted-Magnetic-Recording. *IEEE Transactions on Magnetics*, 49(7):3572–3575, July 2013. [1](#), [18](#)
- [11] S A Wolf, D D Awschalom, R A Buhrman, J M Daughton, S von Molnár, M L Roukes, A Y Chtchelkanova, and D M Treger. Spintronics: a spin-based electronics vision for the future. *Science*, 294(5546):1488–95, November 2001. [2](#)
- [12] S. N. Piramanayagam. Perpendicular recording media for hard disk drives. *Journal of Applied Physics*, 102(011301), 2007. [2](#)

- [13] S. Mitani, K. Takanashi, M. Sano, H. Fujimori, a. Osawa, and H. Nakajima. Perpendicular magnetic anisotropy and magneto-optical Kerr rotation in FePt(001) monoatomic multilayers. *Journal of Magnetism and Magnetic Materials*, 148(1-2):163–164, July 1995. [2](#), [18](#)
- [14] M. H Kryder, E. C Gage, T W McDaniel, W A Challener, R E Rottmayer, G. Ju, Y-t Hsia, and M F. Erden. Heat Assisted Magnetic Recording. *Proceedings of the IEEE*, 96(11), 2008. [2](#)
- [15] C. A. F. Vaz, J. A. C. Bland, and G. Lauhoff. Magnetism in ultrathin film structures. *Reports on Progress in Physics*, 71(5):056501, May 2008. [2](#)
- [16] D. P. Pappas, C. R. Brundle, and H. Hopster. Reduction of macroscopic moment in ultrathin Fe films as the magnetic orientation changes. *Physical Review B*, 45(14):1–4, 1992. [2](#), [117](#)
- [17] P J van der Zaag, Y Ijiri, J a Borchers, L F Feiner, R M Wolf, J M Gaines, R W Erwin, and M a Verheijen. Difference between blocking and Néel temperatures in the exchange biased  $Fe_3O_4/CoO$  system. *Physical Review letters*, 84(26):6102–5, July 2000. [2](#), [19](#), [87](#), [89](#), [90](#), [116](#), [133](#)
- [18] M. Przybylski, M. Dabrowski, U. Bauer, M. Cinal, and J. Kirschner. Oscillatory magnetic anisotropy due to quantum well states in thin ferromagnetic films (invited). *Journal of Applied Physics*, 111(7):07C102, 2012. [2](#)
- [19] E. Jal, M. Dabrowski, J.-M. Tonnerre, M. Przybylski, S. Grenier, N. Jaouen, and J. Kirschner. Magnetization profile across Au-covered bcc Fe films grown on a vicinal surface of Ag(001) as seen by x-ray resonant magnetic reflectivity. *Physical Review B*, 87(22):224418, June 2013. [2](#), [117](#)
- [20] N. W. Ashcroft and Mermin N. D. *Solid state physics*. Kynoch Press, 1976. [5](#), [6](#), [99](#)
- [21] J. Stöhr and H. C. Siegmann. *Magnetism: From Fundamentals to Nanoscale Dynamics*, volume 152. Springer, 2006. [5](#), [6](#), [8](#), [83](#)
- [22] L. Duó, M. Finazzi, and F. Ciccacci. *Magnetic properties of antiferromagnetic oxide materials*. Wiley-Ch, 2010. [6](#), [16](#), [20](#)
- [23] P Bruno. Tight-binding approach to the orbital magnetic moment and magnetocrystalline anisotropy of transition-metal monolayers. *Physical Review B*, 39(1):865–868, January 1989. [7](#)
- [24] M. Finazzi and S. Altieri. Magnetic dipolar anisotropy in strained antiferromagnetic films. *Physical Review B*, 68(5):054420, August 2003. [7](#), [21](#), [81](#), [98](#)
- [25] S. Blundell. *Magnetism in Condensed Matter*. Oxford University Press, 2001. [7](#)

- [26] W. H. Meiklejohn and C. P. Bean. New magnetic anisotropy. *Physical Review*, 102:1413–1414, Jun 1956. [7](#)
- [27] J Nogués and I K Schuller. Exchange bias. *Journal of Magnetism and Magnetic Materials*, 192(2):203 – 232, 1999. [8](#), [10](#)
- [28] M. M. Soares. *Croissance , structure et magnétisme dans les systèmes à décalage d'échange FM / AFM : approche fondamentale par la physique des surfaces*. PhD thesis, Institut Néel, CNRS/UJF, 2011. [9](#), [16](#), [27](#), [52](#)
- [29] R L Stamps. Mechanisms for exchange bias. *Journal of Physics D: Applied Physics*, 33:247–268, 2000. [8](#)
- [30] A. E. Berkowitz and K. Takano. Exchange anisotropy – a review. *Journal of Magnetism and Magnetic Materials*, 200(1-3):552–570, October 1999. [9](#), [10](#)
- [31] Miguel Kiwi. Exchange bias theory. *Journal of Magnetism and Magnetic materials*, 234:584–595, 2001. [9](#)
- [32] K. O Grady, L. E. Fernandez-Outon, and G. Vallejo-Fernandez. A new paradigm for exchange bias in polycrystalline thin films. *Journal of Magnetism and Magnetic materials*, 322(8):883–899, 2010. [10](#)
- [33] H. Ohldag, A. Scholl, F. Nolting, E. Arenholz, S. Maat, a. Young, M. Carey, and J. Stöhr. Correlation between Exchange Bias and Pinned Interfacial Spins. *Physical Review Letters*, 91(1):017203, July 2003. [10](#)
- [34] Y. Shiratsuchi, H. Noutomi, H. Oikawa, T. Nakamura, M. Suzuki, T. Fujita, K. Arakawa, Y. Takechi, H. Mori, T. Kinoshita, M. Yamamoto, and R. Nakatani. Detection and in situ switching of unreversed interfacial antiferromagnetic spins in a perpendicular-exchange-biased system. *Physical Review Letters*, 109:077202, Aug 2012. [10](#), [92](#)
- [35] G. Nowak, A. Remhof, F. Radu, A. Nefedov, H.-W. Becker, and H. Zabel. Structural and magnetic properties of stoichiometric epitaxial CoO/Fe exchange-bias bilayers. *Physical Review B*, 75(174405), May 2007. [10](#), [90](#)
- [36] P. Müller and S. Andrieu. *Les surfaces solides : concepts et méthodes*. EDP Sciences, 2005. [10](#), [11](#), [12](#)
- [37] W Kuch, L I Chelaru, F Offi, J Wang, M Kotsugi, and J Kirschner. Tuning the magnetic coupling across ultrathin antiferromagnetic films by controlling atomic-scale roughness. *Nature materials*, 5:128–33, March 2006. [10](#)
- [38] H. Ibach. *Physics of surfaces and interfaces*. Springer, 2006. [12](#)
- [39] J. H. Van der Merwe and W.A. Jesser. The prediction and confirmation of critical epitaxial parameters. *Journal of Applied Physics*, 64(10):4968–4974, 1988. [12](#)

- [40] M. Kato. Simple criteria for epitaxial relationships between f.c.c, and b.c.c. crystals. *Materials Science and Engineering*, 146:205–216, 1991. [12](#)
- [41] O M Magnussen, L Zitzler, B Gleich, M R Vogt, and R J Behm. In-situ atomic-scale studies of the mechanisms and dynamics of metal dissolution by high-speed STM. *Electrochimica Acta*, 46:3725–3733, 2001. [12](#)
- [42] A. Hahlin, C. Andersson, J. Dunn, B. Sanyal, O. Karis, and D. Arvanitis. Structure and magnetism of ultrathin epitaxial Fe on Ag(100). *Physical Review B*, 73(13):134423, April 2006. [13](#), [117](#)
- [43] W. F. Jr. Egelhoff and I. Jacob. Reflection High-Energy Electron Diffraction (RHEED) Oscillations at 77 K. *Physical Review Letters*, 62(8):921–924, 1989. [13](#), [117](#)
- [44] Z. Q. Qiu, J. Pearson, and S.D. Bader. Two dimensional Ising transition of epitaxial Fe films grown on Ag(100). *Physical Review B*, 49(13), 1994. [13](#), [117](#)
- [45] R. Bali, M. M. Soares, A. Y. Ramos, H. C. N. Tolentino, F. Yildiz, C. Boudot, O. Proux, M. De Santis, M. Przybylski, and J. Kirschner. Magnetic and structural properties of the Fe layers in CoO/Fe/Ag(001) heterostructure. *Applied Physics Letters*, 100(13), march 2012. [13](#), [74](#), [117](#)
- [46] F. Aqra and A. Ayyad. Surface energies of metals in both liquid and solid states. *Applied Surface Science*, 257(15):6372–6379, May 2011. [14](#)
- [47] R J Hicken, S J Gray, A Ercole, C Daboo, D J Freeland, E Gu, E Ahmad, and J A C Bland. Magnetic anisotropy in ultrathin epitaxial Fe/Ag(100) films with overlayers. *Physical Review B*, 55(9):5898–5907, 1997. [14](#)
- [48] M.H. Langelaar and D.O. Boerma. Fe adatoms on Ag(100): site exchange and mobility. *Surface Science*, 395:131–137, 1998. [14](#), [119](#)
- [49] G. Ketteler, W. Weiss, W. Ranke, and R. Schlögl. Bulk and surface phases of iron oxides in an oxygen and water atmosphere at low pressure. *Physical Chemistry Chemical Physics*, 3:1114–1122, 2001. [14](#)
- [50] E. J. W. Verwey. Electronic conduction of magnetite ( $Fe_3O_4$ ) and its transition point at low temperatures. *Nature*, 3642:327, 1939. [14](#)
- [51] Friedrich Walz. The Verwey transition - a topical review. *Journal of Physics: Condensed Matter*, 14(12):R285–R340, April 2002. [14](#)
- [52] M Fonin, Y S Dedkov, R Pentcheva, U Rüdiger, and G Güntherodt. Magnetite: a search for the half-metallic state. *Journal of Physics: Condensed matter*, 19(31):315217, August 2007. [14](#), [15](#), [116](#), [124](#), [132](#)

- [53] R. J Hill, J. R Craig, and G V Gibbs. Systematics of the Spinel Structure Type. *Physics and chemistry of minerals*, 4:317–339, 1979. 15
- [54] J.M. Gaines, P.J.H. Bloemen, J.T. Kohlhepp, C.W.T. Bulle-Lieuwma, R.M. Wolf, A. Reinders, R.M. Jungblut, P.A.A. van der Heijden, J.T.W.M. van Eemeren, J. aan de Stegge, and W.J.M. de Jonge. An STM study of  $Fe_3O_4(100)$  grown by molecular beam epitaxy. *Surface Science*, 373:85–94, 1997. 15
- [55] Florian Bertram. *The structure of ultrathin iron oxide films studied by x-ray diffraction*. PhD thesis, Universität Osnabrück, 2012. 15
- [56] S. A. Chambers and S. A. Joyce. Surface termination, composition and reconstruction of  $Fe_3O_4(001)$  and  $\gamma - Fe_2O_3(001)$ . *Surface Science*, 420:111–122, 1999. 15, 129
- [57] J R Rustad, E Wasserman, and A R Felmy. A molecular dynamics investigation of surface reconstruction on magnetite (001). *Surface Science Letters*, 432:583–588, 1999. 15
- [58] B. Stanka, W. Hebenstreit, U. Diebold, and S. A. Chambers. Surface reconstruction of  $Fe_3O_4(001)$ . *Surface Science*, 448:49–63, 2000. 15, 131, 132
- [59] F C Voogt, T. Fujii, P. J. M. Smulders, L. Niesen, M. A. James, and T. Hibma. NO<sub>2</sub>-assisted molecular-beam epitaxy of  $Fe_3O_4$ ,  $Fe_{3-\delta}O_4$  and  $\gamma - Fe_2O_3$  thin films on MgO(100). *Physical Review B*, 60(15):193–206, 1999. 15
- [60] N. Spiridis, J. Barbasz, Z. Kodziana, and J. Korecki.  $Fe_3O_4(001)$  films on Fe(001): Termination and reconstruction of iron-rich surfaces. *Physical Review B*, 74(15):155423, October 2006. 15
- [61] G. S. Parkinson, T. a. Manz, Z. Novotný, P. T. Sprunger, R. L. Kurtz, M. Schmid, D. S. Sholl, and U. Diebold. Antiphase domain boundaries at the  $Fe_3O_4(001)$  surface. *Physical Review B*, 85(19):195450, May 2012. 15, 132
- [62] R. Pentcheva, F. Wendler, H. L. Meyerheim, W. Moritz, N. Jedrecy, and M. Scheffler. Jahn-Teller Stabilization of a 'Polar' Metal Oxide Surface :  $Fe_3O_4(001)$ . *Physical Review Letters*, 94(12):126101, April 2005. 15
- [63] D. L. Abernathy, S. G. J. Mochrie, D. M. Zehner, G. Grubel, and D. Gibbs. Orientational epitaxy and lateral structure of the hexagonally reconstructed Pt(001) and Au(001) surfaces. *Physical Review B*, 45(16):9272–9291, 1992. 16, 17
- [64] V. Fiorentini, M. Methfessel, and M. Schemer. Reconstruction Mechanism of fcc Transition Metal (001) Surfaces. *Physical Review Letters*, 71(7):1051–1054, 1993. 17
- [65] Paula Havu, Volker Blum, Ville Havu, Patrick Rinke, and Matthias Scheffler. Large-scale surface reconstruction energetics of pt(100) and au(100) by all-electron density functional theory. *Physical Review B*, 82:161418, Oct 2010. 17



- [66] A. Borg, A.-M. Hilmen, and E. Bergene. STM studies of clean, CO- and O<sub>2</sub>-exposed Pt(100)-hex-R0.7Å°. *Surface Science*, 306(1-2):10–20, 1994. 17
- [67] Matthias Batzill and Bruce E Koel. Silver on Pt(100) room temperature growth and high temperature alloying. *Surface Science*, 553(1-3):50–60, March 2004. 18
- [68] B. Schaefer, M. Nohlen, and K. Wandelt. Growth of Copper on Reconstructed Pt(100). *The Journal of Physical Chemistry B*, 108(38):14663–14670, September 2004. 18
- [69] M. Valvidares. *Relationship between Structure and Magnetic Anisotropy of Ultrathin Epitaxial Cobalt films on Platinum substrates*. PhD thesis, Universidad de Oviedo Departamento de fisica, 2005. 18, 99
- [70] A Sakuma. First principle calculation of the Magnetocrystalline Anisotropy Energy of FePt and CoPt Ordered Alloys. *Journal of the Physical Society of Japan*, 63(8):3053–3058, 1994. 18
- [71] H. Kanazawa, G. Lauhoff, and T. Suzuki. Magnetic and structural properties of (Co<sub>x</sub>Fe<sub>100-x</sub>)<sub>50</sub>Pt<sub>50</sub> alloy thin films. *Journal of Applied Physics*, 87(9):6143, 2000. 18
- [72] R. F. C. Farrow, D. Weller, R. F. Marks, M. F. Toney, A. Cebollada, and G. R. Harp. Control of the axis of chemical ordering and magnetic anisotropy in epitaxial FePt films. *Journal of Applied Physics*, 79(8):5967, 1996. 18
- [73] C.-J. Sun, D. Stafford, and R. Acharya. FePt-Based Exchange-Coupled Composite Perpendicular Recording Media. *IEEE Transactions on Magnetics*, 46(6):1795–1797, June 2010. 18
- [74] T W McDaniel. Ultimate limits to thermally assisted magnetic recording. *Journal of Physics: Condensed Matter*, 17(7):R315–R332, February 2005. 18
- [75] J. Honolka, T. Lee, K. Kuhnke, a. Enders, R. Skomski, S. Bornemann, S. Mankovsky, J. Minár, J. Staunton, H. Ebert, M. Hessler, K. Fauth, G. Schütz, a. Buchsbaum, M. Schmid, P. Varga, and K. Kern. Magnetism of FePt Surface Alloys. *Physical Review Letters*, 102(6):067207, February 2009. 18
- [76] S. Okamoto, N. Kikuchi, O. Kitakami, T. Miyazaki, Y. Shimada, and K. Fukamichi. Chemical-order-dependent magnetic anisotropy and exchange stiffness constant of FePt (001) epitaxial films. *Physical Review B*, 66(2):024413, July 2002. 18
- [77] Y. Nosé, A. Kushida, T. Ikeda, H. Nakajima, K. Tanaka, and H. Numakura. Re-examination of Phase Diagram of Fe-Pt System. *Materials Transactions*, 44(12):2723–2731, 2003. 18
- [78] P. Bayliss. Revised unit-cell dimensions, space group and chemical formula of some metallic minerals. *Canadian Mineralogist*, 28:751–755, 1990. 19

- [79] J. Lyubina, O. Isnard, O. Gutfleisch, K.-H. Müller, and L. Schultz. Ordering of nanocrystalline Fe–Pt alloys studied by in situ neutron powder diffraction. *Journal of Applied Physics*, 100(9):094308, 2006. 19, 55
- [80] Y. F. Ding, J. S. Chen, E. Liu, C. J. Sun, and G. M. Chow. Effect of lattice mismatch on chemical ordering of epitaxial  $L1_0$  FePt films. *Journal of Applied Physics*, 97(10):10H303, 2005. 19
- [81] G. Brown, B. Kraczek, A. Janotti, T. Schulthess, G. Stocks, and D. Johnson. Competition between ferromagnetism and antiferromagnetism in FePt. *Physical Review B*, 68(5):052405, August 2003. 19
- [82] Zhihong Lu, Roman V. Chepulskii, and W. H. Butler. First-principles study of magnetic properties of  $L1_0$ -ordered MnPt and FePt alloys. *Physical Review B*, 81(9):094437, March 2010. 19
- [83] A. Cebollada, D. Weller, J. Sticht, G.R. Harp, R.F.C. Farrow, R.F. Marks, R. Savoy, and J.C. Scott. Enhanced magneto-optical Kerr effect in spontaneously ordered FePt alloys: Quantitative agreement between theory and experiment. *Physical Review B*, 50(5), 1994. 19
- [84] C. Antoniak, M E Gruner, M Spasova, A V Trunova, F M Römer, A Warland, B Krumme, K Fauth, S Sun, P Entel, M Farle, and H Wende. A guideline for atomistic design and understanding of ultrahard nanomagnets. *Nature communications*, 2:528, January 2011. 19, 79
- [85] T. Shima, K. Takanashi, Y. K. Takahashi, and K. Hono. Coercivity exceeding 100 kOe in epitaxially grown FePt sputtered films. *Applied Physics Letters*, 85(13):2571, 2004. 19
- [86] S. Imada, A. Yamasaki, S. Suga, T. Shima, and K. Takanashi. Perpendicular magnetization of  $L1_0$ -ordered FePt films in the thinnest limit. *Applied Physics Letters*, 90(13):132507, 2007. 19, 76, 79
- [87] Damien Le Roy. *Anisotropie d'échange dans des agrégats de cobalt et nickel-cuivre posés sur CoO ( 111 )*. PhD thesis, 2009. 19
- [88] J. Tonnerre, M. De Santis, S. Grenier, H. Tolentino, V. Langlais, E. Bontempi, M. García-Fernández, and U. Staub. Depth Magnetization Profile of a Perpendicular Exchange Coupled System by Soft-X-Ray Resonant Magnetic Reflectivity. *Physical Review Letters*, (15):157202, April. 19
- [89] S. Maat, K. Takano, S. Parkin, and E. Fullerton. Perpendicular Exchange Bias of Co/Pt Multilayers. *Physical Review Letters*, 87(8):087202, August 2001. 19

- [90] W. Jauch, M. Reehuis, H. J. Bleif, F. Kubanek, and P. Pattison. Crystallographic symmetry and magnetic structure of CoO. *Physical Review B*, 64:052102, Jul 2001. [19](#), [21](#), [64](#), [69](#), [81](#)
- [91] E. Beaurepaire, H. Bulou, F. Scheurer, and K. Jean-Paul, editors. *Magnetism and Synchrotron Radiation*. Springer, 2010. [21](#), [26](#), [41](#), [42](#), [44](#)
- [92] A. Schrön, C. Rödl, and F. Bechstedt. Crystalline and magnetic anisotropy of the 3d-transition metal monoxides MnO, FeO, CoO, and NiO. *Physical Review B*, 86:115134, Sep 2012. [21](#), [80](#)
- [93] P. W. Anderson. Antiferromagnetism. Theory of Superexchange Interaction. *Physical Review*, 79:350–356, Jul 1950. [21](#)
- [94] P. W. Anderson. *Theory of Magnetic Exchange Interactions: Exchange in Insulators and Semiconductors*, volume 14 of *Solid State Physics*. Academic Press, 1963. [21](#)
- [95] K I Kugel and D I Khomskii. The Jahn-Teller effect and magnetism : transition metal compounds. *Soviet Physics Uspekhi*, 25(231), 1982. [21](#)
- [96] K. Tomiyasu, T. Inami, and N. Ikeda. Magnetic structure of CoO studied by neutron and synchrotron x-ray diffraction. *Physical Review B*, 70:184411, Nov 2004. [21](#), [75](#)
- [97] W. L. Roth. *Physical Review*, 110:1333, 1958. [21](#), [80](#), [81](#)
- [98] S. I. Csiszar, M. W. Haverkort, Z. Hu, A. Tanaka, H. H. Hsieh, H.-J. Lin, C. T. Chen, T. Hibma, and L. H. Tjeng. Controlling Orbital Moment and Spin Orientation in CoO Layers by Strain. *Physical Review Letters*, 95:187205, Oct 2005. [22](#), [81](#), [93](#), [137](#)
- [99] Wikiversité. Introduction à l’infographie : Notions fondamentales. [25](#)
- [100] E. Beaurepaire, H. Bulou, L. Joly, and F. Scheurer, editors. *Magnetism and Synchrotron Radiation: Towards the Fourth Generation Light Sources*, volume 151. Springer. [26](#), [44](#)
- [101] J. P. Pérez, R. Carles, and R. Fleckinger. *Electromagnétisme – Fondements et applications*. Elsevier–Masson, 2001. [26](#)
- [102] Jens Als-Nielsen and Des McMorrow. *Elements of Modern X-ray Physics, Second Edition*. Wiley, 2011. [27](#), [39](#)
- [103] B.E. Warren. *X-ray diffraction*. Addison-Wesley, Reading, 1969. [27](#), [34](#), [55](#)
- [104] I. K. Robinson and J. D. Tweet. Surface diffraction. *Reports on Progress in Physics*, 55(October 1991):599–651, 1992. [27](#)
- [105] I. K. Robinson. Crystal truncation rods and surface roughness. *Physical Review B*, 33(6):3830–3836, Mar 1986. [27](#)

- [106] Christian M. Schlepütz. *Systematic Structure Investigation of YBCO Thin Films with Direct Methods and Surface X-ray Diffraction*. PhD thesis, Universität Zürich, 2009. [27](#), [30](#), [31](#), [33](#)
- [107] M. De Santis. *Structure of ultrathin antiferromagnetic films for exchange coupling systems: metallic Mn alloys and insulating CoO films*. Habilitation à diriger des recherches, Institut Néel, CNRS/UJF, 2014. [27](#)
- [108] E. Vlieg. Integrated Intensities Using a Six-Circle Surface X-ray Diffractometer. *Journal of Applied Crystallography*, (30):532–543, 1997. [34](#), [57](#)
- [109] E. Vlieg. From beam time to structure factors. (August), 2001. [35](#)
- [110] E. Vlieg. Rod: a program for surface crystallography. *J. Appl. Crystallogr.*, 33:401–405, 2000. [35](#), [65](#)
- [111] O. Robach. Appendix to the manual of the ROD program ( experimental version ) : Robach' s extension. (001):1—51, 2001. [35](#)
- [112] R. Baudoing-Savois, M De Santis, M.C. Saint-Lager, P Dolle, O Geaymond, P Taunier, P Jeantet, J P Roux, G Renaud, A Barbier, O Robach, O Ulrich, A Mougin, and G. Bérard. A new UHV diffractometer for surface structure and real time molecular beam deposition studies with synchrotron radiations at ESRF. *Nuclear Instruments and Methods in Physics Research B*, 149:213–227, 1999. [36](#)
- [113] L. G. Parrat. Surface Studies of Solids by Total Reflection of X-Rays. *Physical Review*, 95(2), 1954. [37](#)
- [114] Maurits Haverkort. *Spin and orbital degrees of freedom in transition metal oxide thin films studied by soft x-ray absorption spectroscopy*. PhD thesis, Universität zu Köln, 2005. [40](#), [43](#)
- [115] O Bunău and Y Joly. Self-consistent aspects of x-ray absorption calculations. *Journal of Physics: Condensed matter*, 21(34), August 2009. [40](#)
- [116] F Hippert, E Geissler, J-L Hodeau, E Lelièvre-Berna, and J-R Regnard, editors. *Neutron and x-ray spectroscopy*. Springer, 2006. [42](#)
- [117] G. van der Laan, E. Arenholz, R. Chopdekar, and Y. Suzuki. Influence of crystal field on anisotropic x-ray magnetic linear dichroism at the  $Co^{2+}$   $L_{2,3}$  edges. *Physical Review B*, 77(6):1–11, February 2008. [44](#), [80](#), [84](#), [85](#), [91](#), [113](#)
- [118] T. J. Regan, H. Ohldag, C. Stamm, F. Nolting, J. Lüning, J. Stöhr, and R. L. White. Chemical effects at metal/oxide interfaces studied by x-ray-absorption spectroscopy. *Physical Review B*, 64:214422, Nov 2001. [45](#), [69](#)

- [119] Z. Q. Qiu and S. D. Bader. Surface magneto-optic Kerr effect. *Review of Scientific Instruments*, 71(3):1243–1255, 2000. 45
- [120] K.-M. Schindler, J. Wang, A. Chassé, H. Neddermeyer, and W. Widdra. Low-energy electron diffraction structure determination of an ultrathin CoO film on Ag(001). *Surface Science*, 603(16):2658–2663, August 2009. 51, 139
- [121] M. De Santis, A. Buchsbaum, P. Varga, and M. Schmid. Growth of ultrathin cobalt oxide films on Pt(111). *Physical Review B*, 84:125430, Sep 2011. 51, 57, 58, 73
- [122] L. Gagnaniello, F. Allegretti, S. Agnoli, G. Parteder, A. Barolo, F. Bondino, S. Surnev, G. Granozzi, and F.P. Netzer. Cobalt oxide nanolayers on Pd(100): The thickness-dependent structural evolution. *Surface Science*, 604(21-22):2002, 2010. 51, 57
- [123] W. Meyer, D. Hock, K. Biedermann, M. Gubo, S. Müller, L. Hammer, and K. Heinz. Coexistence of Rocksalt and Wurtzite Structure in Nanosized CoO Films. *Physical Review Letters*, 101:016103, Jul 2008. 51, 97
- [124] A. Boussendel, N. Baadji, A. Haroun, H. Dreyssé, and M. Alouani. Effect of substrate strain on calculated magnetic properties and magnetic anisotropy energy of CoO. *Physical Review B*, 81:184432, May 2010. 51
- [125] K. He, L.J. Zhang, X.C. Ma, J.F. Jia, Q.K. Xue, and Z.Q. Qiu. Growth and magnetism of ultrathin Fe films on Pt(100). *Physical Review B*, 72(15):155432, 2005. 52
- [126] Márcio M. Soares, Hélio C. N. Tolentino, Maurizio De Santis, Aline Y. Ramos, and Júlio C. Cezar. Highly anisotropic epitaxial  $L1_0$  FePt on Pt(001). *Journal of Applied Physics.*, 109(7):07D725, 2011. 52, 55, 71
- [127] D. Goll, A. Breitling, N.H. Goo, W. Sigle, M. Hirscher, and G. Schütz. Hard Magnetic FePt Thin Films and Nanostructures in  $L1_0$  Phase. *Journal of Iron and Steel Research, International*, 13:97–101, January 2006. 52
- [128] Caroline H. MacGillavry and Gerard D. Rieck. *International Tables for X-ray Crystallography Vol3*. Kynoch Press, 1968. 55
- [129] Karine Chesnel. *Diffusion magnétique résonnante des RX appliquée à l'étude des nanostructures magnétiques*. PhD thesis, Université Joseph Fourier, Grenoble, 2002. 75
- [130] M. Blume. Magnetic scattering of x rays (invited). *Journal of Applied Physics*, 57(8):3615, 1985. 75
- [131] Márcio M. Soares, Anne D. Lamirand, Hélio C. N. Tolentino, Aline Y. Ramos, and Maurizio De Santis. Perpendicular magnetic anisotropy of epitaxial ultrathin FePt probed by XMCD. *Physical Review B*, in prep., 2014. 77

- [132] J. Wu, J. S. Park, W. Kim, E. Arenholz, M. Liberati, a. Scholl, Y. Z. Wu, Chanyong Hwang, and Z. Q. Qiu. Direct Measurement of Rotatable and Frozen CoO Spins in Exchange Bias System of CoO/Fe/Ag(001). *Physical Review Letters*, 104(21):3–6, May 2010. [80](#), [89](#), [116](#), [137](#)
- [133] F. Mittendorfer, M. Weinert, R. Podloucky, and J. Redinger. Strain and Structure Driven Complex Magnetic Ordering of a CoO Overlayer on Ir(100). *Physical Review Letters*, 109(1):015501, July 2012. [82](#)
- [134] N. C. Koon. Calculations of exchange bias in thin films with ferromagnetic / antiferromagnetic interfaces. *Physical Review Letters*, 78:4865–4868, Jun 1997. [88](#)
- [135] T. Schulthess and W. Butler. Consequences of Spin-Flop Coupling in Exchange Biased Films. *Physical Review Letters*, 81(20):4516–4519, November 1998. [89](#)
- [136] J. Li, M. Przybylski, F. Yildiz, X.L. Fu, and Y.Z. Wu. In-plane spin reorientation transition in Fe/NiO bilayers on Ag(1,1,10). *Physical Review B*, 83:094436, Mar 2011. [89](#)
- [137] A. E. Berkowitz and Kentaro Takano. Exchange anisotropy – a review. *Journal of Magnetism and Magnetic materials*, 200(1-3):552–570, Oct 1999. [89](#)
- [138] T. Ambrose and C. L. Chien. Finite-Size Effects and Uncompensated Magnetization in Thin Antiferromagnetic CoO Layers. *Physical Review Letters*, 76:1743–1746, Mar 1996. [89](#)
- [139] M. Molina-Ruiz, A. F. Lopeandía, F. Pi, D. Givord, O. Bourgeois, and J. Rodríguez-Viejo. Evidence of finite-size effect on the Néel temperature in ultrathin layers of CoO nanograins. *Physical Review B*, 83:140407, Apr 2011. [89](#)
- [140] N Nakajima, T Koide, T Shidara, H Miyauchi, H Fukutani, A Fujimori, K Iio, T Katayama, M Nývlt, and Y Suzuki. Perpendicular Magnetic Anisotropy Caused by Interfacial Hybridization via Enhanced Orbital Moment in Co|Pt Multilayers: Magnetic Circular X-Ray Dichroism Study. *Physical Review Letters*, 81(23):5229–5232, 1998. [90](#)
- [141] R. Abrudan, J. Miguel, M. Bernien, C. Tieg, M. Piantek, J. Kirschner, and W. Kuch. Structural and magnetic properties of epitaxial Fe/CoO bilayers on Ag(001). *Physical Review B*, 77(1):014411, January 2008. [91](#), [117](#), [138](#)
- [142] Tjipke Hibma and Maurits Haverkort. *Magnetic properties of antiferromagnetic oxide materials*. Wiley-VCH, 2010. [93](#)
- [143] M. Gubo, C. Ebensperger, W. Meyer, L. Hammer, K. Heinz, F. Mittendorfer, and J. Redinger. Tuning the growth orientation of epitaxial films by interface chemistry. *Physical Review Letters*, 108:066101, Feb 2012. [97](#)

- [144] K Heinz and L Hammer. Epitaxial cobalt oxide films on Ir(100)-the importance of crystallographic analyses. *Journal of Physics: Condensed Matter*, 25(17):173001, May 2013. 97
- [145] G. A. Prinz. Stabilization of bcc co via epitaxial growth on gaas. *Physical Review Letters*, 54:1051–1054, Mar 1985. 99, 120
- [146] G Prévot, B Croset, Y Girard, a Coati, Y Garreau, M Hohage, L.D Sun, and P Zeppenfeld. Elastic origin of the O/Cu(110) self-ordering evidenced by GIXD. *Surface Science*, 549(1):52–66, January 2004. 102, 103
- [147] Geoffroy Prévot, Alessandro Coati, Bernard Croset, and Yves Garreau. Direct observation of elastic displacement modes by grazing-incidence X-ray diffraction. *Journal of Applied Crystallography*, 40(5):874–882, September 2007. 102
- [148] P. Torelli, E. A. Soares, G. Renaud, S. Valeri, X.X. Guo, and P. Luches. Nanostructuring of CoO film by misfit dislocations. *Surface Science*, 601(13):2651–2655, July 2007. 103, 133, 139
- [149] C. T. Chen, Y.U. Idzerda, H.-J. Lin, N. V. Smith, G. Meigs, E. Chaban, G. H. Ho, E. Pellegrin, and F. Sette. Experimental Confirmation of the X-Ray Magnetic Circular Dichroism Sum Rules for Iron and Cobalt. *Physical Review Letters*, 75(1):152–155, 1995. 108
- [150] A. Brambilla, P. Sessi, M. Cantoni, L. Duò, M. Finazzi, and F. Ciccacci. Epitaxial growth and characterization of CoO/Fe(001) thin film layered structures. *Thin Solid Films*, 516(21):7519–7524, September 2008. 108, 117
- [151] F. Greullet, E. Snoeck, C. Tiusan, M. Hehn, D. Lacour, O. Lenoble, C. Magen, and L. Calmels. Large inverse magnetoresistance in fully epitaxial Fe/Fe<sub>3</sub>O<sub>4</sub>/MgO/Co magnetic tunnel junctions. *Applied Physics Letters*, 92(5):053508, 2008. 116
- [152] Hui-Qiong Wang, Eric Altman, and Victor Henrich. Interfacial properties between CoO (100) and Fe<sub>3</sub>O<sub>4</sub>(100). *Physical Review B*, 77(8):085313, February 2008. 116, 133
- [153] F. Radu, A. Nefedov, J. Grabis, G. Nowak, A. Bergmann, and H. Zabel. Soft X-ray resonant magnetic scattering studies on Fe/CoO exchange bias system. *Journal of Magnetism and Magnetic Materials*, 300(1):206–210, May 2006. 116
- [154] Z. Q. Qiu, J. Pearson, and S. D. Bader. Asymmetry of the Spin Reorientation Transition in Ultrathin Fe Films and Wedges Grown on Ag(100). *Physical Review Letters*, 70(7):1006–1010, 1993. 116, 117
- [155] J. Li, Y. Meng, J. S. Park, C. Jenkins, E. Arenholz, A. Scholl, A. Tan, H. Son, H. Zhao, Chanyong Hwang, Y. Z. Wu, and Z. Q. Qiu. Determination of the Fe magnetic anisotropies and the CoO frozen spins in epitaxial CoO/Fe/Ag(001). *Physical Review B*, 84(9):2–7, September 2011. 116



- [156] C.L. Wooten, J. Chen, G.A. Mulhollan, J.L. Erskine, and J.T. Markert. Direct observation of enhanced magnetic moments in Fe/Ag(100). *Physical Review B*, 49(14), 1994. [117](#)
- [157] D. M. Schaller, D. E. Bürgler, C M Schmidt, F Meisinger, and H.-J. Güntherodt. Spin reorientations induced by morphology changes in Fe/Ag(001). *Physical Review B*, 59(22):516–519, 1999. [117](#), [126](#)
- [158] M Canepa, P Cantini, O Ricciardi, S Terreni, and L Mattera. Temperature effects on morphology and composition of ultrathin heteroepitaxial films: Fe on Ag(100). *Surface Science*, 429(1-3):34–45, June 1999. [117](#), [119](#)
- [159] H Li, Y S Li, J Quinn, D. Tian, J. Sokolov, F. Jona, and P. M. Marcus. Quantitative low-energy electron-diffraction study of the epitaxy of Fe on Ag(001): Questions about the growth mode. *Physical Review B*, 42(14):9195, December 1990. [117](#)
- [160] E. Młyńczak, J. Gurgul, J. Przewoźnik, D. Wilgocka-Ślęzak, K. Freindl, N. Spiridis, and J. Korecki. Effect of interfacial iron oxidation on the exchange bias in CoO/Fe bilayers. *Applied Surface Science*, 304:86–90, June 2014. [117](#)
- [161] D. Bruns, S. R. Lindemann, K. Kuepper, T. Schemme, and J. Wollschläger.  $Fe_3O_4$  films on Ag(001)—Generation of high-quality epitaxial ferrimagnetic metal oxide films. *Applied Physics Letters*, 103(5):052401, 2013. [125](#)
- [162] J. B. Moussy. From epitaxial growth of ferrite thin films to spin-polarized tunnelling. *Journal of Physics D: Applied Physics*, 46(14):143001, April 2013. [129](#)
- [163] T. Terashima and Y. Bando. Formation and magnetic properties of artificial superlattice of CoO- $Fe_3O_4$ . *Thin Solid Films*, 152:455–463, 1987. [133](#)
- [164] A. P. Malozemoff. Random-field model of exchange anisotropy at rough ferromagnetic-antiferromagnetic interfaces. *Physical Review B*, 35(7), 1987. [135](#)
- [165] S. A. Chambers, R F C Farrow, S Maat, M F Toney, and L Folks. Molecular beam epitaxial growth and properties of  $CoFe_2O_4$  on MgO(001). *Journal of Magnetism and Magnetic Materials*, 246:124–139, 2002. [136](#)
- [166] Myung-Soon Lee, Tae-Young Kim, Choong-Sub Lee, Jung-Chul Park, Yeong Il Kim, and Don Kim. Magnetic and structural anisotropy of the Co- $Fe_3O_4$  films deposited by the thin-liquid film method. *Journal of Magnetism and Magnetic Materials*, 268(1-2):62–69, January 2004. [137](#)
- [167] P. Morrall, F. Schedin, G. Case, M. Thomas, E. Dudzik, G. van der Laan, and G. Thornton. Stoichiometry of  $Fe_{3-\delta}O_4(111)$  ultrathin films on Pt(111). *Physical Review B*, 67(21):214408, June 2003. [137](#)



- [168] E. Arenholz, G. van der Laan, R. Chopdekar, and Y. Suzuki. Anisotropic x-ray magnetic linear dichroism at the  $\text{Fe}L_{2,3}$  edges in  $\text{Fe}_3\text{O}_4$ . *Physical Review B*, 74(9):094407, September 2006. 138
- [169] J Wollschläger, D Erdös, H Goldbach, R Höpken, and K.M Schröder. Growth of nio and mgo films on ag(100). *Thin Solid Films*, 400(1–2):1 – 8. 139
- [170] A. D. Lamirand, M. M. Soares, M. De Santis, A. Y. Ramos, S. Grenier, and H. C. N. Tolentino. Strain driven monoclinic distortion of ultrathin CoO films in CoO/Pt(001) and exchange-coupled CoO/PtFe/Pt(001) systems. *Journal of Physics: Condensed Matter*, in prep., 2015. 144
- [171] A. D. Lamirand, M. M. Soares, A. Y. Ramos, H. C. N. Tolentino, M. De Santis, J. C. Cezar, A. de Siervo, and M. Jamet. Robust perpendicular exchange coupling in an ultrathin CoO/PtFe double layer: Strain and spin orientation. *Physical Review B*, 88(14):140401, October 2013. 144
- [172] A. D. Lamirand, M. M. Soares, A. Y. Ramos, H. C. N. Tolentino, M. De Santis, J. C. Cezar, A. de Siervo, and M. Jamet. Spin orientation in an ultrathin CoO/PtFe double-layer with perpendicular exchange coupling. *Journal of Magnetism and Magnetic materials*, 373:6 – 9, 2015. 144



---

## Résumé

Ce travail de thèse porte sur la détermination de la structure atomique, électronique et magnétique de couches ultraminces ferromagnétique et antiferromagnétique pour une meilleure compréhension du mécanisme de couplage d'échange qui peut avoir lieu à leur interface. Le couplage d'échange, effet de l'interaction entre les deux matériaux, se manifeste par un décalage du cycle d'hystérésis et une augmentation de la coercivité en-dessous de la température de blocage. Nous avons porté notre attention sur les systèmes de CoO/FePt sur Pt(001), CoO/Fe et CoO/Fe<sub>3</sub>O<sub>4</sub> sur Ag(001) et combiné des techniques expérimentales principalement utilisant le rayonnement synchrotron pour les caractériser. Dans un premier temps, nous avons optimisé l'élaboration de ces systèmes dans un environnement d'ultra-haut vide (UHV) par la recherche de surfaces adaptées, le contrôle fin des conditions de croissance et le suivi de la structure par diffraction de surface des rayons X *in situ*. Leur structure cristalline a ensuite été caractérisée avec précision. Dans un deuxième temps, nous avons étudié leurs structure et propriétés magnétiques *ex situ* via le dichroïsme magnétique circulaire et linéaire des rayons X et l'effet Kerr magnéto-optique. La relation entre le couplage d'échange et la structure de l'interface est discutée tout au long de ce manuscrit.

## Abstract

This thesis deals with the determination of atomic, electronic and magnetic structure of ferromagnetic and antiferromagnetic ultrathin layers to better understand the mechanism of the exchange coupling which could takes place at their interface. Exchange coupling, expression of the interaction between the two materials, manifests itself by a shift of hysteresis loop and an increase in coercivity below the blocking temperature. We have paid attention to the systems of CoO/FePt on Pt(001), CoO/Fe and CoO/Fe<sub>3</sub>O<sub>4</sub> on Ag(001). We combined experimental techniques mainly using synchrotron light to characterize them. As a first step, we optimized in a ultra-high vacuum (UHV) environment the elaboration of the systems looking for an appropriate surface, the high control of growth conditions and the supervision of the structure by *in situ* x-ray surface diffraction. The crystalline structure was then precisely detailed. As a second step, we studied the magnetic structure and properties *ex situ* by x-ray magnetic circular and linear dichroism and magneto-optic Kerr effect. The relation between exchange coupling and interface structure is discussed all along the manuscript.